DE GRUYTER

Jianyu Chen, Jun Luo, Qijin Luo et al.

WASTEWATER TREATMENT

APPLICATION OF NEW FUNCTIONAL MATERIALS

CESP

Jianyu Chen, Jun Luo, Qijin Luo, Zhihua Pang

Wastewater Treatment

Also of interest

Materials Science
Volume 1
Structure
Hu, Cai, Rong (Ed.), 2018
ISBN 978-3-11-049512-6, e-ISBN 978-3-11-049534-8

Materials Science
Volume 2
Phase Transformation and Properties
Hu, Cai, Rong (Ed.), 2018
ISBN 978-3-11-049515-7, e-ISBN 978-3-11-049537-9

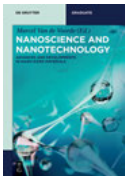

Nanoscience and Nanotechnology
Advances and Developments in Nano-sized Materials
Van de Voorde (Ed.), 2018
ISBN 978-3-11-054720-7, e-ISBN 978-3-11-054722-1

Green Chemical Processing
Volume 1
Sustainable Green Chemistry.
Benvenuto (Ed.), 2017
ISBN 978-3-11-044189-5, e-ISBN 978-3-11-043585-6
ISSN 2366-2115

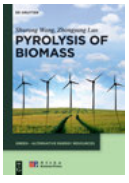

GREEN – Alternative Energy Resources
Volume 1
Pyrolysis of Biomass.
Wang, Luo, 2016
ISBN 978-3-11-037457-5, e-ISBN 978-3-11-036966-3
ISSN 2509-7237

Jianyu Chen, Jun Luo, Qijin Luo, Zhihua Pang

Wastewater Treatment

Application of New Functional Materials

DE GRUYTER

China Environment Publishing Group

Authors
Jianyu Chen
South China Institute of Environmental Sciences
Ministry of Ecology and Environment
People's Republic of China

Jun Luo
South China Institute of Environmental Sciences
Ministry of Ecology and Environment
People's Republic of China

Qijin Luo
South China Institute of Environmental Sciences
Ministry of Ecology and Environment
People's Republic of China

Zhihua Pang
South China Institute of Environmental Sciences
Ministry of Ecology and Environment
People's Republic of China

Translator
Dan Lu
Lederstr. 30
Giengen
Germany

ISBN 978-3-11-054278-3
e-ISBN (PDF) 978-3-11-054438-1
e-ISBN (EPUB) 978-3-11-054298-1

Library of Congress Control Number: 2018947668

Bibliographic information published by the Deutsche Nationalbibliothek
The Deutsche Nationalbibliothek lists this publication in the Deutsche Nationalbibliografie; detailed bibliographic data are available on the Internet at http://dnb.dnb.de.

Typesetting: Integra Software Services Pvt. Ltd.
Printing and binding: CPI books GmbH, Leck
Cover image: BlackJack3D / E+ / Getty Images Plus

www.degruyter.com

Foreword

Functional materials are one of the most active research areas in the field of materials science, and have been widely used in our day-to-day life. Functional materials for water purification technology is an interdisciplinary subject of Engineering Materials Science and Environmental Engineering; the basic feature is the application of naturally or synthetically modified materials (such as zeolite, activated carbon and nano-catalytic iron) to achieve the purpose of removing various types of pollutants in water through the study of physical chemistry or biochemistry and other methods of the latest water purification processes.

The research and utilization of various environmental functional materials are very extensive. The latest research results of the authors are the main narrative objective of this book, and research results from other researchers are also referenced. Besides research focus, advanced technology and engineering applications are also selected and summed up in this book. The main contents include the following: (1) preparation and modification of fly ash artificial zeolite, (2) preparation technology of functional ceramsite and (3) preparation technology of montmorillonite with loaded nanometer iron and their application in the permeable reactive walls, constructed wetlands and aerated biofilters. These research contents are important for further research and applications of environmental functional materials, especially as hot spots in the field of current water purification processes (such as removal of persistent toxic pollutants, improvement of wastewater treatment process and ecological pollution control).

The organization of this book is complete and systematic, the latest national and international research progress and views are reflected and the preparation and optimization of materials and their applications in the actual wastewater treatment projects are also discussed in this book. The book is divided into 8 chapters: Chapter 1 is compiled by CHEN, Jianyu; Chapter 2 compiled by CHEN, Jianyu and LUO, Qijin; Chapter 3 compiled by LUO, Jun and CHEN, Jianyu; Chapter 4 compiled by PANG, Zhihua; Chapter 5 compiled by LUO, Qijin; Chapter 6 to 8 compiled by LUO, Jun and CHEN, Jianyu. Part of the chapters in the book is prepared and compiled by LIU, Chang; HUANG, Rongxin; ZHOU, Xiuxiu. The complete book is unified and edited by CHEN, Jianyu and LUO, Jun. In the process of writing, we earned much encourage and support from predecessors and peers who researched in the field of environmental functional materials. Special thanks to Mr. XU, Zhencheng from South China Institute of Environmental Sciences, MEE and Mr. WU, Wei from Peking University.

This book can be used as a textbook of water treatment technology for bachelor's and master's students, or as a reference book for engineers, technical or operational personnels.

We look forward to corrections from readers for errors and shortcomings in this book!

https://doi.org/10.1515/9783110544381-201

Contents

1 Prolegomenon

1.1 Materials and environmental materials

Material science is an interdisciplinary research field involving mutual relations between the composition, structure, process, performance and performance of various materials. Materials science provides mainly scientific basis for material design, manufacturing, process optimization and rational use. Material science is widely integrated with other disciplines to form a large number of interdisciplinary subjects. According to the physical and chemical properties, material science includes the following categories: (1) polymer materials; (2) inorganic nonmetallic materials, including ceramsite materials, semiconductor materials and so on; (3) metal materials and composite materials and so on. In practice, it is often divided into structural materials and functional materials and so on.

In recent years, environmental materials as a new branch of science has attracted much attention. As the main branch of environmental materials, the development of functional materials for water purification occupies an increasingly important position. China has come to a critical stage of governance and management of the water pollution. The development of effective new technologies for wastewater treatment and restoration is needed. The application of environmental functional materials will be expected to greatly improve the efficiency of traditional water treatment process, and thus promotes the improvement of water quality in China.

1.2 A review of functional materials for water purification

At present, China's water pollution mainly includes nutrient pollution, heavy metal pollution and trace toxicity of organic pollution. The traditional biological methods for wastewater treatment (including activated sludge and biofilm) are effective for the removal of conventional organic pollutants, but they are not ideal for the abovementioned three types of pollutants in which there is still a lot of room for improvement.

In the broad sense, all the functional materials used for wastewater treatment are part of the functional materials for water purification. The current research focuses on the physical or chemical process of wastewater treatment to remove pollutants in water, or functional materials as biofilm carrier by biochemical treatment. Research mainly includes two aspects: first, the development of biofilm carrier filler; second, the development of new adsorption separation materials, including molecular sieve, composite adsorption-reducing materials and so on. From the existing research point of view, molecular sieve and composite multifunctional filler will be the focus of the development of functional materials for wastewater treatment.

https://doi.org/10.1515/9783110544381-001

When the functional materials as a biofilm carrier are called filler, they are mainly used in biological aerated filter (BAF) and constructed wetlands; when they are used jlas core for the filtration of wastewater treatment facilities they are called filtering media, generally used for filter dam, filter reaction wall and various types of filter chamber. The most widely applied functional materials for wastewater treatment include zeolite, ceramsite, basalt, activated carbon, slag, coke, anthracite, fine quartz sand, plastic ball and polymer materials. According to the current application situation, the cost, filtration performance and renewability are restraining factors of the application of filtering media. As biofilm carrier, the specific gravity, specific surface area, film speed, hydraulic shock load, manufacturing costs and raw materials of filler are particularly important. Because the function of natural raw materials is difficult to meet the requirements of water treatment, the use of various raw materials with reasonable price (such as various types of combustion fly ash and natural adsorption materials) to develop functional materials for water purification has a huge developmental potential. Different kinds of new functional materials for wastewater purification will play an increasingly important role in the field of Chinese water pollution control and management.

1.3 Classification of functional materials for water purification

According to its practical use, the functional materials for wastewater treatment can be divided into four categories: (1) biofilm carrier, (2) adsorbent, (3) filter and (4) catalytic oxidation material. According to the acquiring method, they can be divided into natural materials and artificial synthetic materials. They can also be distributed into two classes: (1) organic and (2) inorganic materials. In addition, according to the mechanism of action, functional materials for wastewater treatment can be divided into physical and chemical functional materials; according to hydrophilic performance, they can be divided into hydrophilic and hydrophobic functional materials. The classification provided in this book is based on the practical use of functional materials for water treatment.

1.3.1 Biofilm carrier

Biofilm carrier, also known as biological filler, is one of the most commonly used environment functional materials for water treatment. It mainly includes elastic filler prepared by polymer materials, ceramsite material such as shale, volcanic rock and clay. They may function poorly in the removal of contaminants, but they are all rough, strong and durable, have large specific surface area and cannot be degraded by microorganisms. It is suitable for microbial growth habitat.

1.3.1.1 Polymer synthesis biofilm carrier

Polymer synthetic biofilm carrier can be divided into hard, soft and semisoft materials. The hard material is corrugated or honeycomb in structure, which is made of glass or plastic. Soft materials are fiber-like bundle, made of nylon, polyester, vinylon, acrylic and other chemical fiber, knitted into a bundle and connected with the center rope. Its advantages are as follows: they have large surface area and stable physical and chemical performance, and are easy to transport and assemble. The disadvantage is that the fiber bundle is easy to agglomerate, forming an anaerobic environment, and leading to short service life. Semisoft material is usually made of denatured polyethylene, polyvinyl chloride and other organic plastics. Its advantages include the following: large specific surface area, high porosity, corrosion resistance, no blocking, easy to install and so on. The disadvantage is easy to aging. Polymer synthetic biofilm carrier is generally used in the aerobic treatment process of wastewater treatment.

1.3.1.2 Ceramsite

Ceramsite is the most widely used biofilm carrier for wastewater treatment, such as in biofilters and constructed wetlands. Because of different manufacturing processes, the ceramsite particles are generally spherical or oval. The preparation of ceramsite requires general steam curing or sintering steps to increase its strength; after firing, the ceramsite surface is hard ceramsite or enamel shell, whose strength can meet the needs of wastewater treatment. The particle size of the ceramsite is generally 5 to 20 mm.

Raw materials used to produce ceramsite generally include volcanic rocks, clays and shales. In recent years, the variety of raw materials has been significantly increased; solid waste is also used to produce ceramsite, including fly ash, steel slag, mineral waste residue, cinder, river sludge, sewage sludge, municipal waste combustion ash, straw and so on. Because of the requirements of the strength of the ceramsite, clay has been the most widely used binder in the world. The pore size and distribution of new ceramsite can be determined according to different needs. Compared with the traditional ceramsite, the new type of ceramsite has not only better performance for biofilm growth, but also for removal of nitrogen, phosphorus, organic and heavy metal from wastewater, therefore the new type of ceramsite has good application prospect.

The surface of the ceramsite particles is rough and porous, interior is a fine honeycomb cellular structure, which comes from gas formation and evolution during roasting. This structure leads to lightness. The density of some ceramsite is similar to that of water, which can be suspended in water and can flow evenly in the whole tank. At the same time, this cellular structure creates favorable conditions for microbial attachment on its surface.

The ceramsite made of coal gangue is convenient for film attachment and backwashing that has the advantages of good removal effect of organic and ammonia nitrogen (LI Guochang et al., 2007). The porosity of the filler prepared by dewatered

sewage sludge, clay and fly ash is more suitable for microbial attachment and growth (QI Yuanfeng et al., 2012). DU Fang et al. (2010) used iron tailings as raw material, fly ash and urban sewage sludge as an additive; for ceramsite firing research, the best ratio of iron tailings, fly ash and sludge is 40.3%:44.7%:15%.

Application of ceramsite for wastewater treatment is one of the hotspots of Chinese research in the application of biological carrier materials. XIANG Qianghui et al. (2006) used ceramsite prepared by fly ash to treat wastewater containing metal ions, humus, phosphorus, fluoride or oil. The results show that the fly ash ceramsite has a good effect on the removal of various pollutants. YUE Min et al. (2004) studied the physical and chemical properties of lightweight spherical ceramsite and the properties of the biofilm growth and the effect of organic wastewater treatment in tower anaerobic biofilter. Their studies have shown that this material is suitable for use as an anaerobic microbial carrier. YUAN Xi et al. (2007) treated low concentration of domestic wastewater with ceramsite as the carrier material of the BAF. The removal efficiency of COD (Chemical Oxygen Demand), NH_4-N and SS (Suspended Substance) was studied and the morphology of biofilm was observed. The results showed that the removal rates of COD, NH_4-N and SS after effluent were more than 80%, 90% and 80%, respectively, when the COD concentration in influent was between 30.8 mg/L and 184.8 mg/L; the average concentration of NH_4-N was 25 mg/L; the SS concentration was between 61.2mg/L and 206.9 mg/L; the HRT was 12, 10, 8, 5 and 3h, respectively. SANG Junqiang et al. (2004) investigated the effect of phosphorus on the biofilm of the ceramsite filter. The results showed that the addition of phosphorus source into the raw wastewater can improve the number and activity of microbes in the ceramsite filter, thus improving the pretreatment effect, if the phosphorus source content in the raw wastewater is low and cannot meet the microbial growth requirement.

1.3.2 Adsorbing functional materials

Adsorbing functional materials can remove pollutants in wastewater directly through the adsorption in the water treatment process; it includes two categories: (1) biomass adsorbing materials and (2) inorganic adsorbing materials. Unlike biofilm carrier, adsorbing functional materials mainly rely on their own adsorption capacity of pollutants to completely remove the pollutants. To ensure that its adsorption capacity is sustained and stable, the growth of microorganisms on the adsorption material should generally be avoided.

1.3.2.1 Biomass material

The current range of biomass materials is very extensive. In recent years, a large number of researches carried outside of China are based on biomass materials, including various types of microorganisms, shells, algae, bark, coconut, wood,

shellfish, corn cob, sawdust, starch, chitosan, protein, cellulose, lignin, polymer natural rubber, calcium alginate, agar, carrageenan and so on. After pretreatment, modification and other preparation processes give its different wastewater treatment characteristics. Based on the current reported research, a large number of biomass materials showed excellent performance for wastewater treatment, especially in adsorption performance. This kind of raw material is rich in resources, low cost, nontoxic to microorganisms, harmless and good mass transfer performance, so its research and development application prospects are broad. However, the course of the operation is often affected owing to the decomposition of organic substances.

1.3.2.2 Inorganic adsorbing materials

(1) Carbon adsorbent

Carbon adsorbent mainly refers to activated carbon, in addition to expanded graphite and so on. Activated carbon has been one of the most popular adsorbents because of its excellent adsorption properties and developed pore structure. Activated carbon is amorphous carbon; it is irregularly assembled from a number of graphite-type layered microcrystals with crystal defect. There are numerous micropores in the activated carbon with a pore size of 1×10^{-10}μm–1×10^{-6}μm, especially 1×10^{-10}–1×10^{-9}μm, which lead to the huge surface area (up to1,000 m^2/g) of activated carbon (YANG Huifen et al., 2008). Because of the stability of the chemical properties of carbon adsorbent, it can be widely applied.

Activated carbon is not only good for removal of color and smell, but also has high adsorption capacity for synthetic detergents. Removal of organic matter in water is one of the important applications of activated carbon. In addition, activated carbon can also effectively remove carbamate insecticides that mostly cannot be degraded and other COD. Activated carbon can effectively remove free chlorine and some heavy metals (such as mercury, antimony, tin and chromium) without secondary pollution (The pollution caused by other water treated materials). In the treatment of industrial wastewater, activated carbon is mainly used for advanced treatment, or it is used for secondary treatment combination system of the petrochemical and printing and dyeing wastewater with high content of COD and BOD (Biological Oxygen Demand).

(2) Zeolite

Zeolite is a general term for the porous aquatic aluminosilicate minerals. It contains metal ions such as Na, Ca, Sr, Ba, K and Mg. The general chemical formula can be expressed as $(Na, K)_x(Mg, Ca, Sr, Ba)_y\ [Al_{x+2y}Si_{n-(x+2y)}O_{2n}]\cdot mH_2O$, where x is the number of alkali metal ions, y is the number of alkaline earth metal ions, n is the sum of the number of silicon aluminum ions and m is the number of water molecules.

The crystal structure of the zeolite is composed of silicon (aluminum)–oxygen tetrahedron into a three-dimensional grid; the grid has different sizes of holes and

channels, with great openness. Alkali metal or alkaline earth metal ions and water molecules are distributed in the holes and channels, and the grid is weak. The zeolite can be used in the ion-exchange method of water. The sodium and calcium ions in zeolite can be exchanged with potassium and magnesium in aqueous solution, and are used industrially for hard water softening. Different ion-exchange mediums have little effect on the zeolite structure, but the properties of the zeolite can be changed. There are different sizes of cavities in crystal lattice; they can absorb or filter other different molecules. It is often used as a molecular sieve in the industry to purify or separate substances such as gas separation, oil purification and industrial pollution treatment.

There are more than 30 kinds of zeolites found in nature; the more common are analcime, chabazite, scolecite, heulandite, natrolite, mordenite and stilbite. Because of the natural properties of the zeolite, there is a great deal of research on the synthesis of artificial zeolites by using fly ash, ash and other raw materials. The adsorption capacity is similar to that of natural zeolites, and the cost is lower. Recent studies have focused on the incorporation of rare earth elements and other substances into artificial zeolite to give its new characteristics for wastewater treatment.

(3) Diatomite

Diatomaceous earth (or Diatomite) is a porous, low-density, acid proof, alkali proof and insulated nonmetallic mineral. It has the advantages of high porosity, high pore volume, lightweight, low bulk density, large specific surface area, low thermal conductivity, strong adsorption and good activity. Because of the large number of ordered nanoporous microstructures, diatomite has a large specific surface area; thus, it is a natural nanomaterial that can adsorb liquids 1.5 to 4 times its own mass. The shell of diatomite particles is with natural multilevel ordered micropore structure, which makes it very valuable in applications such as polymer materials, paint filler, enhancers, chemical filter aid, adsorbent, catalyst carrier, surfactant and chromatographic stationary phase or carrier (YANG Huifen et al., 2008). Because its surface is covered by a large number of silicon hydroxyl groups, the surface of diatomite particle is usually negatively charged, so that it has good exchangeability and selectivity for heavy metal ions. Diatomite has a unique characteristic. The treatment of heavy metal pollution with diatomite is not only simple and effective but also inexpensive, and the release rate of heavy metals during desorption is low.

(4) Sepiolite

Sepiolite is a rare nonmetallic mineral with strong adsorption and adhesion. Sepiolite is rich in minerals and organic matter. Sepiolite, with orthorhombic mode, is a layered water magnesium silicate or magnesium aluminum silicate, which presents fine veins and reticulates in the rock. Its main chemical composition is silicon (Si) and magnesium (Mg), the chemical formula is $Mg_8Si_{12}O_{30}(OH)_4(OH_2)_4{\cdot}8H_2O$. The crystal structure is two layers of silicon–oxygen tetrahedron, the middle layer of magnesium–oxygen octahedron. This unique structure allows the sepiolite to have

relatively large specific surface area and ion-exchange capacity for physical adsorption and chemical adsorption. Sepiolite adsorption activity center can be divided into three types: (1) the oxygen atoms in the silicon–oxygen tetrahedron, (2) water molecules coordinate with magnesium ions on the octahedral side and (3) the Si–OH ion complex produced by the rupture of Si–O–Si bonds on the surface of the tetrahedron. These Si–OH ion complexes can interact with the adsorbed molecules of the sepiolite to form covalent bonds.

The sepiolite exists in the neutral adsorption sites formed by the silanol groups, which is located on the "outer surface" of the silicate. In addition, it also exists in the negative adsorption sites, which are formed of low-cost metal ions instead of Si^{4+}. The distribution of these two sites on sepiolite gives it a strong ability to adsorb neutral organic molecules or organic cations. Sabah et al. (2002) had a thermal activation of sepiolite at 300 °C at first, then acidified with nitric acid at room temperature for 3 h to adsorb organic compounds such as dodecyltrimethylammonium bromide, cetyltrimethylammonium bromide, long carbon chain and short carbon chain quaternary ammonium salt in wastewater. The adsorption effect is very good. Sepiolite not only can be used to adsorb organic cations, in recent years it has also been used to adsorb organic anions, and it has also achieved good results. Ozdemir et al. (2004) modified sepiolite with a typical quaternary ammonium surfactant hexadecyltrimethylammonium for adsorption of yellow, black and red anion dyes with sulfonic acid, resulting in a maximum adsorption capacity of 169.1 g/kg, 120.5 g/kg and 108.8 g/kg.

(5) Bentonite

Bentonite is kind of clay rock, the main chemical composition is SiO_2, Al_2O_3 and H_2O, it also contains Fe, Mg, Ca, Na, K and other elements. The contents of Na_2O and CaO have considerable influence on the physicochemical properties and technological performance of bentonite. The bentonite can be divided into sodium bentonite (alkaline soil), calcium bentonite (alkaline soil) and natural bleaching earth (acid soil or acid clay), in which calcium bentonite also includes calcium–sodium-based and magnesium–calcium-based bentonite. Bentonite has a strong hygroscopicity and dilatancy; it can adsorb 8 to 15 times the volume of water of its own, the volume expanded up to several to 30 times. Bentonite can be dispersed into a gel and suspended medium in water, this medium solution has a certain viscosity, variability and lubricating property. Bentonite has a strong cation exchange capacity. Bentonite has a certain adsorption capacity on a variety of gases, liquids and organic substances; the maximum amount of adsorption is up to five times the weight of its own. Acid bleaching earth with surface activity can adsorb colored ions. The blend of bentonite with water, mud or fine sand has plasticity and adhesion.

The silicon oxygen structure on the surface of natural bentonite has strong hydrophilicity. In addition, a large number of exchangeable cations located between the layers can be hydrolyzed, so that there is usually a thin water film on the surface, which cannot effectively adsorb hydrophobic organic pollutants. Natural bentonite is

inorganically polymerized after sodium transition, which can greatly improve the decolorization ability to organic pollutants, can greatly improve the decolorization ability of bentonite to organic pollutants and which can be used for the treatment of printing and dyeing wastewater, COD removal rate is up to 85%.

(6) Montmorillonite

Montmorillonite belongs to monoclinic crystal system. It is usually white soil-like block, sometimes with light red, light green, light yellow, break colors. The hardness of montmorillonite is 1–2 (the Mohs Hardness Scale), and its density is 2–3 g/cm^3. Montmorillonite is a typical 2:1 layered silicate mineral with a large surface area and surface energy. Each montmorillonite unit cell consists of two silicon–oxygen tetrahedrons and alumina octahedral parallel chains; it adsorbs and releases water molecules between each crystal structure layer. Montmorillonite has a high cation exchange performance, showing a strong adsorption, and the particles are easy to split into very fine charged particles. Numerous studies and experiments have shown that natural or modified montmorillonite is effective in handling heavy metal contamination. At present, montmorillonite and bentonite have become one of the hot research directions of environmental functional materials in the world.

(7) Silica gel

Silica gel is a kind of porous material formed by dehydration of white colloidal silicic acid precipitated by water glass and sulfuric acid or hydrochloric acid. It belongs to amorphous structure with large specific surface area, good adsorption performance and radiation resistance and chemical stability. The hydroxyl groups on the surface have a certain degree of polarity, and the microbial cells can be immobilized by the effects adsorption and charge. Porous silica gel is an amorphous material; the surface is rich in silicon hydroxyl. The molecular sieve of silica gel is an inorganic micropore composed of SiO_2, Al_2O_3 and alkali metal or alkaline earth metal, with a uniform pore size as that of a diameter of a molecule. The molecular sieve is mainly prepared by hydrothermal synthesis and hydrothermal conversion (FENG Yujie et al., 2009). In addition, this kind of molecular sieve can be used as adsorption and separation materials, and also as a microbial carrier for wastewater treatment. The molecular sieve has uniform distribution of pore size, high porosity and high specific surface area.

As a separation material, silica gel has its outstanding advantages, especially high mechanical strength and good radiation stability. However, silica gel has only a single functional group of hydroxyl, and the product performance of different types of silica gel is not identical. According to the needs of practical application, silica surface hydroxyl groups can graft some of the groups with specific functions on the surface of silica gel for inside and outside surface modification. The result is a variety of new materials with special separation function; it is one of the hot scientific research topics of the contemporary separation of materials (FANG Yutang, 2007).

1.3.3 Filter

1.3.3.1 Conventional filter for wastewater treatment

Conventional filters for wastewater treatment mainly include ionic resin, quartz sand, manganese sand, mineral fossils, olivine, ceramsite, perlite, zeolite, sepiolite, coral limestone, montmorillonite, diatomaceous earth, bituminous coal, lignite, fiber ball, polystyrene, glass beads, Kinetic Degradation Fluxion (KDF) copper and zinc alloy (one patented product by Don HesKett), magnet, especially quartz sand and ceramsite are most widely used.

Quartz sand is a common filter material widely used in water treatment, wastewater treatment, environmental management and other water purification process. Because of less pores on the quartz sand filter surface, it is not ideal for the removal of toxic and harmful substances in water. At present, the development of quartz sand filter is mainly to improve its surface properties to produce modified filter with excellent mechanical strength and adsorption properties. ZHOU Yuexi et al. (1994) used iron salt surface modifier to produce quartz sand filter to remove phosphate and heavy metal ions in water. DING Chunsheng et al. (2009) used quartz sand as the carrier, with repeated heating steaming method to prepare aluminum salt modified quartz sand. The removal rate of COD and UV254 in water was higher than that before modification. MA Jun et al. (2002) modified quartz sand filter to strengthen the treatment of algae water. The experimental results show that compared with the original quartz sand filter, modified quartz sand filter on the algae water has an excellent treatment effect.

Porous ceramic is a new type of functional material of pore structure, which combines the high specific surface area of porous materials and the physical strength characteristics and chemical stability of ceramic materials. By controlling its pore size, pore shape, porosity and bulk density, different filtering functions can be achieved. WU Jianfeng et al. (2010) prepared a red clay porous ceramic filter with dolomite and graphite as pore-forming agent. The pores were evenly distributed and the pore volume was large, which could meet the requirements as filter for water treatment.

1.3.3.2 Fiber filter

As a developmental direction of fiber filter, an important feature of granular filter is that it can be easily and completely cleaned in the filter pool or filter. The fiber filter has a greater specific surface area and porosity than quartz sand or other solid particulate material. The fiber filter bed has a greater interception capacity, resulting in higher filter efficiency. Fiber filter includes the following: (1) short fiber monofilament scrambling filter, (2) low curled fiber ellipsoid filter, (3) solid fiber ball, (4) center ligation fiber ball, (5) curled fiber center ligation fiber ball, (6) rod fiber filter, (7) comet fiber filter and (8) fiber bundle filter. Different types of fiber filters have been developed based on the abovementioned materials.

1.3.4 Catalytic reaction environment functional materials

Nano environmental functional materials are the most important parts of catalytic reaction materials. Nanomaterials describe materials of which a single unit is sized (in at least one dimension) between 1 to 100 nm. Nanomaterials include zero-dimensional atomic clusters and nanoparticles, one-dimensional nano-multilayers, two-dimensional nanoparticle films and three-dimensional nanophase materials. The size of the material up to the nanometer level produces many performances that the traditional solid does not have, including the surface effect, volume effect, quantum size effect and macroscopic quantum tunneling effect. In addition, owing to their small size, nanomaterials usually have a large surface area. The unsaturation of surface atomic coordination leads to a large number of dangling bonds and unsaturated bonds, which makes the nanomaterials to be highly chemically active. Because of these specificities, nanomaterials have unique properties of separation, photocatalysis, reduction and adsorption. The size of nanomaterial structural unit is small, so that the effective contact area with pollutants is relatively large, and the removal effect of pollutants in water is better than that of traditional water treatment methods. Therefore, nanomaterials have a broad application prospects in the water treatment industry. At present, nanomaterials used for water treatment can be divided into four types: (1) nanofiltration membrane materials, (2) photocatalytic materials, (3) nano-reducing materials and (4) nano-adsorbent materials. The most widely used nanomaterials for wastewater treatment include nanofiltration membrane, titanium dioxide photocatalyst, nano zerovalent iron, nano nickel, nano zinc, carbon nanotubes and so on.

1.3.4.1 Photocatalytic environment functional materials

Semiconductor photocatalysis is a high-level chemical oxidation technology for wastewater treatment. There have been a series of semiconductor photocatalytic materials developed, including oxides (such as TiO_2, ZnO, WO_3, $La_2Ti_2O_7$ and $BiVO_4$), sulfides (such as CdS, ZnS and CdSe) and phosphide (GaP, InP). Among these photocatalysts, TiO_2 has excellent chemical stability, light stability and biocompatibility and other unique properties; it is considered the most popular photocatalyst. The mixed crystal TiO_2, whose mass ration of commercially available anatase and rutile is about 80:20, is used as a research standard for the development of new photocatalyst. The average particle size is 25 nm, and the specific surface area is 50 m^2/g. Because of its high specific surface area and good dispersibility, nano-semiconductor photocatalytic materials with quantum size effect can meet the requirement of high efficiency photocatalytic performance to the maximum extent. However, since the suspended nanoparticles are easily agglomerated, this leads to a rapid decrease in photocatalytic performance. Because of this, people pay more attention to the preparation of porous photocatalytic materials or the nano-photocatalytic materials on the porous solid substrate. At present, many

design methods have been used to prepare nanocomposites with high specific surface area and good crystallinity, as well as morphological control of porous photocatalysts in different scales.

1.3.4.2 Iron-based catalysts

Iron-based nanomaterial refers to the ultrafine iron powder material, whose three-dimensional particle size is in the range of 1–100 nm. Compared with micron-sized iron particles, the nano-iron particles are extremely small in diameter. So the number of atoms on the surface increased dramatically, while increasing the surface tension and surface energy of iron particles. Therefore, nano-iron material shows some unique properties, compared with the conventional fine powder. HU Liujiang et al. (2008) used load-bearing nano-iron material to remove nitrobenzene in wastewater. In 120 min more than 98% nitrobenzene was removed, whose influent concentration was 200 mg/L. The nano-iron material can maintain high removal ability of nitrobenzene in the wide pH range. The results of TANG Cilai et al. (2007) showed that nano-iron has a huge application space in the field of water pollution remediation by virtue of the effective treatment ability of pollutants such as NO_3^-, heavy metals and chlorinated organic compounds.

1.3.5 Comparison of various functional materials for water treatment

The types of functional materials for water treatment are numerous. With the continuous progressing of technology, the development of functional materials for water treatment gradually tends to composite multifunctional. Some functional materials may also have several functions. For example, the multifunctional ceramic is currently researched and developed; it not only can be used as a biofilm carrier, but also has a good pollutant removal performance. However, its functions can generally be classified as the four categories above. Table 1.1 shows the current comparison of the main environment functional materials for water treatment.

1.4 Current problems of research on environmental functional materials

The history of environmental functional materials in China is still very short. Compared to advanced countries outside China such as Japan, the technological development and theoretical research are still lagging behind and still in the time of learning and imitating. At present, the functional materials for conventional wastewater treatment projects to strengthen the removal of pollutants include new artificial zeolite, porous ceramic, modified clay mineral and multifunctional composite materials. However, most of the research is still in the early stages; the

Table 1.1: Comparison of the main environment functional materials for water treatment.

NO.	Type	Characteristics	Main application	Representation materials	Range of application
1	Biofilm carrier	Biological adhesion, stable character	For biofilm adhesion by water treatment	Elastic filler, ceramic and so on	Aeration tank, hydrolytic acidification tank, biological filter, artificial wetlands and so on
2	Adsorbent	With a large number of micropores, or adsorption active sites for different pollutants	Pollutants are directly removed by adsorption, mainly for nitrogen, phosphorus, heavy metals, organic matter and so on	Activated carbon, artificial zeolite, montmorillonite and so on	Various types of adsorption tower
3	Filter	Good liquid permeability, stable traits, not easy to be biofilm attached to avoid affecting its filtration performance	Used as a filter	Quartz sand, bituminous coal, fiber filter and so on	Various types of filters
4	Catalytic reaction functional materials	Good and lasting catalytic activity, less catalyst poisoning	Used for advanced oxidation of refractory organic compounds	Zero price iron, nano TiO_2	Photocatalytic oxidation, zerovalent iron-catalyzed oxidation

mechanism for the removal of contaminants from functional materials is still unclear. The developed materials can be basically used only in the laboratory; there is still a long way to the actual engineering application. The abovementioned problems greatly limit the application of functional materials for wastewater treatment and the overall technical level of China's wastewater treatment. Therefore, the related research on functional materials for wastewater treatment should be further promoted.

Based on above conditions, our research team started working on functional materials for wastewater treatment in 2005. After years of accumulation, we have a comprehensive and in-depth study on artificial zeolite, functional ceramsite, modified mineral materials and zerovalent iron materials and so on. The research results have been used in the permeable reactive barrier (PRB), filter reactive barrier, new aeration

biofilter, constructed wetland and other practical wastewater treatment projects. The results showed that the treatment effect was remarkable, especially in the adsorption and degradation of trace organic pollutants, the adsorption of heavy metals and so on. To this end, this book introduces the research results in the new functional materials for wastewater treatment in recent years for reference.

References

DING Chunsheng, JIANG Zhiyuan, ZHANG Dehua et al.: Study on Preparation and Adsorption Properties of Aluminum Salt modified Quartz Sand, Non-metallic mineral, 2009, (5):17–20.

DU Fang, LIU Yangsheng: Study on the firing of ceramsite prepared by iron tailings and its properties. Environmental Engineering, 2010, 28(1):369–372.

FANG Yutang, JIANG Gan, KUANG Shengyan et al.: Preparation and Adsorption Properties of Silica/Molecular Sieve Composites. Journal of the Chinese Ceramic Society, 2007, 35(6):746–749.

FENG Yujie, SUN Xiaojun, LIU Junfeng: Environmental Functional Materials. Beijing: Chemical Industry Press, 2009.

HU Liujiang, LI Yimin: Removal of Nitrobenzene from Wastewater by Organic Bentonite Supported Nanometer Iron, Journal of Environmental Science, 2008, 28(6):1107–1112.

LI Guochang, WANG Ping, WEI Chuncheng: Preparation and Properties of Coal Gangue Ceramsite. Metal Mine, 2007, (2):78–83.

MA Jun, SHENG Li: Treatment of algae water with modified quartz sand filter, China water and wastewater, 2002,18(10):9–11.

OZDEMIR O, ARMAGAN B, TURAN M et al.: Comparison of the adsorption characteristics of azo-reactive dyes on mezoporous minerals. Dyes and Pigments, 2004, 62(1):49–60.

QI Yuanfeng, YUE Dongting, YUE Qinyan et al.: Study on the Expansion Mechanism of Ultra light Sludge Ceramsite Prepared by dehydrated Sludge. http://www.paper.edu.cn, 2012.

SABAH E, CELIK M.: Adsorption mechanism of quaternary amines by sepiolite. Separation Science and Technology, 2002, 37(13):3081–3097.

SANG Junqiang, ZHANG Xihui, ZHANG Sheng et al.: Comparison of the Operation Effect of Light-weight Filter and Ceramsite Filter in Raw Wastewater by Bio-pretreatment, 2004, 25(3):40–43.

TANG Cilai, ZHANG Zengqiang, ZHANG Yongtao: Preparation of Nanometer Iron and Its Application in Groundwater Pollution Remediation, Environmental sanitation engineering, 2007, 15(3):61–64.

WU Jianfeng, HUANG Xiangkui, XU Xiaohong et al.: Study on the Control of Porosity of Red Mud Porous Ceramic Filter, Journal of Wuhan University of Technology, 2010, (18):24–28.

XIANG Huiqiang, LI Dong, GONG Youkui et al.: Application of Fly Ash Ceramsite in Wastewater Treatment. Journal of Liaoning Technical University, 2006, 25(12):291–292.

YANG Huifen, CHEN Shuxiang: Environmental Engineering Materials. Beijing: Chemical Industry Press, 2008.

YUAN Xi, SHEN Yaoliang, CHEN Jian: Experimental Study on Treatment of Low Concentration Domestic Sewage by Aerated Filter and Porcelain Granule, Water and Wastewater Engineering, 2007, 33(5):142–145.

YUE Min, HU Jiucheng, Zhao Haixia: Study on the Characteristics of Lightweight Ceramsite used for Anaerobic Filter. Environmental Pollution and Control, Environmental Science, 2004, 26(1): 22–24.

ZHOU Yuexi, WANG Xiaosong, KONG Xi et al.: Adsorption and Filtration of Heavy Metal Ion Wastewater (Ⅰ) – Study on New Adsorption Filtration Material. Environmental Science Research, 1994, 6.

2 Preparation and modification of artificial zeolite by fly ash

2.1 Overview of artificial zeolite

2.1.1 Introduction of zeolite and artificial zeolite

Zeolites are hydrated aluminum silicates with monolayer structure, which have good adsorption properties, cation exchange performance and catalytic performance. The chemical composition of the zeolite is complicated. There is a large variation in different kinds of zeolite. Zeolite mainly contains Na and Ca and a few metal ions of Sr, Ba, K and Mg. The general chemical formula of zeolites is $A_mB_pO_{2p}{\cdot}nH_2O$, and the structural formula is $A_{(x/q)}$ $[(AlO_2)_x(SiO_2)_y]n/(H_2O)$, where A represents cations such as Ca, Na, K, Ba and Sr; B represents Al and Si; p is the cationic valence; q is the cationic potential; m is the number of cations; n is the number of water molecules; x is the number of Al atoms; y is the number of Si atoms; (y/x) is usually between one and five; and $(x + y)$ is the number of tetrahedrons per unit cell.

There are more than 80 known natural zeolites, and the most widely distributed zeolites are analcite, heulandite, laumontite, harmotome, chabasite, erionite, mordenite, natrolite and scolecite. With the development of research, new types of zeolites will continue to emerge.

Natural zeolite has many advantages, such as wide distribution, large reserves and low cost. It also has some disadvantages, such as many impurities, low purity and some performance cannot meet the specific needs. Therefore, the artificial zeolite is synthesized, based on the physical and chemical structure and its properties.

In 1948, the first artificial zeolite was successfully synthesized. Up to now, more than 40 kinds of natural zeolites have been synthesized, in addition to more than 100 kinds of new zeolites. The research work of China's synthetic zeolite begins rather later. In 1959 the A, X and Y zeolite molecular sieves were synthesized for the first time. Since then, China's research and the industrial applications of synthetic zeolite improved constantly, and the type and yield of synthetic zeolites are also increasing. At present, some synthetic technologies and products have reached the international advanced level.

Synthetic zeolites are mainly used in detergents and catalysts. Some domestic and foreign companies are developing new zeolite products to expand the scope of application of zeolite products, including alternatives for CFC (chlorofluorocarbons), sealed insulated (thermal insulated) special glass, adsorbents, desiccants and environmental functional materials.

Based on synthetic materials, synthetic zeolites can be divided into two categories: (1) from chemical raw materials (such as $Al(OH)_3$, SiO_2 and Na_2O) and (2)

https://doi.org/10.1515/9783110544381-002

from natural mineral materials. The frequently used industrial zeolite, which is synthesized from traditional chemical raw materials, has the following advantages: (1) technical maturity; (2) technical conditions that are easy to control; and (3) high quality. But the raw material is relatively expensive, and the source is limited, which has seriously affected the wide range of synthetic products. Because of its rich raw materials, the production cost of synthetic zeolites from natural mineral materials is reduced. Up to now, the zeolite products with excellent properties have been successfully synthesized by using natural mineral raw materials such as bentonite, kaolin, pyrophyllite, gangue, tuff, perlite, natural zeolite, potassium feldspar powder and pumice (ZHANG Xihuan et al., 2006).

In addition to the abovementioned two kinds of synthetic materials, in recent years, it has been found that the chemical and mineral composition and the texture and structure of ash from power plant and cinerite, precursor of natural zeolite, are similar. This provides the synthetic possibility from fly ash. Therefore, the use of fly ash to prepare zeolite has a large utility value. Turning waste into treasure makes it the research emphasis of synthetic zeolite.

2.1.2 Mechanism of zeolite synthesis

At present, the following three theories provide the mechanism of zeolite synthesis.

(1) Mechanism for liquid phase transition

Zhdanov (1971) deemed that the zeolite crystal nucleus is formed in the liquid phase or on the interface of gel. The growth of crystal nucleus consumes the silicate hydrate in the solution. The solution provides the soluble structural units for the growth of zeolite crystal nucleus. The consumption of the liquid phase during the crystallization leads to the continued dissolution of the gel solid phase. After mixing all raw materials, the initial aluminosilicate gel is first produced, which is disordered, but it may contain some simple primary structural units, such as four-membered ring and six-membered ring. When the gel and liquid phases established a dissolution equilibrium, the solubility of the aluminosilicate depends on the structure and temperature of the gel; when the temperature rises, it will establish a new equilibrium. The increase in the concentration of aluminosilicate in the liquid phase leads to the formation of nucleus, which promotes crystal growth. The growth of nucleation and crystals consumes the silicate ions in the liquid phase and causes the dissolution of the amorphous gel. Eventually, the gel is completely dissolved and the zeolite crystals are completely grown.

(2) Mechanism for solid-phase transition

The mechanism for solid phase suggests that neither the solid phase dissolves nor the liquid phase directly involved in the nucleation and zeolite crystal growth during the crystallization. When the raw materials are mixed, the silicate and the

aluminate are polymerized to form an aluminosilicate initial gel. Although the intergranular liquid phase is produced, the liquid phase does not participate in the crystallization, and the liquid phase is constant throughout the crystallization. The initial gels are depolymerized and rearranged under the action of OH^- to form primary structural units for zeolites. These primary structural units surround the hydrated cation, and are rearranged into polyhedrons, which are further polymerized to zeolite crystals.

(3) Mechanism for biphasic transformation

The mechanism for biphasic transformation of zeolite crystallization suggests that the mechanism for solid phase and for liquid phase both exist, and they can occur in both systems or in the same system. For example, Gabelica et al. (1983) found that both the transitions of solid phase and of liquid phase in ZSM-5 synthesis system occurred by different reactant ratio and reaction conditions.

The synthesis mechanism of fly ash zeolite is more complicated, and it is influenced by many factors such as the ratio of Si/Al, temperature, concentration of alkali liquor and reaction time, different researchers have put forward various views. Dawson (1988) proposed that the crystal formation under hydrothermal conditions is divided into two stages: "dissolution" and "precipitation." Murayama et al. (2002) argued that the first step for synthetic zeolite crystals of fly ash is the formation of aluminosilicate gels from alkali-dissolving fly ash particles. The polycondensation and the deposition of aluminosilicate gel occurred then on the particles surface. The final deposited gel is translated into zeolite crystals. Murayama et al. (2002) proposed a three-stage theory of zeolite synthesis from fly ash by analyzing the typical product (zeolite P) of hydrothermal synthesis: (1) Si^{4+} and $A1^{3+}$ in fly ash dissolve; (2) SiAl in alkali liquor concentrates and forms a silica-alumina gel; (3) the silica-alumina gel crystallizes under certain conditions to form a molecular sieve crystal. Experiments show that the presence of OH^- in alkali liquor can dissolve Si^{4+} and $A1^{3+}$ in fly ash, while Na^+ controls the crystallization rate. When both Na^+ and K^+ are present in alkali liquor, the crystallization rate decreases with the increase of K^+ concentration. Based on the experiment of preparation of zeolite A from fly ash by the hydrothermal method, Fu Keming et al. (2008) proposed that the growth stage of zeolite A in hydrothermal system includes dissolution of fly ash particles→sedimentation of $Al(OH)_3$ →dissolution of sedimentation→aluminosilicate gel→aggregation →initial crystallization (crystal nucleus) →complete crystallization. The aggregation of aluminosilicate gels is the basis for the formation of nuclei, and the aggregation of nuclei and small particles is the main way of zeolite A grain growth. At present, the understanding of the zeolite crystal formation mainly includes two perspectives: (1) Aggregation growth theory (DU Gaohui et al., 2000), that is, through aggregation of small particles with similar size to form large particles; and (2) attachment growth theory (SCHOEMAN B J., 1998), that is, the small particles attached large particles to form zeolite particles.

The synthesis of zeolite from fly ash can be divided into three processes: (1) dissolution, (2) aggregation and (3) crystallization. The mechanism of synthesis is shown in Figure 2.1.

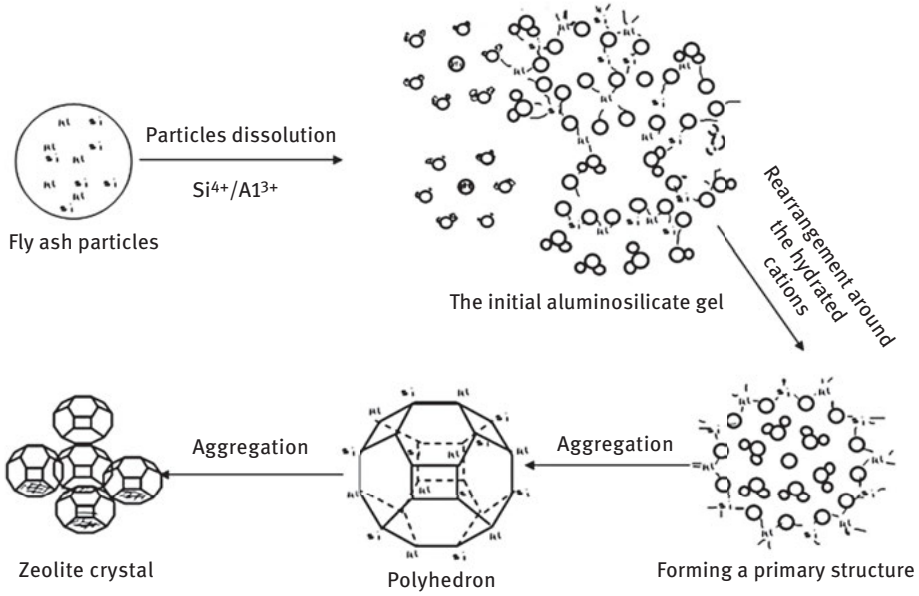

Figure 2.1: Mechanism of zeolite synthesis by fly ash.

2.1.3 Research progress in preparation of artificial zeolite from fly ash

The earliest developed technology of fly ash zeolite is the hydrothermal crystallization synthesis (hydrothermal synthesis), which was completed by Holler and Wirsching in 1985. After nearly 30 years, based on the traditional hydrothermal synthesis, many other synthetic methods have been developed. Although there are many improvements, the hydrothermal synthesis is still a classic process.

(1) Hydrothermal synthesis

The basic process of hydrothermal synthesis is that the glass phase in fly ash is first dissolved under alkaline conditions, and then the aluminosilicate colloid is formed. The colloid is crystallized and converted to zeolite. The following shows the typical technologies:

(i) One-step method

NaOH or KOH is used as an activator to form the alkaline solution with an appropriate concentration. A certain amount of alkaline solution and fly ash are mixed evenly, under

a certain temperature conditions for a period of time, to crystallize. After filtering the solution, the solid is washed with deionized water (to reach pH value 10). After drying at 100 °C, the zeolite is produced. Inada et al. (2005a) synthesized zeolite Na-P1 with one-step method. Steenbruggen et al. (1998) synthesized zeolite Na-P1 under hydrothermal condition. The experimental results show that it has good adsorption capacity for Ba^{2+}, Cu^{2+} and other heavy metal ions.

(ii) Tow-step method

The basic process of two-step method is: in the frist step, add Na_2CO_3, NaOH or KOH solution to a certain amount of fly ash, then allow the solution to stand for a while and finally after filtration zeolite is obtained. In the second step, detect the concentration of silicon and aluminum ions in the filtrate, then add the aluminum and silicon source depending on the requirement. After crystallization under hydrothermal conditions, the zeolite is finally obtained (HOLLMAN, 1999). Zeolites Na-P1, Na-X and Na-A synthesized by Hollman et al. (1999) using two-step method have a high purity of 95%. WANG Chunfeng et al. (2008), using two-step method with fly ash as raw material, synthesized submicron zeolite Na-A [$Na_{12}(Al_{12}Si_{12}O_{48})\cdot 27H_2O$]. The average particle size is 450 and 250 nm, respectively. The size span is 3.84 and 2.44, respectively. The ion-exchange capacities of the synthetic product NH_4^+ and Cu^{2+} increased significantly with the decrease in grains.

(iii) Microwave synthesis method

In the basic process of microwave synthesis, the solution will be heated with microwave instead of a conventional oil bath and electric heating. The zeolite product is obtained after aging at a certain temperature, standing for a period of time, filtration, washing and drying. Inada et al. (2005b) studied the effect of microwave heating on zeolite synthesis. The results show that the microwave heating for 15 min was favorable for the zeolite synthesis in the preliminary stage, but is not conducive to the zeolite synthesis in the medium term (especially 45–60 min after synthesis), and the effect is less in the later stage (after 90 min).

(2) Alkaline fusion method

A certain percentage of the activator such as NaOH or KOH is added to the fly ash and then mixed evenly. The mixture is calcined at a higher temperature so that all of the silica-alumina components in the fly ash, including the inert crystalline phase mullite and quartz, are also activated. A certain amount of distilled water is added into the calcined product after uniform grinding. The zeolite product is obtained after stirring, aging for a period of time, crystallization at the appropriate temperature, filtration, washing and drying. Molina et al. (2004) synthesized the zeolite X by the alkaline fusion method. Because of its special surface area and larger pore size, the zeolite exhibits a high ion exchange performance.

(3) Salt heating method

The activators (NaOH, KOH and NH_4F) and some salts ($NaNO_3$, KNO_3 and NH_4NO_3) were added to the fly ash in the appropriate proportions. The homogeneous mixture is calcined at a high temperature to obtain the zeolite crystal. Although no water is added during the salt heating process, the reaction temperature is high and the synthetic product contains a large amount of salt and requires a large amount of water to wash the product. And the synthesis process requires a lot of salt, which has brought trouble to the subsequent treatment. Park et al. (2000) and Choi et al. (2001) synthesized sodalite and cancrinite crystal by salt heating method. Their ion exchange performance is poor, so this method is not widely used.

(4) Adding alkali liquor gas phase synthesis method

First, a certain percentage of fly ash and NaOH or KOH solution are mixed evenly, and then dried into a solid-state precursor material, after then crystallized in water or water and organic amine vapors (ZHANG Shugen, 2003).

(5) Trace water system solid phase synthesis method

A certain percentage of fly ash and activator with trace water are grinded fully. The homogeneous solid reactants were placed in a stainless steel reactor. Zeolite is obtained after crystallization at the appropriate temperature, washing and drying. Liu Yongmei et al. (2002) synthesized zeolite A by solid phase method. The X-ray diffraction (XRD) and scanning electron microscopic (SEM) images show that the crystallinity of this zeolite is high. Crystalline grains are regular round particles. The Ca^{2+} cation exchange capacity (CEC) of the zeolite reached 300 g ($CaCO_3$)/g (zeolite). But because of less water in the reaction system, the mixing is not uniform. It is difficult to complete the chemical reaction, and the total productive rate and performance of synthetic zeolites are not ideal.

(6) Gradual heating method

In the gradual heating method, zeolite was obtained by crystallizing for 2 h at a lower temperature (90 °C), then warming up to 95 °C and continuously crystallized for another 2 h. Hui et al. (2006) synthesized a single pure phase zeolite Na-A with nearly 80% crystallinity by gradual heating method that greatly shortened the crystallization time.

(7) Dialysis- hydrothermal method

Tanaka et al. (2006) proposed dialysis–hydrothermal synthesis method, whose basic synthesis process is given as follows: NaOH solution and fly ash in a certain proportion are evenly mixed and placed in a semipermeable membrane test tube. And then NaOH solution is dropped into the test tube and activated at a suitable temperature for a period of time. Dissolved Si^{4+} and Al^{3+} in the test tube enter into the NaOH solution through the semipermeable membrane. After analyzing the content of each component in NaOH solution, add proper amount of $NaAlO_2$ solution to adjust the

ratio of silicate to aluminium. After crystallization for a period of time under hydrothermal conditions, zeolites Na-A and Na-X are obtained.

(8) Comparison and analysis of advantages and disadvantages of existing methods
The advantages and disadvantages of the synthesis method are shown in Table 2.1.

Table 2.1: Comparison and analysis of advantages and disadvantages of synthesis methods.

NO.	Methods	Advantages and disadvantages
1	Hydrothermal synthesis (one-step method)	Long aging time; high reaction temperature; large energy consumption; a large amount of quartz and mullite cannot get dissolved; by-product formation affects ion exchange performance.
2	Hydrothermal synthesis (two-step method)	Make full use of waste silicon and aluminum ions from one-step method; by adding aluminate to obtain high purity and adsorption properties of zeolite, compared with the traditional one-step method, greatly improving the total conversion; the shortcomings are the reaction process is long; the need to consume a certain amount of aluminosilicate; and the increase in cost.
3	Hydrothermal synthesis (microwave synthesis method)	The use of microwave to heat the crystallization process of fly ash can improve the reaction speed, greatly shorten the synthesis time and reduce the production cost. It provides a new possibility for the potential industrial production. However, the conversion rate of high-quality zeolite is not very ideal.
4	Alkaline fusion method	The product does not contain mullite and quartz; most of the aluminosilicate in the fly ash is converted to zeolite, which can improve the utilization of raw material fly ash; by adjusting the ratio of silicon to aluminum, optimizing the synthesis conditions, can get higher purity zeolite. But the activation time is longer, which is not suitable for mass production. Stirring heating time is longer, and the reaction of the aqueous solution is easy to evaporate in the reaction of nonsealed containers.
5	Salt heating method	Poor product exchange performance, and has not been widely used.
6	Adding alkali liquor gas phase synthesis method	Long time and low efficiency.
7	Trace water system solid phase synthesis method	The amount of water in the reaction system is very small; the mixing is not uniform; it is difficult to complete the reaction; the total productivity and performance of synthetic zeolite are not ideal.
8	Gradual heating method	Zeolite conversion rate is low (50% or less), and confined to the supernatant reaction range; needs further study.
9	Dialysis–hydrothermal method	The method can synthesize high-quality zeolite with high purity and single phase, but it has the problems of long synthesis reaction time and difficult recovery of dialysate.

At present domestic and foreign experts have done a lot of technology research in the synthesis of artificial zeolite. These include changes in the various factors of the synthesis process, such as improving the utilization of raw materials, increasing the reaction rate, and improving the conversion rate of zeolite and the purity of artificial zeolite. These studies have yielded some results, but there is still much work to be done in the study of the basic and practical aspects.

(1) Existing synthesis methods still have various shortcomings, including long reaction time, high cost, high conversion rate and not ideal product performance. Therefore, optimizing the synthesis process, while reducing the cost and improving the conversion rate, is the focus of the study.
(2) At present, most of the artificial zeolite synthesis methods are still in the laboratory research stage, there is distance to the actual production applications. Therefore, to further optimize the preparation process conditions and to form industrial production technology process is the breakthrough in the study.

2.2 Preparation of artificial zeolite by coal fly ash

2.2.1 Optimization of preparation technology of artificial zeolite

2.2.1.1 Characteristics of coal fly ash

As a synthetic raw material for artificial zeolite, composition of fly ash is an important parameter for the synthesis process. According to the relevant literature, the composition of fly ash in China is given in Table 2.2.

Table 2.2: Composition of fly ash in China.

Component	SiO_2	Al_2O_3	Fe_2O_3	CaO	MgO	SO_3	Na_2O	K_2O	LOI*
Proportion (%)	33.9–59.7	16.5–35.4	1.5–16.4	0.8–10.4	0.7–0.9	0–1.1	0.2–1.1	0.7–2.9	1.2–23.5

*Loss on ignition.

The fly ash used in the synthesis of zeolite for this research is taken from a thermal power plant in Guangdong Province, China. Its composition and structural analysis are shown in Table 2.3.

Table 2.3: Composition of fly ash for the research.

Component	SiO_2	Al_2O_3	Fe_2O_3	CaO	MgO	Na_2O	K_2O	LOI*
Proportion (%)	48.61	33.31	6.56	6.69	0.86	1.15	0.75	2.07

*Loss on ignition.

The raw materials were detected by XRD and SEM. The results are shown in Figures 2.2 and 2.3.

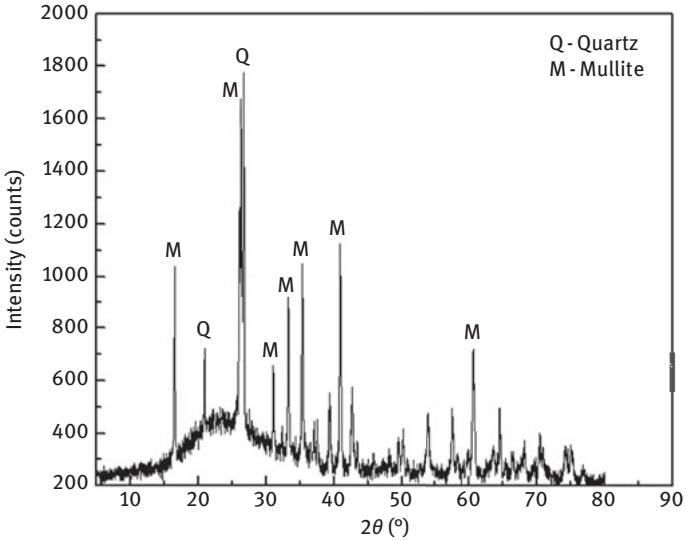

Figure 2.2: XRD patterns of fly ash.

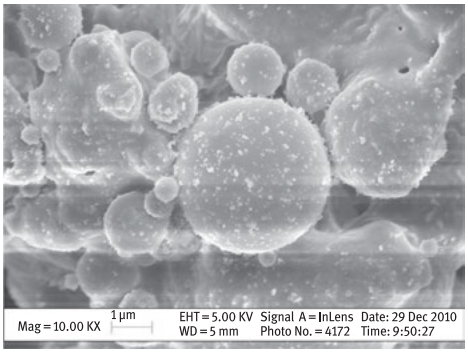

Figure 2.3: Scanning electron microscopy image of fly ash.

Based on the comprehensive analysis of Table 2.3 and Figures 2.2 and 2.3, it is found that the fly ash used in this study has the following characteristics:

(1) The main chemical constituents of fly ash are SiO_2 and Al_2O_3, and the content of aluminosilicate can reach 81.92%.
(2) The amount of unburned carbon in fly ash is low, about 2.07%.
(3) Fly ash has a strong activity. By analyzing the XRD patterns of the raw materials (Figure 2.2), it can be seen that the main crystalline phases are quartz, mullite and so on.

(4) By analyzing the SEM image of the fly ash (Figure 2.3), it can be observed that they are regular spherical particles and the surface is rough.

2.2.1.2 Pretreatment of raw materials

Fly ash contains impurities such as magnetite which are unfavorable to synthetic zeolites, so acid-pickling pretreatment is necessary before synthesis. With reference to the existing research results, the pretreatment steps and parameters of this study are as follows: The fly ash was mixed with 2 mol/L hydrochloric acid following the liquid-to-solid ratio of 3:1. The mixture was stirred for 1 h acid pickling at the temperature between 90 °C and 95 °C in a magnetic stirrer. After removing iron and other impurities, it was washed until the pH reached 7. After drying at 105 °C, it is ground and passed over 200 sieves and stored in a desiccator.

2.2.1.3 Optimization of preparation parameters

(1) Synthetic method

In this study, zeolite was synthesized by hydrothermal method. About 300 g pretreated fly ash and the prepared NaOH solution were added to the stainless steel reactor. The experimental device is shown in Figure 2.4. The reaction was carried out with 300 r/min at a certain temperature. After the reaction time, the mixture is cooled to room temperature. It was then repeatedly washed with tap water to pH 7. After drying at 105 °C, it is ground and passed over 200 sieves. The synthetic process is shown in Figure 2.5.

Figure 2.4: The device diagram of lab test.

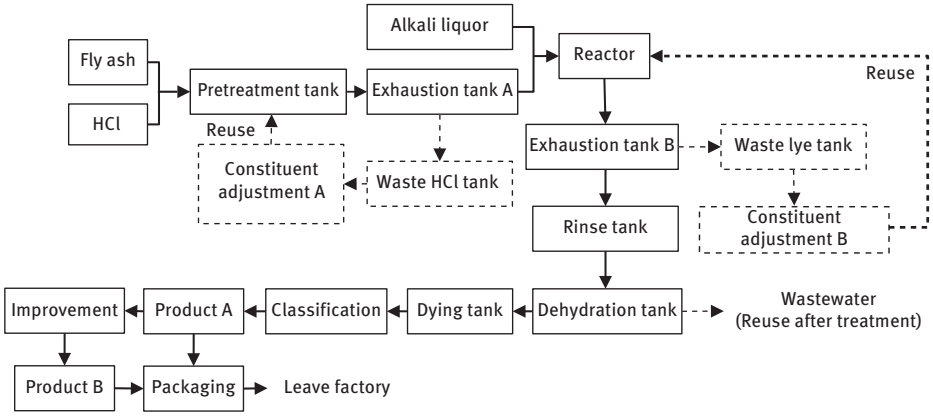

Figure 2.5: Process diagram of zeolite synthesis from fly ash.

(2) Optimization of synthetic parameters

Based on the results of many scholars in China and across the world and on the exploration of the previous experiments, the four factors at three-level (nine runs, namely L9 or 3^4) orthogonal array testing was used to determine the synthetic conditions. The factors are shown in Table 2.4. The removal rate of ammonia and phosphate is the measurable indicator, and the results of the orthogonal array testing were range analyzed. Table 2.5 is an orthogonal array testing table.

Table 2.4: Level factors of orthogonal array testing.

No.	1	2	3	4
Factors	**Liquih-to-solih ratio (L/S)**	**Alkali liquor concentration (mol/L)**	**Temperature of reaction (°C)**	**Reaction time (h)**
Level 1	3∶1	1	90	12
Level 2	4∶1	2	100	24
Level 3	5∶1	3	120	36

(3) Sample characterization

(i) XRD analyses

The crystalline component of the synthesized product was identified by a Rigaku X-ray powder diffractometer D/Max-3A. Cu Kα1, and the scanning range is 3–80 °C.

(ii) Morphology observation with SEM

The product morphology was observed by LEO1530VP field-emission SEM.

Table 2.5: Orthogonal array testing table of fly ash synthesis.

Int iCol	1	2	3	4
Factors	**Liquih-to-solih ratio (L/S)**	**Alkali liquor concentration (mol/L)**	**Temperature of reaction (°C)**	**Reaction time (h)**
1st group	3∶1	1	100	12
2nd group	3∶1	2	90	24
3rd group	3∶1	3	120	36
4th group	4∶1	1	90	36
5th group	4∶1	2	120	12
6th group	4∶1	3	100	24
7th group	5∶1	1	120	24
8th group	5∶1	2	100	36
9th group	5∶1	3	90	12

(iii) Determination of CEC

Ammonium acetate method: The fly ash zeolite product was dried at 100 °C for 1 h; after cooling, 5 g sample was added into 100 mL ammonium acetate solution with 1 mol/L. The adsorption reaction time was 24 h (25 °C, 150 r/min). After filtration, the excess ammonium acetate solution on the surface of the zeolite was rinsed with 95% ethanol solution until the pH was about 7 (measured with pH test strips). The filtered sample was transferred to a Kjeldahl flask, 250 mL distilled water, glass beads and 0.25 g MgO powder were added. With 50 mL boric acid solution with 2% as the absorption solution, the mixture was distilled. The distillation was stopped until the aqueous solution in the flask reached the bottom of the bottle. The absorbent solution was dropped into two drops of mixed indicator and titrated with standard sulfuric acid solution.

The CEC is calculated by

$$\mathrm{CEC} = \frac{N \times (V - V_0)}{W} \times 100 \tag{2.1}$$

where N is the equivalent concentration of standard sulfuric acid solution; V is the amount of standard hydrochloric acid for titration of solution, mL; V_0 is the amount of standard hydrochloric acid for titration of blank solution, mL; W is the weight of zeolite sample, g.

(4) Experimental results and analysis

(i) XRD analyses

As shown in the spectra (Figures 2.6–2.15), compared to the fly ash, the wave crest of synthetic zeolite changed significantly. The synthetic product has the characteristic wave crest of zeolite P (PDF25-0778), and the diffraction peak is sharp and strong, which

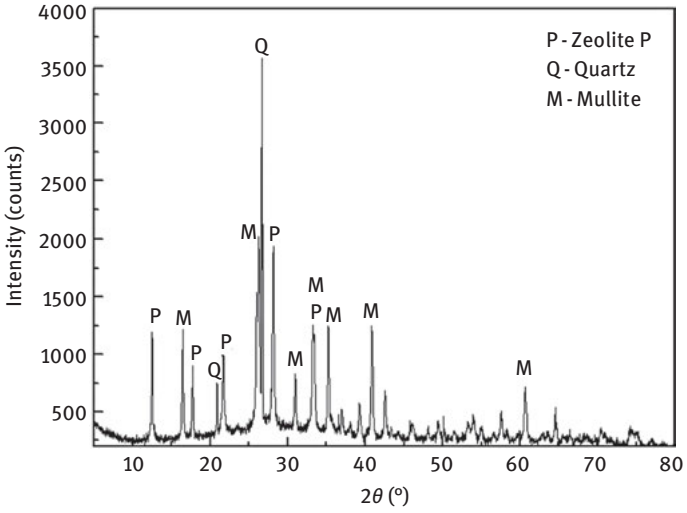

Figure 2.6: XRD patterns of the 1st group.

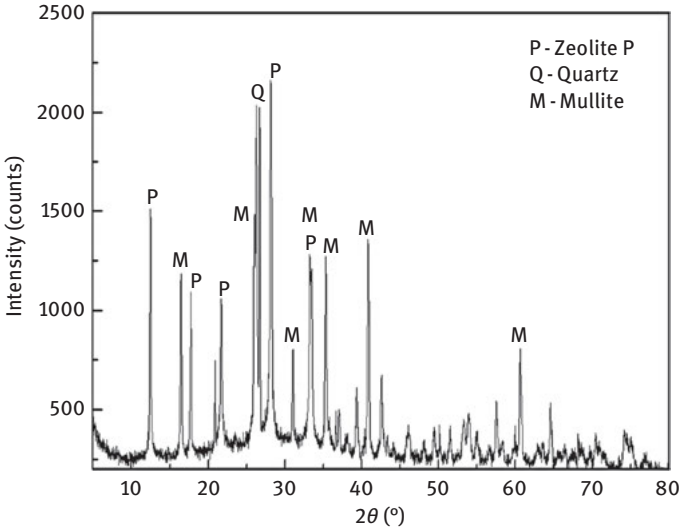

Figure 2.7: XRD patterns of the 2nd group.

indicates that the synthetic product is well crystallized. Especially, the peak shape of the samples from sixth, eighth and ninth groups are sharp. This shows that the zeolite was synthesized very well under test conditions of these three groups. Combined with the subsequent analysis, especially the CEC determination, the CEC of synthetic zeolite from sixth group reached 249.52 cmol/kg, and the comprehensive performance was the best. The silicon–aluminum ratio of China's fly ash is generally from 2:1 to 5:1, which is

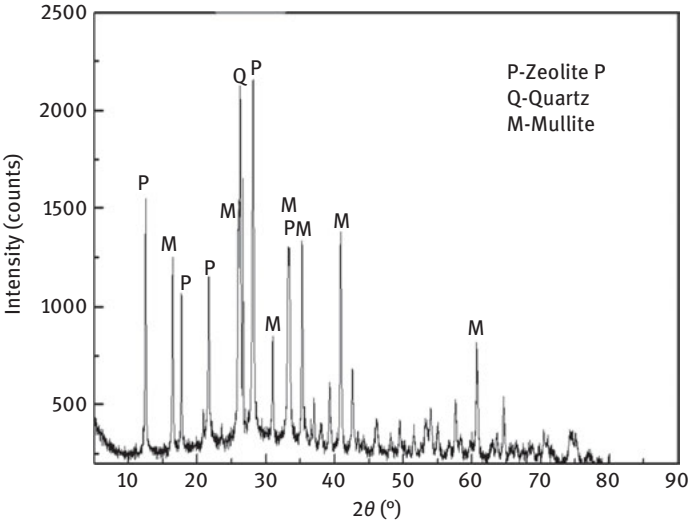

Figure 2.8: XRD patterns of the 3rd group.

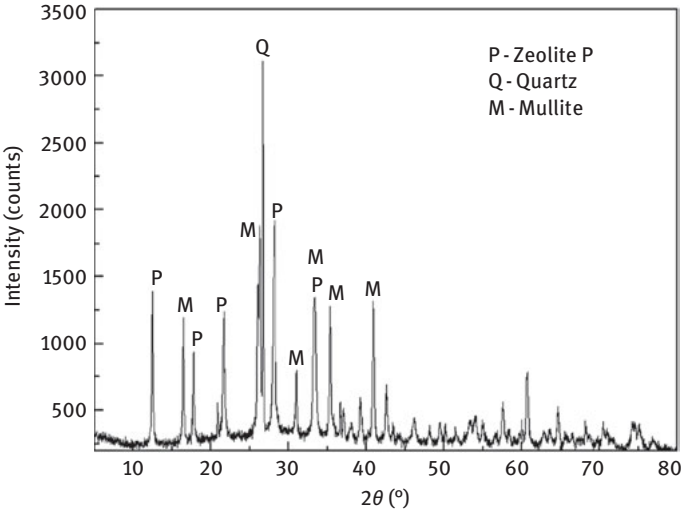

Figure 2.9: XRD patterns of the 4th group.

more suitable for the synthesis of zeolite A, X or P. In this study, zeolite P ($Na_6Al_6Si_{10}O_{32}{\cdot}12H_2O$) was synthesized. Because of the two different sizes of pore size, zeolite P has satisfactory performance of ion exchange and adsorption (YU & SONG, 2005).

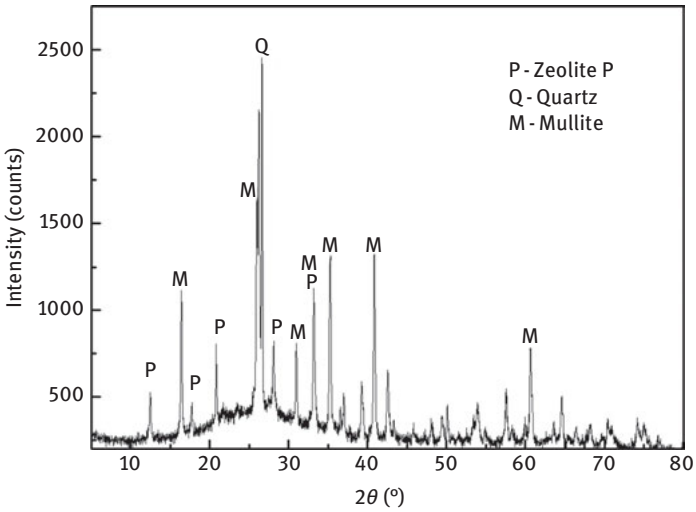

Figure 2.10: XRD patterns of the 5th group.

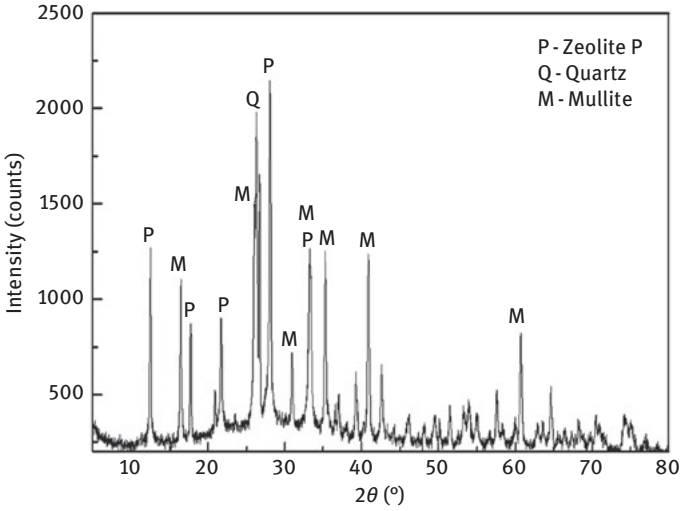

Figure 2.11: XRD patterns of the 6th group.

(ii) SEM analyses

The samples of nine groups were analyzed by SEM. Figures 2.16–2.24 show the different morphologies of zeolite crystal under various synthetic conditions. The morphology of the samples before and after the synthesis was obviously different. Compared with the single spherical particles before synthesis, the particles of the synthesized product are crystal cluster, with obvious crystal characteristics, and have a large number of pore structure, thereby the generation of zeolite crystals can be confirmed (Figure 2.25).

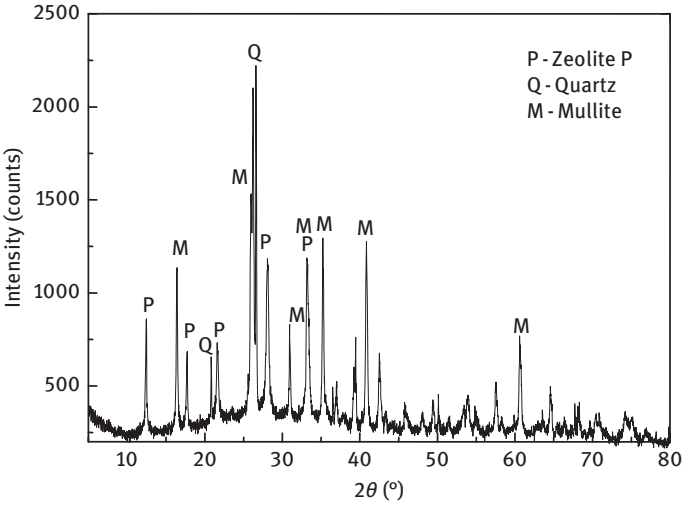

Figure 2.12: XRD patterns of the 7th group.

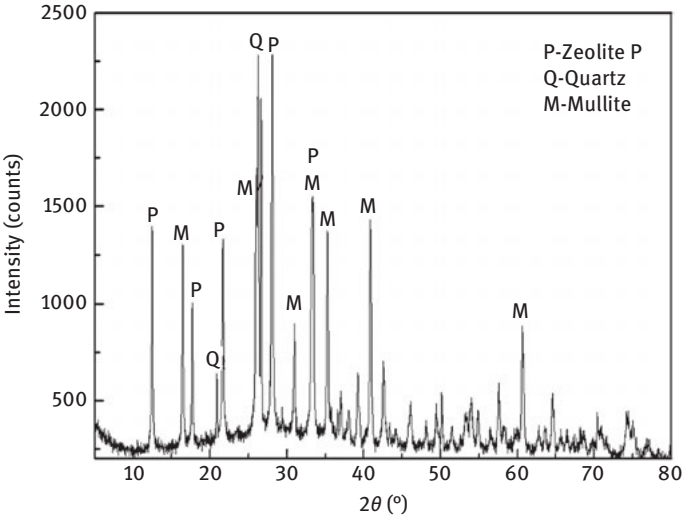

Figure 2.13: XRD patterns of the 8th group.

(iii) Analysis of CEC results

The results of CEC are shown in Table 2.6: and Figure 2.26. The CEC value of the synthetic zeolite from the 6th group was the largest (249.52 cmol/kg, while 8.59 cmol/kg of fly ash). And the adsorption performance of ammonia was the best.

The further range analysis shows that the lye concentration has the greatest influence on the CEC value of synthetic zeolite, and the reaction time is the second;

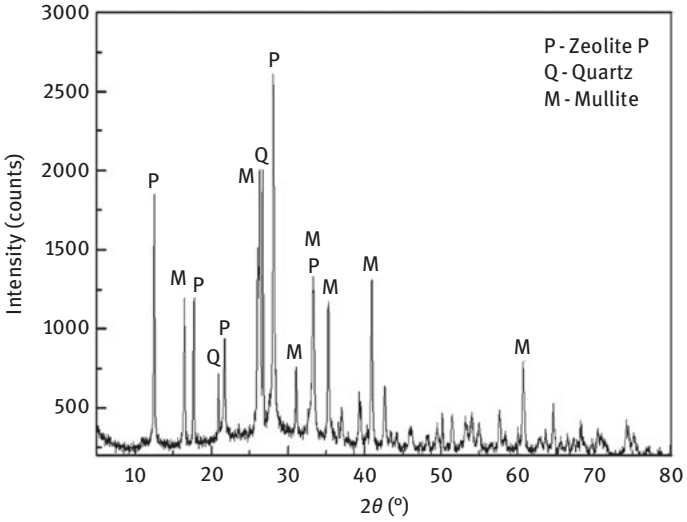

Figure 2.14: XRD patterns of the 9th group.

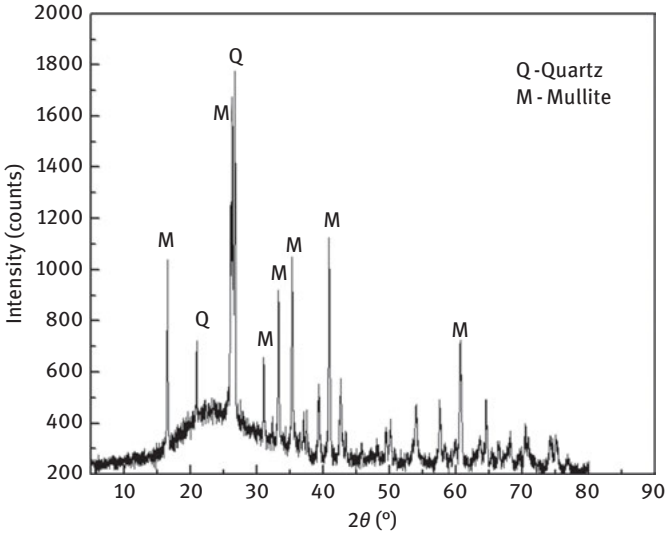

Figure 2.15: XRD patterns of fly ash.

the reaction temperature and the liquid-to-solid ratio have only little effect on it. The effect graph of the orthogonal test also reflects this trend. In addition, the effect graph shows that the CEC value of the synthetic zeolite increases with increasing lye concentration, but this condition is limited by economic cost. Considering that the parameters of 6th group can be selected, namely the liquid-to-solid ratio is 4:1, the lye concentration is 3 mol/L, the reaction temperature is 100 °C and the reaction time is 24 h.

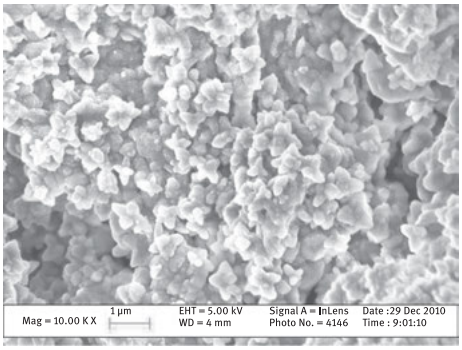

Figure 2.16: SEM image of the 1st group.

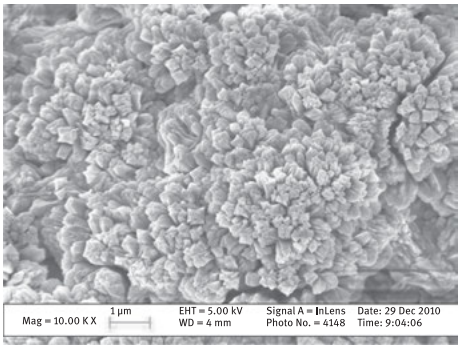

Figure 2.17: SEM image of the 2nd group.

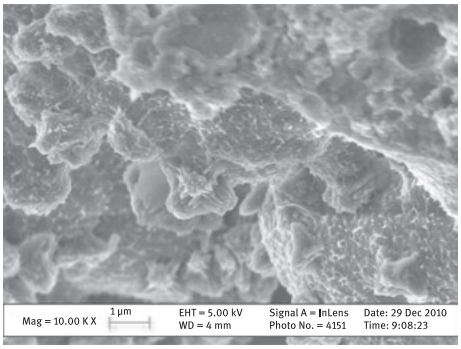

Figure 2.18: SEM image of the 3rd group.

2.2.1.4 Determination of preparation parameters

The low-cost zeolite from fly ash was synthesized by improved hydrothermal method and the orthogonal test was used to optimize the synthetic parameters. The synthetic products were analyzed by XRD and SEM. Finally, the adsorption performance of synthetic zeolite was evaluated by CEC. Based on the comprehensive analysis, it can be seen that the parameters of synthetic artificial zeolite under the test conditions of 6th group can meet the requirements of the subsequent zeolite.

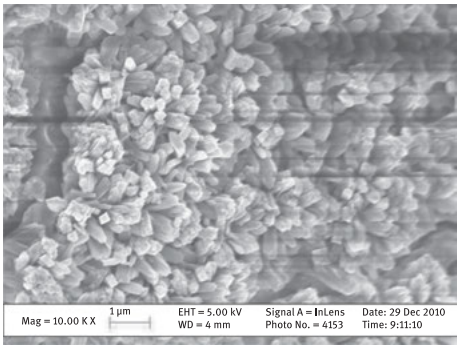

Figure 2.19: SEM image of the 4th group.

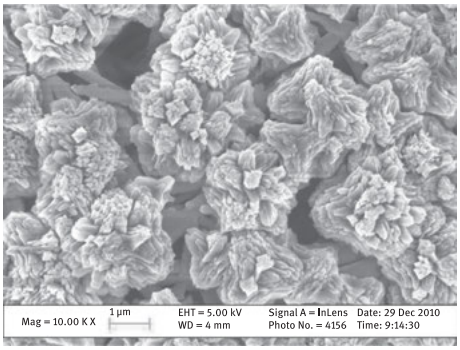

Figure 2.20: SEM image of the 5th group.

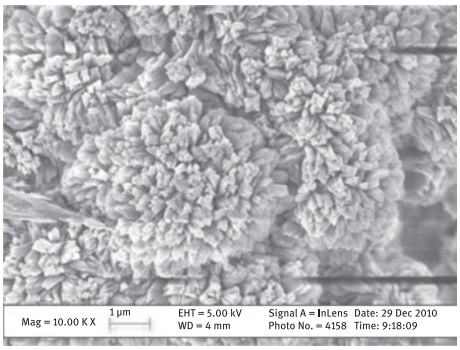

Figure 2.21: SEM image of the 6th group.

(1) The results of XRD show that the synthetic zeolite is well crystallized and the peaks are intact.
(2) SEM shows that the surface area of synthetic zeolite is several times higher than that of fly ash. Fly ash particles were smooth, regular spherical. And after synthesis, zeolite particles have lost spherical morphology, and the surface is rough, which is a clear crystal form. This change is conducive to adsorption. So the application performance is improved.

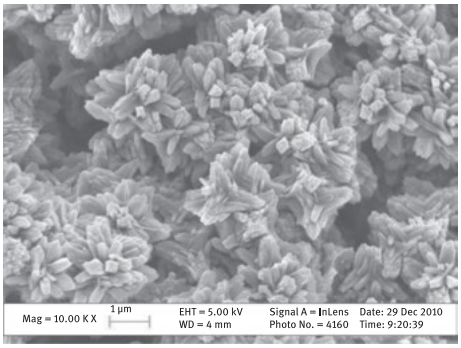

Figure 2.22: SEM image of the 7th group.

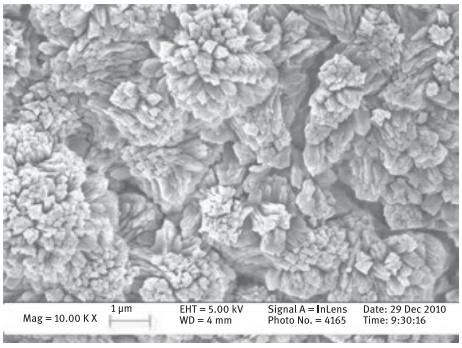

Figure 2.23: SEM image of the 8th group.

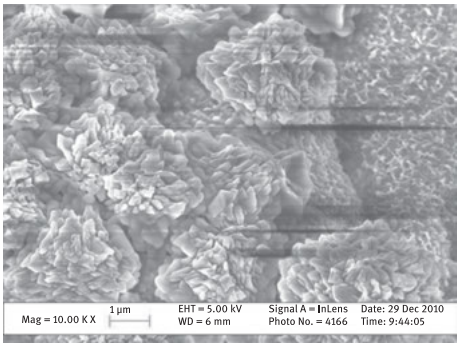

Figure 2.24: SEM image of the 9th group.

(3) The CEC value of synthetic zeolite was increased from less than 9 cmol/kg of fly ash to 250 cmol/kg.

The conversion of fly ash to zeolite was relatively successful, and the synthesized zeolite has high quality and is of low cost.

Table 2.6: Experimental results of orthogonal array testing.

Int iCol	1	2	3	4	CEC (cmol/kg)
Factors	**Liquih-to-solih ratio (L/S)**	**Alkali liquor concentration (mol/L)**	**Temperature of reaction (°C)**	**Reaction time (h)**	
1st group	3∶1	1	100	12	98.24
2nd group	3∶1	2	90	24	209.7
3rd group	3∶1	3	120	36	222.56
4th group	4∶1	1	90	36	159.65
5th group	4∶1	2	120	12	175.58
6th group	4∶1	3	100	24	249.52
7th group	5∶1	1	120	24	172.53
8th group	5∶1	2	100	36	177.31
9th group	5∶1	3	90	12	219.29
Mean value 1	176.833	143.473	175.023	164.370	
Mean value 2	194.917	187.530	196.213	210.583	
Mean value 3	189.710	230.457	190.223	186.507	
Range	18.084	86.984	21.190	46.213	

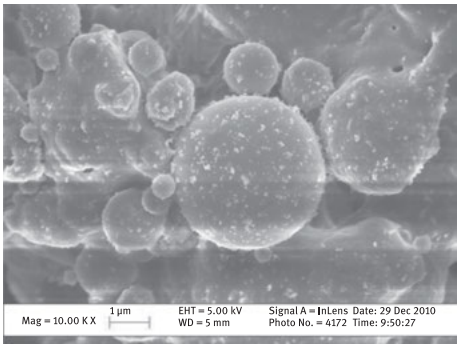

Figure 2.25: SEM image of fly ash.

2.2.2 Recycling technology of waste acid and waste alkali

Product cost is an important factor in its market prospects. In order to solve the problem of large amount of acid and alkali in the process of zeolite synthesis, high cost, secondary pollution caused by waste acid and alkali, based on the determination of parameters, the recycling and utilization of waste acid and waste alkali in the zeolite synthesis was researched. So far, only a handful of researchers have been engaged in this research. Wu Deyi et al. (2005) added industrial silicon and aluminum in the waste lye to adjust the Si/Al ratio, then full recycling to reduce costs. But the impurities in the waste lye will affect the quality of synthetic products. Moreover,

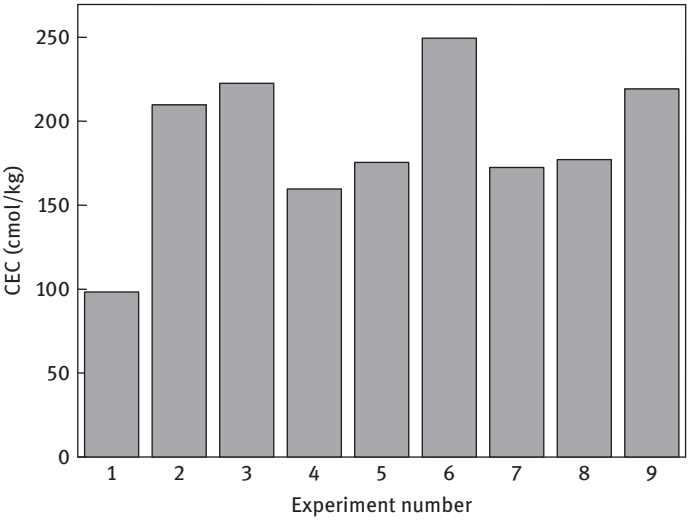

Figure 2.26: CEC results of orthogonal array testing.

the addition of industrial silicon and aluminum also increased the cost. Therefore, this study uses the following recycling techniques: Waste acid and waste alkali was reused in the appropriate proportion to adjust the acid–base concentration. This technology controls the amount of waste acid and alkali, to avoid the impact of impurities on the quality of synthetic zeolite, which will be able to ensure the quality of synthetic zeolite, but also reduce the amount of fresh acid and alkali and the cost, to achieve the reuse of waste acid and alkali.

2.2.2.1 Process flow of reuse of acid and alkali

The synthetic process of zeolite is shown in Figure 2.27.

The traditional hydrothermal synthetic process has been improved as follows:

(1) Increase reuse system of waste acid to reduce costs
(2) Increase reuse system of waste alkali to reduce costs

(1) Acid and alkali recovery method

(i) Recycling of acid and alkali

At 90–95 °C, after about 1 h reaction, the 2 mol/L hydrochloric acid with a liquid-to-solid ratio of 3:1 was used for pickling pretreatment, and then the waste acid is recovered. The zeolite synthesis experiment was carried out under the following conditions: liquid-to-solid ratio of 4:1, alkali concentration of 3 mol/L, reaction temperature of 100 °C and reaction time of 24 h. The alkali liquor was recovered after the end of the experiment.

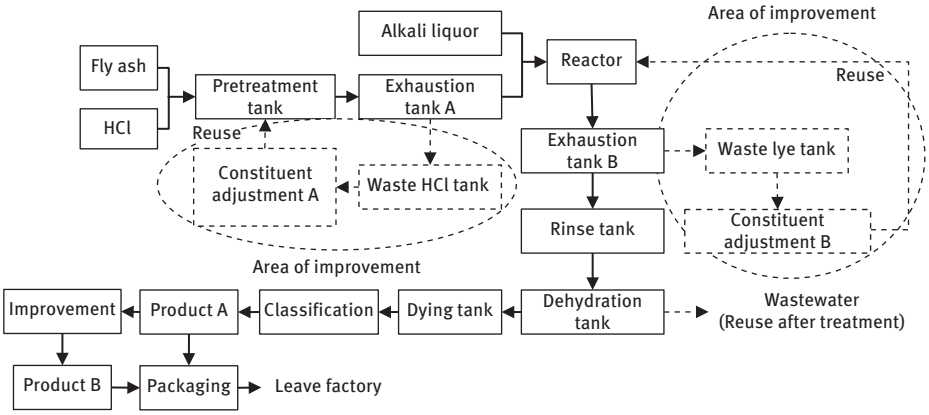

Figure 2.27: Process diagram of zeolite synthesis from fly ash and areas of improvement.

(ii) The effect of recycled acid

The hydrochloric acid solution of 2 mol/L was compounded of recycle acid and concentrated hydrochloric acid in proportion of 3:1, 2:1 and 1:1. After pickling, the fly ash was washed until neutral and then dried. The zeolite was synthesized with 3 mol/L NaOH solution in batches, then washed until neutral and dried.

(iii) The effect of recycled alkali

Fly ash was acid washed with 2 mol/L hydrochloric acid solution, formulated with concentrated hydrochloric acid, then washed until neutral and dried. The NaOH solution of 3 mol/L was compounded of recycled alkali and concentrated NaOH solution in proportion of 3:1, 2:1 and 1:1. Other parameters are unchanged. The zeolite was synthesized, then washed until neutral and dried.

(2) Experiment of ammonia absorption

(i) Simulated wastewater

The simulated wastewater with the ammonia concentration of 25 mg/L was prepared from ammonium chloride (analytical grade) according to GB 7479-87.

(ii) Absorption experiment

A sample of 0.5 g was placed in 250 mL Erlenmeyer flask, and 50 mL of water (with ammonia concentration of 25 mg/L) was added to it. The adsorption reaction was carried out at 25 °C (constant temperature) in the air bath thermostat oscillator with 150 r/min for 1 h. After centrifugation at 5,000 r/min for 10 min, the concentration of ammonia in the supernatant was determined by spectrophotometric method using Nessler's reagent.

(iii) Calculation of removal rate and adsorption capacity

$$\text{The removal rate } (\%) = (C_0 - C_t)/C_0 \tag{2.2}$$

$$\text{The adsorption capacity } Q = (C_0 - C_t)V/m \tag{2.3}$$

where C_0, C_t are the concentrations of ammonia in solution before and after adsorption, mg/L; V is the solution volume, mL; m is the dosage of recycled acid and alkali.

2.2.2.2 Effect of recycling ratio on properties of artificial zeolite

(1) Characterization of synthetic zeolite with recycled acid and alkali

(i) SEM of synthetic zeolite with recycled alkali

Figure 2.28 shows the SEM photographs of the synthetic zeolite with recycled alkali. Fly ash is composed of spherical vitreous and some irregular melting particles, and the spherical surface is relatively smooth. Inorganic components in fly ash are burned at a high temperature of 1,000 °C, and then suddenly cooled in the flue. Under the action of the surface tension, the above structure is formed. Compared with the raw material, the synthetic zeolite product has obvious crystal characteristics, and a large number of pore structure. Synthetic zeolites have a certain ion exchange performance and adsorption properties owing to their different pore sizes. The SEM photographs of the synthetic zeolite of recycled alkali have no significant difference in crystal form compared with that of the synthetic zeolite. The zeolite surface still has a large number of pore structures. In general, the alkali material can destroy the hard shell of the surface of fly ash particles so that the soluble substance on the vitreous surface reacts with the alkaline oxide to form a gelling substance.

(a) Fly ash (×10,000)
(b) Synthetic zeolite (× 10,000)
(c) RA:NA* = 1:1 (×10,000)
(d) RA:NA* = 2:1 (×10,000)
(e) RA:NA* = 3:1 (×10,000)

(ii) SEM of synthetic zeolite with recycled acid

Figure 2.29 shows the SEM photographs of the synthetic zeolite with recycled acid of different ratio. It is shown in the figure that the synthetic zeolite of recycled acid crystallizes well. They also have a large number of pore structure, with a certain ion exchange performance and adsorption capacity. However, compared with synthetic zeolite and the above-mentioned synthetic zeolite with recycled alkali,

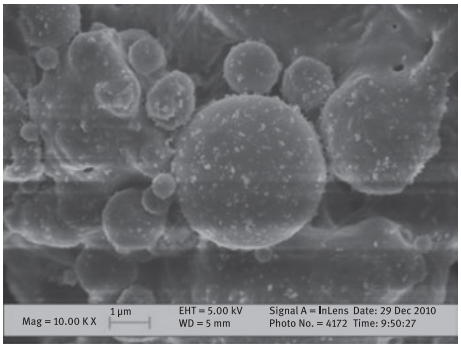

(a) Fly ash (×10,000)

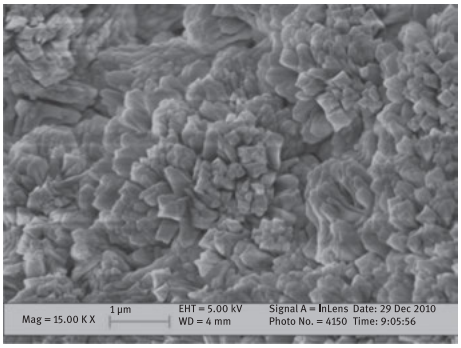

(b) Synthetic zeolite (×10,000)

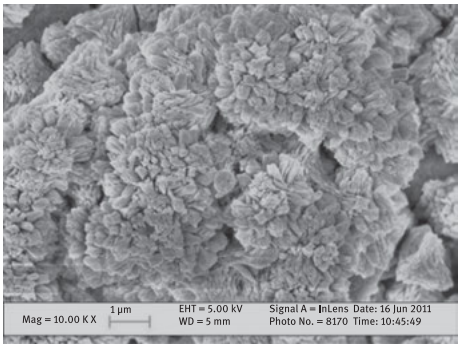

(c) RA:NA*=1:1 (×10,000)

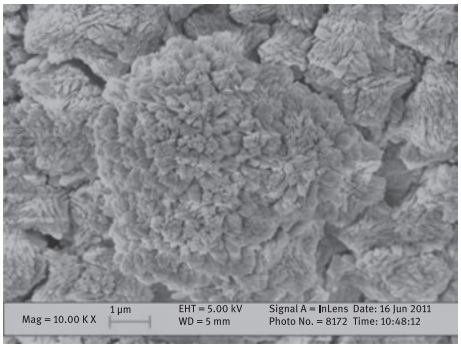

(d) RA:NA*=2:1 (×10,000)

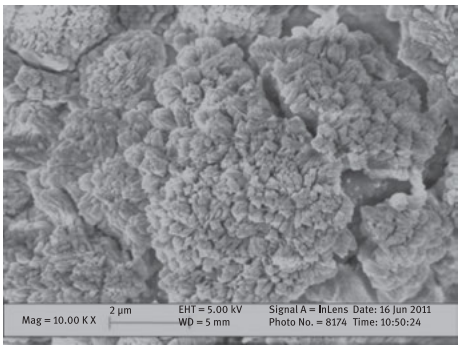

(e) RA:NA*=3:1 (×10,000)

Figure 2.28: SEM photographs of the synthetic zeolite and fly ash.
Note: *RA:NA is the ratio of recycled alkali and new alkali.

the amount of crystal and porosity decreased. This shows that the synthesis of zeolite is not complete. With the increase of the proportion of recycled acid, the amount of synthetic zeolite and the crystallization decreased. The reason may be that the fly ash contains hematite and magnetite, which are unfavorable to

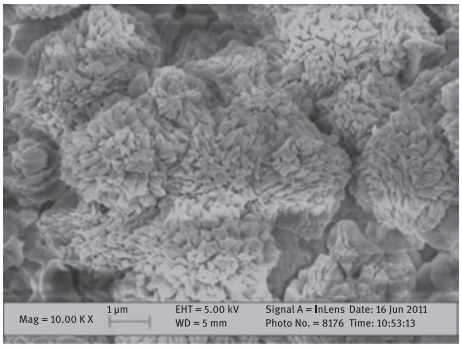

(a) RA:NA*=1:1 (×10,000)

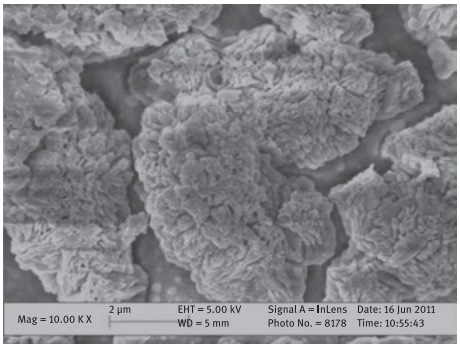

(b) RA:NA*=2:1 (×10,000)

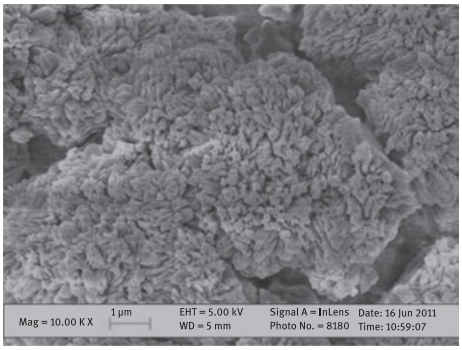

(c) RA:NA*=3:1 (×10,000)

Figure 2.29: SEM photographs of the synthetic zeolite with different ratios of recycled acid.
Note: *RA:NA is the ratio of recycled acid and new acid.

synthetic zeolite. The presence of iron can seriously affect the crystallinity. When hydrochloric acid after pickling was reused, iron was actually reconcentrated. This greatly increased the iron content in the recycled acid, thereby affecting the zeolite synthesis:

(a) RA:NA* = 1:1 (×10,000)
(b) RA:NA* = 2:1 (×10,000)
(c) RA:NA* = 3:1 (×10,000)

(iii) XRD pattern analysis of recycled acid and alkali

As shown in Figure 2.30, the peak shape of the synthetic zeolite and that with recycled acid and alkali are equivalent, and the diffraction peaks are sharp and strong, indicating that the synthesized product is well crystallized. The diffraction peak shows that their main phase composition is 43-0052> $Na_3{\cdot}6Al_3{\cdot}6Si_{12}{\cdot}4O_{32}{\cdot}14H_2O$-Zeolite P, (Na), 39-0219> $Na_6Al_6Si_{10}O_{32}{\cdot}12H_2O$-Zeolite P1, (Na). And the peaks are almost consistent in intensity. This shows that the required zeolite is obtained.

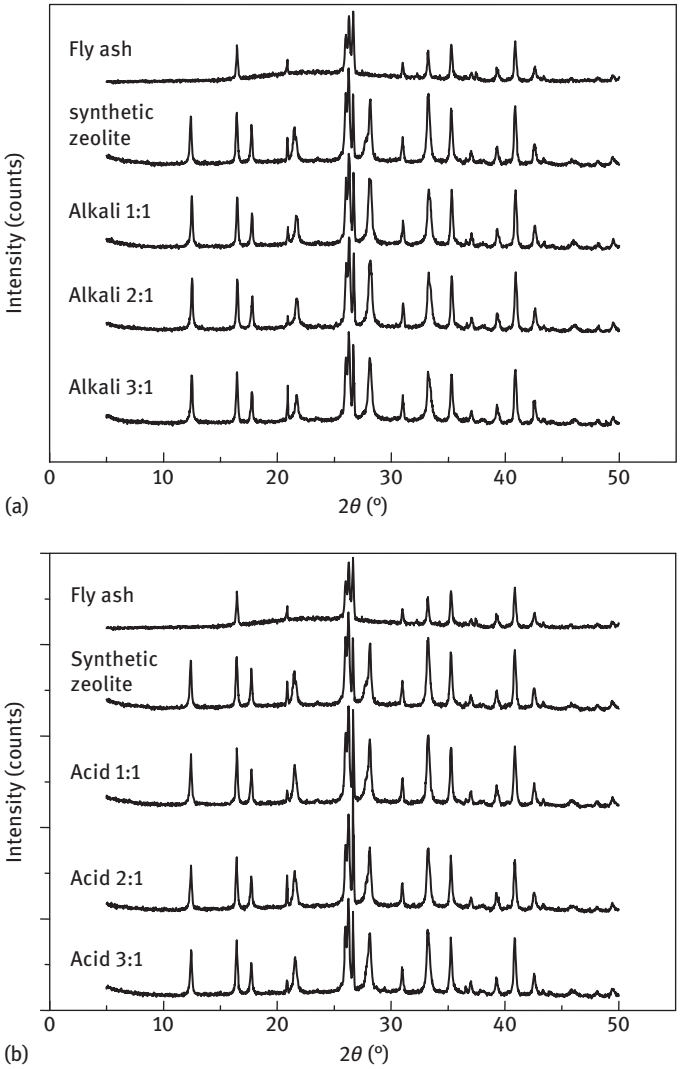

Figure 2.30: XRD patterns of synthetic zeolite and that with recycled acid and alkali.

(2) Removal effect of synthetic zeolite with recycled acid and alkali on ammonia

As shown in Figure 2.31, results on the nitrogen removal of the synthetic zeolite with recycled alkali are almost the same as that of the synthetic zeolite completely with the new alkali. This is because OH^- plays a major role during the dissolution phase of synthetic zeolite from fly ash. Therefore, the synthesis can be ensured as long as the lye concentration reaches the optimum synthetic conditions. But pickling with recycled acid has a bad effect on the nitrogen removal of the synthetic zeolite.

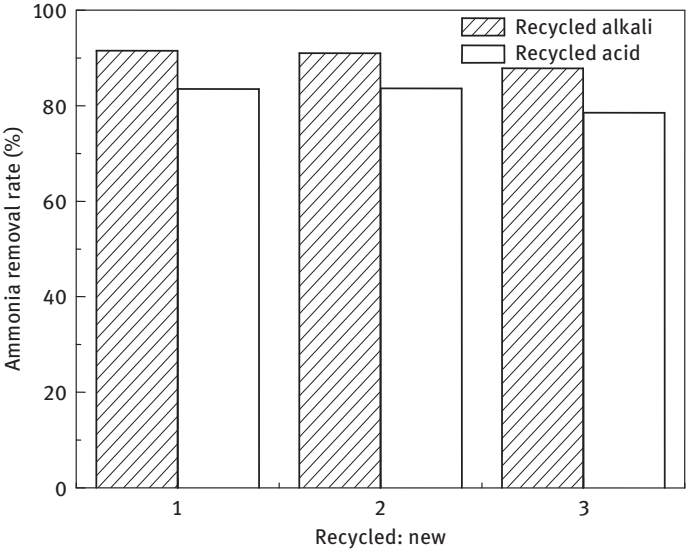

Figure 2.31: Ammonia removal rate of synthetic zeolite with recycled acid and alkali.

Originally, the hematite and magnetite in fly ash can be washed off through pickling, because they are unfavorable to synthesis. However, the high concentration of impurities such as iron ions in the recycled acid affects the synthetic quality of the zeolite.

(3) Isothermal adsorption test of synthetic zeolite with recycled acid and alkali

Langmuir equation:

$$C_e/Q_e = C_e/Q_{max} + 1/(Q_{max} \cdot b) \tag{2.4}$$

Freundlich equation:

$$\lg Q_e = (1/n)\lg C_e + \lg K_F \tag{2.5}$$

where Q_{max} is the maximum mass of adsorbate, mg/g; Q_e is the mass of adsorbate at equilibrium, mg/g; C_e is the equilibrium concentration of adsorbate in solution, mg/L; b is the adsorption strength, L/mg; K_F is the adsorption coefficient, L/mg; $1/n$ is the adsorption index.

Figure 2.32 shows the adsorption isotherms of ordinary synthetic zeolite and that with recycled acid and alkali (ratio 1:1). The experimental data are fitted using the above two equations. It is found that the Freundlich equation can better describe the adsorption behavior of the three zeolites. As shown in Table 2.7, the squared correlation coefficients (r^2) are all close to 0.99. And the fitting result with Langmuir

Table 2.7: Freundlich adsorption isotherm of three zeolites and related parameters.

Synthetic zeolite			Zeolite with recycled acid			Zeolite with recycled alkali		
K_F	n	r^2	K_F	n	r^2	K_F	n	r^2
0.270 5	1.28	0.990 9	0.275 5	1.54	0.987 1	0.268 3	1.28	0.990 1

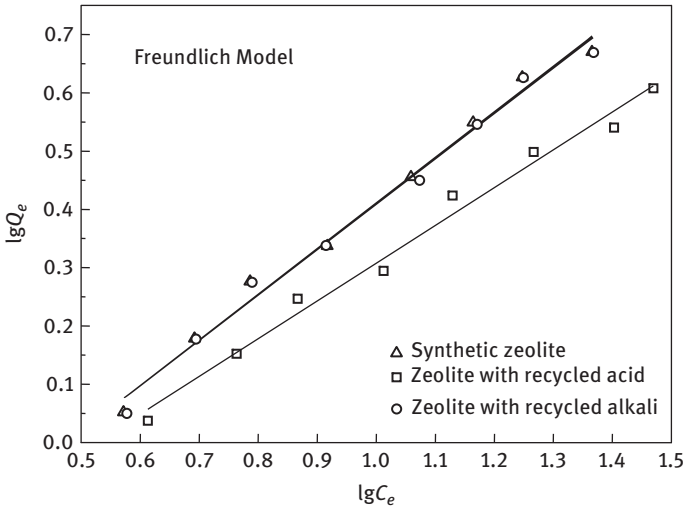

Figure 2.32: Adsorption isotherms of synthetic zeolite with recycled acid and alkali.

equation does not match (not shown here). As shown in Figure 2.32, the adsorption isotherms of general synthetic zeolite and synthetic zeolite with recycled alkali are basically coincident, while the adsorption isotherm of recycled acid has been moved down. This shows that recycled alkali has scarcely any effect on zeolite synthesis, but recycled acid has an impact on zeolite quality.

(4) Dosing test of synthetic zeolite with recycled acid and alkali

As shown in Figure 2.33, the ammonia removal rate of zeolite with recycled acid and alkali (both with ratio 1:1) increased with the increase in dosage, and then the removal rate was relatively stable to achieve adsorption equilibrium state. Compared to ordinary synthetic zeolite, not only the ammonia removal rate decreased slightly, and the equilibrium state also lagged behind. The synthetic zeolite reached the equilibrium state, when the dosage was 10 g/L, but the zeolite with recycled acid and alkali was basically in equilibrium, when the dosage was more then 15 g/L. In addition, the ammonia removal effect of zeolite with recycled alkali is better than that of zeolite with recycled acid.

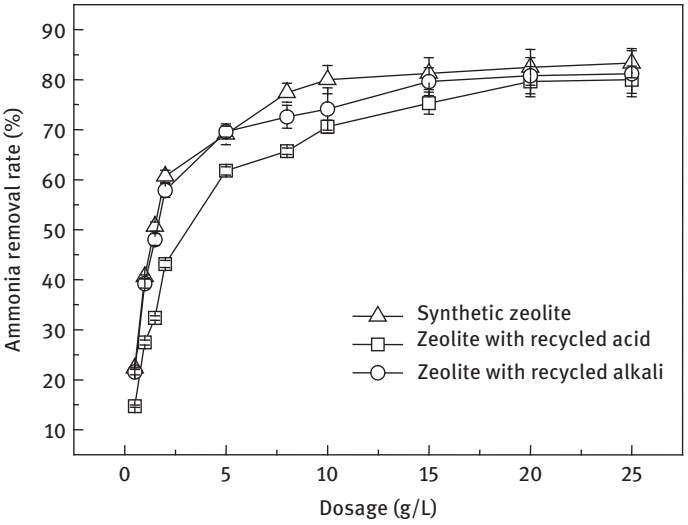

Figure 2.33: Comparison of ammonia removal rate with dosage.

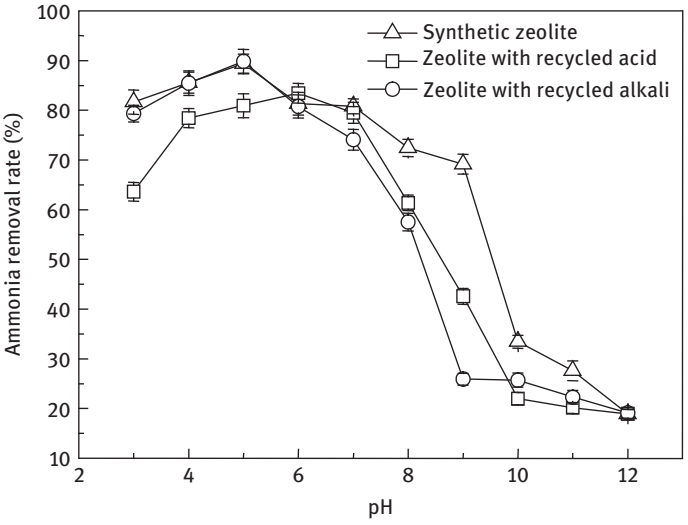

Figure 2.34: Comparison of pH effects on ammonia removal rate.

(5) Effect of pH on ammonia removal of zeolite with recycled acid and alkali

The effect of pH on the ammonia removal of the zeolite with recycled acid and alkali (both with ratio 1:1) is shown in Figure 2.34. The pH influence rule of the three zeolites was similar. The removal of ammonia was the best under weak acid condition (pH is 4–6). When the pH <4 and pH >8, the removal efficiency of ammonia decreased obviously.

2.2.2.3 Determination of recycling parameters

Artificial zeolite is synthesized with an appropriate proportion of recycled alkali, which has little effect on the ammonia removal. The performance is almost consistent with the ordinary synthetic zeolite. But pickling with recycled acid has a bad effect on the nitrogen removal. Considering the factors of product quality and cost, a certain amount of recycled alkali can be used in the actual production for synthetic zeolite, together with new alkali. The ratio of recycled alkali to new alkali should be less than 2:1, and the ratio of recycled acid to new acid should be less than 1:1 for the pretreatment of raw material.

2.3 Modification and functionalization of artificial zeolite prepared by coal fly ash

The existing researches on artificial zeolite are mainly focused on its cation exchange performance and the removal of heavy metal ions in water, while zeolite is less used for the removal of wastewater. The treatment of low concentration of phosphorus-containing wastewater with existing synthetic zeolite is not ideal. So the modification is necessary to strengthen its removal capacity of ammonia and phosphorus.

The modification is mainly through chemical methods to treat the surface of the artificial zeolite to improve the porosity, CEC and adsorption of other nonpolar organic materials. Lanthanum, cerium and other rare earth elements have a strong adsorption on orthophosphate. The use of rare earth elements for zeolite modification can not only improve its CEC and also increase its phosphorus removal rate. China leads the world in reserves and production of rare earth. The wastewater from rare earth enterprises contains a certain amount of rare earth elements. This study has realized the recycling of rare earth industrial wastewater in order to achieve the purpose of waste treatment with waste.

2.3.1 Effect of lanthanum ion concentration on nitrogen and phosphorus removal

Synthetic zeolite from fly ash can remove a certain amount of phosphorus with high concentrations, but has little adsorption on phosphorus with low concentrations (≤5 mg/L) (Liu Yikai et al., 2008). But the phosphorus in domestic wastewater is in the low concentration range, which requires reducing the adsorption initiation point of synthetic zeolite. From Figure 2.35, it is shown that the phosphorus removal after the modification by lanthanum ion increased significantly, from less than 10% to more than 95%. And it reached the maximum at the lanthanum ion concentration of 0.5%, and then the removal rate of phosphorus began to decrease slowly. This is because of the increase in the concentration of lanthanum ions, and the coordination complex was generated, which initially adsorbed anions and

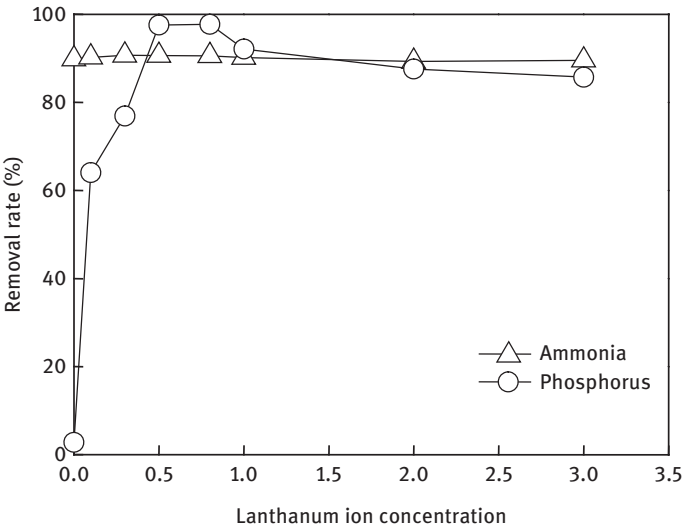

Figure 2.35: Effect of lanthanum ion concentration on nitrogen and phosphorus removal.

cations, but eventually clogged the pores, resulting in reduced removal rate of synthetic zeolites. The removal rate of ammonia of the modified zeolite did not increase significantly, but its adsorption rate increased. For the ammonia solution with 25 mg/L, the ordinary synthetic zeolite needs more than 24 h to achieve adsorption equilibrium, while the modified zeolite takes only about 30 min. This greatly reduces the adsorption time, and is much convenient in practical application.

2.3.2 Effect of the modified solution pH on nitrogen and phosphorus removal

The effect of pH on the modification is shown in Figure 2.36. pH had little effect on the ammonia removal, but a great effect on the phosphorus removal. In the low pH conditions, phosphorus removal effect was poor, that is, less than 50%. With the increase of pH, the removal rate of phosphorus was significantly improved. At pH up to about 10, the removal rate of phosphorus reached its maximum and then decreased significantly.

2.3.3 Effect of the modification time on nitrogen and phosphorus removal

The modification time had a significant effect on the nitrogen and phosphorus removal of modified zeolite. From Figure 2.37, it is shown that the phosphorus removal efficiency of the modified zeolite was gradually improved with the increase of time, from less than 40% at 2 h to 95% at 24 h. After that, with the time accumulation, phosphorus

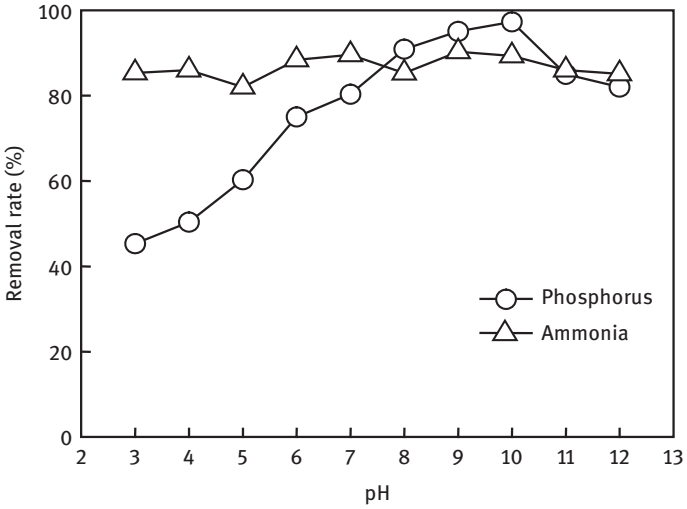

Figure 2.36: Effect of the modified solution pH on nitrogen and phosphorus removal.

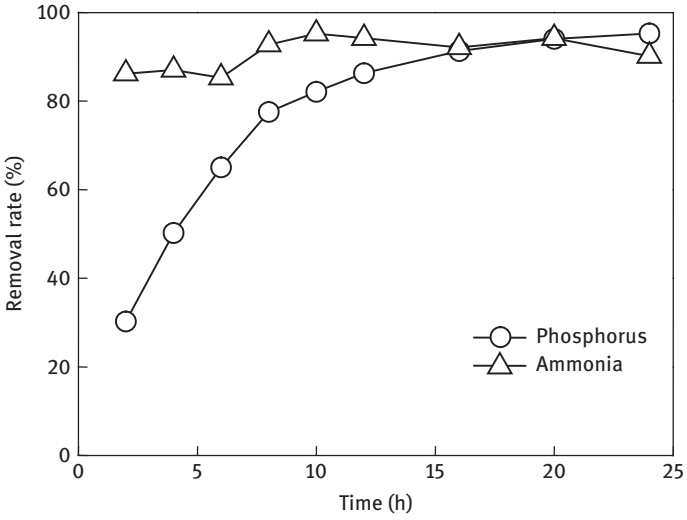

Figure 2.37: Effect of the modification time on nitrogen and phosphorus removal.

removal efficiency increased little. The main reason is: The surface of the modified synthetic zeolite was covered with hydroxyl radical, which was easily reacted with cations and anions to form surface-coordinated complex that can also remove phosphorus. At the beginning, the coverage of the hydroxyl radical increased with time; after the saturation, the modified zeolite has the largest removal efficiency of phosphorus.

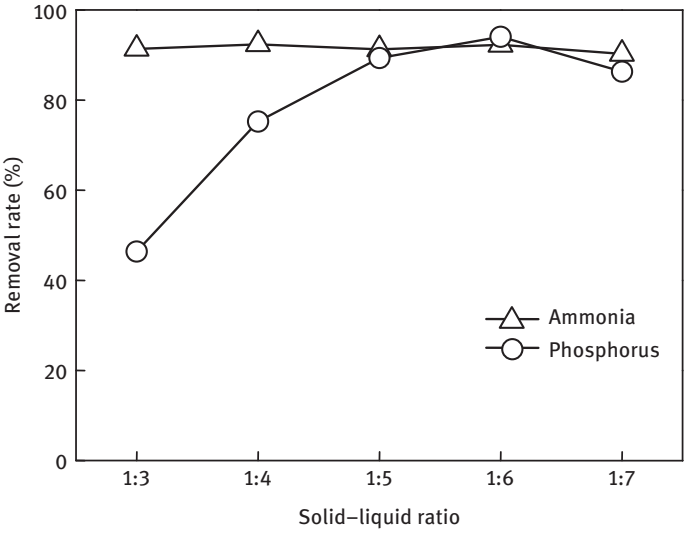

Figure 2.38: Effect of the solid–liquid ratio on nitrogen and phosphorus removal.

2.3.4 Effect of the solid–liquid ratio on nitrogen and phosphorus removal

Solid–liquid ratio is an important indicator of the economic cost of modification. The larger solid–liquid ratio will undoubtedly increase cost, affecting the practical application of modification. From Figure 2.38, it is shown that the phosphorus removal rate of the modified zeolite was only 40% when the solid–liquid ratio was 1:3. With the decrease of solid–liquid ratio, the removal rate of phosphorus is gradually increased. When the solid–liquid ratio was 1:6, the removal rate of phosphorus was the largest, and then slowly decreased and tended to be stable. This is because of the increase in the amount of lanthanium so that the hydroxyl, the active substance loaded on the molecular sieve, also increased accordingly. Hydroxyl has a good adsorption effect on the phosphate, so the removal of phosphate was stable after increase.

2.3.5 Optimization of modification conditions

On the basis of the above single-factor experiment, the influence factors of modification were optimized by four factors at three-level (nine runs, namely L9 or 3^4) orthogonal array testing to determine the optimal modification conditions. The factors are shown in Table 2.8. The removal rate of phosphate is the measurable indicator, and the results of the orthogonal array testing were range analyzed. The analysis results are shown in Table 2.9.

According to the range analysis, the modification time had the greatest influence among the four investigated factors. Followed by the pH and solid–liquid ratio, the

Table 2.8: Level factors of modification orthogonal array testing.

No.	1	2	3	4
Factors	**Modification concentration (%)**	**Modification pH**	**Modification time (h)**	**Solid–liquid ratio**
Level 1	0.4	9	18	1 : 4
Level 2	0.5	10	24	1 : 5
Level 3	0.6	11	30	1 : 6

Table 2.9: The analysis results of orthogonal array testing.

Int iCol	1	2	3	4	Removal rate of phosphate (%)
Factors	**Modification concentration (%)**	**Modification pH**	**Modification time (h)**	**Solid–liquid ratio**	
1st group	0.4	9	18	1 : 4	85.36
2nd group	0.4	10	24	1 : 5	95.98
3rd group	0.4	11	30	1 : 6	93.26
4th group	0.5	10	30	1 : 4	95.01
5th group	0.5	11	18	1 : 5	89.87
6th group	0.5	9	24	1 : 6	93.14
7th group	0.6	9	30	1 : 5	91.57
8th group	0.6	10	18	1 : 6	90.25
9th group	0.6	11	24	1 : 4	92.68
Mean value 1	91.53	90.02	88.49	91.02	
Mean value 2	92.67	93.74	93.93	92.60	
Mean value 3	91.50	91.94	93.28	92.21	
Range	1.17	3.72	5.44	1.58	

modification concentration had the minimum effect. From Table 2.8, the optimized modification parameters were as follows: the modification concentration is 0.5%, the modification pH is 10, the modification time is 24 h and the solid–liquid ratio is 1:5.

2.3.6 Effect of modification on physical structure of artificial zeolite

(1) BET (Brunauer-Emmett-Teller) analysis

The specific surface area of lanthanum-modified zeolite synthesis from coal fly ash (LaZP), P-type synthetic zeolite (ZP) and fly ash was measured using ASAP2010M automatic surface pore size analyzer (Micrometics, USA). The results are shown in Table 2.10.

As given in Table 2.10, the specific surface area of ZP is greatly increased from 0.867 to 45.804 m^2/g compared to fly ash. The pore structure is dominated by mesopores and the total pore volume is more than 0.137 cm^3/g. The average aperture is small, about

Table 2.10: Measured result of specific surface area.

	BET specific surface (m^2/g)	Langmuir specific surface (m^2/g)	Pore volume (cm^3/g)	Aperture (nm)
Fly ash	0.867	1.137	–	–
ZP	45.804	63.575	0.137	11.935
LaZP	43.761	60.751	0.138	12.654

11.94 nm. And the specific surface area of ZP decreased from 45.804 m^2/g down to 43.761 m^2/g after modification. The aperture *e* is expanded from 11.935 to 12.654 nm. The pore volume increased slightly from 0.137 to 0.138 cm^3/g.

In general, if the number of channels unchanged, the pore volume and specific surface area will increase with the increase in aperture. However, if the zeolite pore size increases after treatment, the micropores will be certainly destroyed, so that the average pore size increases and the surface area decreases. Pore volume may at this time also be reduced or slightly increased.

(2) Scanning electron microscopy

Figure 2.39 shows the electrophotographic scan of fly ash, ZP and LaZP. It can be shown from the figure that the fly ash is mainly composed of spherical particles, and

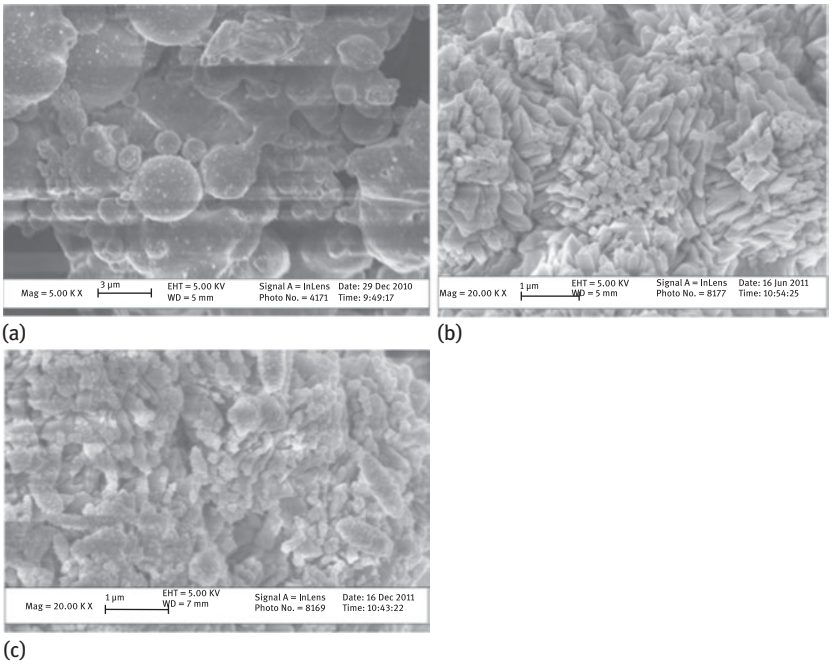

Figure 2.39: Electrophotographic scan of fly ash (a), ZP (b) and LaZP (c).

the composition is mainly amorphous SiO_2 and Al_2O_3 (see Figure 2.39a). Compared with fly ash, ZP surface was clustered (cluster surface is smooth), has good crystal characteristics and has a large number of pore structure (see Figure 2.39b). LaZP retains the crystal form and pore structure of ZP. On the surface of the cluster, a white granular material with good dispersion effect is obtained, that is, hydrated hydroxy compound supported on lanthanum (see Figure 2.39c).

(3) XRD analysis

Figure 2.40 shows the comparison of XRD of ZP, LaZP and fly ash. It shows that the XRD pattern of fly ash is small and the strength is low, which is mainly composed of quartz and mullite. The diffraction peaks of the synthetic zeolite and the modified zeolite are sharp and strong, and have obvious peaks of P-type zeolite. And before and after modification the modified zeolite did not change significantly on its skeleton, that is, still Na-P zeolite structure. This shows that lanthanum modification did not cause damage to its molecular sieve skeleton, and this modification is just on the zeolite surface.

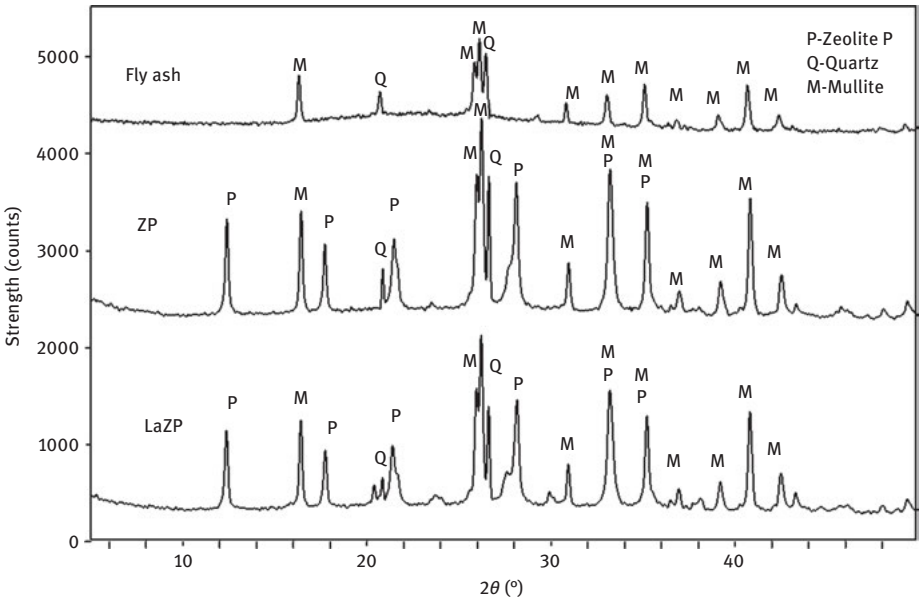

Figure 2.40: XRD patterns of fly ash, ZP and LaZP.

(4) Thermogravimetric (TG)-differential scanning calorimetry (DSC) analysis

Figure 2.41 shows the TG-DSC of ZP and LaZP. From the TG curve in the graph, we can see that the weight loss of ZP is 6.74% and the weight loss of LaZP is 6.49%, which is not a much difference. In the DSC curve, ZP has a strong exothermic peak near 120 °C

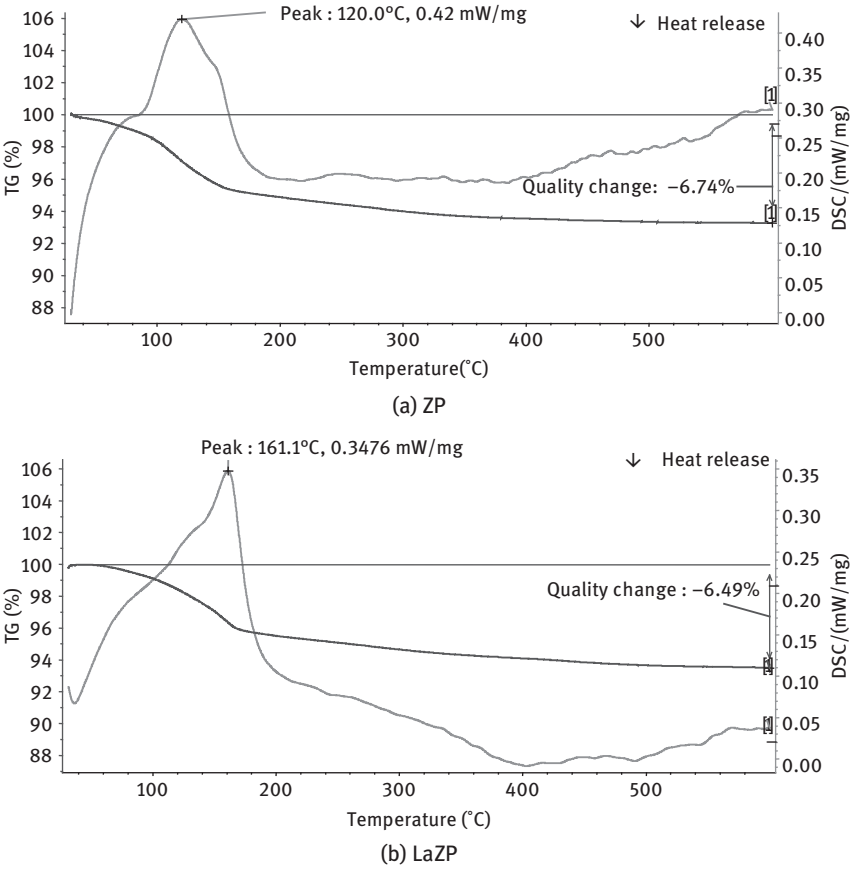

Figure 2.41: TG-DSC curve of ZP and LaZP.

due to the combustion of a small amount of organic matter remaining in the zeolite and the change in the crystalline structure of the zeolite. At this point the main weight loss process occurred. Compared with ZP, LaZP has a strong exothermic peak at 161 °C, and the main weight loss process is also accompanied at this stage. Comparison of the two can be seen; lanthanum ion modification improves the heat resistance of zeolite.

2.4 Simultaneous removal of nitrogen and phosphorus of modified zeolite

2.4.1 Effect of dosing amount on nitrogen and phosphorus removal

In order to study the effect of dosing on nitrogen and phosphorus removal, the dosage of 1–20 g/L was studied. The reaction conditions were as follows: constant

temperature of 25 °C, in the air bath thermostat oscillator at 150 r/min adsorption reaction for 1 h, remove and centrifuge at 5,000 r/min for 10 min. It can be seen from Figure 2.42 that for simulated wastewater with ammonia concentration of 25 mg/L and phosphorus concentration of 5 mg/L, when the dosage of LaZP was less than 5 g/L, the removal rate of ammonia and phosphorus increased with the increase of dosage. And then continue to increase the dosage of LaZP, the removal rate of ammonia and phosphorus was not significantly increased. The removal rate of ammonia and phosphorus was 90% and 95%, respectively, when the dosage was 10 g/L. Their effluent concentration was 2.5 and 0.2 mg/L, and reached the level A of the municipal sewage treatment plant emission standards. From the perspective of engineering applications, 2–7 g/L is the best dosage.

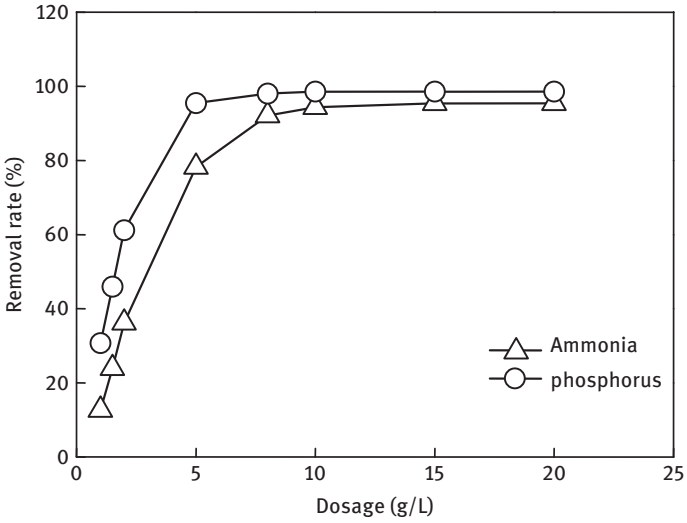

Figure 2.42: Relationship between removal rate of ammonia and phosphate, and dosing.

The simulated water quality was with ammonia of 8 mg/L and phosphorus of 1.5 mg/L, and the effluent quality was with ammonia 5 mg/L and phosphorus 1.0 mg/L. After 24 h of reaction in a thermostat, when the dosage of LaZP was less than 2 g/L, the removal rate of nitrogen and phosphorus increased significantly with the increase of dosing. By continuing with the increase in dosage, removal rate of ammonia and phosphate was no longer significantly increased. When the dosage is 1 g/L, the ammonia effluent concentration is 3.6 mg/L and the phosphate concentration is 0.19 mg/L, which reaches the level A of the municipal sewage treatment plant emission standards (see Figure 2.43).

It can be seen from Figure 2.44 that the ammonia and phosphate can reach the adsorption equilibrium within 30 min when the dosage is 1 g/L. With the increase in

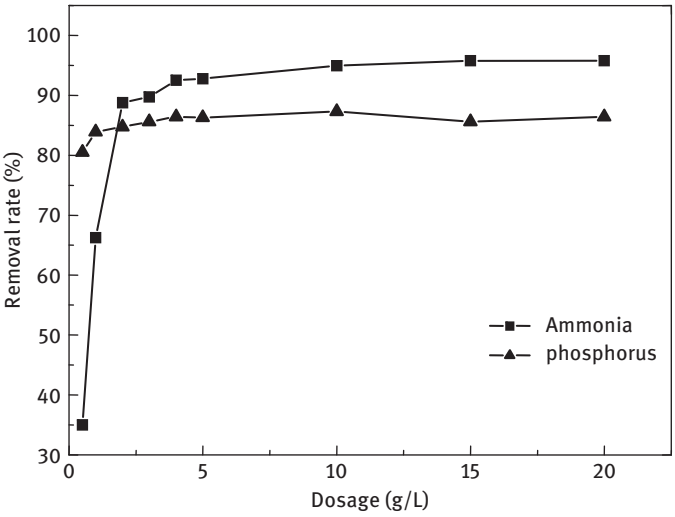

Figure 2.43: Relationship between removal rate of ammonia and phosphate, and dosing.

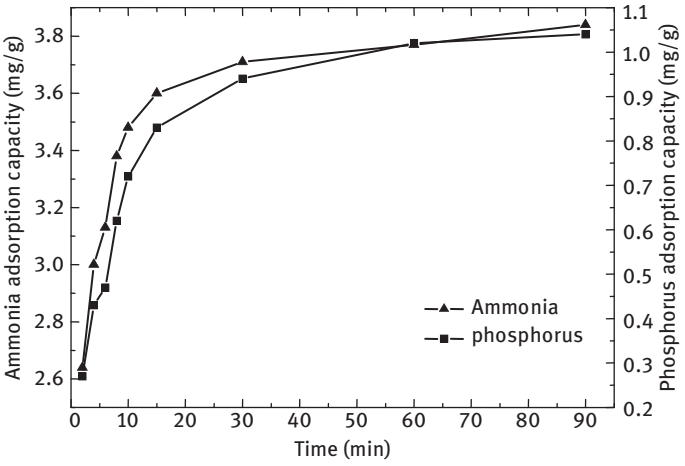

Figure 2.44: Relationship between removal rate of ammonia and phosphate, and dosing.

reaction time, the removal rate is not obvious, which means that LaZP removal rate of ammonia and phosphate is very fast.

2.4.2 Effect of reaction time on nitrogen and phosphorus removal

Ammonia and phosphorus removal rate of modified zeolite over time is shown in Figure 2.45. As shown in the figure, the LaZP adsorption rate of ammonia and

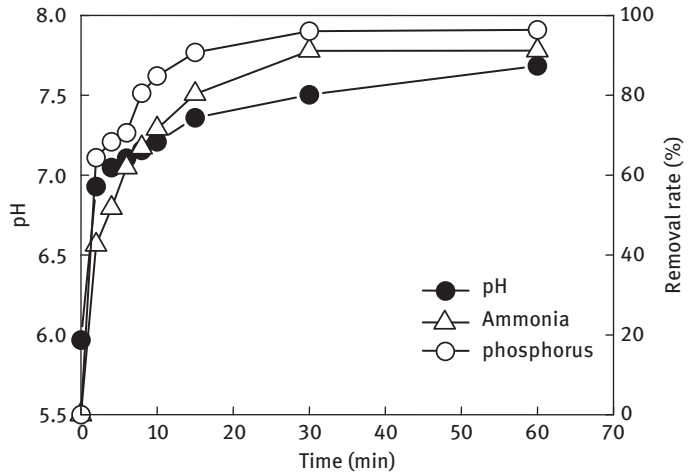

Figure 2.45: Relationship between removal rate of ammonia and phosphate, and time.

phosphorus is very fast, both of which can be basically absorbed equilibrium within 30 min, and the deviation was not more than 2% as compared with the result of 24 h adsorption reaction. The hydroxyl, covering the LaZP surface, was easy to generate surface coordination complex with cation and anion. The unmodified zeolite mainly relies on ion exchange reaction with zeolite components, or the metal ions (such as Ca^{2+} and Al^{3+}) in the synthesized intermediate product are reacted with the ions in the solution to achieve the purpose of nitrogen and phosphorus removal. So LaZP reaction rate is higher than that of ZP. During the reaction, the pH slowly increased from 6.0 to about 7.8. This is mainly due to Al^{3+}, Mg^{2+} and other metal ions from synthetic zeolite participated in the reaction, so that the pH of the solution increased.

2.4.3 Effect of influent pH on nitrogen and phosphorus removal

The effect of pH on nitrogen and phosphorus removal is shown in Figure 2.46. The reaction conditions of adsorption test are: lanthanum ion concentration is 0.5%, and pH of the solution adjusted from NaOH and hydrochloric acid is from 3 to 12. It can be seen from the figure that under the condition of faintly acid neutrality, the effect of nitrogen and phosphorus removal by LaZP was better, both of which can reach more than 90%. And reached the maximum when the pH is around 5, and basically remain stable afterward. At pH <3 and pH >8, the nitrogen and phosphorus removal rates decreased significantly. The reason may be: At pH <3, the acidic conditions changed the pore structure of the synthesized zeolite, destroying its crystal structure. The large increase of H^+ changed the surface properties of the adsorbent, which lead to the desorption of the lanthanum ion on the surface. And at the solution pH <3, the balance

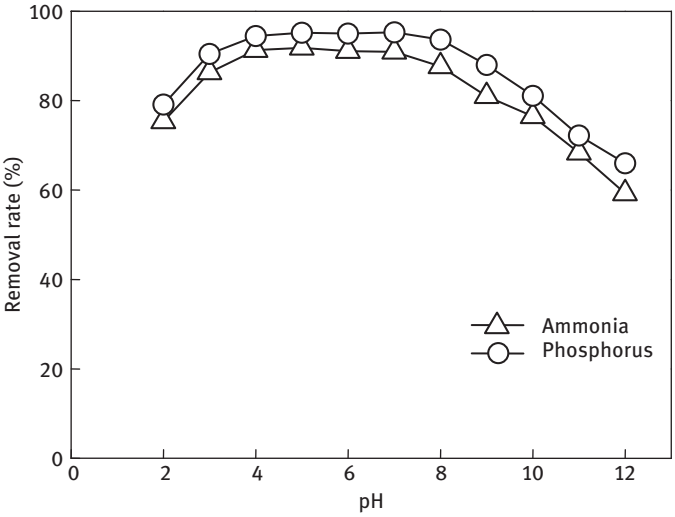

Figure 2.46: Effect of pH on nitrogen and phosphorus removal.

of dissolution in solution dominates. Lanthanides tended to dissolve and therefore can not immobilize phosphate, so it is not conducive to nitrogen and phosphorus adsorption removal. As the pH increased, the OH^- in the solution increased. NH^{4+} and OH^- combined to generate more stable $NH_3{\cdot}H_2O$, which was not easily adsorbed. Excessive OH^- competed with the phosphate in solution, resulting in a significant reduction in nitrogen and phosphorus removal. Pengthamkeerati et al. (2008) analyzed the XRD of phosphate-adsorbed zeolite and found that there was a large number of calcium phosphate precipitation. This showed that the phosphorus removal mechanism was mainly the chemical reaction of Ca^{2+} and Al^{3+} from synthetic zeolite with phosphate. This is also the reason for better removal under alkaline conditions. In this experiment, the phosphorus removal effect of modified synthetic zeolite is better in the acidic environment; obviously, they have different removal mechanism.

2.4.4 Adsorption kinetic experiment of ammonia nitrogen and phosphorus by LaZP

The kinetic model is usually used to study the changes in the adsorption process. However, pseudo-first-order and pseudo-second-order kinetic models are often used to describe the liquid–solid adsorption process. Therefore, this study of the adsorption of ammonia and phosphorus by LaZP process used both the models to fit. The equation is as follows.

Pseudo-first-order kinetic model:

$$\ln(Q_e - Q_t) = \ln Q_e - K_1 t \tag{2.6}$$

Pseudo-second-order kinetic model:

$$t/Q_t = 1/K_2Q_{e2} + t/Q_e \tag{2.7}$$

where Q_e, Q_t are adsorption capacities of adsorption equilibrium and time t, mg/g; t is the adsorption time, min; K_1, K_2 are adsorption rate constants, min^{-1}.

The reaction conditions are given as follows: ammonia concentration of simulated wastewater is 25 mg/L; phosphorus concentration is 5 mg/L (appropriate amount of ammonium chloride and potassium dihydrogen phosphate dissolved in distilled water at the same time); LaZP is 0.5 g; sampling times were 2 min, 4 min, 6 min, 8 min, 10 min, 15 min, 30 min, 60 min and 24 h.

Figure 2.47 shows the fitting curves of pseudo-first-order and pseudo-second-order equations. By comparing the fitted curves of the kinetic equations in the figure and the kinetic parameters in Table 2.11, we can see that the fitting correlation coefficients r^2 of the pseudo-second-order kinetic model of ammonia and phosphorus were all larger than that of pseudo-first-order kinetic model, and the Q_e value calculated by the pseudo-second-order equation is close to the experimental value. The above results show that the pseudo-second-order equation can better describe the LaZP adsorption of ammonia and phosphorus. The limitation of pseudo-first-order kinetic model is that it is usually used to describe the initial stage of the reaction and cannot be used to accurately describe the entire adsorption reaction process. And the Q_e value must be known before fitting, but it is impossible to accurately determine the equilibrium adsorption quantity in the experiment. The pseudo-second-order model contains the entire adsorption process, such as liquid film diffusion, surface adsorption and internal diffusion, to better describe the adsorption reaction of the whole process.

2.4.5 LaZP isothermal adsorption on ammonia and phosphorus

Langmuir and Freundlich equations can be used to describe the LaZP adsorption isotherms on nitrogen and phosphorus [ref (2–4) and (2–5)].

Modified zeolite of 0.5, 0.6, 0.7, 0.8, 0.9, 1.0 and 1.2 g were, respectively, added to the solution with ammonia concentration of 50 mg/L and phosphorus concentration of 25 mg/L. Isothermal adsorption experiments were performed at 25 °C. Using the above two equations to fit the data, the result is shown in Figure 2.48. The correlation coefficients of the calculation equation are shown in Table 2.12. Compared with r^2, Langmuir equation can better describe the adsorption of ammonia and phosphorus, and the result of fitting with Freundlich equation was not so good. The maximum Langmuir adsorption capacities of ammonia and phosphorus were 3.94 and 1.65 mg/g, respectively.

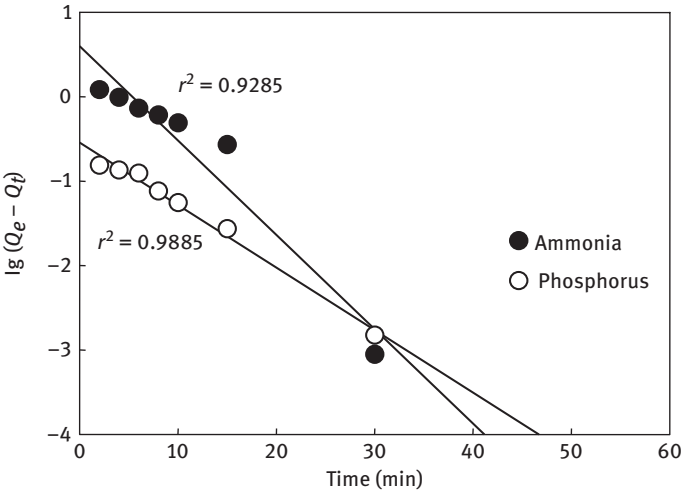

(a) Pseudo-first-order equation

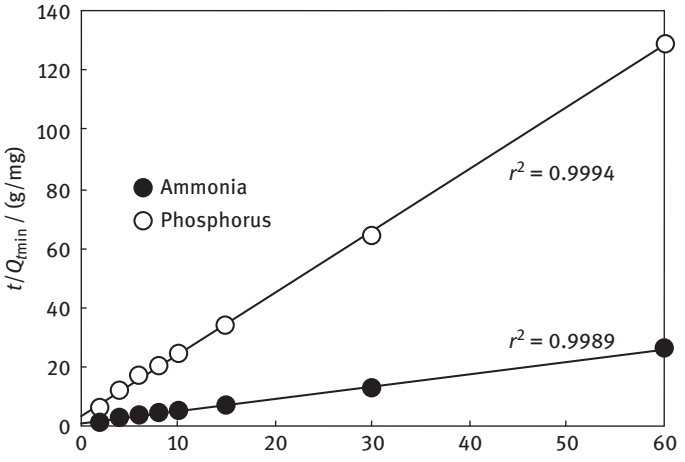

(b) Pseudo-second-order equation

Figure 2.47: Kinetic model fitting curves of ammonia and phosphorus.

Table 2.11: Kinetic parameters.

Adsorbate	Q_{e1} (mg/g)	Pseudo-first-order equation		Pseudo-second-order equation	
		K_1 (min^{-1})	Q_{e2} (mg/g)	K_2 [g/(mg·min)]	Q_{e2} (mg/g)
Ammonia	2.277	0.257 2	3.949	0.132 4	2.415
Phosphorus	0.466	0.170 4	0.288	1.233 8	0.481

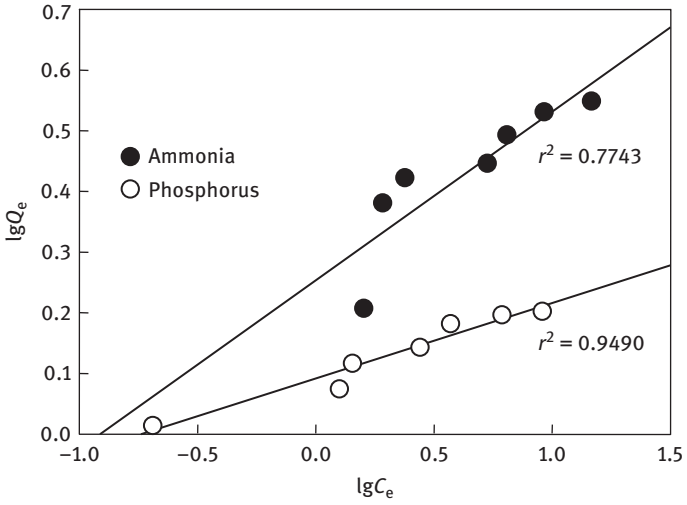

(a) F-type curve

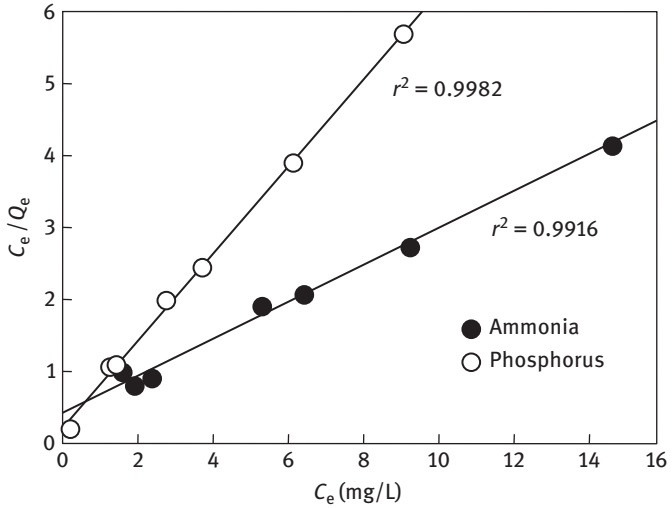

(b) L-type curve

Figure 2.48: Adsorption isotherms.

Table 2.12: Parameters of adsorption isotherm.

Ahsorbate	Langmuir equation			Freunhlich equation		
	Q_{max} (mg/g)	b (L/mg)	r^2	K_F (L/mg)	n	r^2
Ammonia	3.94	0.595	0.991 6	1.795	3.599	0.774 3
Phosphorus	1.65	2.857	0.998 2	1.235	8.058	0.949 0

2.5 Preparation of artificial zeolite loaded with TiO_2 photocatalytic composite

Using synthetic zeolite as carrier, TiO_2 is loaded at low temperature (80 °C). During the loading process, rare earth cerium ions are doped to improve the photocatalytic activity, to prepare the zeolite from fly ash loaded with Ce^{3+}/TiO_2 photocatalyst, which can reduce the cost of synthesis and improve the pollutant degradation efficiency.

2.5.1 Overview

Fujishima (1972) discovered for the first time that the redox reaction of water persistently occurs on the surface of TiO_2, which is irradiated by a photovoltaic cell. This finding opens the research and application of photocatalytic materials. Carey et al. (1976) reported that TiO_2 aqueous turbidity can dechlorinate PCBs (Polychlorinated biphenyls) under the irradiation of near-ultraviolet (UV) light. Frank et al. (1977) also photocatalytically degraded the CN-containing solution with TiO_2 powder. Thus, in China and across the world began the application of TiO_2 photocatalytic technology in the field of environmental protection, which led to technical revolution in wastewater treatment.

TiO_2 is an n-type semiconductor material with strong oxidizing and reducing properties. With its high catalytic activity, thermostability, long acting time, low prices and other advantages to become a much-watched photocatalyst. Common TiO_2 is powder, although photocatalytic strong, but in the wastewater treatment process there are issues of separation, recovery. Therefore, how to fix TiO_2 on the carrier has become a very important issue. Common carriers are glass, ceramics and activated carbon (LIU & GONG, 2007; LIU et al., 2000; LIU & CHEN, 2008). There are many studies using zeolite as a TiO_2 photocatalyst carrier (ANANDAN & YOON, 2003; SHANKAR et al., 2006; CHEN et al., 2002). However, most studies have chosen natural zeolite as a carrier, and there are few studies on using synthetic zeolite, which can adsorb organic pollutants. The traditional loading method needs high-temperature calcination to obtain composite photocatalyst. The equipment is complex and needs more energy. Therefore, preparation of TiO_2 at low temperature is also a hot topic in recent years (NA et al., 2006).

2.5.2 Basic principle of TiO_2 photocatalysis

TiO_2 is an n-type (electron conductive) semiconductor oxide, whose photocatalytic principle can be explained by the energy band theory of semiconductors. According to the band-based electronic theory, the semiconductor's basic band results are as follows: There is a series of full bands, the top of which is called valence band (VB);

there is a series of empty belts, the bottom of which is called conduction band (CB); forbidden band (FB) between VB and CB. When the semiconductor is irradiated with light having an energy equal to or greater than the FB width (E_g), the VB electrons (e^-) are excited, crossing the FB into the CB; at the same time, the corresponding holes (h^+) are generated on the VB. This is the production process of photogenerated electron and photogenerated hole (Liu & Liu, 2006).

The FB gap of TiO_2 is 3.2 eV. When irradiated with light of a wavelength of 387.5 nm or less (UV light), the electron transition occurs. Electrons on the VB are excited beyond the FB to form a highly negatively charged electron (ecb^-), and a positively charged hole (hvb^-) on the VB. Because of the discontinuity of the semiconductor band, the life of electrons and holes is longer. Under the action of the electric field, electrons and holes are separated and migrate to different positions on the surface of TiO_2 particles, respectively. They are involved in accelerating the redox reaction on the particle surface so that the material adsorbed on the particle surface is oxidized or reduced. Water molecules and oxygen molecules on the membrane surface are excited into highly active free radicals (·OH) and negative oxygen ions (O^{2-}). The reaction equation is as follows (EPA, 2004):

$$TiO_2 + h\nu \rightarrow h^+ + e^- \tag{2.8}$$

$$h^+ + H_2O \rightarrow OH + H^+ \tag{2.9}$$

$$e^- + O_2 \rightarrow \cdot O^{2-} \rightarrow HO_2\cdot \tag{2.10}$$

$$2HO_2\cdot \rightarrow O_2 + H_2O_2 \tag{2.11}$$

$$H_2O_2 + \cdot O_2 \rightarrow \cdot OH^- + O_2 \tag{2.12}$$

The hydroxyl groups ·OH generated on the surface are highly reactive and can oxidize and decompose various compounds adsorbed on the surface of the catalyst. These radicals can decompose organic compounds to generate H_2O and CO_2.

In theory, the photocatalytic reaction on the semiconductor surface is achieved through the following steps (KAMAT & MEISEL, 1997): (1) electron–vacancy pairs are created by irradiating the semiconductor with light having an energy greater than the bandgap of the semiconductor; (2) semiconductor surface adsorbed material, so that photogenerated electrons and vacancies separated; (3) redox reactions take place in the trapped electrons and vacancies and on the surface adsorbed species; and (4) desorption of the product and remodeling of the surface. The detailed reaction mechanism of many photocatalytic oxidation of organic compounds is still under discussion.

It is noteworthy that photocatalysis requires the photoactive semiconductor surface. Although anatase TiO_2 has excellent photocatalytic activity, its adsorption

capacity is poor (KIM & YOON, 2001), especially for nonpolar molecules, which limits its further application. Zeolite, owing to its porous structure, has good adsorption properties. The combination of the two, resulting in a synergistic effect, can well improve the photocatalytic properties of TiO_2. The TiO_2 particles, which are inserted into the pores of the zeolite and supported on the surface of the zeolite, generate hole–electron pairs under the irradiation of UV light. Because the zeolite has a strong electric field in the hole and its surface is also electron rich, it can inhibit the electron–hole recombination. As a result, the zeolite adsorbed organic matter can be easily excited by UV light and react with water and oxygen to generate active groups. The photocatalytic activity is thereby increased.

2.5.3 Modification of TiO_2 photocatalyst

Currently developed modification techniques of photocatalyst can be broadly divided into the following categories: nonmetallic ion doping, transition metal ion doping, precious metal deposition, semiconductor composites, organic dye photosensitization, using the modification technology to expand its light absorption capacity and the quantum efficiency of the photocatalytic process.

Sato (1986) first doped with nonmetallic ions. $Ti(OH)_4$ with NH_4OH was calcined to prepare n-doped TiO_2 photocatalyst. Based on the density function theory calculation of substitution doping of C, N, F, P and S elements on O in anatase TiO_2, Asahi et al. (2001) argued that the N (2 p) level can be hybridized with the O (2 p) level, resulting in a narrower bandgap of the material that extends the absorption edge of the TiO_2. The nonmetallic N to replace a small amount of lattice oxygen (0.175%) to bring the visible light activity from Asahi et al. was undoubtedly a groundbreaking work, which stimulated the interest of many researchers in the field. Since then, researchers from all over the world have successively developed N-doped, S-doped, C-doped, F-doped and two nonmetallic ion-doped TiO_2. The corresponding theoretical research showed that the mechanism of nonmetallic ions doping to improve the visible light response of TiO_2 can be divided into two types: One is that the doping causes the decrease of the FB width of TiO_2 and the other is that the doping causes the generation of an intermediate level in the bandgap of TiO_2.

Some researchers studied metal ion-doped TiO_2 and found that it can indeed significantly improve the photocatalytic activity of TiO_2. Li et al. (2004) doped lanthanum metal La^{3+} into TiO_2 and found that the doping of lanthanum can prevent the phase transformation of TiO_2, improve its thermal stability, reduce the grain size and increase the content of Ti^{3+} on the surface, which can improve the photocatalytic activity of TiO_2. Different from the doping mechanism of nonmetallic ions, the doping of metal ions enhances the photocatalytic activity by inhibiting the growth of nano-TiO_2 particles and the phase transformation.

2.5.4 Research progress on preparation of zeolite-supported TiO_2 catalytic materials

The TiO_2 photocatalyst decomposes the pollutants adsorbed on the surface by photocatalytic reaction. Although direct use of TiO_2 powder has a good effect, but it is not conducive to the recovery of the catalyst, which is easy to cause waste. (Thevenet et al., 2005; Minero et al., 1992). Immobilized technology solved the recovery problems of nano-TiO_2 photocatalyst. TiO_2 is oxidative and can decompose organic matter, so it can not be used directly on organic carrier, must be supported on an inert carrier or fixed on the surface of the substrate by suitable means to exert photocatalytic effect. The immobilization technology of nano-TiO_2 has become an effective way to solve the problem of nano-TiO_2 photocatalyst recovery. A large number of studies have been carried out on nano-TiO_2 supported on the surface of glass, quartz, zeolite and titanium plate (YANG Xiaoru et al., 2007). However, the photocatalytic efficiency is reduced because of the reduction of the contact area between the catalyst and light because of the planar load. Loading nano-TiO_2 on the surface of inert porous support material can effectively solve the problem of recovery and difficult loading (AO Yanhui et al., 2006). Inert porous materials include activated carbon, zeolites, activated carbon fibers and so on. Because of its uniform, nanoscale pore structure, zeolites can form stable, molecular-sized semiconductor nanoclusters, and show higher activity than other carriers. Therefore, zeolite as a carrier of photocatalyst has attracted many researchers.

Nano- or sub-nanoscale holes and voids within the zeolite framework can accommodate guest photoactive materials, such as organic photosensitizers and inorganic semiconducting materials. In addition, replacing the Si or Al in the zeolite framework with Ti, V or other transition metal elements to form a heteroatom-containing zeolite can directly give the zeolite a photocatalytic activity. As the main body of the composite photocatalytic material, zeolite has large specific surface area and strong adsorption capacity, which can improve the efficiency of the photocatalytic process. The internal discrete spatial structure facilitates the gradual introduction of multicomponent guest materials. When the organic photosensitizer is loaded on the zeolite pore, the photostability is greatly improved. Semiconductors located in zeolite cages exhibit quantum effects at the nanoscale. Under the influence of the polar environment of zeolite internal structure, it showed more sensitive photoelectron transfer and the photocatalytic efficiency was enhanced.

The preparation method of TiO_2/zeolite composite material is simple. And it is applicable to a wide range, so get more attention. Because of limited pore capacity of the zeolite, the amount of TiO_2 loaded in zeolite pores is too low, resulting in a lower overall catalytic activity of the composite material. Therefore, to improve the TiO_2 content, preparation of the loaded composite has become an important

research direction. The zeolite TiO_2 material is prepared by calcining a mixture of TiO_2 sol and zeolite (NOORJAHAN et al., 2006). Alternatively, nano-TiO_2 is mixed with the zeolite using a mechanical mixing method (YONEYAMA et al., 2000). The products showed good catalytic performance. At present, the most common methods for preparing TiO_2/zeolite composite materials are sol–gel method, ion exchanging method and solid-state dispersion method.

(1) Sol–gel method

Sol–gel method is a new process, which developed in the 1960s for preparation of glass, ceramic and other inorganic materials. Sol–gel technology has the advantages of simple and easy operation, no large equipment, mild preparation conditions, high purity and the formation of ultrafine particles on the substrate. FANG Songsheng et al. (2003) used sol–gel method to load TiO_2 on natural clinoptilolite. The results showed that the prepared catalyst has the maximum photocatalytic activity after being dried at 120 °C for 6 h and calcined at 200 °C, and at this lower temperature, anatase TiO_2 appeared. Reddy et al. (2003) supported 25% (mass ratio) TiO_2 on MCM-41 by sol–gel method and performed a photocatalytic experiment of salicylic acid and found that the hydrophilicity of the matrix and the catalyst was a decisive factor in the photocatalytic performance.

(2) Ion exchanging method

Ion exchanging is a common method of supporting metal ions on a carrier with a porous or lamellar structure. The general formula is:

$$AZ + B^+ \rightleftharpoons BZ + A^+$$

where Z is the anionic framework of zeolite; B is the metal cations in aqueous solution; and A represents the cations in the zeolites prior exchange and are generally alkaline earth metal ions.

TiO_2 was loaded on Na-, H- and Y-zeolites by ion exchanging method. They found that the ion exchange process is governed by the type of Ti atoms, the channels of zeolites and the pore size of the cage structure.

(3) Solid-state dispersion method

Durgakumari et al. (2002) loaded 2%, 5%, 10% and 15% (mass ratio) TiO_2 on HZSM-5 by solid-state dispersion diffusion method, respectively. TiO_2 and zeolite are placed in an agate mortar, and then the alcohol is poured, fully grinding until the alcohol is evaporated. After drying at 110 °C, the sample was calcined at 450 °C for 6 h to obtain the photocatalyst. Characterization of the catalyst showed that TiO_2 was dispersed in the zeolite structure and did not react with the zeolite. Degradation of phenol and chlorophenol in aqueous solution with the prepared photocatalyst showed that the optimal loading of TiO_2 was between 10% and 15% (mass ratio).

2.5.5 Preparation of photocatalytic composite materials (Ce^{3+}–TiO_2-loaded zeolite)

2.5.5.1 Preparation method

The photocatalyst (TiO_2-supported zeolite) was prepared by sol–gel method at 80 °C. About 34 mL of tetrabutyl titanate was placed in a 250 mL triangular Erlenmeyer flask. Absolute ethanol (100 mL), glacial acetic acid (25 mL) and concentrated nitric acid (2 mL) were added and stirred vigorously at constant speed for 30 min. Appropriate amount of zeolite from fly ash was added and stirred at constant speed for 2 h. The return pipe was connected and heated to maintain the temperature at 80 °C water bath and continuously stirred. Meanwhile, the cerium nitrate/ethanol solution was slowly dropped into the Erlenmeyer flask from the top of the return pipe using a burette. The reflux device was removed, the triangular flask was placed in a constant temperature water bath, and after an appropriate period of time it was removed. Ethanol was volatilized under natural conditions. Suspended solids and impurities were rinsed with deionized water. It was dried at 105 °C for 24 h, then ground and passed through a 200 mesh sieve.

2.5.5.2 Characterization of photocatalytic composite

(1) SEM–EDX analysis

Figure 2.49 shows the SEM–EDX (Energy Dispersive X-Ray Spectroscopy) diagrams of fly ash zeolite and synthetic photocatalyst. After TiO_2 loading, the surface morphology of zeolite has clearly changed. Zeolite had obvious crystalline features and a large number of pore structure. The synthetic photocatalyst surface becomes smoother and shinier, with no large particles on the surface. This showed that TiO_2 is relatively uniformly supported on its surface. The elements in the sample can be analyzed semiquantitatively by spectrum (EDX). A small amount of Ti was present on the zeolite surface, and Ce was not detected, because fly ash contains a small amount of titanium. The content of Ti element on the surface of the synthesized photocatalyst was more than 30% and contained a small amount of Ce element, indicating that TiO_2 was successfully supported on the surface of zeolite.

(2) XRD analysis

Figure 2.50 shows the XRD pattern of the zeolite sample from fly ash and the synthesized photocatalyst. Comparing the two results showed that the main peak structure of zeolite did not change after loading TiO_2, but the intensity of the peak decreased, because the surface is loaded with amorphous and crystalline Ce^{3+}–TiO_2. And Ce^{3+}–TiO_2 zeolites have obvious characteristic peaks at $2\theta \approx 25.4°$ (d = 0.346 nm) and $2\theta \approx 37.8°$, which indicated that most of the TiO_2 on the zeolite surface were anatase.

(3) Fourier transform infrared spectroscopy

Figure 2.51 shows the Fourier transform infrared spectroscopy (FTIR) spectra of fly ash zeolite, anatase and the mixed sample of both (hereinafter referred to as mixed

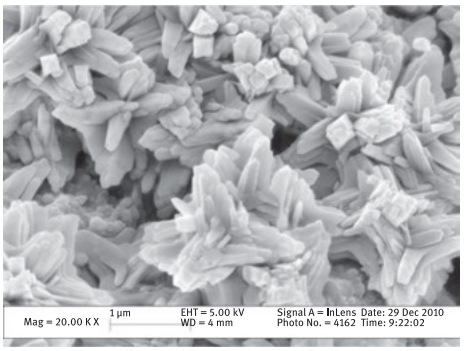

(a)

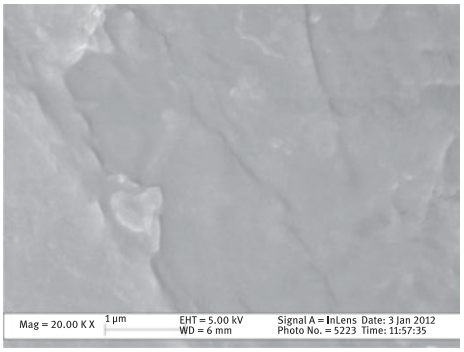

(b)

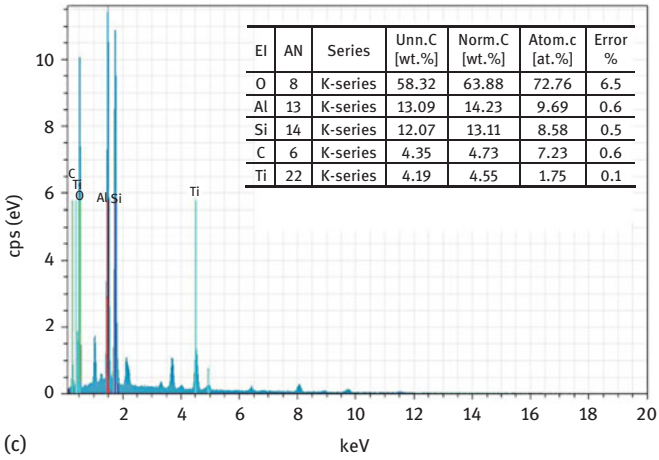

El	AN	Series	Unn.C [wt.%]	Norm.C [wt.%]	Atom.c [at.%]	Error %
O	8	K-series	58.32	63.88	72.76	6.5
Al	13	K-series	13.09	14.23	9.69	0.6
Si	14	K-series	12.07	13.11	8.58	0.5
C	6	K-series	4.35	4.73	7.23	0.6
Ti	22	K-series	4.19	4.55	1.75	0.1

(c)

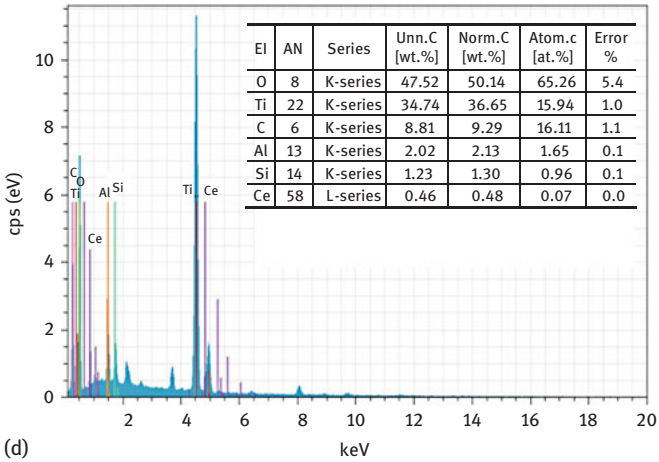

El	AN	Series	Unn.C [wt.%]	Norm.C [wt.%]	Atom.c [at.%]	Error %
O	8	K-series	47.52	50.14	65.26	5.4
Ti	22	K-series	34.74	36.65	15.94	1.0
C	6	K-series	8.81	9.29	16.11	1.1
Al	13	K-series	2.02	2.13	1.65	0.1
Si	14	K-series	1.23	1.30	0.96	0.1
Ce	58	L-series	0.46	0.48	0.07	0.0

(d)

Figure 2.49: SEM-EDX images of zeolite and synthetic photocatalysts. (a) and (c) SEM-EDX images of zeolite; (b) and (d) SEM-EDX images of synthetic photocatalysts.

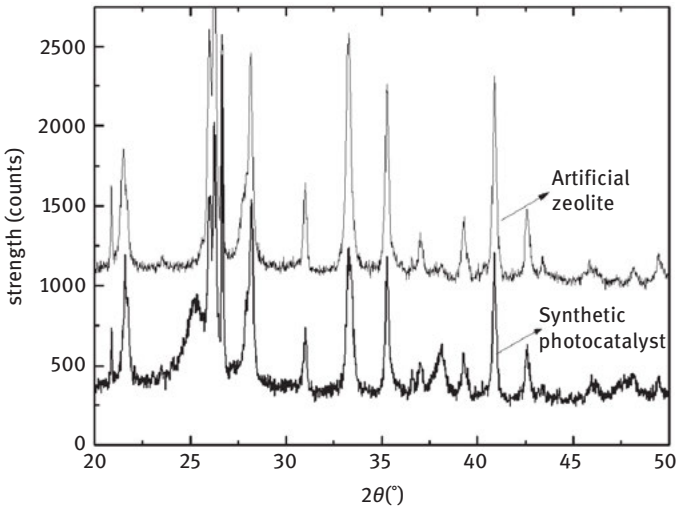

Figure 2.50: XRD pattern of zeolite and synthetic photocatalysts.

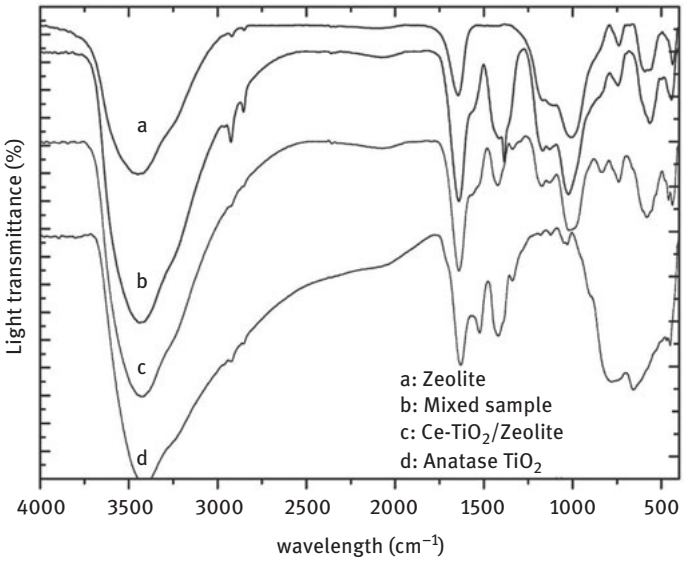

Figure 2.51: FTIR analysis of samples.

sample). It can be seen from the figure that the FTIR spectra of the synthesized photocatalyst and the mixed sample are basically the same, indicating that the supported TiO_2 were mainly anatase. At 960 cm^{-1}, a new small absorption peak appeared on the synthesized photocatalyst, which is assigned to the Si–O–Ti bond,

indicating that part of the $(TiO_2^+)_n$ is embedded in the zeolite framework (YOON et al., 2007). Excluding the original zeolite, anatase, the mixed sample and synthetic photocatalyst had a larger absorption peak near 1,380 cm^{-1}, which was caused by the vibration of Ti–O bond in TiO_2, indicating that the synthetic photocatalyst had a good loading effect.

2.5.6 Factors affecting the photocatalytic activity of TiO_2

2.5.6.1 Photocatalytic reactor and analysis method

The structure of the photoreaction device is shown in Figure 2.52. The photoreactor is 300 mm high with an outer diameter of 250 mm and with a 250 mL reaction beaker. An UV high-pressure mercury lamp was placed above the reactor with a lamp source of 300 W and a wavelength of 365 nm. The reactor was filled with cooling water to ensure the room temperature.

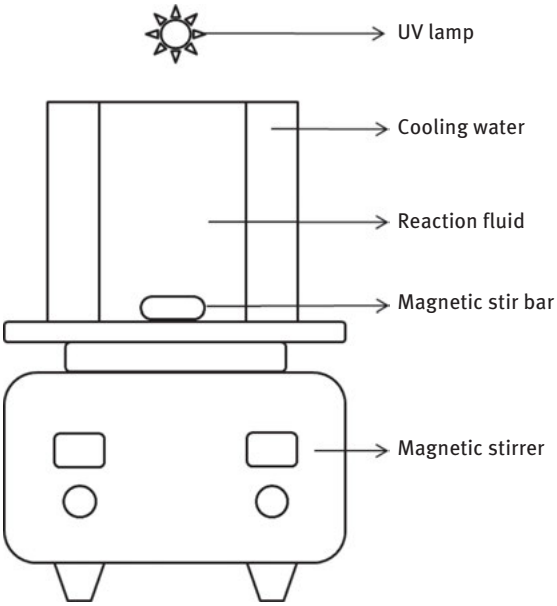

Figure 2.52: Photodegradation reaction device schematic.

About 100 mL polycyclic aromatic hydrocarbon (PAH) solution was placed in a beaker, and a certain amount of zeolite-supported Ce–TiO_2 photocatalyst was added to the beaker. The thermostatic magnetic stirrer is agitated at a constant agitation rate to adsorb PAHs. To maintain saturated adsorption, turn on the UV lamp, preheat 5 min then start noting the time. After reaction, the water sample was centrifuged, and the

supernatant was subjected to a series of pretreatments such as liquid–liquid extraction, rotary evaporation and nitrogen blowing. Finally, the concentration was determined by gas chromatography-mass spectrometry (GC-MS).

PAHs were detected by Agilent-7890GC-5975 MS. Deuterated PAHs (phenanthrene-d10) was used as an indicator of recovery and hexamethylbenzene as an internal standard. An Agilent HP-5MS (30 × 0.25 × 0.25 μm) column was used. The inlet temperature was 280 °C and 1 μL is injected in splitless mode. Helium is the carrier gas, controlling a constant flow rate of 1.2 mL/min. Temperature program: 55 °C (1 min), with 4 °C/min speed up to 290 °C (20 min). The ion source is an EI (Electron ionization source) source at a temperature of 230 °C and the detector is fully scanned in the m/z range of 50–500. The chromatographic data were processed on an Agilent chromatographic workstation and the compounds were quantified using a 6-point calibration curve and an internal standard method.

2.5.6.2 Effect of different Ce^{3+} concentrations on activity of TiO_2 zeolite

Figure 2.53 shows the comparison of phenanthrene and fluoranthene degradation effect with different rare earth-doped photocatalysts. It can be seen from the figure that effluent concentration of rare earth cerium-doped catalysts is lower than that of the nondoped cerium catalyst. When the doping amount of rare earth is less than 0.5%, the photocatalytic degradation of phenanthrene and fluoranthene increases with the increase of rare earth doping amount. Continue to increase the amount of rare earth doping, effluent concentration of phenanthrene and fluoranthene increased slightly. That is, the best rare earth doping amount is 0.5%, which is consistent with the conclusion of Song Mianxin et al. (2007). This is mainly because rare earth-doped TiO_2 can promote the production of oxygen defects and play a role in capturing photogenerated electrons or holes. Rare earths promote the separation of photoelectron–hole pair and inhibit their recombination. However, excessive rare earth doping reduces the space charge layer thickness of the TiO_2 surface. The results show that only when the space charge thickness approximates the penetration depth of the incident light into the solid, all the electron–hole pairs generated by the absorbed photons can be effectively separated. Therefore, excessive doping may reduce the photocatalytic efficiency of TiO_2 (YUE Linhai, 1998).

2.5.6.3 Effect of solution pH on the degradation of phenanthrene and fluoranthene

The pH of the reaction solution is adjusted by dilute HCl or NaOH solution. The effects of pH from 3 to 11 on the degradation of phenanthrene and fluoranthene were investigated. The result is shown in Figure 2.54. It can be seen from the figure that pH can affect the degradation efficiency of PAHs. When pH is close to alkaline, the degradation efficiency is higher than that in acidic environment. It has been pointed out in the literature that the isoelectric point of TiO_2 is about pH 6.8 (FANG

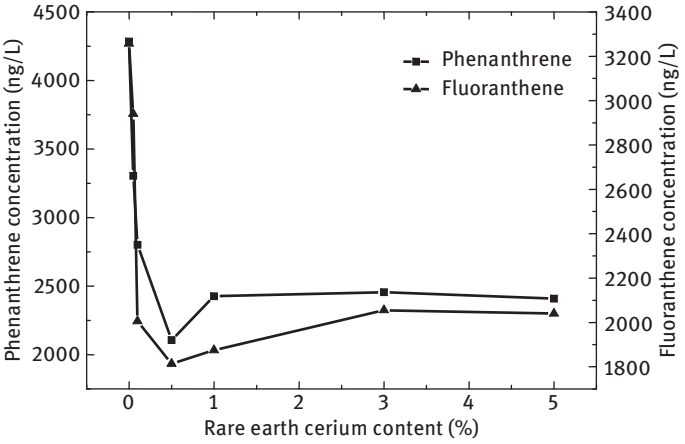

Figure 2.53: Effect of rare earth cerium doping on the degradation of phenanthrene and fluoranthene.

et al., 2003). When the pH of the solution is acidic, the surface of TiO_2 is positively charged and negatively charged under alkaline conditions. When the pH of the solution is increased, the electrostatic interaction between the PAHs and the TiO_2 surface enhances its adsorption. At the same time, OH^- ions in the solution are increasing continuously, and the corresponding degradation effect is strengthened. This fully shows that the pH of the solution can change the electronic behavior of the photocatalyst surface, thus affecting the adsorption and desorption properties of the target pollutants and the production of intermediates (HUANG et al., 2008).

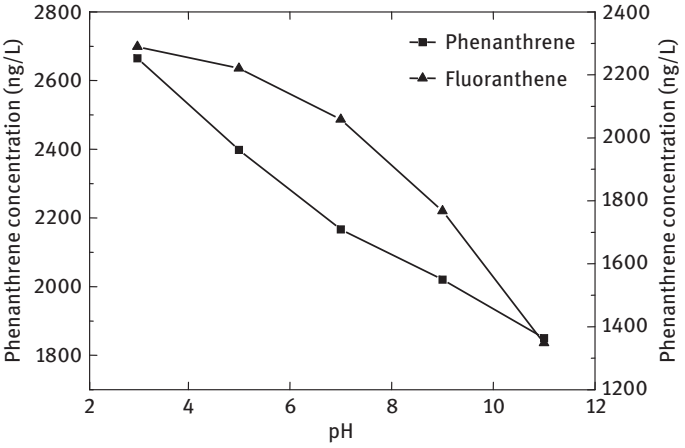

Figure 2.54: Effect of pH on the degradation of phenanthrene and fluoranthene.

2.5.6.4 Effect of dosage on the degradation of phenanthrene and fluoranthene

Figure 2.55 shows the relationship between the amount of photocatalyst and the degradation rate of phenanthrene and fluoranthene solutions. It can be seen from the figure that the degradation rate of phenanthrene and fluoranthene reached the highest when the catalyst dosage was 3 g/L. With the increase in dosage, photocatalytic effect decreased, and effluent concentration of phenanthrene and fluoranthene increased. This is because within a certain range, as the amount of photocatalyst increases, the photogenerated electron–hole pairs are also increased, which promotes the formation of hydroxyl radicals ·OH to accelerate the reaction until saturated (CHANG M Y et al., 2009). If the amount of photocatalyst continue to be increased, the incident UV light is shielded and scattered, reducing the utilization of light energy and affecting the absorption of UV light by the catalyst particles in the solution (SHI Zhongliang et al., 2007), which decreasing the degradation rate of phenanthrene and fluoranthene, increasing their effluent concentration.

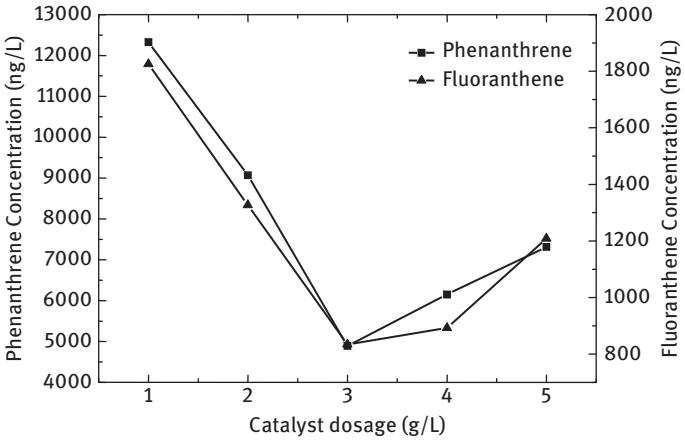

Figure 2.55: Effect of catalyst amount on the degradation of phenanthrene and fluoranthene.

2.5.6.5 Effect of initial concentration of phenanthrene and fluoranthene on degradation

Four different concentrations (5×10^5 ng/L, 10^6 ng/L, 5×10^6 ng/L, 10^7 ng/L) of phenanthrene solution and four different concentrations (2.5×10^5 ng/L, 5×10^5 ng/L, 2.5×10^6 ng/L, 5×10^6 ng/L) of fluoranthene solution were configured. The amount of immobilized catalyst was 1 g, the volume of solution was 100 mL and the degradation time was 120 min. The photocatalytic test results are shown in Figure 2.56. It can be seen that as the initial concentration increased, the degradation efficiency decreased and the effluent concentrations of phenanthrene and fluoranthene increased. When the concentration of phenanthrene was low, with the initial concentration increasing,

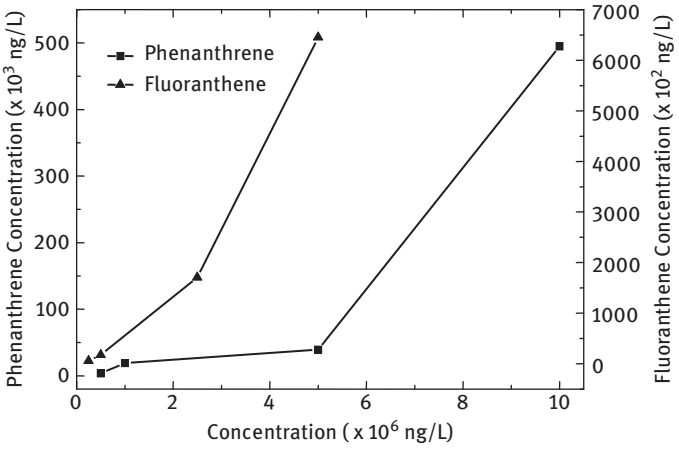

Figure 2.56: Effect of initial concentration on the degradation of phenanthrene and fluoranthene.

the effluent concentration of phenanthrene was not particularly obvious, and the efficiency of degradation was increased. When the initial concentration of phenanthrene increased to 10^7 ng/L, the effluent concentration increased greatly and the degradation efficiency decreased. During the degradation of fluoranthene, when the concentration was lower than 2.5×10^6 ng/L, with the increase of pollutant concentration, the effluent concentration did not increase obviously, and the degradation efficiency increased. When the fluoranthene initial concentration increased to 2.5×10^6 ng/L, the effluent concentration was greatly increased and the degradation efficiency was decreased. According to the analysis of relevant literature (Konstantinou I K et al., 2009), when the amount of catalyst is constant, the active site provided by the reaction is certain. When the target pollutants are below a certain concentration, with the increase of pollutant concentration, the degradation efficiency increased. When this concentration exceeded, excess intermediate products impeded the OH^- generation in the solution, resulting in the lack of ·OH radicals for photocatalysis, thereby degrading the photodegradation efficiency.

2.5.6.6 Study on kinetics of phenanthrene and fluoranthene degradation

Photodegradation kinetics of experimental conditions: phenanthrene (10^6 ng/L), fluoranthene (5×10^5 ng/L), pH is not adjusted, The volume of the reaction solution is 100 mL, dosage is 3 g/L and other conditions are unchanged. Assuming that the change of target pollutant concentration is taken into account and the influence of intermediate products is neglected, the Langmuir–Hinshelwood kinetic equation can be used to indicate the first-order kinetic equation (KONSTANTINOU I K et al., 2001):

$$\ln c = -Kt + \ln c_0 \tag{2.13}$$

where t is the reaction time, min; c is the instantaneous concentration of phenanthrene and fluoranthene in solution, ng/L; c_0 is the initial concentration of phenanthrene and fluoranthene in solution, ng/L; K is the reaction rate constant.

The phenanthrene and fluoranthene degradation processes were fitted by using the above Langmuir–Hinshelwood kinetic equation. The fitting results are shown in Figure 2.57. The related linear parameters are shown in Table 2.13. Through the fitting of the two, the correlation coefficients of $r^2 \geq 0.99$ for phenanthrene and $r^2 \geq 0.98$ for fluoranthene show that the photodegradation rates of phenanthrene and fluoranthene all conform to the first-order reaction kinetics model.

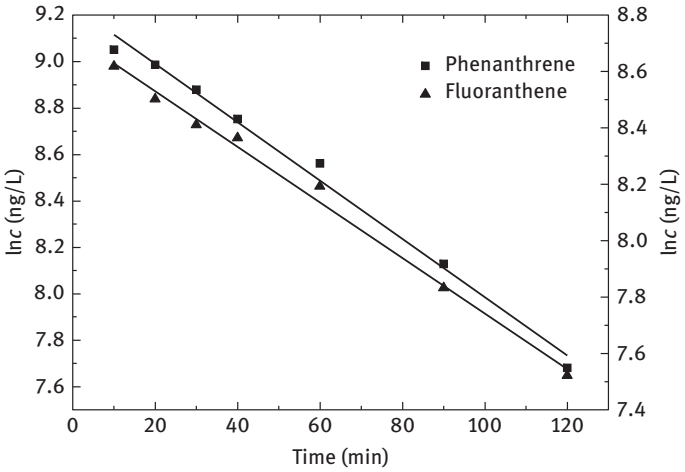

Figure 2.57: Kinetic fitting curves of phenanthrene and fluoranthene degradation.

Table 2.13: Parameters of phenanthrene and fluoranthene photodegradation linear relationship.

Pollutant	First-order reaction kinetics equation	K (min^{-1})	r^2
Phenanthrene	$y = -0.0126x + 9.2407$	0.012 6	0.989 7
Fluoranthene	$y = -0.0099x + 8.726\,6$	0.009 9	0.992 1

2.5.6.7 Photocatalytic mechanism of photocatalytic composite Ce^{3+}–TiO_2

Through the analysis of experimental results, it can be seen that the combination of rare earth-doped TiO_2 and zeolite can effectively remove PAHs in water. From the mechanism analysis, the removal of PAHs by composite photocatalysts mainly includes two processes of adsorption and photocatalytic oxidation. Its removal effect is much higher than adsorption of pure zeolite and photocatalytic oxidation of TiO_2 powder.

Zeolite of fly ash has a relatively large specific surface area, and TiO_2 is uniformly supported on it by sol–gel method. PAHs in water can be quickly enriched on the surface under stirring conditions. The enrichment process is physical adsorption. Removal of PAHs is limited, and cannot really remove PAHs, but played a role in the transfer. TiO_2 prepared at low temperature contains anatase phase and has photocatalytic activity under UV light degradation. Photocatalytic oxidation can degrade most organic pollutants. Under ultraviolet light, it will produce a large number of electrons and holes, with strong redox properties, and can complete refractory organic mineralization, and eventually with CO_2 and H_2O, other simple inorganic products appear (SUN Zhenfan, 2003).

When titanium dioxide is irradiated by UV light with the wavelength less than 387.5 nm, the electrons in the VB transition to the CB, and the ions are excited to separate out the electrons and generate positive holes to form electron–hole pairs, which reacted oxygen and water on the surface. OH^- and H_2O on the surface oxidize HO· radicals. The oxidation ability of HO· radicals is the strongest among the oxidants present in the water and can oxidize most of the organic and inorganic pollutants and has almost no selectivity for the reactants and plays a decisive role in photocatalytic oxidation effect. The electrons on the titanium dioxide surface can be dissolved by oxygen to form O^{2-}, while the surface of the electron has high reducibility, which can remove the water metal ions. The resulting atomic oxygen and hydroxyl radicals can oxidize and decompose the organic matter. The final products are CO_2, H_2O and inorganic. The specific reaction process is as follows (wherein h^+ represents a positively charged hole, e^- is a photo-exciton, ·OH is a hydroxyl radical, OH^- is a hydroxide ion, O^{2-} is a negatively charged oxygen radical, $\cdot HO_2$ is the reaction intermediate):

$$TiO_2 + h\nu \rightarrow h^+ + e^-$$
$$h^+ + H_2O \rightarrow \cdot OH + H^+$$
$$h^+ + OH^- \rightarrow \cdot OH$$
$$e^- + O_2 \rightarrow \cdot O^{2-}$$
$$\cdot O^{2-} + H^+ \rightarrow HO_2\cdot$$
$$2HO_2\cdot \rightarrow H_2O_2 + O_2$$
$$H_2O_2 + \cdot O^{2-} \rightarrow \cdot OH + OH^- + O_2$$
$$\text{Organics} + \cdot OH + O_2 \rightarrow CO_2 + H_2O + \text{Other products}$$

The photodegradation mechanism of PAHs has aroused the interest of many scholars: Kong Lingren (1986) studied the photochemical decomposition of benzo[a]anthracene and benzo[a]pyrene. Photolysis products of benzo[a]anthracene were benzo[a]anthracene-7-quinone, and benzo[a]pyrene degradation products were not detected. The photolysis of 17 PAHs in aqueous solution was studied comprehensively. It is pointed out that most PAH photodegradation rate constants (k) are related to their polarographic half-wave potentials ($E_{1/2}^{ox}$). When

$E_{1/2}^{ox}$ is low (easy to be oxidized), then k value is large (fast response). In the dark conditions of the controlled trials, PAHs were not degraded. The photolysis product of naphthalene was phthalic acid, and naphthalene was not photolyzed after the removal of dissolved oxygen in the solution. All these show that most PAH photolysis is photooxidation. Wen's team (2003) spent 2 years studying the photodegradation of phenanthrene and pyrene under the catalysis of TiO_2, respectively, and the intermediates were detected by GC-MS, and the detailed methods for their photocatalytic degradation were given. It is pointed out that all the major functions are ·OH, ·OOH, and some long-chain alkanes and alkanoic acids are formed during the reaction. The main approach of phenanthrene is shown in Figure 2.58.

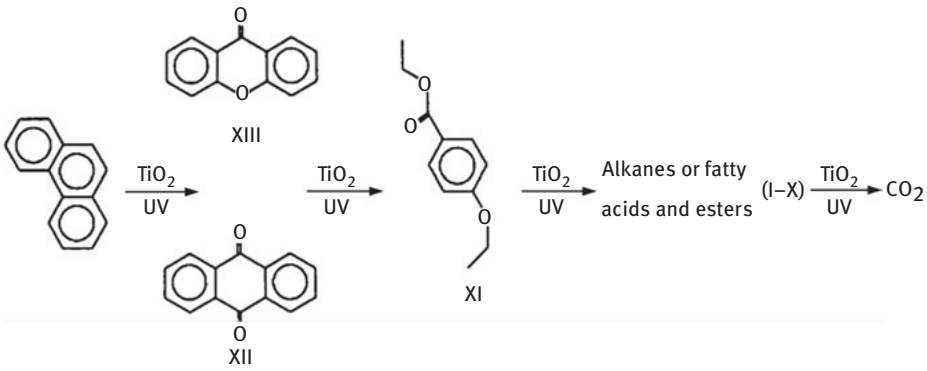

Figure 2.58: Photodegradation pathway of phenanthrene under TiO_2 catalysis.

Existing understanding of photodegradation mechanism of PAHs is obtained mainly through some indirect experimental evidence, such as photolysis products. In the reaction mechanism study, the intermediates and active species have not been identified, and most of the mechanism studies remain at the stage of imagination and speculation. Therefore, in the future, new analytical methods should be developed to identify photodegradation products, or directly study the active intermediates of PAH photolysis process by means of laser flash photolysis spectroscopy and fluorescence lifetime. In addition, the photochemical degradation of PAHs at multiphase interface is still weak. The establishment of kinetic mathematical models and their mechanism studies have yet to be further studied. The QSPR model for predicting indirect photodegradation of PAHs has yet to be established. In the actual environment, PAHs exist in multicomponent mixed form and the environment of the medium is complex and changeable. Therefore, it is very important to study and establish the method for simultaneous determination of multicomponent PAH

photodegradation and to carry out related researches as far as possible under actual environmental conditions.

2.6 Regeneration and recycling of artificial zeolite prepared by fly ash

Desorption regeneration capacity is an important performance of artificial zeolite from fly ash, but also affects the recycling of artificial zeolite and reduces the cost of an important factor. Studying the desorption behavior of adsorbate helps to reveal its adsorption mechanism (SATO S, 1986).

2.6.1 Comparison of desorption results of different NaCl concentrations at 72 h

Obviously, the efficiency of ammonia desorption by synthetic zeolite and lanthanum-modified zeolite mainly depends on the concentration of NaCl solution. With the increase of NaCl concentration, the desorption effect showed an increasing trend. Desorption rate of synthetic zeolite is relatively low, so the maximum desorption rate is about 71%. The desorption rate of lanthanum-modified zeolite can be up to 90%. Desorption rate of modified zeolite was significantly higher than that of unmodified zeolite. The lanthanum ions are easily combined with the hydroxyl groups in the aqueous solution to form the hydroxylated surface, which makes the ammonia ions in solution more accessible. Therefore, the ammonia adsorption rate of the modified zeolite compared to that of the general synthetic zeolite is faster, and due to the presence of lanthanum ions, ammonia adsorbed on the hydroxylated surface can easily be desorbed by NaCl (Figure 2.59).

2.6.2 Desorption amount of synthetic zeolite and modified zeolite with time

Figure 2.60 shows the effect of desorption time on the desorption of synthetic zeolite and lanthanum-modified zeolite. In the desorption process of synthetic zeolite, the substitution of Na^+ for NH_4^+ is relatively slow. This is because the initially adsorbed ammonia not only binds strongly to the zeolite surface but also migrates to the interior and is not easily replaced by other ions. However, after adsorption of sufficient ammonia on the zeolite surface, the adsorption effect is getting weaker. Therefore, the ammonia can easily be desorbed and ammonia in the zeolite pore is more difficult to desorb (ASAHI et al., 2001). Lanthanum-modified zeolites reached desorption equilibrium within 6 h compared to synthetic zeolites. Compared with the traditional ion exchange, La^{3+} is more likely to produce steric hindrance because of the larger hydration radius, which limits the access to zeolite pores. Even if the concentration of La^{3+} is very low or repeated many times, more complex multiphase

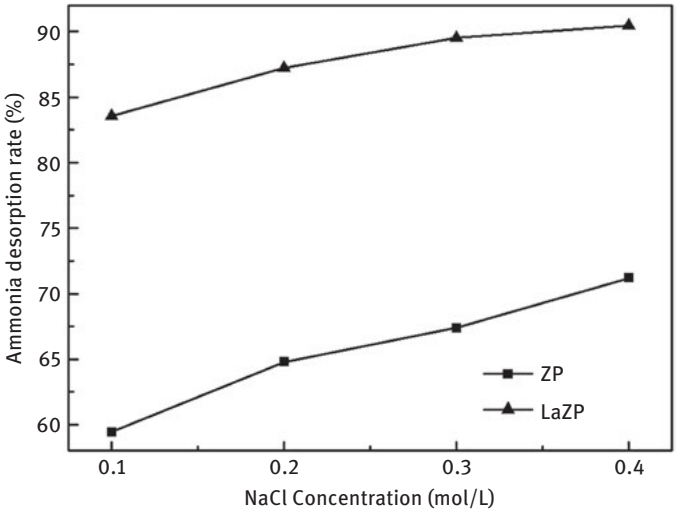

Figure 2.59: Desorption results of synthetic zeolite and lanthanum-modified zeolite after 72 h.

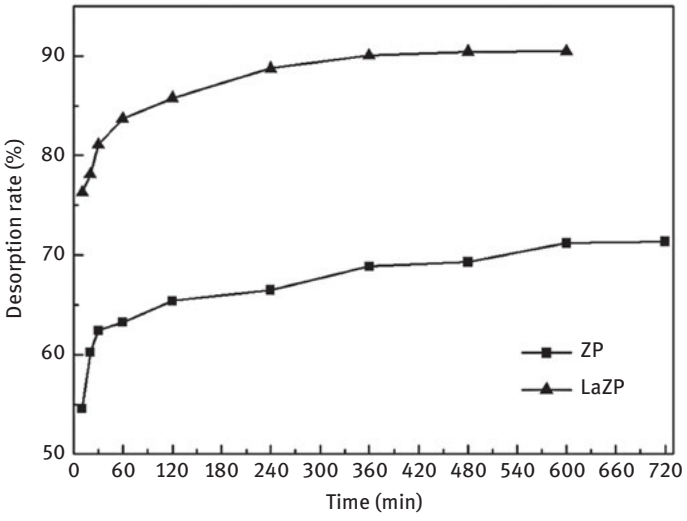

Figure 2.60: Effect of reaction time on ammonia desorption.

reactions can react on the surface of La^{3+}-containing crystalline materials (Li F et al., 2004). Therefore, ammonia adsorption principle of lanthanum-modified zeolite is mainly to promote large amounts of ammonia in the zeolite ion exchange effect, thus speeding up the desorption.

2.6.3 Effect of desorption times on removal of ammonia

According to the conditions of the adsorption reaction, the lanthanum-modified zeolite with equilibrium adsorption is desorbed and regenerated under the condition of NaCl, and the desorption regeneration reaction formula is as follows:

$$\text{Zeolite} - NH_4 + Na^+ = Na - \text{Zeolite} + NH_4{}^+ \tag{2.14}$$

where NH_4 in zeolite-NH_4 means adsorbent active site. Figure 2.61 shows that lanthanum-modified synthetic zeolite has good stability. The results of this study on the application of modified zeolite from fly ash are of great significance.

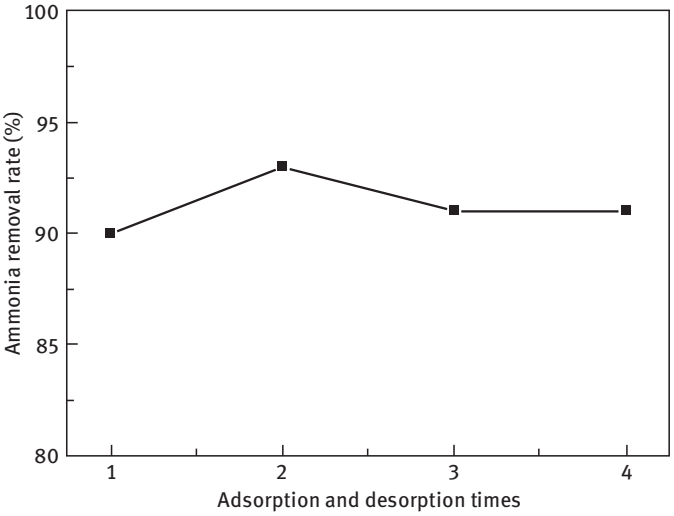

Figure 2.61: Effect of adsorption and desorption times on ammonia removal efficiency.

2.7 Product application prospect analysis

(1) Raw materials availability and preparation process analysis

Artificial zeolite synthesis is based on solid waste from coal-fired power plant – fly ash, industrial sodium hydroxide as the main raw material. The price of fly ash is relatively low, and can basically guarantee long-term stable supply. Industrial sodium hydroxide is a common industrial raw material, although the price is high, the amount of the production process is very small, and the recovery technology of waste acid and alkali further decreases the amount of industrial sodium hydroxide, so production costs are low. Artificial zeolite from fly ash is prepared by improved hydrothermal method, and the technology is mature and stable. The main equipment is the reaction still, which is commonly used in industrial production. It is easy to operate, the training is relatively

simple and there is no technical obstacle. In the actual production process can be easily achieved in a short period of mass production.

(2) Market analysis of products

At present, zeolites on the market can be divided into natural zeolite and artificial zeolite. Most of the natural zeolite is formed by the reaction of volcanic ash in alkaline solution. They are rich in nature, and the disadvantage is the poor efficiency of the application. Artificial zeolite is synthesized with silicon salts, aluminum salts and other chemical raw materials. Its adsorption, ion exchange and other performance are superior, but the price is expensive.

Artificial zeolite is prepared by silicon salts, aluminum salts and other chemical raw materials, owing superior adsorption, ion exchange and other performance, but it is expensive. Natural zeolite and artificial zeolite have been widely used in the removal of ammonia in water and heavy metal ions. Therefore, the application of zeolite in phosphorus removal from wastewater, especially the simultaneous removal of ammonia and phosphorus, will become an important direction for the application of zeolites.

Artificial zeolite products from fly ash has the characteristics of low cost, adsorption and ion exchange performance and easy regeneration. Modified artificial zeolite has a good simultaneous nitrogen and phosphorus removal performance. They have good market application prospects in the prevention and control of water environment pollution and protection, especially in the removal of ammonia and heavy metal pollutants and the simultaneous removal of nitrogen and phosphorus.

(3) Product replacement, maintenance and regeneration prospects analysis

Artificial zeolite from fly ash has a large amount of ammonia adsorption, with a CEC of 210–250 cmol/kg, which can be used for a long time in the treatment of slightly nitrogen- and phosphorus-polluted wastewater. The product form of artificial zeolite products from fly ash is varied. Powder products can be used as pharmaceuticals. After processing, it can be used as a filler. Artificial zeolite from fly ash can be desorbed and regenerated by salt solution such as sodium chloride. The experiment shows that after the regeneration for four times, the adsorption effect has not obviously decreased. However, the price of fly ash is relatively low, and the cost of adsorption–desorption–reutilization is relatively high and uneconomical. Therefore, it is not recommended to recycle in general and should be replaced by the new artificial zeolite directly.

References

ANANDAN S, YOON M.: Photocatalytic activities of the nano-sized TiO_2-supported Y-zeolites. Journal of Photochemistry and Photobiology C:Photochemistry Reviews, 2003, 4(1): 5–18.

AO Yanhui, SHEN Xunwei, YUAN Chunwei et al.: Research Progress on Degradation of Organic Pollutants with TiO_2 supported by Inorganic Adsorbents, Safety and Environmental Engineering, 2006, 13(1): 37–40.

ASAHI R, MORIKAWA T, OHWAKI T, et al.: Visible-light photocatalysis in nitrogen-doped titanium oxides. Science, 2001, 293(5528): 269–271.

CAREY J H, LAWRENCE J, TOSINE H M.: Photodechlorination of PCB's in the presence of titanium dioxide in aqueous suspensions. Bulletin of Environmental Contamination and Toxicology, 1976, 16(6): 697–701.

CHANG M Y, HSIEH Y H, CHENG T C, et al.: Photocatalytic degradation of 2,4-dichlorophenol wastewater using porphyrin/TiO_2 complexes activated by visible light. Thin Solid Films, 2009, 517(14): 3888–3891.

CHEN J, EBERLEIN L, LANGFORD C H.: Pathways of phenol and benzene photooxidation using TiO_2 supported on a zeolite. Journal of Photochemistry and Photobiology A:Chemistry, 2002, 148(1): 183–189.

CHOI C L, PARK M, LEE D H, et al.: Salt-thermal zeolitization of fly ash. Environmental Science & Technology, 2001, 35(13): 2812–2816.

DAWSON W J.: Hydrothermal synthesis of advanced ceramsite powders. American Ceramsite Society Bulletin, 1988, 67(10): 1673–1678.

DU Gaohui, WEI Yinghui, DOU Tao et al.: Study on Synthesis and Growth Mechanism of Nanometer HS Zeolite, Journal of Inorganic Materials, 2000, 15(6): 1073–1076.

DURGAKUMARI V, SUBRAHMANYAM M, SUBBA RAO K, et al.: An easy and efficient use of TiO_2 supported HZSM-5 and TiO_2+HZSM-5 zeolite combinate in the photodegradation of aqueous phenol and *p*-chlorophenol. Applied Catalysis A:General, 2002, 234(1): 155–165.

EPA. Drinking Water Standards and Health Advisories. US EPA. 2004.

FANG Songsheng, JIANG Yinshan, WANG Yujie et al.: Photocatalytic performance of natural clinoptilolite supported TiO_2, Environmental Science, 2003, 24(4): 113–116.

FRANK S N, BARD A J.: Semiconductor electrodes. 12. Photoassisted oxidations and photoelectrosynthesis at polycrystalline titanium dioxide electrodes. Journal of the American Chemical Society, 1977, 99(14): 4667–4675.

FU Keming, LIU Taoxiang, ZHANG Qinshan et al.: Fly Ash Hydrothermal Synthesis A Study on Zeolite and Its Growth Mechanism, Journal of Wuhan University of Technology, 2008, 30(2): 25–36.

FUJISHIMA A.: Electrochemical photolysis of water at a semiconductor electrode. Nature, 1972, 238: 37–38.

GABELICA Z, BLOM N, DEROUANE E G.: Synthesis and characterization of zsm-5 type zeolites:III. A critical evaluation of the role of alkali and ammonium cations. Applied Catalysis, 1983, 5(2): 227–248.

HOLLMAN G, STEENBRUGGEN G, JANSSEN-JURKOVIČOVÁ M.: A two-step process for the synthesis of zeolites from coal fly ash. Fuel, 1999, 78(10): 1225–1230.

HUANG M, XU C, WU Z, et al.: Photocatalytic discolorization of methyl orange solution by Pt modified TiO_2 loaded on natural zeolite. Dyes and Pigments, 2008, 77(2): 327–334.

HUI K., CHAO C.: Effects of step-change of synthesis temperature on synthesis of zeolite 4A from coal fly ash. Microporous and Mesoporous Materials, 2006, 88(1): 145–151.

INADA M, TSUJIMOTO H, EGUCHI Y, et al.: Microwave-assisted zeolite synthesis from coal fly ash in hydrothermal process. Fuel, 2005b, 84(12): 1482–1486.

INADA M, EGUCHI Y, ENOMOTO N, et al.: Synthesis of zeolite from coal fly ashes with different silica–alumina composition. Fuel, 2005a, 84(2): 299–304.

KAMAT P, MEISEL D.: Semiconductor Nanoclusters-Physical, Chemical, and Catalytic Aspects. Studies in Surface Science and Catalysis, Elsevier, 1997.

KIM Y, YOON M.: TiO_2/Y-Zeolite encapsulating intramolecular charge transfer molecules:a new photocatalyst for photoreduction of methyl orange in aqueous medium. Journal of Molecular Catalysis A:Chemical, 2001, 168(1): 257–263.

KONG Lingren: Photodegradation of Polycyclic Aromatic Hydrocarbons in Water, Environmental Chemistry, 1986, 3: 002.

KONSTANTINOU I K, SAKELLARIDES T M, SAKKAS V A, et al.: Photocatalytic degradation of selected s-triazine herbicides and organophosphorus insecticides over aqueous TiO_2 suspensions. Environmental Science & Technology, 2001, 35(2): 398–405.

LI F, LI X, HOU M.: Photocatalytic degradation of 2-mercaptobenzothiazole in aqueous La^{3+}-TiO_2 suspension for odor control. Applied Catalysis B:Environmental, 2004, 48(3): 185–194.

LIU Chunying, GONG Xiaofeng: Study on Photocatalytic Degradation of Landfill Leachate by Glass load with TiO2 Film, Ecological science, 2007, 25(4): 363–366.

LIU Ping, WANG Xinchen, FU Xianzhi: Preparation and Characteristics of Photocatalytic Self Cleaning Ceramic, Journal of Inorganic Materials, 2000, 15(1): 88–92.

LIU Shouxin, CHEN Xi: Synthesis and Characterization of Photocatalyst loaded with TiO_2/Activated Carbon with Sol - Gel Method, Journal of Catalysis, 2008, 29(1): 19–24.

LIU Shouxin, LIU Hong: Photocatalysis and Photoelectrocatalysis Fundamentals and Applications, Beijing: Chemical Industry Press, 2006.

LIU Yongmei, LI Debao: Synthesis of Small – diameter Round Zeolite A Molecular Sieve by Solid Method - based Industrial Coal Waste, China Surfactant Detergent & Cosmetics, 2002, 32(2): 53–56.

LIU Yikai, WU Deyi, ZHENG Xiangyong et al.: Effect of Several Common Ions on Phosphorus Removal of Synthetic Zeolite from Fly Ash, Environmental Pollution and Prevention, 2008, 30(11): 49–52.

MAHALAKSHMI M, VISHNU PRIYA S, ARABINDOO B, et al.: Photocatalytic degradation of aqueous propoxur solution using TiO_2 and Hβ zeolite-supported TiO_2. Journal of Hazardous Materials, 2009, 161(1): 336–343.

MINERO C, CATOZZO F, PELIZZETTI E.: Role of adsorption in photocatalyzed reactions of organic molecules in aqueous titania suspensions. Langmuir, 1992, 8(2): 481–486.

MOLINA A, POOLE C.: A comparative study using two methods to produce zeolites from fly ash. Minerals Engineering, 2004, 17(2): 167–173.

MURAYAMA N, YAMAMOTO H, SHIBATA J.: Mechanism of zeolite synthesis from coal fly ash by alkali hydrothermal reaction. International Journal of Mineral Processing, 2002, 64(1): 1–17.

NA Wei, LIU Qingju, ZHU Zhongqi: Study on the Preparation of Anatase TiO_2 Sol at Low Temperature, Functional Materials, 2006, 37(10): 1667–1669.

NOORJAHAN M, DURGA KUMARI V, SUBRAHMANYAM M, et al.: A novel and efficient photocatalyst: TiO_2-HZSM-5 combinate thin film. Applied Catalysis B:Environmental, 2004, 47(3): 209–213.

PARK M, CHOI C L, LIM W T, et al.: Molten-salt method for the synthesis of zeolitic materials:I. Zeolite formation in alkaline molten-salt system. Microporous and Mesoporous Materials, 2000, 37(1): 81–89.

PENGTHAMKEERATI P, SATAPANAJARU T, CHULARUENGOAKSORN P.: Chemical modification of coal fly ash for the removal of phosphate from aqueous solution. Fuel, 2008, 87(12): 2469–2476.

REDDY E P, DAVYDOV L, SMIRNIOTIS P.: TiO_2-loaded zeolites and mesoporous materials in the sonophotocatalytic decomposition of aqueous organic pollutants:the role of the support. Applied Catalysis B:Environmental, 2003, 42(1): 1–11.

SATO S.: Photocatalytic activity of NO_x-doped TiO_2 in the visible light region. Chemical physics letters, 1986, 123(1): 126–128.

SCHOEMAN B J.: Analysis of the nucleation and growth of TPA-silicalite-1 at elevated temperatures with the emphasis on colloidal stability. Microporous and Mesoporous Materials, 1998, 22(1): 9–22.

SHANKAR M, ANANDAN S, VENKATACHALAM N et al.: Fine route for an efficient removal of 2,4-dichlorophenoxyacetic acid(2,4-D)by zeolite-supported TiO_2. Chemosphere, 2006, 63(6): 1014–1021.

SHI Zhongliang, YAO Shuhua, HUA Li: Study on Photocatalytic Degradation of Papermaking Wastewater by TiO_2 Loaded on Zeolite, Non-metallic mineral, 2007, 30(4): 46–49.

SONG Mianxin, ZHOU Tianliang, DING Jianxu et al.: Study on Properties of Rare Earth – Zeolite Ternary System Photocatalytic Materials, Chinese Journal of Rare Earths, 2007, 25(2): 172–177.

STEENBRUGGEN G, HOLLMAN G.: The synthesis of zeolites from fly ash and the properties of the zeolite products. Journal of Geochemical Exploration, 1998, 62(1): 305–309.

SUN Zhenfan: Study on the Surface Morphology and Physicochemical Properties of TiO_2 Nanometer Membrane, Guangzhou: Zhongshan University, 2003.

TANAKA H, EGUCHI H, FUJIMOTO S, et al.: Two-step process for synthesis of a single phase Na–A zeolite from coal fly ash by dialysis. Fuel, 2006, 85(10): 1329–1334.

THEVENET F, GUAITELLA O, HERRMANN J, et al.: Photocatalytic degradation of acetylene over various titanium dioxide-based photocatalysts. Applied Catalysis B:Environmental, 2005, 61(1): 58–68.

WANG Chunfeng, LI Jiansheng, HAN Weiqing et al.: Synthesis of submicron zeolite NaA by two - step method using fly ash as raw material, Journal of the Chinese Ceramic Society, 2008, 36(11): 1638–1643.

WU Deyi, KONG Hainan, ZHAO Tonggang et al.: Effect of Synthesis Conditions on Zeolite Formation and Quality in Zeolite Synthesis from Fly Ash, Journal of Inorganic Materials, 2005, 20(5): 1153–1158.

YANG Xiaoru, GUO Zhenning, LI Junren et al.: Preparation and Photoluminescence Study of Nanometer Titanium Dioxide Film, Functional Materials, 2007, 38(6): 1016–1018.

YONEYAMA H, TORIMOTO T.: Titanium dioxide/adsorbent hybrid photocatalysts for photodestruction of organic substances of dilute concentrations. Catalysis Today, 2000, 58(2): 133–140.

YOON S-J, LEE Y H, CHO W-J, et al.: Synthesis of TiO_2-entrapped EFAL-removed Y-zeolites:Novel photocatalyst for decomposition of 2-methylisoborneol. Catalysis Communications, 2007, 8(11): 1851–1856.

YU Zhenbao, SONG Naizhong: Zeolite Processing and Application, Beijing, Chemical Industry Press, 2005.

YUE Linhai: Study on photodegradation of monocrotophos by rare earth doped titanium dioxide catalyst, Shanghai Environmental Science, 1998, 17(9): 17–19.

ZHANG Shugen, SHEN Shaohua, LI Yan: Study on Zeolite Synthesis of Inexpensive Mineral Raw Materials, Central South University Press, Chang Sha, 2003.

ZHANG Xihuan, MA Hongwen, BAI Feng: Study on Synthesis of Zeolite from Natural Mineral Materials, China Mining Magazine, 2006, 14(11): 34–37.

ZHDANOV S.: Molecular sieve zeolites. Advances in Chemistry Series, 1971, 101: 20.

3 Preparation technology of functional ceramsite

3.1 Overview

Biofilm carrier materials in conventional wastewater treatment processes include zeolites, activated carbon, ceramsite, plastic spheres, basalts, slags, coke, anthracite, fine quartz sand and the like. With the continuous improvement of technology and the increase of wastewater treatment requirements, the traditional biofilm carrier material has large specific gravity, small specific surface area, slow hanging film, poor wear resistance, unsatisfactory reactor flow state, high cost and difficult to obtain materials and other issues. In recent years, polymer organic material carrier technology has been developed, but usually there are shortcomings of small amount of biofilm, unstable treatment and high prices. Therefore, the development of new biofilm carrier is still one of the hot spots in the research of water treatment technology. The ideal new biofilm carrier should have the following characteristics: (1) anti-hydraulic impact load is good, (2) physical and chemical properties are stable, (3) performance of hanging film is good and (4) no biological toxicity; these will not produce secondary pollution.

Ceramsite is one of the most commonly used biological carriers for wastewater treatment. It is widely used in wastewater treatment facilities such as artificial wetlands and biological aerated filters. Ceramsite mainly include two types: (1) natural ceramsite and (2) artificial ceramsite. At present, shale ceramsite and clay ceramsite are commonly used in wastewater treatment projects. The former is made from crushed natural shale and belongs to natural ceramsite, whereas the latter is made from natural clay such as bentonite, obtained by sintering with high temperature after granulation, belongs to a kind of artificial ceramsite. Compared to natural ceramsite, the cost of artificial ceramsite is relatively higher because of the need to granulate and consume energy for sintering. However, because of its preparation process that can be controlled by hand, especially in material forming and sintering process, the size and distribution of its aperture can be controlled by different manufacturing processes, or by different composition ratio; artificial ceramsite has more specific surface area, stronger removal of pollutants and better hydrophilic properties; it is more conducive to the growth of organisms than natural ceramsite, so the application of artificial ceramsite in wastewater treatment is also more promising.

Traditional ceramsite is sintered of clay and shale, which needs a large number of high-quality clay and shale mines, it causes certain degree of damage to the environment. Solid waste ceramic is a new type of environmental materials, representing the development direction of ceramsite. In future, more than 95% of ceramsite will use solid waste as raw material for production. Solid waste that can be used for the production of ceramsite includes the following: fly ash, steel slag, mineral waste residue, cinder, river sludge, sewage treatment plant sludge, domestic waste residue,

https://doi.org/10.1515/9783110544381-003

straw ash and the like. With the increasing demand for water treatment effect, in addition to as being a common biofilm carrier, composite functional ceramsite will be an important direction for the development of ceramsite. In addition, the traditional ceramsite needs shale; clay minerals such as bentonite as the main raw material, raw materials are limited, and the cost is relatively high. At present, more and more studies are focused on the preparation of composite functional ceramsites with various inexpensive raw materials (such as combustion ash and natural adsorbent), which can effectively conserve resources and comprehensively use all kinds of waste, turning waste into treasure. Fly ash is one of the most commonly used cheap raw materials.

The composition of fly ash is more complex. They have large specific surface area and more reactive sites. The composition of fly ash and clay are more similar; they mainly contain silicon and aluminum compounds that have good sintering properties. So it can be used as raw materials for ceramic. The produced ceramsite has physical characteristics of original ceramsite and the chemical characteristics of the fly ash. Compared with the traditional clay ceramsite and shale ceramsite, fly ash ceramsite is not only cheap and easy to obtain raw materials, but also has a good removal effect on the pollutants in the sewage. In recent years, the research on fly ash ceramsite as a filter or filler for wastewater treatment has been very common. Fly ash ceramsite is widely used in the treatment of metal ion-containing wastewater, humic wastewater, phosphorus-containing wastewater, fluorine-containing wastewater and oily wastewater. From the existing research, if the possible problem of leaching toxicity of heavy metals can be properly solved, fly ash will be a promising environmental functional material with a wide range of applications.

Preparation of fly ash ceramsite: fly ash is used as the main raw material; by adding clay and other substances, it will be sintered at high temperature. Fly ash ceramsite is generally spherical; the surface is rough and hard. After sintering, it often presents a light yellow color, microporous distribution is rich, and shows honeycomb structure. The particle size is often 5–20 mm. They have large specific surface area and high surface energy. It has aluminum, silicon oxide and other active sites, good adsorption properties and it is easy to regenerate and reuse. Therefore, fly ash ceramic is a cheap adsorbent. In addition, fly ash ceramsite is a porous lightweight material that has the advantages of developed specific surface, high porosity, rough surface, strong adsorption capacity and effective biodegradation, which are widely used as filter for wastewater treatment.

(1) As filler for wastewater treatment

Biological aerated filter is a wastewater treatment process, which rose in the late 1980s and early 1990s. This process is currently popular in Europe, the United States and Japan. In recent years, China has also carried out research on aerated biofilter technology, but its core problem of filter still has various unresolved shortcomings. The options of filter are rich and varied. The common domestic contact filler are as follows: FRP, plastic honeycomb packing, three-dimensional corrugated packing,

soft fiber packing, semisoft packing and irregular granular packing such as sand, gravel, slag, coke, anthracite and so on. They all have the shortcomings of smooth surface, poor biofilm adhesion, aging and easy to plug. Fly ash ceramsite as a filler for aerated biofilter has been widely concerned.

According to the principle of aerated biofilter, structure and its filter mechanism, ZHANG Wenyi et al. (2006) provided a formula for the production of ceramic biofilter using fly ash and clay. The production process is as follows: first, the clay is dried and crushed to a particle size of about 100 mesh. Then, according to the formula, clay powder (45%), fly ash (50%) and pore former (5%) dry powder are mixed. 10%–20% water is added and mixed well to granulate, particle size φ is 3–6 mm. The wet granules are dried at about 100 °C, calcined in a muffle furnace at 950 °C–1,000 °C.

WANG Jian et al. (2004) successfully developed a method of adding organic pore-forming to produce lightweight porous spherical biofilter. Fly ash is the main raw material, clay is binder, pelletizing and high temperature sintering is the main process. The basic process parameters are the amount of fly ash, clay and pore former; the sintering temperature is 1,050 °C–1,150 °C, and the sintering time is 10 min. Pore size distribution is 5–25 nm, and the specific surface area is 8–9 m^2/g. Compared with the traditional biological filter, it has the advantages of small apparent density, large specific surface area and rough surface.

ZHAO et al. (2009) studied the use of sludge-fly ash ceramsite particles (SFCP) and clay ceramsite particles (CCP) as a filler in aerated biofilters to treat municipal wastewater. The results show that under the conditions of hydraulic retention time (HRT) of 1.5 h, 0.75 h and 0.37 h, respectively, the removal effect of SFCP on COD and NH3-N is 10% higher than that of CCP. WANG Ping et al. (2008) uniformly mixed fly ash, clay and coal, according to mass ratio of 6: 3: 1. After sintering at 1,300 °C, the fly ash ceramsite was used in aerated biological filter. When the roasting temperature was 950 °C–1,050 °C, it is found that the specific surface area of the filter media was 4.26–7.24 m^2/g, the pore size range was 0.003–10 μm, the apparent porosity was 72.29%–73.21%, the bulk density was 0.73–0.74 cm^3/g, the surface was rough, and the physicochemical stability and the microbial adaptability were good, the average removal rate of COD_{Cr} was over 85% and the average removal rate of NH_3-N was over 65%.

(2) For direct treatment of wastewater

TONG Jingjing et al. (2009) developed two kinds of high-performance ceramic, using fly ash, sawdust and iron ore and other wastes with granulation and high temperature sintering. Ceramsite and zeolite were filled with “brick wall” type nesting to build a high efficiency ceramic/zeolite biological filters. The effects of nitrogen and phosphorus removal on domestic sewage (COD of 200 mg/L, NH_3-N of 20 mg/L and TP (total phosphorus) of 4.0 mg/L) were studied. The results show that the high-performance functional ceramsite has the advantages of rough surface, large specific surface area, high mechanical strength, good acid and alkali resistance and no heavy metal dissolution. The upper and the lower part of the biological filter form an aerobic

zone and an anaerobic zone, respectively. When theHRT was 2.15–5.73 h and the hydraulic load was 2.8–7.5 $m^3/(m^2 \cdot d)$, the biofilters had significant effect on NH_3-N, TP and COD. The removal rates of the two functional ceramic biofilters reached 83.6%–98.3%, 89.1%–99.7% and 84.4%–95.2%, which was better than that of the common biofilter.

Fly ash and sewage sludge were used as the main raw materials and clay was used as a binder for the development and application of sintered ceramsite, CAI Changfeng et al. (2007) obtained the best sintering conditions: the firing temperature is 1,050 °C,the proportion of sludge is 35%–40%, the content of fly ash is 53% and the sintering time is 15 min; fly ash/sludge ceramsite bulk density is 0.79–0.90 g/m^3; water absorption is 68.95%–80.01%; the ammonia adsorption capacity of 0.030–0.052 mg/g; total phosphorus adsorption capacity of 0.005–0.022 mg/g.

Non-burning ceramic due to energy saving has also been a greater concern. PENG Weihua et al. (2011) prepared non-burning ceramic by power plant fly ash and with cement, lime, gypsum or water glass. And it is used as a biological aerated filter (BAF) filler to treat municipal wastewater. The experimental results show that when the gas temperature is 18 °C–21 °C, the gas–water ratio is 4:1, dissolved oxygen is 2.5–3.5 mg/L, the HRT is 8–9 h, the removal efficiency of COD and ammonia is better and the average removal rates were 93.1% and 99.3%, respectively.

LIU Baohe et al. (2010) used white calcium silicate cement, fly ash, clay and calcium oxide as the main raw material; he added a small amount of calcium silicate and xonotlite fibers, and appropriate amount of additives to regulate hydration reaction rate. Water–solid ratio was 0.55. Aluminum powder was used to make holes and high-temperature steam curing was carried out in the high pressure reactor and dried at 105 °C.Through examining the leaching rate of calcium ions and pH of the leaching solution, the preparation process of high efficiency phosphorus absorption filter was determined. The results of the application of the filter preparation to treat low-concentration phosphorus-containing wastewater showed that the phosphorous content of the residual liquid reduced from 10 to 0.2 mg/L after the dosage of 1% phosphoric acid solution for 2 h adsorption, which is far below the urban sewage treatment plant integrated emission level A standard.

XIANG Huijiang et al. (2006) used fly ash ceramsite to treat wastewater containing metal ions, humic wastewater, phosphorus-containing wastewater, fluorine-containing wastewater and oily wastewater. Relevant test results showed that fly ash ceramsite has a good removal effect for various pollutants. YUE Min et al. (2004) had studied the physical and chemical properties of domestic light spherical ceramsite, hanging film characteristics and the effect of the tower for the treatment of organic wastewater with anaerobic biological filter. Research showed that the material is suitable as anaerobic microbial carrier. YUAN Xu et al. (2007) used the ceramsite as the carrier material of biological aerated filter to treat low-concentration domestic sewage, studied the removal effect of COD, NH_3-N and SS, and observed the morphology of biofilm. The results showed that when the influent COD was 30.8–184.8 mg/L, the NH_3-N average

was 25 mg/L, the SS was 61.2–206.9 mg/L, the HRTs were 12, 10, 8, 5 and 3 h, the removal efficiencies of COD, NH_3-N and SS were more than 80%, 90% and 80%, respectively. SANG Junqiang (2004) investigated the impact of phosphorus source on the biofilm of ceramic filter. The results showed that during the pretreatment of bio-ceramic filter, if the content of phosphorus source in raw water is low and cannot meet the needs of microbial growth, adding phosphorus source to raw water can increase the quantity and activity of microorganisms in the ceramic filter, which is a new way to improve pretreatment effect of ceramsite filter.

3.2 Preparation goal of fly ash ceramsite

Functional ceramsite of fly ash used for wastewater treatment should have the following characteristics:

(1) Large specific surface area
For water pollution treatment, the specific surface area of fly ash ceramic should be large enough, and the surface is rough, which is conducive to microbial growth and hanging film. In addition, the larger specific surface area can also increase the contact area between ceramsite and sewage, which is good for the removal of pollutants.

(2) High porosity
Unburned charcoal in fly ash can increase the porosity of the product during firing of the ceramsite. The higher the porosity, the larger the pore volume, the more suitable for microbial attachment, fixation and growth. The more abundant pores can also shield the attached microorganisms from the scouring effect of the hydraulic shear.

(3) Suitable particle size and density
Fly ash ceramsite should not be too small or too large, under normal circumstances, the particle size of ceramsite should be 6–15 mm. Particle size is too small for clogging, too large particle size will lead to its too small specific surface area is and further affect the mechanical strength of fly ash ceramsite. The density of fly ash ceramsite should also meet the requirements of general wastewater treatment. If the density is too large, the filler will have difficulty in suspension or energy consumption increase in backwashing. If the density is too small, it is easy to run material during backwashing. So the density must meet the relevant standards.

(4) High mechanical strength
The water treatment filler must have a sufficiently high mechanical strength so that it can withstand the hydraulic shear of different intensities and rolling friction between the fillers and reduce the wear of the filter during the backwashing or it is broken that result in smaller or even loose particles.

(5) Strengthen the sewage treatment effect

The biggest difference between fly ash ceramsite and general bentonite ceramsite is that fly ash ceramsite not only has the characteristics of larger specific surface area and higher surface energy than conventional ceramsite, but also because the main component of the ceramsite is fly ash, which has good adsorption of pollutants, especially for phosphorus. Therefore, in the preparation process of fly ash ceramsite, attention should be paid to retain the characteristics of fly ash to remove N, P pollutants to strengthen the sewage treatment.

3.3 Properties and research status of fly ash ceramsite

Fly ash is a good material for wastewater treatment; its composition is complex, it has large specific surface area and the large number of active positions. So not only its adsorption property is better, but also it has stronger reactivity. In addition, the composition of fly ash and clay are similar; they are mainly composed of silicon and aluminum compounds, which have good sintering properties and can be used as raw materials for ceramic production. The produced ceramsite has the physical characteristics of the original ceramsite and the chemical characteristics of the fly ash. Compared with the traditional clay ceramsite and shale ceramsite, the fly ash ceramsite is not only cheap and easy to obtain raw materials, but also has a good removal effect on the pollutants in the sewage.

Fly ash is the main raw material for preparation of fly ash ceramsite by adding clay and other materials, which are sintered at high temperatures. Fly ash ceramsite is generally spherical, the surface is rough and hard, after sintering it is light yellow, micropore distribution is rich and honeycomb. Fly ash ceramic particle size is often 5–20 mm, has large specific surface area and high surface energy. There are aluminum and silicon oxide in fly ash, which have good adsorption properties, is easy to regenerate and easy to reuse. Therefore, fly ash ceramic is a cheap adsorbent. Fly ash ceramsite can be widely used in sewage treatment; it is mostly used as a core filler in aerated biological filter. At present, some people in China have carried out relevant research, but the large-scale production and application are few.

3.4 Preparation, functionalization and scale application of phosphorus removal functional ceramsite

3.4.1 Preparation of fly ash ceramsite

3.4.1.1 Basic process of preparation

There are two common preparation methods of ceramsite: (1) sintering method and (2) chemical curing method. The former is widely used conventional water

treatment ceramsite preparation technology. The latter is a fly ash shell non-burning ceramic technology, commonly used in the preparation of building ceramsite.

Sintering method to prepare ceramic is shown in Figure 3.1.

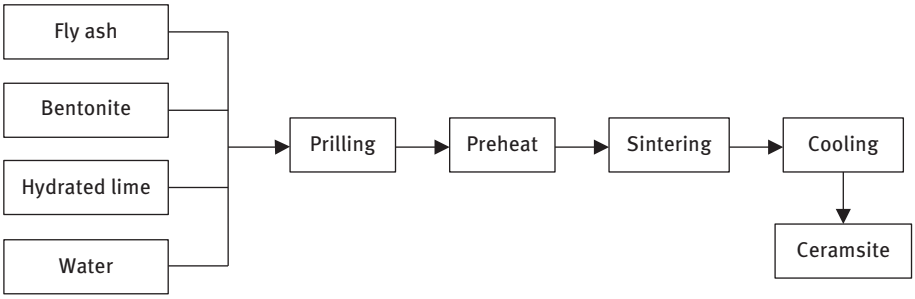

Figure 3.1: Sintering method for preparing ceramsite.

Admixtures include the following: (1) binder (high quality clay), (2) pore former (quicklime or pulverized coal) and (3) flux (alkali metal oxide). It is generally required to produce a certain amount of liquid phase with certain viscosity and certain amount of gas at the firing temperature to expand. In the expansion temperature range, the resulting gas pressure slightly greater than the expansion of pore wall damage strength will produce micropores.

3.4.1.2 Main influencing factors of performance of fly ash ceramsite

In the process of preparing fly ash ceramsite, the important process parameters that affect the performance are as follows: raw material ratio and chemical composition, swelling agent and cosolvent, preheating method, firing temperature and firing temperature holding time, heating rate and so on.

(1) Effect of raw material ratio on the properties of ceramsite

Raw material ratio is one of the important factors affecting the performance of fly ash ceramsite. The chemical composition of the high-strength fly ash ceramsite raw material should be within the swelling area of the Riley three-phase diagram (see Figure 3.2), which meet the performance requirements of lightweight high-strength fly ash ceramsite.

The results show that, when the value of easy to burn coefficient P_k is 3.5–10, it can be fired to sintering-expanded haydite, the performance index is better. The so-called easy to burn coefficient P_k is calculated as follows:

$$P_k = SiO_2 + Al_2O_3/CaO + Fe_2O_3 + MgO + R_2O \tag{3.1}$$

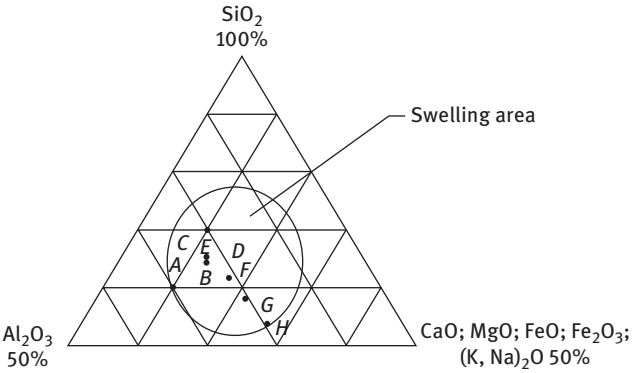

Figure 3.2: Riley three-phase diagram.

That is, the ratio of the sum of the silicon and the aluminum oxides in the raw material to the sum of the alkali oxides. The value of easy to burn coefficient P_k is an important reference coefficient for the preparation of fly ash ceramsite. The P_k value has a good linear relationship with the porosity and particle strength of fly ash ceramsite. Calculating P_k can predict ceramsite well.

(2) Influence of raw material composition on porosity formation of ceramsite

Ceramsite pore causes can be divided into the following: molding, burning loss and swelling. Different ingredients play a role in different stages. Water hardness in the molding, the residual carbon loss in the early roasting and mineral decomposition at high temperatures have an impact on the pore structure. Fly ash contains low ash melting point materials such as CaO, Fe_2O_3 and MgO, which will reduce the firing temperature and porosity. Fly ash after high temperature treatment and sintering will produce 50% to 80% (mass fraction) of Al–Si glass. The surface of small particles is a honeycomb structure. The chains between some atoms are relatively weak, and only a weak energy can break the bonds of these atoms. There is no regular microporous grid, so the water absorption of ceramsite has rebounded.

(3) Influence of expanding aid and flux on pore structure of fly ash ceramsite

Usually phenomenons occur while expanding aid at high temperatures of structural water removal and the layered structural destruction. Structure water evaporates to form gas to escape. Under suitable liquidus viscosity conditions, the gaseous structural water is trapped in the hot melt, causing expansion of the interior ceramsite. At high temperature, the flux and main components generate eutectic mixture with a lower melting point, which causes a large amount of liquid phase to form and the material reaches the desired viscosity for expansion.

The pore structure of fly ash ceramsite, which is only mixed with the expanding aid is irregular. In addition, as the amount of expanding aid is gradually increased, the pore size also becomes larger, which shows that the expanding aid has the effect of increasing the pore size. With the increase in expanding aid, the internal structure of ceramsite gradually evolved into pore structure with closed circular holes. This shows that expanding aid helps reduce liquid viscosity. Stomata was easily formed in a stable liquid environment, the number of closed circular holes greatly increased, thereby increasing the strength of ceramsite and to maintain a low water absorption. Common cosolvent include lime, pulverized coal and the like.

(4) Effect of preheating method

Preheating is another important factor affecting ceramsite performance. The purpose of preheating is to remove most of the volatile organic matter in the raw material and to avoid the occurrence of burst deformation during rapid heating. Fly ash ceramsite requires preheating before firing. However, if the preheating temperature is too high or the preheating time is too long, the gas will escape when the preform has not reached its optimum viscosity, causing poor expansion of the ceramsite and increasing the cost. Therefore, the process of preparation of ceramsite should choose the appropriate preheat temperature and time to ensure the performance of ceramsite.

(5) Effect of firing temperature on properties of ceramsite

(i) Ceramisite compressive strength and firing temperature are positively correlated

When the firing temperature is below 900 °C, the strength of fired sample is relatively low, and the internal structure is relatively loose. When the temperature rose to 1,250 °C, the samples of ceramsite is fluidized and deformed, and the dense enamel is formed on the surface. The volume decreased, the specific surface area and pore volume decreased rapidly. Therefore, the firing temperature of ceramsite is usually selected between 900 °C–1,250 °C.

(ii) The water absorption of ceramsite monotonically decreases when the sintering temperature is> 1,050 °C, and the porosity decreases

When the firing temperature is lower than 1,050 °C, the change of water absorption is complicated. When the pores have formed, the water hardness of the fly ash results in pore structure and early roasting water, loss of organic matter and mineral decomposition. Penetration of low melting point material has a negative impact. When the firing temperature is higher than 1,050 °C, the influence of the densification of the molten liquid phase is dominant. Melting quartz and other glassy materials have small viscosity; they easily penetrate into a variety of crystal particles. This makes the adsorption material particle structure too dense with fewer pores. With the increase

in calcination temperature, the dense structure inside the granule increases, and the porosity of the fly ash ceramsite decreases, which leads to the rapid and monotonous decrease in the water absorptivity of the granule.

(iii) Bulk density increases with increasing sintering temperature

When the sintering temperature is at 900 °C–1,100 °C, the increase of ceramic bulk density is small. More than 1,100 °C, the bulk density of ceramsite increases rapidly with the increasing sintering temperature.

3.4.1.3 Trial production of fly ash ceramsite and its performance test

According to the abovementioned theory, trial production of fly ash ceramsite and its performance test were carried out. The main purpose is to explore the impact of different formulations on the performance of ceramsite, as well as to find a relatively feasible sintering conditions, and to provide data support for the future optimization of fly ash ceramsite preparation.

Fly ash and bentonite are the main raw materials of fly ash ceramsite. The calcium hydroxide [$Ca(OH)_2$] is used as a expanding agent and pore generating agent. A small granulator was used for granulation. The ballability of first test without binder was poor. The latter experiment was improved by adding sodium silicate (Na_2SiO_3) as binder.

(1) Experimental materials and methods

(i) Experimental materials

Preparation materials of fly ash ceramsite are as follows: fly ash (Jiangnan thermal power plant, Nanhai District, Foshan City, Guangdong Province), sodium bentonite, $Ca(OH)_2$, NH_4HCO_3, Na_2SiO_3 and so on.

Instruments: Small Ball Mill, YCM5 Mixer, DZ-20C Mini Granulator, PHG-9145A Blast Oven, KLS05/13 Muffle Furnace, 3001-8 Portable pH Meter, HZ-03MZR Stationary Shaker, R-5000 UV Spectrophotometer and H-3000N scanning electron microscope.

(ii) Preparation method of fly ash ceramsite

Fly ash, bentonite and quick lime were placed in the blast oven and dried at 105 °C for 2 h, then ground and passed through 200 mesh sieve. Fly ash was the main raw material, bentonite was supplemented and a certain mass fraction of quick lime and sodium silicate were mixed, then a certain amount of water was added and stirred into a uniform liquid, then was put into a small pelletizer to form a ball with a particle size of 4 to 6 mm. The formed ceramsite was dried in natural state for 6 h, then put into the muffle furnace to be preheated, and then sintered at the set sintering temperature. After the natural cooling of the hearth, the fly ash ceramsite was obtained.

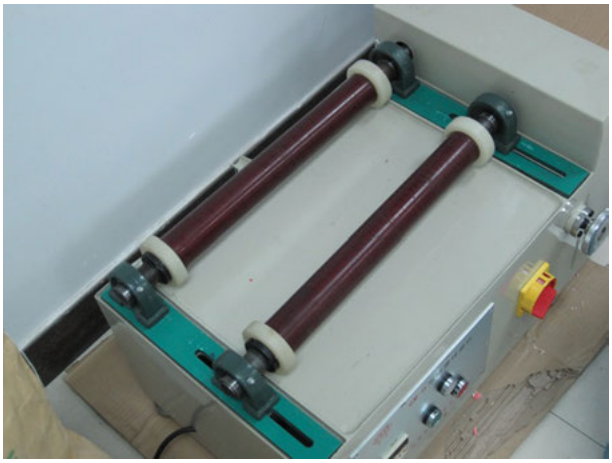

Figure 3.3: Small ball mill.

Figure 3.4: Mini ceramic granulator.

(2) Ceramics trial firing results

(i) The first fly ash ceramics trial

(a) Conditions of the first fly ash ceramics trial firing

Pretreatment: Fly ash, bentonite and hydrated lime were oven dried at 105 °C for 2 h in the laboratory and then ground separately and passed through a 200-mesh screen.

Figure 3.5: Blast oven and high temperature muffle furnace.

Table 3.1: The main component analysis of fly ash and clay (mass fraction).

Raw material composition	SiO_2	Al_2O_3	Fe_2O_3	CaO	MgO	LOI
Fly ash(%)	46.51	34.61	5.08	3.72	0.96	5.37
Clay(%)	58.43	11.26	1.06	1.78	1.50	—

Raw material ratio: Bentonite: fly ash is prepared according to the mass fraction of 100%: 0; 25%: 75%; 75%: 25% and 0: 100%. Dosage of lime, NH_4HCO_3 and water are 10% (mass ratio). The sphericals with a diameter of 6 mm were made with semiautomatic pelletizing machine. In the laboratory environment they were dried for 5–7 h, then were preheated.

Preheating: preheated at 500 °C for 20 min, and then gradually increased to a predetermined temperature to be sintered.

Sintering: Each batch of samples were sintered at 1,050 °C for 20 min, then heating was stopped and cooled to room temperature naturally. After cooling, the mass of ceramsite was weighed and its particle size was measured.

(b) Trial firing results

Four different kinds of ceramsite were fired by the first fly ash ceramics trial firing as shown in Figure 3.6.

Fly ash ceramsite can be fired by trial firing. However, the four batches of fired fly ash ceramsite strength are not large. The strength of ceramsite and fly ash content has a more obvious relationship, that is, the higher the content of fly ash, the lower the strength of fly ash ceramsite. When the content of fly ash reaches 75%, its

Figure 3.6: Comparison of five types of clay ceramsite and ceramsite with different fly ash sintered by muffle furnace: (a) 100% bentonite ceramsite, (b) 50% bentonite: 50% fly ash ceramsite, (c) clay ceramsite, (d) 75% bentonite: 25% fly ash ceramsite and (e) 25% bentonite: 75% fly ash ceramsite.

Figure 3.7: 100% bentonite ceramsite sintered in muffle furnace.

strength is significantly reduced, and even can be crushed by hand. The firing of ceramsite structure was more loose, but the pores were very rich. When the content of fly ash is larger, the color of fly ash ceramsite is white, whereas fly ash is yellowish when the content is small. The loss on ignition before and after sintering of fly ash ceramsite is shown in Table 3.2.

(c) Preliminary static adsorption tests and results

The purpose of the preliminary static adsorption test is to examine the effect of trial firing of ceramsite on nitrogen and phosphorus removal of wastewater. The wastewater was taken from South China Institute of Environmental Science housing estate as a research object. After cooling and air-drying, four kinds of ceramsite of 2.0 g each were

Figure 3.8: 75% bentonite: 25% fly ash ceramsite sintered in muffle furnace.

Figure 3.9: 50% bentonite: 50% fly ash ceramsite sintered in muffle furnace.

Figure 3.10: 25% bentonite: 75% fly ash ceramsite sintered in muffle furnace.

placed in 250 mL conical flask and 100 mL of domestic sewage was added. The conical flask was then placed on a rotary shaker (150 rpm for 3 h). After standing, the contents of ammonia and phosphorus in the supernatant were measured. Experiments were conducted at 25 °C. The experimental results are shown in Table 3.3.

Table 3.2: Mass comparison of fly ash ceramics before and after sintering.

Sample number	Mass *m* (before sintering) (g)	Mass *m* (after sintering) (g)	LOI(%)
1. No fly ash	24.392 6	18.795 5	22.9
2. 25% fly ash	33.072 0	26.852 0	18.8
3. 50% fly ash	53.586 5	43.513 5	18.7
4. 75% fly ash	27.265 4	22.161 3	18.7

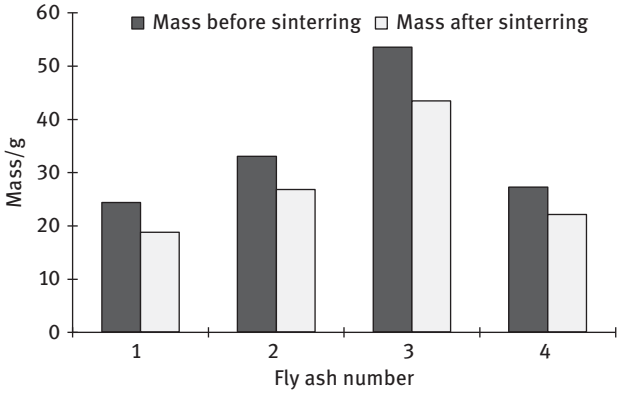

Figure 3.11: The mass contrast histogram of fly ash ceramsite before and after sintering.

Table 3.3: Static adsorption test results.

Samples	COD (mg/L)	NH_3-N (mg/L)	TP (mg/L)
Raw water	146.21	138.46	3.542
Raw water after oscillation	143.44	94.438	3.534
1. No fly ash	134.59	94.645	3.370
2. 25% fly ash	108.61	98.812	2.344
3. 50% fly ash	123.98	96.248	1.944
4. 75% fly ash	125.90	95.901	1.012

The experimental results show that the four types of ceramsite have a certain degree of removal of COD and TP in wastewater. Fly ash ceramsite has better adsorption performance on TP; TP removal rate of No.4 fly ash ceramsite reached 71%.

NH_3-N removal effect of the first trial firing fly ash ceramsite is not satisfactory. Even in the blank experiment (empty shake raw water), NH_3-N concentration reduction occurs when adding fly ash ceramsite was even slightly larger. NH_4HCO_3 was added as an expansion aid in the manufacturing process, dissolution of residual NH_4^+ in the water treatment process may also be one of the factors that causes no decrease in NH_3-N concentrationafter treatment.

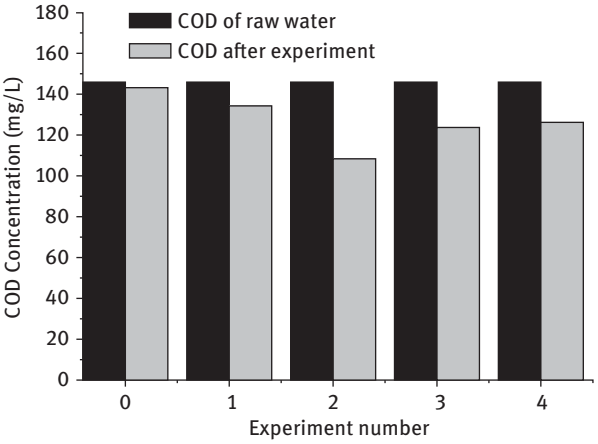

Figure 3.12: COD removal efficiency of trial firing ceramic.

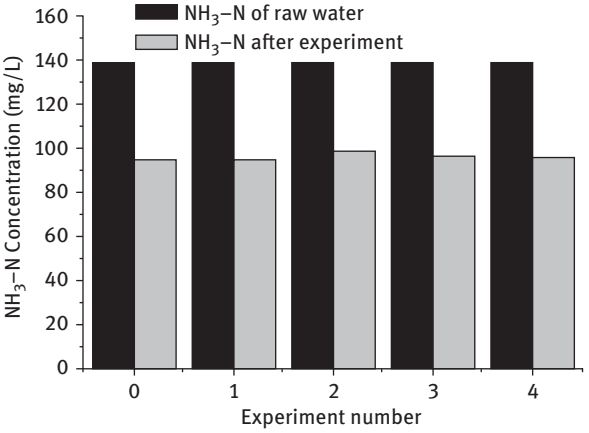

Figure 3.13: NH_3–N removal efficiency of trial firing ceramic.

The strength of this batch of ceramsite was not good. As a filler for water treatment, the poor strength of ceramsite will affect the effectiveness of its application in wastewater treatment projects, increase the SS concentration of the effluent and may cause clogging. Therefore, the formula and firing method of fly ash ceramsite were optimized, and the second trial firing was prepared.

(ii) The second fly ash ceramics trial firing

(a) Sintering composition

The second trial firing of fly ash ceramsite improved the first composition. As the moisture will escape from the slaked lime during the calcination process, so

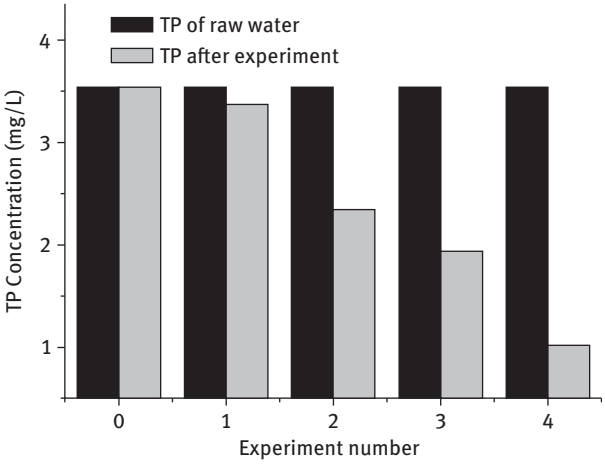

Figure 3.14: TP removal efficiency of trial firing ceramic.

it can replace the function of pore-forming aid of NH_4HCO_3 in the original composition. In order not to affect the removal of ammonia in the sewage treatment process after the sintering of ceramsite, the NH_4HCO_3 is removed in the composition. As the strength of ceramsite of the first trial firing is too low, the second preparation of ceramsite was carried out by adding sodium silicate (Na_2SiO_3) as a binder to enhance the bonding between different components of ceramsite. Experiments according to raw material ratio and granulation with a small granulator are shown in Table 3.4.

Table 3.4: The raw material quality ratio of the second trial firing.

Fly ash (%)	Bentonite (%)	Slaked lime (%)	Sodium silicate (%)
50	35	10	5
55	30	10	5
60	25	10	5
65	20	10	5
70	15	10	5

(b) Sintering conditions

According to the experimental results, the sintering conditions were finely adjusted. The preheating temperature was changed from 500 °C to 400 °C, and the preheating time was adjusted to 25 min. In view of the fact that the strength of ceramsite for the first trial firing was generally low, the second trial firing increases the sintering temperature to 1,150 °C, 1,180 °C and 1,200 °C.Sintering time is 45 min.

(c) Experimental results

Ten sets of ceramsite were sintered according to the abovementioned experimental plan. The higher the sintering temperature, the more yellowish the color of fly ash ceramsite. With the increase in sintering temperature, the strength of fly ash ceramsite also increases. It was found by observing the surface morphology that after sintering at 1,200 °C, fly ash ceramsite was not only very strong, but also its surface will be sintered to a dense enamel. At the same time, the roughness of the ceramsite and the number of stomata are obviously not as good as those of the temperature of 1,150 °C and 1,180 °C.

(d) Experimental study on removal of phosphate

The experimental results are shown in Table 3.5. The experimental results show a consistent law. At sintering temperatures of 1,150 °C and 1,180 °C, the phosphate removal rates were relatively high. However, when the sintering temperature is increased to 1,200 °C, the removal rate of phosphate from the fly ash ceramsite decreased sharply. Ceramsite in the oscillation process have varying degrees of quality loss. The batch of ceramsite basically showed that the higher the sintering temperature, the smaller the mass loss, the lower the degree of ash loss. With the increase in the content of fly ash, the resistance to hydraulic impact of ceramsite is worse.

Table 3.5: Ceramics' phosphate removal efficiency at different sintering temperatures.

Fly ash ratio (%)	Sintering temperature (°C)	Phosphate removal rate (%)	Fly ash ratio (%)	Sintering temperature (° C)	Phosphate removal rate (%)
50	1,150	98.3	65	1,150	97.2
	1,180	19.8		1,180	99.3
	1,200	1.09		1,200	4.55
55	1,150	99.4	70	1,150	91.9
	1,180	98.83		1,180	96.9
	1,200	1.11		1,200	1.65
60	1,150	97.6			
	1,180	95.7			
	1,200	2.73			

From the second batch of trial firing ceramsite situation, the lower the amount of fly ash, the higher the sintering temperature; fly ash ceramsite has better resistance ability to hydraulic impact. However, when the sintering temperature was raised to 1,200 °C, it had almost no effect on the phosphate removal, and the energy loss was also very high. This study does not consider in the case of 1,200 °C; from the energy point of view, the temperature should better be selected as 1,150 °C.

From the abovementioned experimental results, when the amount of fly ash reached 60% or more; if the sintering temperature is 1,150 °C or 1,180 °C, its resistance ability to

hydraulic impact is not strong. After 24 h oscillation, ceramsite dropped ash seriously, and even ceramsite was disintegrated. Therefore, the amount of fly ash should not be higher than 60%, it should preferably be 50%.

Based on the abovementioned considerations, the main preparation of fly ash ceramsite and the sintering conditions were preliminarily determined as follows: 50% fly ash content, sintering temperature at 1,150 °C.Products have rough surface, rich pores, resistant to a certain degree of hydraulic impact and good removal of phosphate by water treatment.

3.4.2 Experimental research on enhancing phosphorus removal by using fly ash ceramsite

(1) Morphology of fly ash ceramsite

The morphology of the fly ash ceramsite was observed by scanning electron microscopy (SEM) [Figure 3.15(a) and Figure 3.15(b)]. Ceramsite is spherical; the surface is rough with many micropores. The coverage area of the micropores is large and the distribution of the micropores is not uniform, which is favorable for the attachment and growth of the hanging film and the microorganisms. From the cross-sectional view (Figure 3.15[c]), the interior of the fly ash ceramsite is honeycomb. Its pores are well-developed, its shape is irregular and its size is different. The three-dimensional interlaced network of pores runs through them, the pore surface is uneven with a large specific surface area, which can enhance the adsorption of pollutants in the wastewater by ceramsite.

(2) Effect of fly ash ceramsite addition on adsorption

Adsorbent dosage is an important factor in the adsorption experiment, which determines the adsorption capacity. To determine the appropriate dosage of ceramsite, 0.5 g, 1.0 g and 2.0 g of fly ash ceramsite were added separately for experiments. The effect of adding amount of fly ash ceramsite on phosphate adsorption and removal was studied under different initial concentrations impact.

As shown in Figure 3.16, with the increase of fly ash ceramsite dosage, the concentration of phosphate in the solution decreases, and the removal rate of phosphate increases. Under different dosage, the adsorption rate of fly ash ceramsite on phosphate was different in the first 6 h, and the adsorption rate was 2.0 g> 1.0 g> 0.5 g. After 6 h, the adsorption rate of fly ash ceramsite to phosphate gradually slowed down and stabilized. Comparing Figure 3.16 (a) and (b), we can see that with the same addition of fly ash ceramsite, the phosphate removal rate of ceramsite increases with the phosphate concentration. When the dosage was 2.0 g and the initial concentration was 3 mg/L, the residual phosphate concentration was about 1.3 mg/L within 15 min. After 24 h, the residual phosphate concentration in the solution was about 0.1 mg/L, much lower than emission standards level A of 0.5 mg/L; when

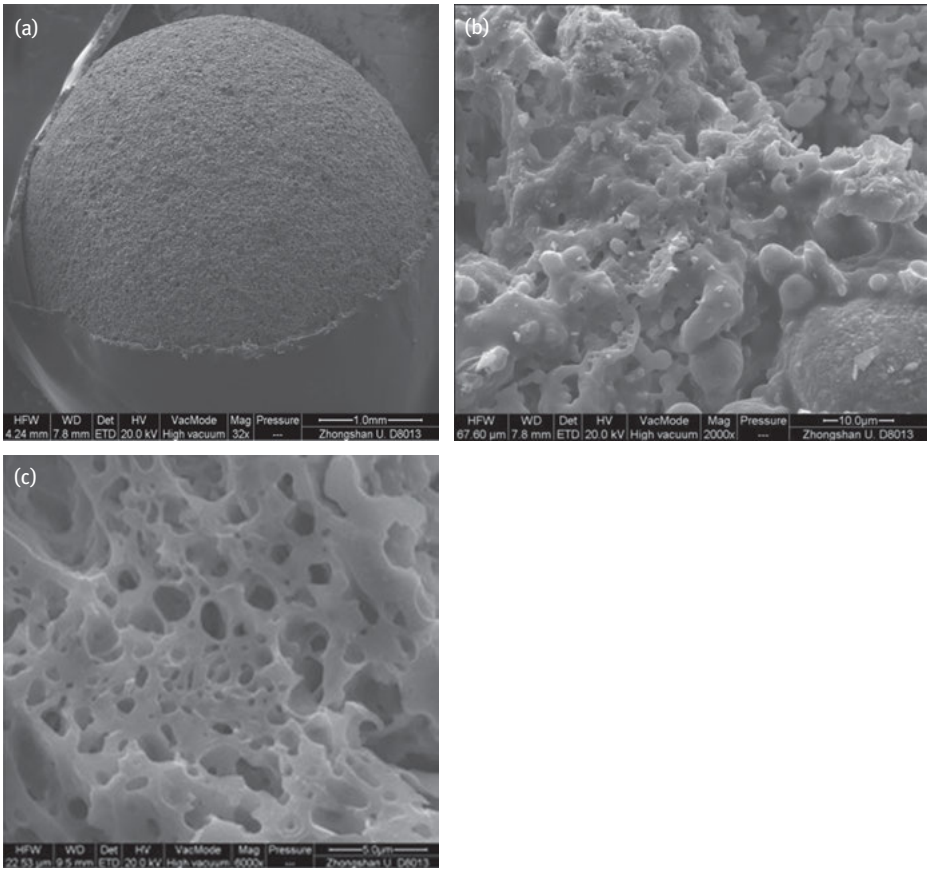

Figure 3.15: Fly ash ceramsite scanning electron micrograph ([a] 32×; [b] 6000×; [c] 3000×).

the initial concentration was 1 mg/L, the concentration of phosphate did not change obviously in 15 min, and the adsorption rate was slow.

(3) Effect of pH on adsorption

pH is one of the most important factors that affect the adsorption of metal oxides on anion. To study the effect of different initial pH on the adsorption, the relevant experiments were carried out. Figure 3.17 shows that in acidic environment, the adsorption capacity of fly ash ceramic particles to phosphate increases with the increase of the initial pH of the solution. When the initial pH was 2.0, the removal rate was only about 50.1% after 4 h reaction, and the adsorption was greatly weakened after 8 h. At 12 h, the adsorption basically reached equilibrium. When the initial pH was 4.0, the phosphate concentration in the solution rapidly dropped to 0.51 mg/L after 2 h reaction, and the removal rate reached 82.9%. After 4 h, the

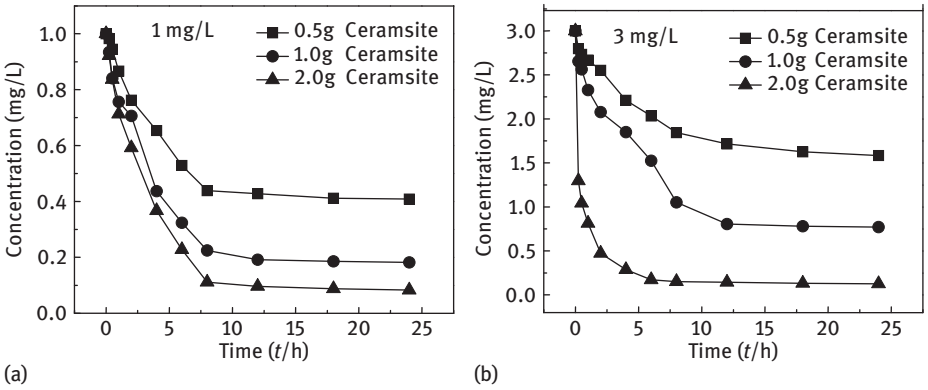

Figure 3.16: Phosphate removal at different initial concentrations.

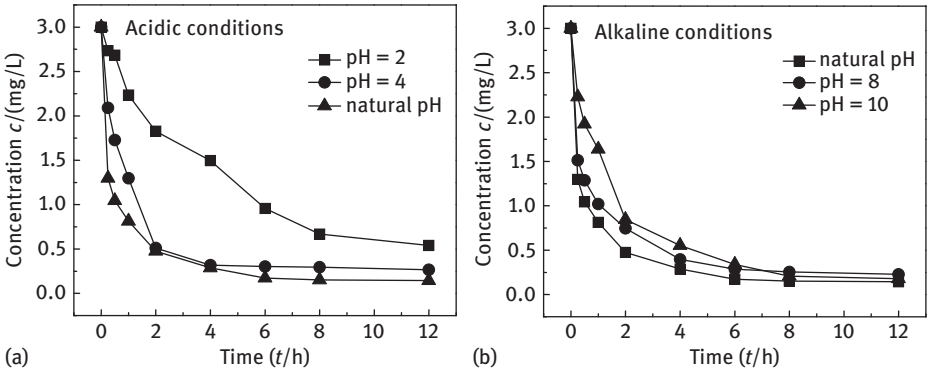

Figure 3.17: Phosphate removal by ceramsite in acid and alkaline conditions.

concentration did not change. In alkaline environment, when the initial pH was 8.0 and 10.0, the removal rate reached 93.7%. The adsorption rate of initial pH of 8.0 is faster than that of the initial pH of 10.0. However, compared with the natural pH, phosphate removal efficiency in both conditions was slightly lower.

(4) Adsorption rate of phosphate on fly ash ceramsite

In order to determine the time required for the adsorption experiment to reach the equilibrium of adsorption, experiments on the adsorption rate of phosphate rock by fly ash ceramsite were carried out. The adsorption rate reflects the amount of adsorption in the liquid phase per unit time. As shown in Figure 3.18 for the fly ash ceramic adsorption rate curve of phosphate, at the beginning of the reaction (2–6 h), the adsorption rate of phosphate was very fast and its adsorption capacity increased rapidly. With the extension of reaction time, the adsorption rate

gradually slowed down to almost equilibrium at 12 h. In addition, the adsorption amount of phosphate within 24 h shows a good linear relationship with time, and fits very well as pseudo-second-order kinetic equation $dQ_t/dt=K_2(Q_e-Q_t)^2$, The formula is as follows:

Lagrange pseudo second-order kinetic model:

$$\frac{t}{Q_t} = \frac{1}{K_2 Q_e^2} + \frac{t}{Q_e} \tag{3.2}$$

where Q_e, and Q_t are the adsorption capacities of adsorption equilibrium and adsorption time t, mg/g; t is the adsorption time,min; K_2 is the adsorption rate constant, min^{-1}.

From Figure 3.18 easy to get pseudo-second-order kinetic equation is as follows: $t/Q_t = 6.8808t + 1.6540$. At the same time, the following equilibrium adsorption capacity is obtained: 0.1453 mg/g. Phosphate adsorption capacity of 12 h is 0.1428 mg/g, and the relative balance of the amount of adsorption deviation does not exceed 2%. Therefore, the choice of 12 h reaction time can basically meet the adsorption equilibrium requirements.

(5) Effect of temperature on phosphorus adsorption

As shown in Figure 3.19, the removal rates of phosphate of fly ash ceramsite at different temperatures are in the order of 15 °C> 25 °C > 35 °C. At different temperatures, the amount of phosphate adsorbed by fly ash ceramsite basically increases with the increase in concentration, until the maximum adsorption capacity of fly ash ceramsite is reached. Fly ash ceramsite is more sensitive to temperature changes.

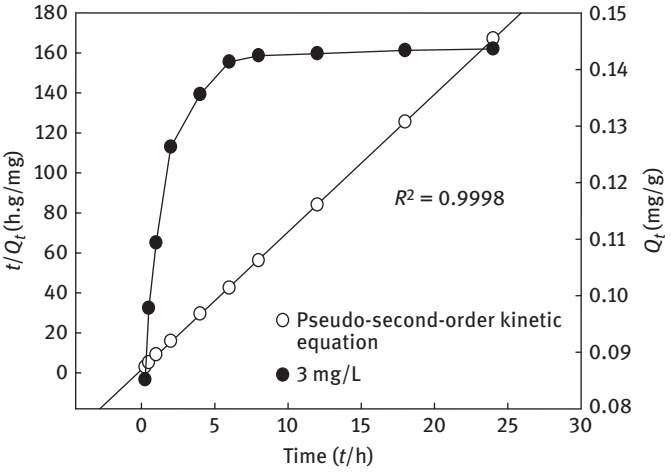

Figure 3.18: Phosphate adsorption rate curve of fly ash.

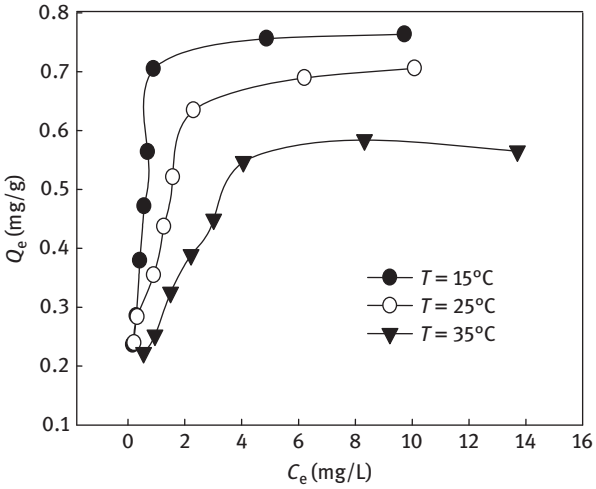

Figure 3.19: Phosphate adsorption equilibrium of fly ash ceramsite.

Although increasing the temperature can speed up its phosphate adsorption, the maximum phosphate adsorption capacity (Q_{max}) of fly ash ceramsite gradually decreases. When the temperature increased from 15 °C to 35 °C, the maximum phosphate adsorption capacity of fly ash ceramsite decreased from 0.7903 mg/g to 0.6111 mg/g. At the same time the solution began to appear at a certain degree of turbidity. In addition, the maximum adsorption saturation at the three temperatures were 0.7903 mg/g, 0.7426 mg/g and 0.6111 mg/g, respectively (see Table 3.6).

Table 3.6: Langmuir and Freundlich adsorption isotherm equations and parameters.

°C	Langmuir equation	Q_{max}/(mg/g)	r^2	Freundlich equation	1/n	r^2
15	$C_e/Q_e = 1.2652\ C_e + 0.3821$	0.7903	0.9973	$\lg Q_e = 0.2882\ \lg C_e - 0.2700$	0.2882	0.5834
25	$C_e/Q_e = 1.3466\ C_e + 0.7394$	0.7426	0.9928	$\lg Q_e = 0.2775\ \lg C_e - 0.3473$	0.2775	0.5378
35	$C_e/Q_e = 1.6361\ C_e + 1.4506$	0.6111	0.9885	$\lg Q_e = 0.2080\ \lg C_e - 0.4383$	0.2080	0.2216

Langmuir isotherm and Freundlich isotherm, these two isothermal adsorption mathematical models are commonly used to describe the adsorption isotherms in aqueous solutions. The linear expressions of the two equations are as follows:
Langmuir equation:

$$\frac{C_e}{Q_e} = \frac{C_e}{Q_{max}} + \frac{1}{Q_{max} b} \tag{3.3}$$

Freundlich equation:

$$\lg Q_e = \frac{1}{n}\lg C_e + \lg K_F \tag{3.4}$$

where Q_{max} is the maximum adsorption capacity of Langmuir monolayer (mg^{-1}); the larger the parameter indicates the greater the adsorption capacity of the adsorbent; b is the adsorption strength; Q_e is the amount of adsorption at equilibrium, mg; C_e is the concentration of adsorption at equilibrium, mg/L; K_F is the Freundlich adsorption coefficient; $1/n$ is theFreundlich adsorption index; larger K_F and n value also means adsorbent with good adsorption properties.

Figure 3.20 shows the Langmuir isotherm and Freundlich isotherm fitted at three different temperatures. Compared with the Freundlich isothermal model, the Langmuir isotherm model has a better fitting effect and can better describe the isothermal adsorption effect of fly ash ceramsite on phosphate. It shows that the phosphate adsorption in solution of fly ash ceramsite accords with the monolayer adsorption theory. The results obtained by the Langmuir model fitting well with the experimental results of adsorption experiments.

3.4.3 Optimization of preparation methods of biological fly ash ceramsite for strengthening phosphorus removal

Preliminary experiments show that the fly ash as the main raw material to prepare fly ash biological ceramic is feasible. Developed products not only have good compressive strength, rich pore distribution and the removal of phosphate in water is also very good. But the ceramsite prepared by the abovementioned method still has some obvious shortcomings: (1) ceramsite granulation with a small granulator, whose mechanical strength is low, still failed to achieve the desired ability to resist hydraulic shock load; (2) sodium silicate is a binder, whose market price is high; if the strength of ceramsite can be enhanced by physical methods, the formulation of ceramsite can be further simplified and the cost of ceramsite preparation can be saved; (3) ceramics sintering temperature is still high. Sintering temperature of 1,150 °C and sintering time of 45 min will lead to excessive energy consumption, this is not conducive to the future large-scale production and promotion of applications. The method of optimizing the sintering process needs to be studied to reduce energy consumption and cost.

The mechanical strength of fly ash ceramsite is a problem to be overcome. When the fly ash ceramic used in biologicallly aerated filter, the water flow impacts the strength. The filler must have sufficient mechanical strength to reduce wear and to control the SS concentration in the water. Increasing the mechanical strength of

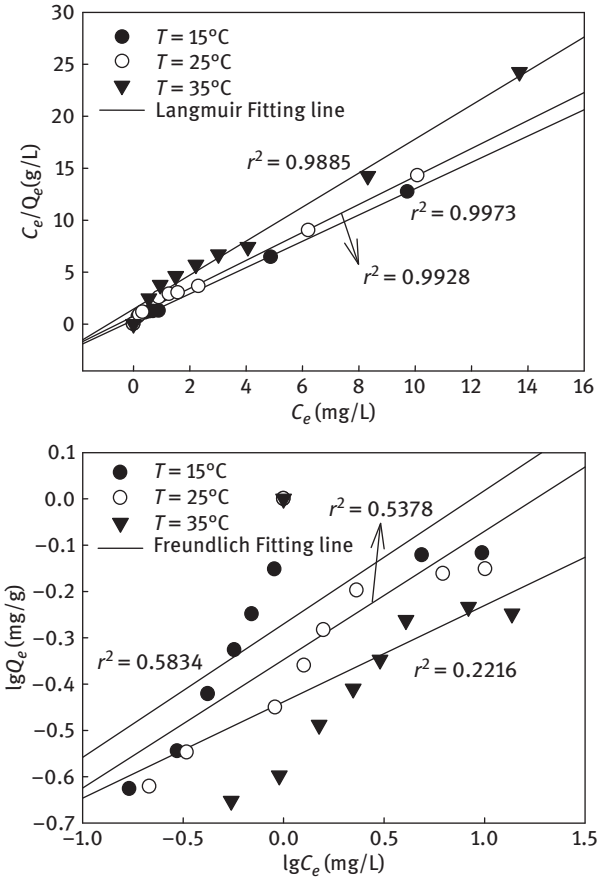

Figure 3.20: Phosphate adsorption isothermal model of fly ash ceramsite.

ceramsite can be pelletized using a disc pelletizer. Through the centrifugal effect, the disc pelletizer can make the raw materials to be bound tightly during the long granulation process.

3.4.3.1 Fly ash ceramsite firing process

According to the ratio of 50% (mass fraction) fly ash, 35% bentonite, 10% hydrated lime and 10% tap water, raw materials are put into a ball machine to make into a ball. Spherical particles are tiled onto a refractory steel pan and preheated for a certain amount of time in a muffle furnace that has reached preheat temperature. The muffle furnace program is seted so that after the end of the preheating, temperature was continuously raised to the sintering temperature and a certain sintering time at this temperature is maintained. After the sintering is finished, the coal particles are obtained after cooling.

3.4.3.2 Preparation and analysis of fly ash ceramsite

(1) Raw material composition analysis and formulation

Riley in his study of ceramic briquette found that raw materials in a certain range can get a good finished ceramsite. According to this ratio, the range of raw material composition ratio (mass fraction) for firing appropriate viscosity ceramsite is given as follows: SiO_2 is 53%–79%, Al_2O_3 is 10%–25%, the total of CaO, MgO, Na_2O, K_2O and other fluxes are 13% to 26%. Through the chemical composition analysis of fly ash and bentonite in the raw materials, the results listed in Table 3.7 are obtained.

Table 3.7: Raw material chemical composition analysis.

Raw material	SiO_2	Al_2O_3	Fe_2O_3	CaO	MgO	Na_2O	K_2O	LOI
Fly ash (%) (Quality score)	46.51	34.61	5.08	3.72	0.96	0.93	0.73	5.37
Bentonite (%)(Quality score)	58.43	11.26	1.06	1.78	1.50	—	—	—

Fe_2O_3, CaO, MgO, Na_2O, K_2O and other flux component ratio in raw material cannot reach the request of Riley component of the three-phase diagram of 13% to 26%. Therefore, the preparation of ceramic needs to add a certain amount of flux. In alkaline conditions, calcium ions with phosphate ions can generate less soluble Ca–P compounds, which makes phosphorus effectively fixed. It is possible to use the cheapest hydrated lime as a supplementary flux. Some studies are conducted to increase the strength of ceramsite to use sodium silicate and other adhesives, which will increase the cost of preparation. However, when a pelletizer is prepared by a disk pelletizer, since the components of the ceramsite are closely bonded during granulation, the strength of the ceramsite is large even without sintering, so that additional binder is not required. Through the abovementioned comprehensive consideration, the formula for preparing fly ash ceramsite with enhanced phosphorus removal was determined as follows: fly ash 50%, bentonite 35%, hydrated lime 10% and water 5%.

(2) Single-factor experiment

In order to get the best sintering process of fly ash ceramsite with good phosphorus removal function, L_9 (3^4) orthogonal method was adopted for the experimental analysis. Preheat time, sintering temperature and sintering time of the three influencing factors were selected. In order to determine the level of factors in the orthogonal experiment, a scientific orthogonal table was designed and a series of single-factor experiments were carried out.

(i) Preheat temperature and preheat time

The role of preheating is mainly the oxidation of organic matter in the raw materials and the removal of various forms of water in carbon. According to the

burning experience, the preheating temperature is set at 400 °C.The material ball was placed in a muffle furnace at 400 °C for 10 min and then taken out. At this moment most of the material ball turned white, the water was fully removed. In addition, the loss on ignition of raw materials was only 5.37%, so the organic content was very small, the amount of carbonized material after heating was also less.

In order to determine the preheat time gradient for the level design of this factor, two sets of experiments with time gradients of 5 min and 10 min were performed. The results are shown in Table 3.8.

Table 3.8: Comparison of phosphorus removal efficiency by preheating time gradient of 5 min and 10 min.

Time gradient (min)	Preheat temperature (°C)	Preheat time (min)	Sintering temperature (°C)	Sintering time (/min)	TP Removal rate(%)
5	400	25	950	30	99.57
		30	950	30	99.57
10		15	1,000	45	71.98
		25	1,000	45	40.62

When the time gradient is 5 min, it is difficult to measure the removal rate of TP under the current experimental conditions, and the obvious difference is observed at 10 min. Therefore, the preheat time is determined as 10 min, and the preheat time should be no less than 10 min.

(ii) Sintering temperature and sintering time

Under the conditions of preheating temperature of 400 °C, preheating time of 25 min, sintering time of 45 min and sintering temperature of 850 °C, 900 °C, 950 °C, 1,000 °C, 1,050 °C, 1,100 °C, 1,150 °C, respectively, sintered ceramsite was subjected to static phosphorus removal experiments. The result is shown in Figure 3.21. When the sintering temperature is 950 °C, the phosphate removal rate is the highest, close to 100%. With the further increase in the temperature, the phosphate removal rate gradually decreased, at 1,150 °C there was almost no phosphorus removal.

Observed sintered ceramsite section at different temperatures found that the surface of sintered ceramsite appears yellow at 850 °C, but the section has still some gray color. Sintered ceramsite at other temperatures exhibit a uniform yellow color both on the surface and in the cross section. This indicates that fly ash ceramsite failed to reach a sufficient sintering temperature at 850 °C. In combination with phosphorus removal efficiency, 900 °C, 950 °C and 1,000 °C were selected as the three sintering temperature levels.

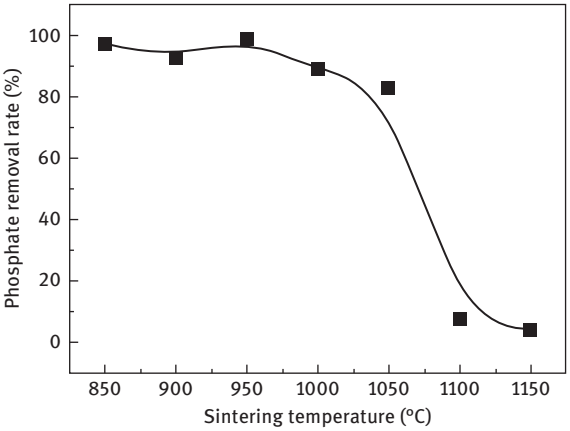

Figure 3.21: Effect of sintering temperature on phosphate removal.

In addition, under the conditions of preheating temperature of 400 °C, preheating time of 25 min and sintering temperature of 900 °C, sintering time of 10 min, 20 min, 30 min and 40 min, respectively, sintering experiments were carried out. The cross-sectional observation shows that when the sintering time was less than 30 min, the centroid of the ceramsite still was gray in color; this shows that under these conditions the sintering has not completed. Only when the sintering time is not less than 30 min, the ceramsite profile shows a uniform yellow color, so the sintering time should not be less than 30 min.

(3) Orthogonal experiment

According to the results of single factor experiments, the L_9 (3^4) orthogonal experimental scheme shown in Table 3.9 was designed. The experimental results are shown in Table 3.10.

Table 3.9: L_9 (3^4) Factor level table.

Factor	Level 1	Level 2	Level 3
A. Sintering time (min)	30	40	50
B. Sintering temperature (°C)	900	950	1,000
C. Preheat time (min)	10	20	30

Among nine groups of ceramsite, which are sintered under different working conditions, the phosphorus removal efficiencies of six groups were above 97%; only three groups were less than 90%, of which the removal efficiency was up to 99.51% and the lowest was 42.30%.

Table 3.10: L_9 (3^4) Experimental results and range analysis.

Experiment number	A	B		C	Phosphate removal rate (%)
1	1	1	1	1	99.11
2	1	2	2	2	99.51
3	1	3	3	3	80.93
4	2	1	2	3	98.93
5	2	2	3	1	98.60
6	2	3	1	2	69.65
7	3	1	3	2	97.53
8	3	2	1	3	97.53
9	3	3	2	1	42.30
K_1	279.55	295.57	266.29	240.01	—
K_2	267.19	295.64	240.74	266.69	—
K_3	237.37	192.88	277.06	277.39	—
k_1	93.18	98.52	88.76	80.00	—
k_2	89.06	98.55	80.25	88.90	—
k_3	79.12	64.29	92.35	92.46	—
Range *R*	14.06	34.25	12.11	12.46	—

Among all the factors, the largest average phosphate removal rate (reaching 98.55%) was level 2, sintering temperature at 950 °C.The lowest removal rate (64.29%) was the sintering temperature of the level 3 of 1,000 °C.The range of sintering temperature was 34.25%, which is twice than that of other factors. It can be seen that sintering temperature has the highest influence on phosphate removal efficiency. The second highest influence is the sintering time, the range is 14.06% but this is only less than 2% larger than the preheat time. Therefore, the effect of each factor on phosphate removal efficiency is B> A> C, that is, sintering temperature> sintering time> preheating time.

For the sintering time, the average phosphorus removal efficiency of the three levels was the highest at 30 min, reaching 93.18%. Preheating time of 30 min had the highest removal efficiency, up to 92.46%. For the sintering temperature, the highest removal efficiency happened at 950 °C, reaching 98.55%, but little difference with that at 900 °C. In order to further determine the optimal sintering temperature, the compressive strength of ceramsite sintered at preheating temperature of 400 °C, preheating and sintering time of 30 min, sintering temperature of 900 °C and 950 °C respectively was tested. The experimental results show that the compressive strength of ceramsite at 900 °C and 950 °C are 6.39 MPa and 6.94 MPa. According to the requirements of "Light aggregate and the test method Part 1: Light aggregate" (GB/T 17431.1-1998), it should not be lower than 6.5 MPa, so choose 950 °C as the best sintering temperature to achieve high strength ceramic standards. The best sintering process is $A_1B_2C_3$, that is, the preheating time is 30 min, the sintering temperature is 950 °C and the sintering time is 30 min.

With the prolongation of sintering time, the phosphate removal rate decreased slowly first and then rapidly, from about 30 min to 40 min, it dropped about 4%. From 40 min to 50 min, the removal rate decreased to below 80%, a decrease is nearly 10%. It can be seen that with the further increase of sintering time, the decrease of phosphorus removal efficiency will gradually increase. This is because, under high temperature conditions, the SiO_2 and Al_2O_3 components in the raw material form an enamel layer on the surface of the ceramsite and are further vitrified. Prolonging the sintering time will increase the degree of chemical reaction that forms more vitreous. This makes the ceramsite phosphate minerals in the crystal difficult to dissolve the calcium oxide, magnesium oxide and other active ingredients, resulting in decreased phosphorus removal efficiency.

Similarly, as the sintering temperature increases, the phosphorus removal efficiency also decreases. From 900 °C to 950 °C, the downward trend is not obvious, but when it rises to 1000 °C, the phosphorus removal efficiency drops sharply by more than 30%. This is presumably because when the temperature exceeds 950 °C, the structure and the mineral composition of the sintered ceramsite is greatly changed. Phosphorus removal performance is also decreased. Sintering temperature has become a key factor in the preparation of high-performance phosphorus removal fly ash ceramsite. At a high temperature of 900 °C, the carbonate component in the feedstock gradually melts and decomposes. When the sintering temperature rose to 950 °C, the carbonate component is further decomposed. The escaped gas increases the surface porosity, so that the specific surface area increases, the metal oxide dissolution channel increases, but on the other hand it also improves the compressive strength of ceramsite, so that it reaches strength standards of a high strength lightweight aggregate. However, as the temperature continues to rise, the enamel layer gradually forms and becomes denser and thicker. The degree of vitrification is higher. The composition of minerals gradually reduces, which have phosphorus removal function. A large quantity of vitreous body is produced, which led to a substantial decline in the efficiency of ceramsite phosphorus removal, the sintering temperature should not exceed 950 °C.

In addition, with the preheating time, phosphate removal rate increased slightly. Because the evaporation of water to form pores on the surface of ceramsite not only increases the specific surface area, but also conducive to the dissolution of metal oxides. Excessive prolongation of time will thicken the ceramsite shell, thus affecting the dissolution of metal oxides and phosphorus removal efficiency.

(4) Microstructure Analysis of Fly Ash Ceramsite

Ceramics, which was prepared by the best production process, were observed by SEM. Its surface and cross-sectional enlarge 1,000 times (see Figure 3.22). Ceraminite surface is rugged with a high degree of roughness; pore distribution is wide. Its aperture is mainly concentrated in the range of 1–5 μm. Rough and microporous surfaces increase the specific surface area of the ceramsite and increase the elution path for effective phosphorus removal, thereby enhanced phosphorus removal.

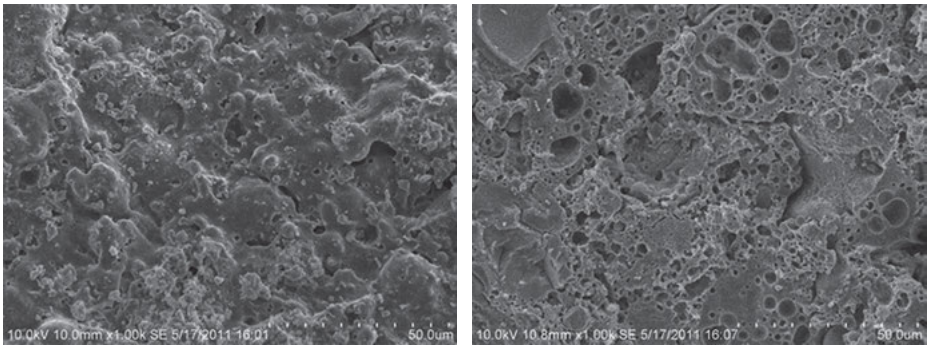

Figure 3.22: SEM image of the surface and section of ceramsite.

It can be seen from the SEM images of the section that the pore structure of the ceramsite is developed and has a honeycomb shape with different pore sizes. Large aperture can be up to 10 μm and the smaller is about 0.5 μm; its micropore is deep. It is speculated that when the ceramsite abrasion surface is under long-term hydraulic erosion conditions, the original interior will become a new ceramsite surface. At this time, the rich pore structure will make the specific surface area larger, and the dissolution path of minerals will be more and more conducive to phosphorus removal, which prolongs the service life of ceramsite.

(5) Phase analysis of Fly Ash Ceramsite

Sintered ceramsite was analyzed using a D8 ADVANCE X-ray diffractometer (XRD) from Bruker, Germany. The XRD spectrum is shown in Figure 3.23.

Fitting through the bell function to find the crystallinity of the ceramic was 29.22%, this shows that most of the ceramsite does not exist in the crystalline state. The spectrum shows that ceramsite has produced a certain amount of vitreous during the sintering process. The vitreous formation occurred with the increase in the sintering temperature, which shows that it is possible to melt the ceramsite component to produce the vitreous at a temperature of 950 °CThe presence of vitreous also shows that the mechanical strength of ceramsite after sintering is higher.

Through the retrieval and analysis of characteristic peak, it was found that the main phases of self-made ceramsite are soda-lime feldspar, quartz and mullite. Using K value method, the three mass fractions were calculated, respectively, that is, about 57.46%, 6.87% and 6.46%. The large presence of soda-lime feldspar shows that ceramsite can dissolve a greater amount of calcium ions during water treatment. The dissolution of calcium ions provide good conditions for the adsorption of phosphorus and chemical precipitation.

According to the abovementioned study, the mechanism of enhanced phosphorus removal of fly ash ceramsite is showed in Figure 3.24. Phosphorus adsorption of ceramsite is mainly through chemical reactions. Because of the presence of a large

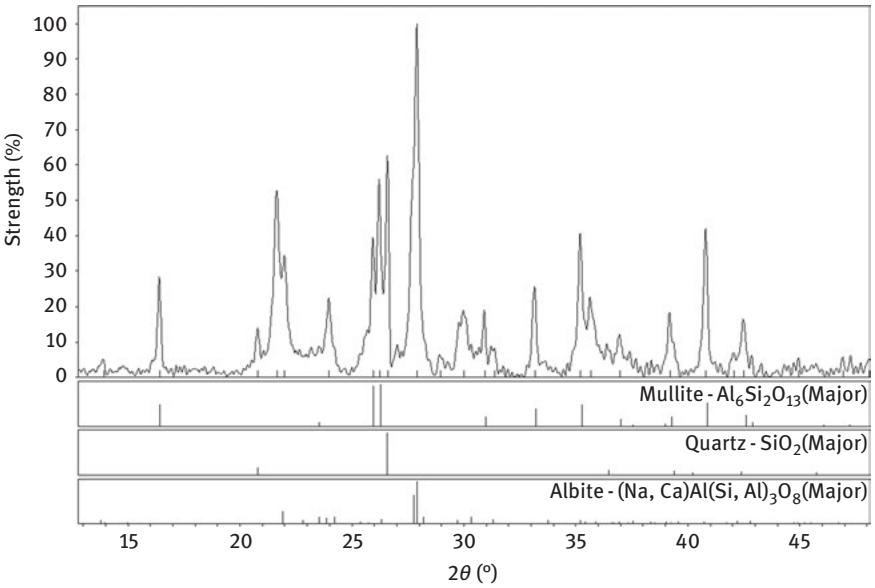

Figure 3.23: XRD spectrum of fly ash ceramsite.

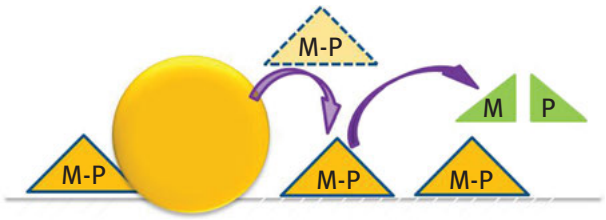

Figure 3.24: Enhanced phosphorus removal mechanism of fly ash ceramsite.

number of phosphorus adsorption sites on the ceramsite surface, calcium oxide, iron oxide, aluminum oxide and the like can be combined with the phosphate to remove the phosphate from the water. As the ceramsite surface is rough, the pore volume is rich; most of the phosphate can be adsorbed on the surface of the ceramsite, whereas a small part of the phosphate is removed with the precipitation. With the wear of ceramsite, there will be a new surface exposed to further enhance the adsorption of phosphorus on the ceramsite.

(6) Physical and chemical properties determination of fly ash ceramsite

The physical and chemical properties of ceramsite were measured (see Table 3.11), which was sintered by the best process. The bulk density is 877 kg/m^3, the density level is 900, which is slightly higher than the bulk density (700–850 kg/m^3) of the domestic

Table 3.11: Physical and chemical properties of fly ash ceramsite.

Performance	Homemade ceramsite
Bulk density (kg/m^3)	877
Apparent density (kg/m^3)	1,509
Porosity (%)	41.9
Numerical tube pressure (MPa)	6.94
Solubility of hydrochloric acid (%)	2.3

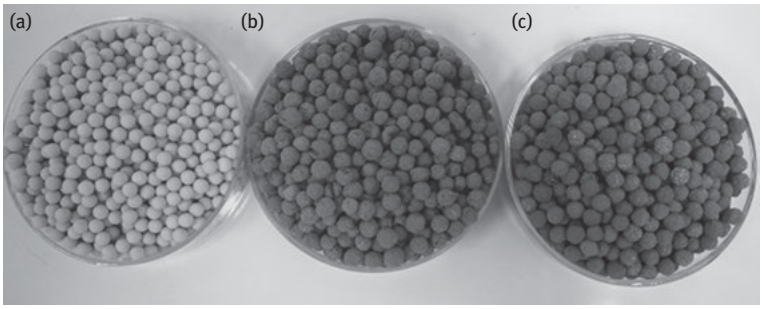

Figure 3.25: Homemade ceramsite (a), commercial ceramsite A (b) and commodity ceramsite B (c).

common fly ash ceramsite products. Disc granulator can produce regular particles with more density. After sintering, the cylinder pressure reached 6.94 MPa, exceeding the national standard of 6.5 MPa. In addition, the hydrochloric acid soluble rate and porosity were 2.3% and41.9%,repectively; it has a strong acid corrosion resistance and a certain particle gap. Different sources of ceramsite are shown in Figure 3.25.

3.4.3.3 Phosphate removal test and comparison of homemade ceramsite and commercial ceramsite

The phosphate removal experiments on homemade ceramsite, commercial ceramsite A and commercial ceramsite B were carried out. The results are shown in Table 3.12. The prepared fly ash ceramsite has higher phosphorus removal efficiency than the traditional commercial ceramsite, which is mainly because the raw materials and the firing processes of the homemade ceramsite and the traditional commercial ceramsite are quite different. This leads to large differences in mineral composition and surface structure. The fly ash ceramsite prepared by the best sintering process has a low glass content and a low degree of vitrification, and the component is easy to be eluted. Through the observation of the microstructure, it can be seen that the surface porosity is high and the specific surface area is relatively large. The traditional commodity ceramsite is generally fired at above 1,000 °C high temperature, its degree

Table 3.12: Phosphorus removal efficiency of homemade and commercial ceramsite.

Test products	Phosphorus Removal Efficiency (%)
Homemade ceramsite	99.83
Commercial ceramsite A	0.75
Commercial ceramsite B	3.25

of vitrification is high. And because of differences of composition, the phosphorus removal effect is very weak, mainly relying on the surface adsorption. In addition, the color, particle size and spherical shape of homemade ceramsite are more uniform than those of two kinds of commercial ceramsite. The particle size coefficient is lower, the product shape difference is smaller and is closer to the standard ceramsite.

Phosphate removal effect of fly ash ceramsite: Self-prepared fly ash ceramsite is a new bio-filler with the function of denitrogenation and phosphorus removal in sewage treatment. Particle size is uniform, the surface is rough and ceramic has a rich pore size and pore volume; it is very conducive to microbial hanging membrane. In addition, the ceramsite also has a good phosphorus removal effect. When the ceramsite is used as a sewage treatment engineering filler, good enhanced phosphorus removal effect can be achieved. Therefore, to determine the phosphorus removal ability of the slightly polluted wastewater, a one-factor experiment of adding dosage was conducted to provide a reference for practical engineering demonstration and application.

Dosages were 6 g/L, 10 g/L, 16 g/L and 20 g/L, respectively. Phosphorus wastewater is 100 mL with concentrations of 1 to 5 mg/L, respectively. Oscillation speed is 150 r/min, oscillation time is 24 h. The experimental results are shown in Table 3.13. As can be seen from the experimental results in the table, as the dosing amount increases, the effect of ceramsite on phosphorus removal in water will continue to increase. When the dosage of ceramsite reaches 20 g/L, even if the initial concentration of total phosphorus is 5 mg/L, it can be completely removed by ceramsite within 24 h, and the phosphorus removal efficiency can reach more than 99%. When the dosage of ceramsite is 16 g/L, the total phosphorus concentration of 5 mg/L can be reduced to 0.5 mg/L or less, the total phosphorus concentration in the treated water can reach the effluent of a municipal sewage treatment plant standard level 1-A.

3.5 Pilot experimental research on sintering of fly ash ceramsite

In order to achieve pilot-scale production of fly ash ceramsite and provide technical basis for the large-scale production of fly ash ceramsite, large-scale disc granulator and large-scale industrial kiln are used to carry out fly ash ceramsite pilot experiment. A glass processing plant is a pilot base. The production scale is 2,000 kg/d.

Table 3.13: Phosphorus removal effect on finished product of fly ash ceramsite.

Dosage (g/L)	TP initial concentration (mg/L)	TP effluent concentration (mg/L)
6	1.00	0.25
	1.50	0.46
	2.00	0.61
	3.00	1.49
	4.00	2.03
10	1.00	0.11
	1.50	0.10
	2.00	0.20
	3.00	0.24
	4.00	0.54
	5.00	1.26
16	1.00	0.15
	1.50	0.25
	2.00	0.25
	3.00	0.35
	4.00	0.28
	5.00	0.45
20	1.00	0.01
	1.50	0.01
	2.00	0.02
	3.00	0.02
	4.00	0.02
	5.00	0.03

(1) Pilot-scale experiment of fly ash ceramsite

Large disc granulator was used to prepare fly ash ceramsite. A total of ceramsite preparation is 4 m^3. Daily output is about 0.25 m^3, the daily running time is 16 h. The formulation of ceramsite preparation is determined according to laboratory experiments: the fly ash (fly ash from Jiangnan Power Plant in Nanhai District, Foshan City), 50% (mass ratio), bentonite 35%, hydrated lime 10% and the remaining component is water.

Disc granulator is shown in Figure 3.26, prepared ceramsite without sintering is shown in Figure 3.27.

(2) Pilot-scale experiment of fly ash ceramsite sintering

Pilot experiment of fly ash ceramsite sintering was carried out according to the following conditions: the kiln was warmed to 400 °C and maintained at this temperature. Ceramsite was placed in a furnace at the temperature of 400 °C for about

Figure 3.26: Large disc granulator.

Figure 3.27: Prepared ceramsite without sintering.

Figure 3.28: Fly ash ceramsite products of pilot sintering experiment.

30 min. The kiln was warmed to 950 °C and held at this temperature, and ceramisite sintering was performed. After 30 min, it naturally cools down. Temperature pyramid is used to control temperature.

The finished product of ceramsite is uniform, the color is offwhite, similar to the ceramsite prepared in a small experiment. Its physical and chemical properties of the measured results are shown in Table 3.14.

Table 3.14: Physical and chemical properties of fly ash ceramsite.

Performance	Homemade ceramsite
Bulk density (kg/m^3)	872
Apparent density (kg/m^3)	1495
Porosity(/%)	42.3
Numerical tube pressure(MPa)	6.87
Solubility of hydrochloric acid(/%)	2.2

Phosphorus removal experiments were performed with this ceramsite. Ceramsite dosage was 2 g. Phosphate concentration in simulated wastewater was 10 mg/L. The volume of the solution was 50 mL, the shaking speed was 150 r/min and the shaking time was 8 h; the removal efficiency of phosphorus can reach above 99% on average (average after five parallel experiments). This shows that the production of ceramsite fully meets its performance quality requirements.

3.6 Initial cost accounting of ceramsite phosphorus removal

(1) Daily production costs

The initial accounting for the cost of preparing fly ash ceramsite was carried out on the basis of small and pilot experimental data. Only the production cost of ceramsite is accounted for, whereas the investment in fixed assets and depreciation are not counted. It mainly includes the following aspects: (1) direct material costs, (2) direct wages, (3) fuel power and (4) manufacturing costs.

Take a fly ash ceramsite factory with an annual output of 10,000 m^3 as an example. Calculated with a bulk density of 0.85 t/m^3, it is converted into about 85,500 t of raw materials. According to the cost of raw materials listed in Table 3.15 the cost is initially estimated.

Power consumption: The total power of the equipment is 40 KW and it runs for 8 hours per day. The daily power consumption is 320 kWh, and the annual power consumption is 300 days. The industrial electricity cost is 0.9 yuan/kWh, and the electricity consumption is 86,400 yuan/a.

Labor cost: It is calculated according to 20 persons, each person produces 500 m^3 ceramsite annually, and the annual working time is 300 days. Wages of each worker is 4,000 Yuan/month. The annual labor cost is 800,000 Yuan.

Table 3.15: Initial cost calculation of raw material of fly ash ceramsite.

No.	Raw material	Unit Price/ (Yuan/t)	The required amount/10,000 t	Total price/ 10,000 Yuan	Remarks
1	Fly ash	150	0.425	63.75	Transport is calculated within the unit price
2	Sodium bentonite	600	0.2975	178.50	—
3	Hydrated lime	350	0.085	29.75	—
4	Tap water	2.53	0.0425	0.11	—
5	Summation	—	0.85	272.11	—

Other manufacturing costs: According to the current conditions, other manufacturing costs and taxes are difficult to be quantified. However, as a general rule of thumb, 10% of the abovementioned three direct costs can be estimated at 360,000 Yuan.

Total production costs: 3,967,500 Yuan (estimate). The average production cost per cubic ceramsite is 396.75 Yuan/t.

(2) Transportation cost

China is vast in size and there may be some differences in transportation costs in different regions. And transportation costs will fluctuate with the cost of oil. Therefore, this report only makes simple calculations. According to the current transport prices of ordinary logistics companies, transport mileage is calculated by 1,000 km on average. The authorized load of the vehicle is 30 t (about 35.3 m^3), so its transportation cost is about 350 Yuan/t.

(3) Total cost

The total cost of ceramsite is the sum of production cost and transportation cost. Therefore, according to this estimate, the total cost of ceramic is about 750 Yuan/t (including transport prices).

(4) Operating costs of engineering application

As a functional material for wastewater treatment, when it is used as a biofilm carrier filler, it can be used for a long time without serious wear and tear and does not need to be replaced. When it is used as a phosphorus adsorption material, especially when the effluent concentration of TP has been specially requested due to the phosphorus adsorption capacity of ceramsite and the adsorption reaches saturation, the ceramsite needs to be replaced and regenerated before reuse, so there will be a corresponding cost.

According to the difference of water quality, the amount of ceramsite and the use of time will be different. In general, when it is used to enhance phosphorus removal, the adsorption effect on the low-concentration phosphorous-containing wastewater

can last long. From the current pilot test situation, the replacement frequency of ceramsite can be more than 5 years, that is, the operating cost per ton of filler is about 150 yuan per year.

3.7 Cu (II) removal behavior and adsorption isotherm simulation of fly ash ceramsite

The foregoing study found that ceramsite can effectively strengthen the removal of phosphate in wastewater. According to the phosphate removal mechanism of ceramsite, the adsorption of heavy metal ions may exist. Therefore, to expand the pollutant removal characteristics of ceramsite, the research group carried out the preliminary research on the heavy metals adsorption effect of fly ash ceramsite, and selected copper as the target pollutant in the early stage of the research.

Copper is one of the most common heavy metals. The common control technologies of heavy metal pollution in wastewater mainly include ion exchange, chemical precipitation, adsorption and membrane filtration. The effect of ion exchange and membrane filtration is easily affected by wastewater quality, and the treatment cost is high. Chemical precipitation and traditional dispersed adsorbents, such as activated carbon, will produce more chemical sludge and the Cu (II) removal efficiency is low. In recent years, Cu (II) adsorption experiments of mineral adsorbents, such as sepiolite, modified bentonite, modified montmorillonite and so on, have been carried out, and has achieved good results. Cu (II) is adsorbed by sepiolite (XU Yingming et al., 2009), the saturated adsorption capacity is 22.10 mg/g. CHENG Jiemin et al. (2012) developed an organically modified bentonite adsorption of Cu (II), the adsorption capacity is 6.25 mg/g. ZHOU Jianbing et al. (2010) adsorped Cu (II) with sodium dodecyl sulfate modified montmorillonite, the adsorption effect at lower concentrations is up to 99%. Mineral adsorbents have received more attention in recent years, and the existing researches provide useful new ideas for the breakthrough in this field. However, this type of adsorbent is mostly dispersed small particles, the particle size of the powder is too small. Because of the restrictions of settlement performance, solid–liquid separation, there is still some distance to the actual application. Currently, they are still only in the laboratory research stage. From the practical point of view, ceramic should have a better application prospects.

3.7.1 Effect of amount of fly ash ceramics on Cu (II) adsorption

The amount of ceramsite for the Cu (II) adsorption experiment was 1 g, 2 g and 3 g, respectively. The adsorption experiment was performed in a 150 mL Erlenmeyer flask. The concentration of Cu (II) is 100 mg/L. As can be seen in Figure 3.29 (a), the different amounts of Cu (II) greatly affect the efficiency of adsorption. The adsorption

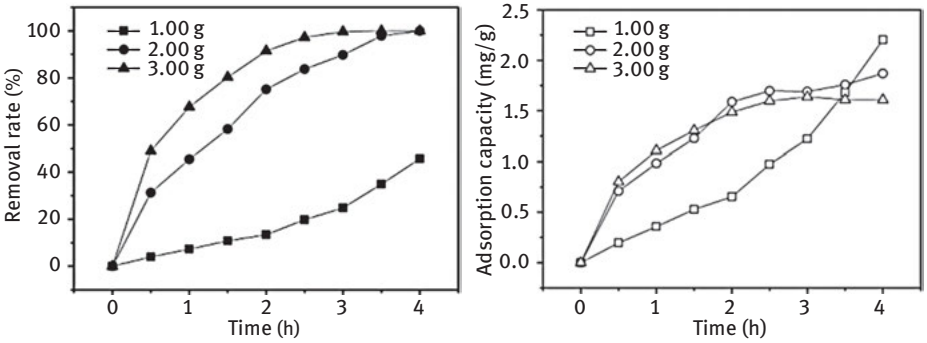

Figure 3.29: Adsorption effect of ceramsite on Cu in different amount of application. (25 °C, 50 mL,, pH=4.5, Cu 100 mg/L, 150 r/min)

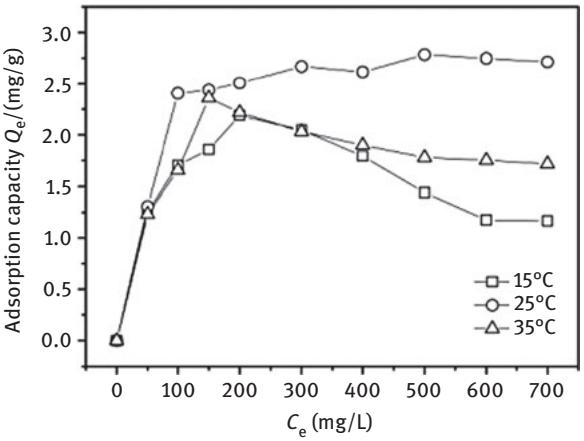

Figure 3.30: Cu adsorption isotherm of ceramsite at 15 °C, 25 °C and 35 °C. (50 mL, pH=4.5, 2 g)

rate of Cu (II) was only 45.7% within 4 h at the Cu (II) dosage of 1 g, while that could reach 100 %.at the dosage of 2 g and 3 g. Figure 3.29 (b) is the amount of Cu (II) adsorbed by the unit mass of ceramsite at different amounts of ceramsite, which increases with the adsorption time until Cu (II) is adsorbed completely. From the experimental results it can be initially estimated that when the adsorption time is 4 h, the amount of ceramic should be 2 g.

3.7.2 Effect of temperature on Cu adsorption

Temperature is usually one of the most important factors that affect the adsorption effect. In this study, isothermal adsorption experiments were carried out at 15 °C, 25 °C

and 35 °C. The adsorption time was 4 h, the amount of ceramsite was 2 g, the concentration of Cu (II) was 50 mg/L, 100 mg/L, 150 mg/L, 200 mg/L, 300 mg/L, 400 mg/L, 500 mg/L, 600 mg/L and 700 mg/L. Figure 3.31 shows the isotherm results. Within 4 h, Cu (II) had the best adsorption effect at 25 °C, and its maximum adsorption capacity reached

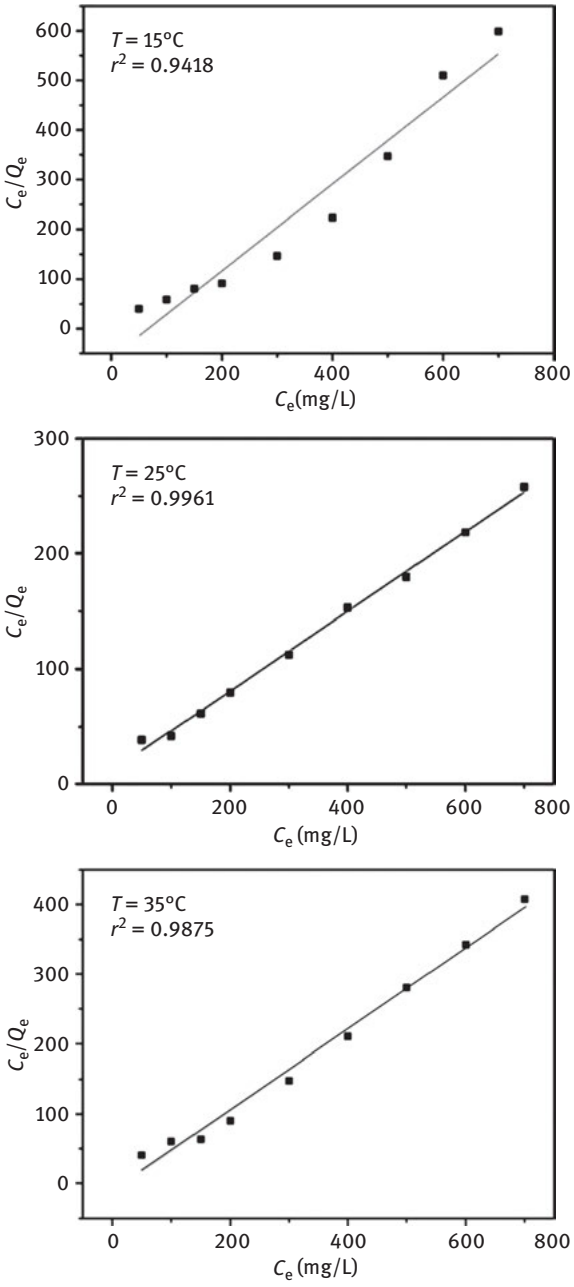

Figure 3.31: Fitting results of Langmuir isotherm model.

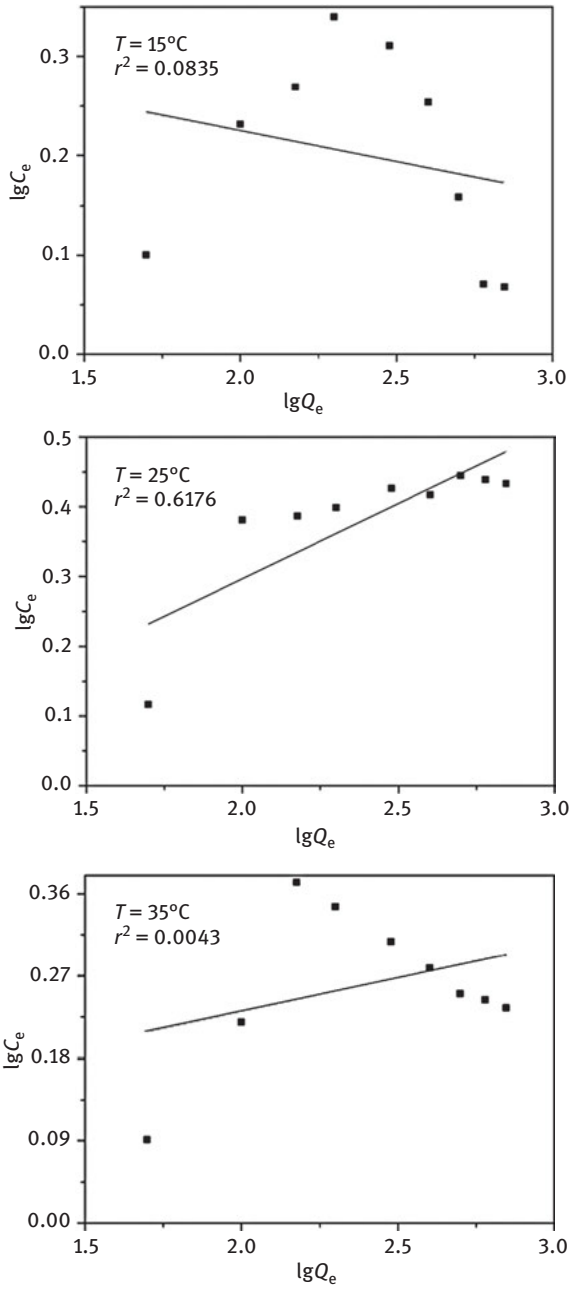

Figure 3.32: Fitting results of Freundlich isotherm model.

2.78 mg/g. The maximum adsorption capacities at 15 °C and 35 °C were 2.19 mg/g and 2.36 mg/g, respectively. From the experimental results, the Cu (II) adsorption effect of ceramsite according to the temperature is about 25 °C > 35 °C > 15 °C.

The abovementioned three temperature adsorption isotherms were fitted. The Langmuir isotherm model and the Freundlich isotherm model are expressed as follows:

$$\begin{aligned} C_e/Q_e &= 0.8739C_e - 58.4579(15°C) \\ C_e/Q_e &= 0.3454C_e + 11.8281(25°C) \\ C_e/Q_e &= 0.5820C_e - 11.4107(35°C) \end{aligned} \tag{3.5}$$

$$\mathrm{lgQ_e} = \mathrm{lgK} + \frac{1}{\mathrm{n}}\mathrm{lgC_e} \tag{3.6}$$

where $Q_{\max}$ is the maximum adsorption capacity, mg/g.

The fitting results of the Langmuir isotherm model are shown in Figure 3.31. C_e and Q_e at three temperatures are basically linear relationship. The r^2 of the Langmuir isothermal adsorption model at 25 °C was 0.9961, whereas it was 0.9418 and 0.9875 at 15 °C and 35 °C, respectively. Relatively speaking, the Langmuir isotherm model fitting at 25 °C was particularly suitable. The fitting equations for the three temperatures are as follows:

$$C_e/Q_e = 0.8739C_e - 58.4579(15°\,C) \tag{3.7}$$

$$C_e/Q_e = 0.3454C_e + 11.828\,1(25°C) \tag{3.8}$$

$$C_e/Q_e = 0.5820C_e - 11.4107(35°) \tag{3.9}$$

When fitted by the Freundlich isotherm model, r^2 was −0.0835, 0.6176 and −0.0043, respectively. The correlations are all small, indicating that the Freundlich isotherm model is not suitable in this case.

3.7.3 Comparison of oscillation and resting conditions

In general, the oscillation accelerates the mass transfer of the adsorbate in the adsorbent, which facilitates the adsorption. In this study, the Cu (II) adsorption of ceramsite by oscillation with 150 r/min and by static state was compared, as shown in Figure 3.33. Under the same conditions, the Cu (II) adsorption efficiency of ceramsite by static state was obviously lower than that at 150 r/min. After 4 h, the Cu adsorption rate was about 30%, whereas Cu (II) has been adsorbed completely during oscillation. When standing, the unit Cu (II) adsorption capacity Qe was less than 0.8 mg/g, much lower than the Cu (II) maximum adsorption capacity (2.78 mg/g).

3.7.4 Experimental study on Cu (II) removal by ceramsite column

Figure 3.34 shows the Cu (II) removal effect of ceramsite after five consecutive uses. In the first four adsorption experiments of Cu (II) removal, the adsorption column had

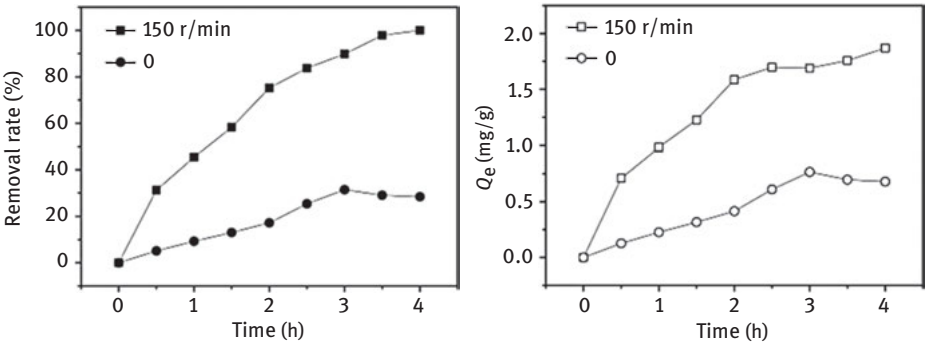

Figure 3.33: Comparison of Cu (II) adsorption effect between oscillation and standing.

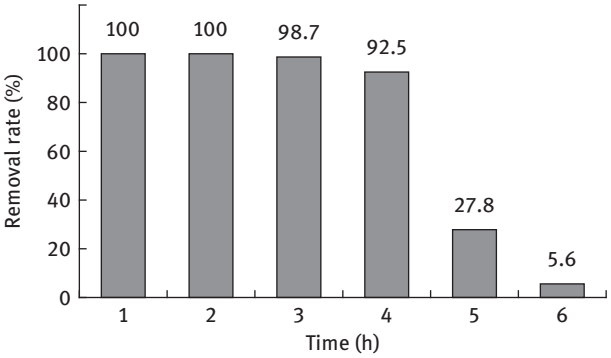

Figure 3.34: Repeated Cu (II) adsorption removal of ceramsite column.

a good removal effect on 250 mL Cu (II) solution with a concentration of 100 mg/L. Cu (II) removal rate can reach more than 90%. The first two removal rates were 100%, but the 5th adsorption rate was reduced to 27.8%, whereas the sixth adsorption rate was only 5.6%.

3.7.5 Adsorption effect comparison with conventional water treatment ceramsite

The comparison of Cu (II) adsorption between two conventional water treatment ceramsite and fly ash ceramsite is shown in Figure 3.35. The conventional water treatment ceramsite has no significant effect on Cu (II) adsorption; at 4 h it was only 14.6% and 6.3%, respectively. The adsorption capacity per unit mass was 0.35 mg/g and 0.15 mg/g, respectively.

The high Cu (II) adsorption rate of adsorbents such as fly ash are obtained when the initial pH of the solution is high. At this time, Cu (II) has an obvious coprecipitation

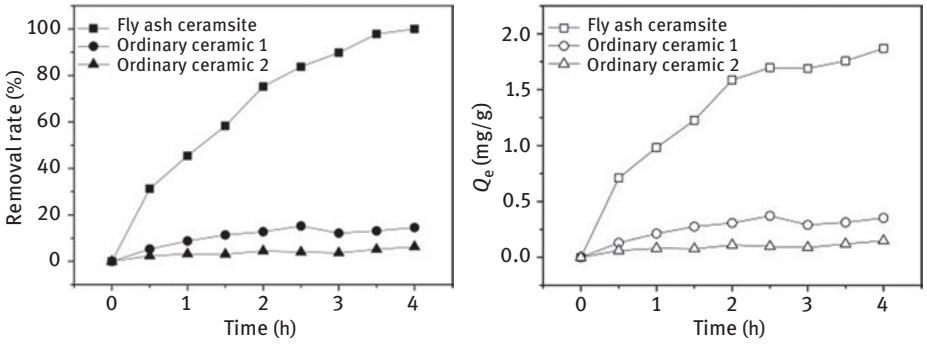

Figure 3.35: Cu removal performance comparison between fly ash ceramsite and conventional ceramsite.

effect with the OH^-existing in solution. In this process, the Cu (II) adsorption did not really reflect. The modified fly ash can be beneficial to the Cu (II) adsorption. For example, CAO Shuqin et al. (2012) used $Fe(NO_3)_3$ and $Al(NO_3)_3$ as the main raw material to prepare fly ash/hydrated metal oxide composite adsorbent. When the amount of adsorbent is 20 g/L, the pH of the solution is 8, the adsorption time is 90 min and the concentration of Cu (II) is 40 mg/L; the removal rate can reach 97.8%. LU Zhijiang et al. (2008) modified fly ash with high concentrations of HCl and H_2SO_4. The removal rate of Cu (II) reached 97.49% when the initial concentration of Cu (II) was 40 mg/L, pH=7, stirring for 3 h, and the dosage of fly ash was 12 g/L, respectively. However, at present, the study of Cu (II) removal of fly ash ceramsite is still lacking. This fly ash ceramsite can still get about 100% Cu (II) removal rate when the initial pH of the solution is 3.5, whereas that of the conventional ceramsite is only 15% or less. The function of this fly ash ceramsite has transformed from a single biofilm carrier to multifunction, and it has the function of phosphate and Cu (II) removal. The hardness and wear resistance is strong, the wear rate is low and the adsorption process basically completed on the ceramsite surface. At 25 °C, the maximum unit adsorption capacity of Cu was 2.78 mg/g. However, when the ceramsite layer is worn away, its new surface can further adsorb Cu (II), thereby further increasing its Cu (II)adsorption capacity.

Similar to other adsorption processes, the large amount of adsorbent, high oscillation speed and suitable temperature all contribute to the Cu (II) adsorption of ceramsite. It can be seen from Figure 3.30 that the Cu (II) adsorption of ceramsite at 25 °C is better than that at 15 °C and 30 °C.The maximum adsorption capacity and the Cu(II) adsorption capacity of at 4 h were optimal at 25 °C.It is generally believed that when the adsorption temperature is too low it will slow the rate of adsorption, whereas the temperature is too high; although the adsorption rate can be accelerated, at the same time equilibrium adsorption capacity will reduce. For the adsorption process, speeding up the mass transfer between solid and liquid phase is an important means to improve the adsorption efficiency. The experimental results also show

that when the oscillation speed was 150 r/min, the adsorption rate and adsorption capacity were significantly higher than those when standing. In practical application, Cu (II) in solution can be accelerated to transmit to ceramsite by increasing influent flow rate, increasing aeration intensity. Similar to most heavy metals, Cu (II) can form Cu (II) precipitate at high pH. It is of little significance to study the influence of pH on its removal process. Therefore, it is not covered in this book.

The Cu (II) adsorption process of ceramsite can be roughly fitted by the Langmuir adsorption isotherm model with correlations r^2 of 0.9418, 0.9961 and 0.9875 (at 15 °C, 25 °C and 35 °C). Taking the case of 25 °C as an example, the calculated Q_{max} is 2.79 mg/g, and the measured Q_{max} was 2.78 mg/g, which were very close. However, the Freundlich isotherm model fitting error was larger. The simulation results of adsorption isotherms indicate that the Cu adsorption of ceramsite may be monolayer adsorption, and the two effects of chemical and physical adsorption may coexist. From the chemical composition point of view, there were Na_2O, CaO, MgO and other alkaline metal oxide components in the ceramsite, which can be beneficial to the Cu chemical adsorption of ceramsite. From its physical structure point of view, there are a large number of shallow and deep micropores on the ceramsite surface, a large specific surface area and plentiful pore volume, all of which are conducive to Cu (II) adsorption.

3.8 Prospect analysis of application of fly ash ceramsite

(1) Raw materials availability and preparation process analysis

The main raw material of fly ash ceramsite is fly ash, bentonite, hydrated lime and water; they are very easy to obtain. Fly ash is a by-product of coal-fired power plants, the price is relatively low, and long-term stable supply can basically be guaranteed. Bentonite, hydrated lime and other materials can be obtained with lower prices from the market. The main equipment for the preparation of fly ash ceramsite is granulator. It is a common equipment in the ceramsite preparation; it is easy to operate, the training is relatively simple and there is no technical obstacle. The prepared ceramsite can be sintered in two ways, including: (1) high temperature electric furnace sintering and (2) conventional gas furnace sintering. In the laboratory, it can be sintered by high temperature electric furnace. Because of the generally large amount of sintering, the conventional gas furnace sintering method is used for industrial purposes, which can effectively save energy and increase the production capacity of ceramsite. As the raw materials of ceramsite is easy to obtain and the preparation process is relatively simple, it is easy to realize mass production in a short time in the actual production process.

(2) Application analysis of finished products of ceramsite

At present, most of the phosphorus removal in China's conventional wastewater treatment plant is not satisfactory. The biochemical effect is poor and dosing, and

other ways are needful, thereby increasing the cost of running and sludge treatment. Most of the ecological treatment projects for controlling the concentration of phosphorus in the lake and river do not even have the conditions of chemical phosphorus removal. For this reason, it is important to develop wastewater treatment fillers with enhanced phosphorus removal capabilities. This ceramsite can be used as wastewater treatment filter of reaction wall, artificial wetland and biological aerated filter. Ceramsite is a kind of structured filler, ceramsite particle diameter is 4–6 mm, they are nearly regular ball, the mechanical strength after sintering is large, the ceramsite loss in working process is small, so it is a ideal water treatment function filler. This ceramsite also has good characteristics of phosphorus removal from wastewater. At present, there are only a few types of ceramsite that have the function of strengthening phosphorus removal, and there are no relevant reports in the practical application both at home and abroad. Therefore, this ceramsite possesses good marketing space. In addition, in the follow-up study, this ceramsite shows good adsorption capacity for heavy metals such as Cu, Ni, Hg and so on. Therefore, this ceramsite have multifunctionalization and can be used for large-scale engineering applications.

(3) Replacement, maintenance and regeneration prospects analysis of ceramsite material

Phosphorus adsorption capacity of ceramsite is large. In addition, because of the characteristics of ceramic, in the water treatment process, no replacement within 5 years can be guaranteed. When used as a filler, the ceramsite is similar to the filler of conventional constructed wetland and BAF, such as gravel, volcanic rock and the like. The maintenance management is quite easy. And there are almost none of knot, clogging phenomenon, which are ubiquitous by general shale ceramsite, volcanic rocks and other fillers. In the existing pilot, demonstration projects and other practical applications, the phenomenon of clogging was not obvious during the ceramsite long-term use. Ceramsite replacement can be completed in a relatively short period of time. Although the adsorbed phosphorus can be desorbed by acid, the ceramsite is not generally recommended to be regenerated and reused because the cost of the adsorbate-desorption-recycle is relatively high and the ceramsite is relatively inexpensive. So it should be replaced directly with new ceramsite.

(4) Prospect Analysis of Material Reuse and Resource Disposal

Ceramsites that have been replaced from wastewater treatment projects can be used as soil amendments or flower media (see Chapter 8 for details). Environmental tests on ceramsite show that this method of application is safe, and nutrients such as nitrogen and phosphorus absorbed by the ceramsite can be slowly released during plant growth, so they can effectively promote plant growth. Because of the long replacement period of ceramsite, ceramsite wastes can be recycled.

References

CAI Changfeng, XU Jianping, ZHE Qian et al.: Development and Application of Fly Ash/Sludge Sinter Ceramsit, 2007, 29(1): 26–29.

CAO Shuqin, HOU Xing, LIU Jing et al.: Study on Removal of Cu^{2+} in Industrial Wastewater by Fly Ash/Hydrated Metal Oxides, Non-metallic mineral, 2012, 35(5): 66–68.

CHENG Jiemin, ZHAO Cong, XIE Minli: Adsorption – Desorption of Cu^{2+} and Zn^{2+} by Two Kinds of Organobentonites, Ion Exchange and Adsorption, 2012, 28(2): 126–134.

LIU Baohe, ZHANG Linsheng, MENG Guanhua et al.: Preparation of TBX Porous Ceramsite Filter and Experimental Study on Adsorption and Phosphorus Removal from Wastewater, Journal of Peking University: Natural Science Edition, 2010, 46(3): 389–394.

LU Zhijiang, LIU Yunguo, FAN Ting et al.: Experimental Study on Adsorption of Cd^{2+}, Pb^{2+} and Cu^{2+} in Wastewater by Modified Fly Ash, Non-metallic mineral, 2008, 31(3): 57–59.

PENG Weihua, GUI Herong, XIANG Xian et al.: Non burning fly ash ceramsite as BAF filler to treat municipal wastewater, Environmental Science and Technology, 2011, 34(8): 156–159.

SANG Junqiang, ZHANG Xihui, ZHANG Sheng et al.: Raw water biological pretreatment of lightweight filter and ceramic filter efficiency comparison, Environmental Science, 2004, 25(3): 40–43.

TONG Jingjing, JI Guodong, ZHOU You et al.: Study on Treatment of Rural Domestic Sewage by Efficient Functional Ceramsite Biofilter, Journal of Agro – Environment Science, 2009, 28(9): 1924–1931.

WANG Jian, JIN Minglin, WEI Lin et al.: Preparation of a new type of water treatment filter with fly ash, Chemical environmental protection, 2004, 23(6): 352–355.

WANG Ping, LI Guochang: Orthogonal Experiment on Preparation of Biofilter from Fly Ash, China Non-metallic Minerals Industry Guide, 2008(6): 32–33.

XIANG Huiqiang, LI Dong, GONG Youkui et al.: Application of Fly Ash Ceramsite in Wastewater Treatment, Journal of Liaoning Technical University, 2006, 25(12): 291–292.

XU Yingming, LIANG Xuefeng, SUN Guohong et al.: Chemical Properties of Sepiolite and Its Adsorption Mechanism on Heavy Metal Pb^{2+} Cd^{2+} Cu^{2+}, Journal of Agro – Environment Science, 2009, 28(10): 2057–2063.

YUAN Xi, CHEN Yaoliang, CHEN Jian: Experimental study on the treatment of low concentration household wastewater by pellette and ceramic filler oxygenic biological filter, Water Supply and Sewerage, 2007, 33(5): 142–145.

YUE Min, HU Jiucheng, ZHAO Haixia: Study on Characteristics of Domestic Lightweight Ceramsite Used in Anaerobic Filter, Environmental Pollution and Prevention, 2004, 26(1): 22–24.

ZHANG Wenyi, ZHAI Jianping, ZHENG Jun et al.: Biological Aerated Filter Wastewater Treatment Process and Design, Environmental Engineering, 2006, 24(1): 9–13.

ZHAO Y Q, YUE Q Y, LI R B, et al.: Research on sludge-fly ash ceramsite particles(SFCP)for synthetic and municipal wastewater treatment in biological aerated filter(BAF). Bioresource technology, 2009, 100(21): 4955–4962.

ZHOU Jianbing, WU Pingxiao, ZHU Nengwu et al.: Adsorption of Cu^{2+} and Cd^{2+} by Sodium Dodecyl Sulfate (SDS) Modified Montmorillonite, Journal of Environmental Science, 2010,30(1): 88–96.

4 Preparation and application of montmorillonite-loaded nano-iron material

4.1 Overview of montmorillonite

4.1.1 Montmorillonite

(1) Origin and application of montmorillonite

Montmorillonite is the main mineral component of bentonite; it is also known as microcrystalline kaolin. Its content in bentonite is generally 20% to 90%. Montmorillonite is widely distributed in natural clay minerals and has a strong water absorbing capacity. It is easy to expand after water absorption. Currently, bentonite can be widely used as binder, suspending agent, thickener, flocculant, stabilizer, purifying decolorizing agent and catalyst carrier in metallurgy, drilling, pharmaceutical, petrochemical, light industry, agriculture, forestry, animal husbandry, construction and other industries.

(2) Structure of montmorillonite

The theoretical chemical formula of montmorillonite is $Al_2O_3 \cdot 4SiO_2 \cdot nH_2O$ (n is usually more than 2). The crystal structure of montmorillonite is $Al_4(Si_8O_{20})(OH)_4 \cdot nH_2O$. The theoretical chemical composition is as follows: 66.7% of SiO_2, 25.3 % of Al_2O_3 and 5% of H_2O. Montmorillonite is a clay mineral, which is a layered silicate. Its basic structural units are Si–O tetrahedrons and Al–(O, OH) octahedrons. In the silicon tetrahedron, the oxygen atoms are located at the four corners of the equilateral tetrahedron and the silicon atom is located in the center. The silicon atoms coordinate with the oxygen atoms. Each tetrahedron and the three vertices are connected to each other on the same plane to form a hexagonal symmetrical three-dimensional grid, whereas the grid in the two-dimensional space can extend infinitely, forming tetrahedral wafers. The unit cell constitutes an upper and a lower layer of Si–O tetrahedron, and a middle layer of Al–O (OH) or Mg–O (OH) octahedrons. The cell layers are bonded to each other by electrostatic attraction or Van der Waals bonding, and the bottom of the tetrahedron is a ditrigonal cavity structure. In Al–(O, OH) octahedrons, Al atoms (or Mg atoms) coordinate to hydroxyls or six oxygen atoms. Hydroxyls or oxygen atoms around the Al or Mg atoms are located on the octahedral six corners and arranged in two parallel planes. Al or Mg is in the middle of both planes, forming an Al–(O, OH) octahedral wafer.

Montmorillonite has an alternant structure with aluminum–oxygen octahedrons and silicon–oxygen tetrahedrons. The octahedron layer lies between two tetrahedron layers. This structure is called 2:1 layered structure. The structure is shown in Figure 4.1.

https://doi.org/10.1515/9783110544381-004

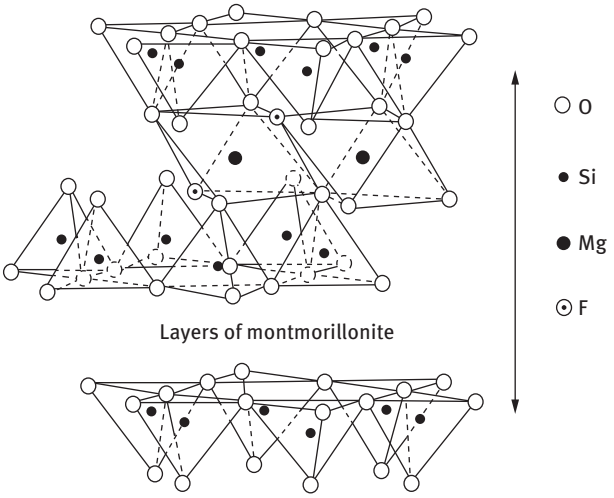

Figure 4.1: Layered structure of montmorillonite.

In the structural diagram of montmorillonite, Si (IV) in the tetrahedron is partially replaced by Al (III) and the Si (IV) in the octahedron is replaced by Mg(II), Fe(II), Zn(II) and Li(I). The replacement of high-valent cations with low-valent cations can result in an excessive negative charge, or a lack of positive charge. This excessive negative charge is compensated by cations on the surface of the layer or between the layers.

(3) Properties of montmorillonite

The density of montmorillonite is 2–3 g/cm^3. The melting point is 1,330–1,430 °C. The crystal grain size is 0.02–0.2 μm. The color of montmorillonite is usually white. Montmorillonite has the properties of ion exchangeability, swelling, dispersibility, suspendability, stability, adsorption ability, hydrophilicity and non-toxicity.

(i) Hydrophilicity

In montmorillonite, two crystal layers are bonded with a weak Van der Waals force, which is easily dissociated. Water molecules can enter between the crystal layers, so that the interlayer spacing increases and the crystal layer bonds are broken, causing directional expansion of the crystal lattice. Meanwhile, the unit cell has many metal cations and hydroxyl hydrophilic groups, and shows strong hydrophilicity.

(ii) Adsorption and ion exchange

When high-valent ions in montmorillonite are replaced by low-valent cations, an equivalent negative charge is generated, which is compensated by the interlayer adsorption of cations. In-between the cations and the crystal lattice electric dipoles are formed. In addition, with the weak binding force between crystal layers, polar

water molecules can be adsorbed, and one or two layers of water molecules can be adsorbed in the interlayer, according to the type of the cations and the relative humidity. In montmorillonite tetrahedrons, a small part of tetravalent silicon is replaced by trivalent aluminum. In the octahedral sheet, part of the trivalent aluminum is replaced by divalent magnesium. With the replacement of the positive ions in the lattice with lower-valent ions, the surface of the crystal layer is negatively charged, so that it has the ability to adsorb cations and polar water molecules. This is also the basic reason for the ion exchangeability, adsorption ability and swelling properties of montmorillonite. Montmorillonite is a natural inorganic cation exchanger.

(iii) Dispersibility and suspendability

Because of its special structure, inorganic montmorillonite can be dissociated into unit cell in water, and its unit cell particles are very subtle (0.02–0.2 μm). Each montmorillonite cell has the same number of negative charges und repels each other. In dilute solutions, it is difficult to gather into large particles, thus good dispersibility and suspendability are shown. After adding water to high-purity sodium montmorillonite and by forming a gelling solution, the montmorillonite is almost always in a suspended state.

(iv) Stability and non-toxicity

This fine thixotropic gel of montmorillonite can withstand high temperature of 300 °C. At 140 °C free water and adsorbed water escapes, whereas at 300 °C the interlayer water escapes and at 500 °C the crystal water is lost. Thus, montmorillonite has good thermal stability. Montmorillonite is almost insoluble in water and organic solvents, slightly soluble in strong acid and alkali. At room temperature, it will not be damaged by strong oxidants or strong reductants and has good chemical stability. Montmorillonite is nontoxic to humans, livestock and plants.

4.1.2 Organically modified montmorillonite

(1) Preparation of organically modified montmorillonite

Montmorillonite minerals have many important physicochemical properties. Among them, the exchangeability of interlayer cations is the most important feature. Other exchangeable cations in the solution can be exchanged into the interlayer of montmorillonite through exchange processes. The interlayer spacing of the montmorillonite can vary with the volume of the exchangeable cations entering the mineral layer. When the interlayer cation is exchanged by smaller ions or molecules, the interlayer spacing of montmorillonite becomes smaller; on the contrary, the interlayer spacing increases. This structural characteristic of montmorillonite can be used to prepare modified montmorillonite with special properties by ion exchange and insertion of various kinds of cationic and neutral

molecules. In recent years, the application of montmorillonite modification has been greatly broadened. The commonly used methods for the modification of montmorillonite can be divided into three categories: (1) inorganic modification, (2) organic modification and (3) organic–inorganic composite modification. Among them, research and application of the organic modification are relatively more.

The organic modification of montmorillonite mainly utilizes the exchangeability of interlayer ions. The organic modifier is introduced into the interlayer of the montmorillonite to replace the original hydrated ions and water molecules with various organic ions. The alkyl groups of the organic cation form an organic phase between the layers of the montmorillonite, rendering hydrophobic nature to the montmorillonite, thereby enhancing the adsorption of hydrophobic organic pollutants. According to the different characteristics of the production process, there are mainly three kinds of methods of the organic modification of montmorillonite: (1) wet method, (2) dry method and (3) pre-gel method. Wet method is the main method. The reaction diagram is shown in Figure 4.2. The wet method is to use water as the dispersion medium. The sodium-modified montmorillonite is made into slurry, and after separation, purification, modification, activation and exchange reaction with the modifier, the product is obtained through filtration, drying, milling and sieving.

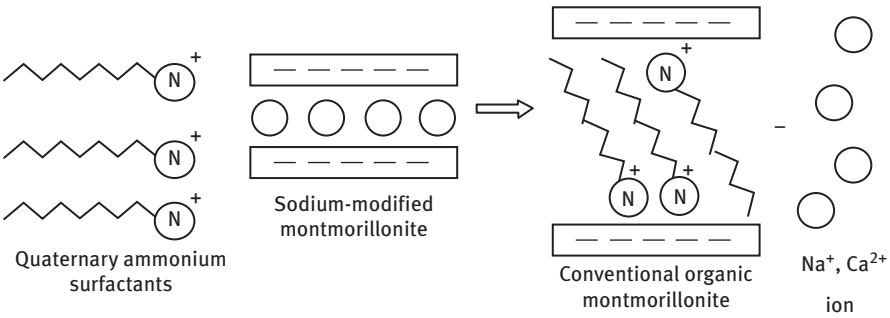

Figure 4.2: Reaction diagram of wet synthetic organic montmorillonite.

Currently, modifiers used for the organic modification of montmorillonites include macromolecular organic compounds (such as octadecyltrimethylammonium bromide (ODTMA), dioctadecyldimethylammonium chloride, cetyltrimethylammonium bromide (CTAB), tetradecylbenzyldimethylammonium bromide, tetradecylpyridinium bromide and the like), anionic surfactants (such as sodium lauryl sulfate and sodium dodecylbenzenesulfonate), organic chelating agents (such as tetraethylenepentamine and diethylenetriaminepentaacetic acid) and nonionic surfactants such as TritonX-100. The most widely studied organic modifiers are mainly quaternary ammonium compounds such as CTAB, ODTMA, cetylpyridinium bromide (CPB) and so on.

ZHU Lizhong et al. (1997) modified bentonite (montmorillonite) with CTAB. The results showed that the synthetic material could effectively remove organic

pollutants in water. Shen (2001) modified the bentonite with nonionic surfactants. It was shown that the modifier could enter the interlayer of bentonite and improve the adsorption capacity of the bentonite. MO Wei et al. (2008) also found similar results result. The modified organic montmorillonite with aluminate coupling agent had higher hydrophobicity. FU Guizhen et al. (2006) improved the sodium-modified montmorillonite through intercalation with CTAB. Characterization results showed that the interlayer spacing of montmorillonite increased from the original 1.555 nm to 2.045 nm. So the interlayer spacing after the organic modification increased significantly. Bentouami et al. (2006) utilized 8-hydroxyquinoline citrate to modify montmorillonite. The specific surface area of the modified montmorillonite doubled, greatly enhancing the adsorption capacity. CHEN Defang et al. (2000) used different quaternary ammonium salts to modify montmorillonite. The results showed that the hydrophobicity of the montmorillonite was related to the interlayer spacing. The greater the interlayer spacing, the better was the hydrophobicity of the material.

(2) Organically modified montmorillonite for removal of halogenated organic pollutants

Organic pollutants in water (especially halogenated organic pollutants) are far more harmful than inorganic pollutants. The United States National Environmental Protection Agency announced that among the 129 types of basic pollutants, 114 kinds are organic matter, of which more than half are toxic and widely distributed halogenated organic compounds such as chlorine or bromine, including dioxin. The modified organic montmorillonite is hydrophobic and its ability to adsorb hydrophobic organic pollutants is greatly increased. Therefore, in recent years, researchers mainly focused on the study of the adsorption of organic pollutants (especially halogenated organic pollutants) by organic montmorillonite, and achieved good results.

The research of the removal of organic pollutants by organic montmorillonite (or bentonite) began as early as 1977. McBride et al. (1977) first studied the modified bentonite to remove organic matter from water and proved that the modified organic clay had a good effect on removing halogenated organic pollutants in water. Later, many researchers constantly used different modifiers (such as long-chain quaternary ammonium salt) and improved methods to study the effect of organically modified montmorillonite on organic pollutants (such as phenol and carbon tetrachloride). ZHU Lizhong et al. (1997) systematically studied the adsorption of organic pollutants in water by the bentonite (montmorillonite) modified by different types of ionic surfactants, and found that the adsorption properties of the organically modified bentonite were much stronger than the original bentonite. Its adsorption properties were related to the nature of organic modifiers and the water solubility of organic pollutants.

Yildiz et al. (2005) made use of ODTMA and cetyltrimethylammonium bromide (CTMB) to prepare organic bentonite (montmorillonite), and studied adsorption of

benzoic acid and hydroquinone. The results showed that the adsorption effect was good. The adsorption capacity increased with the decrease of pH and the rise in temperature. At the same time, the ability of organic bentonite to remove hydrophobic organic pollutants obviously enhanced when the content of organic matter increased. LIU Ying et al. (2002) studied the adsorption and degradation of benzene, toluene, *o*-xylene and ethylbenzene in water on organic bentonite (montmorillonite). The results indicated that the adsorption capacity of organic bentonite to *o*-xylene was much stronger than that of natural bentonite. SHEN Xueyou et al. (2003) prepared a series of double cationic organic bentonite (montmorillonite) with constant organic modifier and studied adsorption behavior of aniline, 2,4-dichlorophenol and *p*-nitrophenol in water. The relative contribution of sorption and partitioning on the material surface was described in detail.

SUN Hongliang (2007) prepared modified bentonite composites with CTMB-organometallic chelating agent and studied its treatment by mixing wastewater with *p*-nitrophenol and heavy metal ions. It was found that the organically modified bentonite (montmorillonite) could effectively remove organic pollutants and heavy metal ions. Chen et al. (2008) prepared organic bentonite (montmorillonite), using cetyltrimethylammonium bromide (CTMB), and studied adsorption of naphthalene and nitroaromatic compounds. Good results were achieved. The addition of CTMB cetyltrimethylammonium helped to enhance the adsorption capacity of the material. Shakir et al. (2008) made use of the CTMB-modified bentonite to study the removal of catechol under different conditions. The results showed that the organically modified material had a good effect on the removal of catechol, and the adsorption process accorded with Langmuir equation and Freundlich equation.

The abovementioned results showed that the organically modified montmorillonite had high surface area and strong adsorption characteristics. Its hydrophilic property was changed to hydrophobic property. Its ability to adsorb and degrade hydrophobic organic pollutants was greatly enhanced. The modified material could be widely used in the treatment of organic wastewater. Meanwhile, montmorillonite can be used as a good carrier and dispersant. Other materials (such as metals) can be loaded on the material; however, there are few reports on this topic and the research is not deep enough.

4.1.3 Materials loaded with nanoscale zerovalent iron

Nanoscale zerovalent iron (NZVI) is a zerovalent iron material with a particle size in the range of 1 to 100 nm. Because of its remarkable performance and great potential of application, NZVI is widely used in environmental catalysis, wastewater treatment and environmental remediation, and has become the current international focus of environmental research. Compared to particulate zerovalent iron, NZVI has the advantages of small particle size, large specific surface area, good reactivity, strong

reduction ability and low cost. It can be widely used for remediation and degradation of various pollutants, and in particular, effective degradation of various halogenated organic pollutants.

(1) Preparation of nanoscale zerovalent iron

At present, the preparation method of NZVI can be divided into two categories: (1) physical method and (2) chemical method, according to different preparation technologies.

(i) Physical method

The physical method makes use of light and electricity technology to make zerovalent iron evaporate in vacuum or inert atmosphere, or through other physical effects, the atoms or molecules form nanoparticles. The methods include evaporative coacervation (also known as low-pressure coacervation), sputtering and high-energy mechanical ball milling. Physical methods are easy for mass production and are often used in industrial application.

(ii) Chemical method

Chemical methods include liquid phase chemical reduction, gas phase chemical reduction and microemulsion. The liquid phase chemical reduction method is the most widely used and the earliest studied method.

The liquid phase chemical reduction method mainly uses strong reducing agents such as KBH_4, $NaBH_4$, hydrazine hydrate or organometallic reducing agent to reduce Fe^{2+} and Fe^{3+} in the solution to obtain zerovalent iron particles. Wang et al. (1997) used $NaBH_4$ to reduce Fe^{3+} to prepare pure iron nanoparticles. Liquid reduction method has the advantage of obtaining good particle dispersion. The particle shape is basically spherical and the process is controllable. The reaction equation is as follows:

$$2Fe^{2+} + BH_4^- + 3H_2O \rightarrow 2Fe^0 + B(OH)_3 + 2H_2 + 3H^+ \tag{4.1}$$

$$2Fe^{3+} + BH_4^- + 3H_2O \rightarrow 2Fe^0 + B(OH)_3 + H_2 + 5H^+ \tag{4.2}$$

The gas phase chemical reduction method mainly produces nano-iron particles by reduction of solid metal iron salt by H_2 or CO. The short reaction residence time and the rapid cooling are the key points in the preparation process.

The microemulsion method is a new method developed on the basis of chemical reduction method. This method has the characteristics of cheap raw materials, easy preparation, mild reaction conditions and it does not require special conditions such as high temperature and pressure. It mainly uses two immiscible solvents, which form an emulsion under the action of surfactant. Through the nucleation, coalescence, agglomeration and heat treatment in microbubbles, iron nanoparticles are formed. DING Jianxu et al. (2007) prepared the nano iron with water-in-oil (w/o)

microemulsion system. The characterization results showed that the size of nano iron ranged from 20 nm to 100 nm.

(2) Study progress of preparation of loaded nanoscale zerovalent iron

Although NZVI iron has been widely used in the remediation of pollutants, there are still many problems to be solved. On the one hand, iron nanoparticles are easy to agglomerate due to its high specific surface energy and strong internal magnetic interaction force. On the other hand, the iron nanoparticles are very small, which are easily oxidized in air and form an oxide layer on the outer layer of the particles. These deficiencies will greatly reduce the reduction activity and the processing efficiency of the nanoscale zerovalent iron. In view of the shortcomings of the nano iron, that is, agglomeration, oxidability and poor dispersability, many researchers have studied ways to solve these problems. There are two main ways. First, dispersants or surfactants are added to modify the particle surface of nano iron, which can improve its dispersion in aqueous solution, preventing the agglomeration of nano-iron particles, and smaller particle size can be achieved. The second way is loading the nano iron to carriers. That is to disperse the nanoparticles to the support material, so as to increase the effective surface area of the nanoparticles and enhance their reactivity. On the one hand, the total contact area of the nanoparticles with the pollutants can be increased, and on the other hand the nanoparticles can be prevented from agglomerating. In recent years, researchers have used a lot of materials to load or fix the NZVI, and achieved good results.

Zhang et al. (2012) used flake graphite as a carrier to prepare loaded nano-iron particles. The characterization results showed that the material was spherical, with a particle size of 50–100 nm. Lee et al. (2004) successfully prepared nano-iron material with zeolite as carrier. The results showed that nano iron could be loaded on the zeolite and the specific surface area was 25.26m^2/g. Zhu et al. (2009) prepared activated carbon loaded by nano-iron particles. It was shown that the nano-iron particles were formed in the carbon channels. They were acicular and had a particle size from 30 to 500 nm. About 8.2% (mass ratio) iron was loaded on the activated carbon. ZHAO Zongshan et al. (2008) successfully loaded NZVI on the surface of cation exchange resin. The experimental results indicated that the diameter of NZVI was 100–160 nm, which were uniformly dispersed on the resin surface, forming some gullies on the surface of the particles. Üzüm et al. (2009) prepared kaolin-supported nano-iron particles by using kaolin as carrier, and found that the nano-iron particles adhered to the surface and edge of kaolin, with a particle size ranging from 10 to 80 nm. The addition of kaolin could effectively prevent the agglomeration of nano-iron particles.

Wang et al. (2010) used carboxymethylcellulose as dispersant to prepare supported nano-iron particles. The TEM characterization results showed that the particles were nearly spherical with high dispersion. The particle size ranged from 20 nm to 100 nm. Fang et al. (2011a) used mesoporous silica microspheres as carrier and

synthetized supported nano-iron particles. The experimental results showed that the mesoporous silica microspheroidal nano-iron material had an average particle size of 450 nm and specific surface area of 383.48 m^2/g. Zhang et al. (2010) successfully prepared a nanocomposite with pillared clay as support material. The characterization results showed that the dispersion of nanoscale iron particles was good, with a particle size range of 30–70 nm. Zhuang et al. (2010) prepared a nano-iron composite with organic bentonite as carrier. The results showed that the specific surface area of the composite was 8.82 m^2/g and the content of iron in the composite was 24.7%, indicating that iron particles were successfully loaded on the organobentonite. Gu et al. (2010) used montmorillonite clay plate as the carrier material and successfully prepared zerovalent nano-iron material. The results showed that the montmorillonite clay plate could provide support and space for nano iron. The synthesized nano-iron particles dispersed well.

In general, the preparation of supported nano-iron composites has been studied often in recent years. However, the cost of many support materials is relatively high and the preparation process is complicated. Therefore, we need to find a carrier material with low cost, easy preparation, environment compatibility and non-toxicity.

(3) Degradation of halogenated organic pollutants by supported zerovalent nano-iron material

(i) Mechanism of degradation of halogenated organic pollutants by zerovalent nano iron

It is generally believed that the degradation of organic halides by the nano-iron particles is a surface redox reaction, and iron is an excellent reducing agent that acts as an electron donor in the reaction. When a hydrogen atom of the halogenated organic compound is replaced by a halogen atom, the oxidation reaction takes place. If the dehalogenation reaction occurs, the halogenated organic compounds obtain electrons and are considered to be dehalogenated. The following reaction occurs:

$$RX + e \rightarrow R + X^- \tag{4.3}$$

As a strong reducing agent, zerovalent iron can provide halogenated organic electrons and promote the occurrence of the following dehalogenation reaction:

$$Fe + RX + H^+ \rightarrow Fe^{2+} + RH + X^- \tag{4.4}$$

(ii) Research status of degradation of halogenated organic pollutants by zerovalent nano-iron material

The zerovalent iron has been widely used in water treatment projects to deal with various pollutants in water bodies, including heavy metals, organic compounds,

natural organic matter and disinfection by-products. Especially in the treatment of halogenated organic compounds, it is more widely used. Zerovalent iron nanoparticles are much smaller than the particulate zerovalent iron particles, ranging in size from 1 to 100 nm, and have relatively large surface area and high surface energy, which can effectively degrade many kinds of environmental pollutants. In the late 1980s, as an effective dehalogenation reducing agent, zerovalent iron nanoparticles have drawn people's attention. In recent years, studies found that nano iron could catalyze and reduce a variety of organic halides, such as trichloroethylene, vinyl chloride, lindane, chlorinated alkanes, chlorobenzene, polychlorinated biphenyls, chlorophenols (CPs), polybrominated diphenyl ethers, polychlorinated dibenzodioxins, pentachlorophenol (PCP), hexachlorobenzene (HCB) and other persistent pollutants. Through reduction reaction, nano iron can convert organic pollutants into nontoxic or low-toxic compounds.

(iii) Research progress of degradation of halogenated organic pollutants by supported NZVI materials

Apart from overcoming the disadvantages of easy agglomeration, oxidability and poor dispersibility, the supported nano-iron material has also become the focus and hotspot in the study of degradation of organic pollutants, especially halogenated organic pollutants. In recent years, the study of this aspect reported in the literature also proved it.

Wu et al. (2006) prepared a supported iron–nickel bimetallic nano-iron material with cellulose acetate as carrier and studied the degradation effect of trichloroethylene. The results showed that the reaction conformed to the first-order kinetic model, and the nickel content had a great impact on the degradability of the composite material. Li et al. (2006) loaded nano iron on cation-exchange resin and used this synthetic material to study the degradation of decabromodiphenyl ether (BDE-209). The study found that the degradation process of BDE was a gradual debromination process and the first-order reaction constant was 0.28 h^{-1} ± 0.04 h^{-1}. Meyer et al. (2004) prepared the supported nano-iron material by using membrane as support material and studied its degradation effect on trichloroethylene. The results showed that the degradation effect was good and the existence of the support material was in favor of the reduction reaction. The reaction process conformed to pseudo-first-order reaction model.

HU Liujiang et al. (2008) synthesized supported nano-iron material with organic bentonite as carrier, and studied the treatment effect of nitrobenzene and dichlorophenol, respectively. The results showed that the effect of the synthesized loaded material was significantly better than the iron nanoparticles with the same iron content. The removal rate of 2,4-dichlorophenol was 90.6% after 120 min, whereas 98% nitrobenzene was removed after 20 min. It was also found that in the treatment of nitrobenzene with organic bentonite supported nano-iron material, there was clearly a synergistic effect of adsorption and reduction. ZHAO Zongshan et al.

(2008) utilized synthetic cation exchange resin loaded with nano iron to study its degradation of water-soluble azo dyes. The experimental results showed that the material had excellent degradation of azo dyes such as methyl orange. Within 4 min the removal rate achieved 95% or more. Frost et al. (2010) used palygorskite as a supporter to synthesize supported nano-iron material and studied degradation of methylene blue. The experimental results indicated that within 10 min, the removal rate of methylene blue was about 90%, far greater than that of non-supported nano-iron materials.

Fang et al. (2011b) investigated the degradation of BDE-209 using supported nano-iron particles synthesized with mesoporous silica microspheres. The experimental results showed that the reaction conformed to the first-order reaction kinetic model. The reaction rate constant increased with the dosage of the material, and the prepared material could be recycled many times. Tseng et al. (2011) studied the effect of degradation and dechlorination of trichlorethylene by granular activated carbon supported nano-iron materials. The results showed that the dechlorination reaction occurred on the surface of the composites and mainly was zero-order dechlorination reaction. The removal rate was almost 100% within 200 min. Chen et al. (2011) studied the degradation of methyl orange by bentonite-supported nano-iron materials. The results showed that the reaction was in accordance with the pseudo-first-order reaction model and the removal rate of methyl orange was 99.75% within 20 min.

Li et al. (2011) synthesized supported nano-iron materials with organobentonite as carrier and studied its degradation of pentachlorophenol. The results showed that the dispersibility of the supported nano-iron material was good and the removal rate of pentachlorophenol was 96.2 %, which was much higher than that of pure nano-iron material. Zhang et al. (2011b) also obtained similar results to those of Li et al. in experiments using organobentonite to support iron nanoparticles and then to degrade atrazine. Jia et al. (2012) synthesized nanocomposites with organic montmorillonite template as carrier and studied the dechlorination effect of dichlorophenol. The results showed that the dichlorophenol could gradually dechlorinate and rapidly consume the zerovalent iron in the Fe^0/H_2O system. Weng et al. (2012) degraded the amoxicillin in water by using synthetic bentonite loaded with nano iron. The results showed that the degradation efficiency of amoxicillin of the composite material was as high as 93.10%. Degradation kinetics studies showed that the amoxicillin degradation process accorded with the pseudo-first-order reaction kinetics.

Numerous previous studies have shown that the degradation of halogenated organic pollutants by supported nano-iron material is feasible. The study of the dehalogenation degradation can be summed up to three main points. First, the effect of the supported nano-iron materials on the degradation of halogenated organic pollutants is much better than pure nano-iron materials. The second is the gradual dehalogenation by the supported nano iron. Third, the dehalogenation reaction basically conforms to the pseudo-first-order reaction model.

4.2 Preparation of montmorillonite-supported nanoscale iron materials

4.2.1 Overview

For the shortcomings of nanosized zero-valent iron, researchers have used a lot of materials to load or fix the NZVI and achieved certain results. However, we also need to find a load material that is low cost, easy to prepare, environment-friendly and nontoxic. Montmorillonite is an environmental friendly material; it is also a good carrier and dispersant. Its mineral resources in China are very rich and inexpensive. Montmorillonite has a unique cation exchangeability and expansibility, it can be modified by the surfactant into an organic montmorillonite, which is changed from hydrophilic to hydrophobic and can better adsorb hydrophobic halogenated organic pollutants. Therefore, by modifying the sodium-based montmorillonite by cation exchange reaction, organically modified montmorillonite can be prepared, which has good adsorption capacity of hydrophobic halogenated organic compounds. And then the supported nano-iron material can be prepared by liquid phase reduction with the montmorillonite as the carrier. The montmorillonite resources used in the preparation of composite materials are natural, abundant, low cost and environment friendly, which indicates that the research, development and application of this technology will have broad application prospects.

4.2.2 Determination of the nature of the original sodium montmorillonite

In order to select the sodium montmorillonite with good quality, and to understand the nature of the selected sodium montmorillonite, we chose sodium montmorillonite from two producing areas: (1) Zhejiang and (2) Inner Mongolia, and analyzed their properties, with the national montmorillonite quality standards as reference. The results are shown in Table 4.1.

The test results showed that the quality of sodium montmorillonite in Zhejiang was good. The high-purity sodium montmorillonite could meet the requirements of material preparation. Therefore, it was determined that the montmorillonite from Zhejiang was selected as the raw material.

4.2.3 Preparation of organically modified montmorillonite

Sodium montmorillonite was first activated at 105 °C and and cooled. Then 5.0 g was weighed with a balance and put into an Erlenmeyer flask followed by addition of 200 mL of deionized water and 1.0 CEC of cetyltrimethylammonium bromide (CTMB) modifier. The solution was stirred at 60 °C for 2 h and was centrifuged after the

Table 4.1: Determination results of sodium montmorillonite.

Sample name	Glial price (mL/15 g)	Methylene blue absorption (g/100 g)	pH	Swelling index (mL/g)	Cation exchange capacity (CEC)/ (100 mL/100 g)
Sodium montmorillonite from Inner Mongolia	470	32	10.30	48	105
Sodium montmorillonite from Zhejiang	540	38	10.40	53	118
Quality indicators of first-class product	600	35	8.5–10.3	55	60–150
Quality indicators of second-class product	500	30	45	6.9–8.5	–

reaction. The organic montmorillonite was washed three times, and then placed in a dry oven at 70 °C for 12 h. The montmorillonite product was taken out of a grinding machine and then passed through a 100 mesh sieve. Finally, the product was activated at 115 °C for 2 h and cooled for use in the experiment.

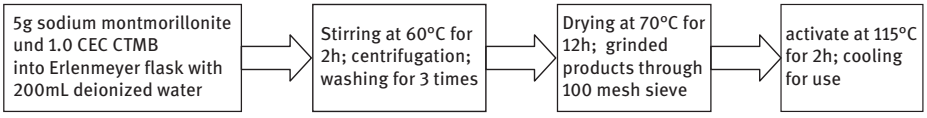

Figure 4.3: Flow chart of preparation of organically modified montmorillonite.

4.2.4 Preparation of organic montmorillonite loaded nano-iron material

5 g of organically modified montmorillonite was added in a beaker containing 200 mL of deionized water without oxygen. A certain amount of $FeSO_4 \cdot 7H_2O$ for a soil/iron mass ratio of 4:1 was also added, then stirred and dispersed at room temperature for 9.0 h. Then 100 mL of freshly prepared $NaBH_4$ solution with 3:1 molar ratio of B/Fe was added dropwise. With the addition of $NaBH_4$, a large number of bubbles overflowed and the solution became darker. The reaction process is as follows:

$$Fe(H_2O)_6^{2+} + 2BH_4^- \rightarrow Fe + 2B(OH)_3 + 7H_2 \quad (4.5)$$

After the addition was completed, the stirring was continued for 0.5 h. The product was then subjected to suction filtration and separation, and then washed with absolute ethanol solution for three to four times and vacuum dried at 60 °C for 12 h. The resulting supported nano iron was named M-nanoscale zero-valent iron (M-NZVI). For the purpose of comparison, unsupported nano-iron particles were also prepared under natural conditions in the same way as the preparation of supported nano iron. The product with no montmorillonite involved in the preparation process was named NZVI.

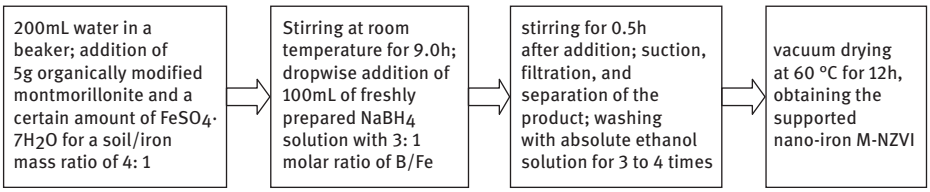

Figure 4.4: Flow chart of preparation of organic montmorillonite loaded nano-iron material.

4.3 Characterization of montmorillonite-loaded nano-iron material

The montmorillonite-loaded nano-sized zerovalent iron material was named M-NZVI. The nano-sized iron particles without montmorillonite were named NZVI, prepared with the same method as that for the supported nano-sized iron. The organically modified montmorillonite was named CMT.

4.3.1 Crystal structure of the materials

(1) X-ray Powder Diffraction (XRD) analysis of different materials

The wide-angle XRD pattern of CMT, NZVI and M-NZVI is shown in Figure 4.5. It can be seen from the figure that the M-NZVI material had a clear diffraction peak at $2\theta = 44.78°$, compared to CMT, indicating that the iron particles have been supported on the organic montmorillonite. At the same time, as can be seen from the figure, NZVI and M-NZVI showed significant characteristic diffraction peaks of α-Fe at $2\theta = 44.78°$, which was also consistent with the previous literature, indicating that the material was loaded with zerovalent iron. In addition, Figure 4.5 also shows that there was a weaker peak of iron oxide ($2\theta = 35.85°$) on the diffraction patterns of NZVI and M-NZVI, which indicates that the main phase of iron on M-NZVI contained iron oxide, apart from α-Fe. It can be told that the iron nanoparticles loaded on the organic montmorillonite had a core–shell structure, the core was α-Fe, and the

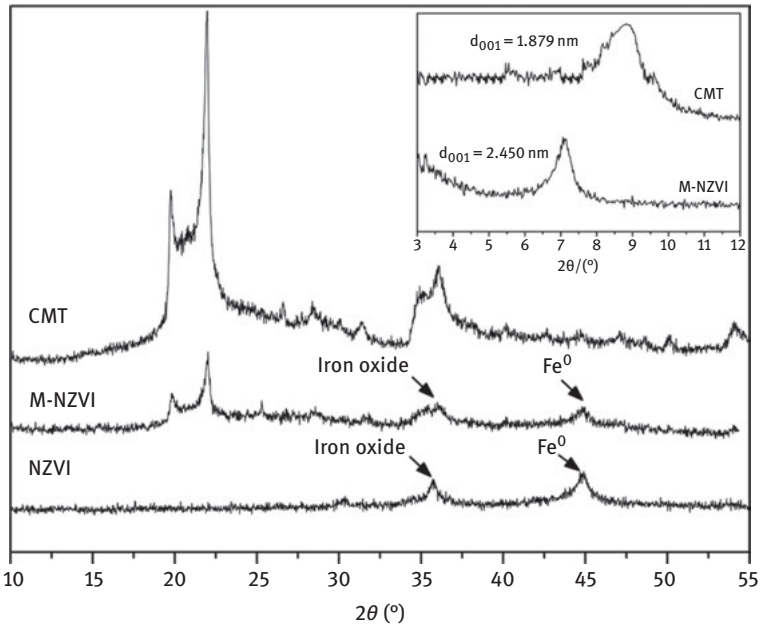

Figure 4.5: X-ray diffraction patterns of different materials.

surface was coated with an iron oxide shell. Compared to the weaker and wider peak at 44.78° of NZVI and M-NZVI, the size of iron nanoparticles supported on organically modified montmorillonite was much smaller than that of NZVI, which was not supported.

From the XRD spectrum of Figure 4.5, the calculation based on Bragg's equation showed that the substrate spacing d_{001} of M-NZVI was 2.450 nm, which was 0.571 nm larger than that of CMT (d_{001} = 1.879 nm). In addition, the characteristic peaks of M-NZVI were shifted to a lower angle, indicating that the nano-iron particles have been successfully inserted into the montmorillonite interlayer and a large number of nano-iron groups formed a support between the montmorillonite interlayers, thereby expanding the montmorillonite interlayer distance.

(2) Layer spacing analysis of different materials

As sodium montmorillonite is made of a large number of irregular unit layers; in-between the layers there is a certain area, known as the interlayer area, and the height between layers is called the layer spacing. The layer spacing is an indicator of the size of the interlayer space, and its size determines the size of the internal surface area of the layered silicate minerals, such as montmorillonite. Therefore, after the montmorillonite is organically modified, the layer spacing will change, which can be calculated from the XRD diffraction peak.

The montmorillonite layer spacing can be calculated by Bragg's equation, which is as follows:

$$2 \times d \times \sin\theta = n \times \lambda \tag{4.6}$$

θ is the diffraction angle corresponding to the d_{001} characteristic peak, obtained by XRD characterization and detection; d is the distance between the bottom and surface of the montmorillonite material; λ is the diffraction wavelength in nm and the wavelength is assumed to be 0.1543 nm; n is the diffraction order and in this experiment it is taken as 1; then, with the obtained height of montmorillonite unit layer d = 0.96 nm, the layer spacing can be calculated.

The three kinds of materials: (1) montmorillonite-loaded nano iron, (2) organically modified montmorillonite and (3) sodium montmorillonite were respectively characterized by XRD. The calculated results are shown in Table 4.2.

Table 4.2: Layer spacing of different materials.

Type	2θ	Distance between bottom and surface (nm)	layer spacing (nm)
Montmorillonite	6.506	1.385	0.425
Organically modified montmorillonite	4.736	1.879	0.919
Organic montmorillonite loaded nano iron	3.627	2.450	1.490

According to the detection and calculation, it can be seen from Table 4.2 that the interlayer distance of original sodium montmorillonite was 0.425 nm. After the modification by the organic modifier cetyltrimethylammonium bromide (CTMB), the layer spacing of the organic montmorillonite could be increased to 0.919 nm. The modifier had obviously a pillared role for the montmorillonite. The interlayer spacing of the organic montmorillonite material loaded with the nano iron reached 1.490 nm, which was the largest value among the three materials. It is indicated that the introduction of organic modifier helps to improve the layer spacing.

4.3.2 Surface characteristics of the material

(1) Specific surface area analysis of different materials

The specific surface area is a major indicator of the sorption capacity of synthetic materials. This property is measured by the BET–N_2 surface area analyzer and the results are shown in Table 4.3. It can be seen from Table 4.3 that the specific surface area of M-NZVI was 36.431 m^2/g, which was larger than that of NZVI with 26.875 m^2/g

Table 4.3: Surface parameters of different materials.

Sample	BET surface area (m^2/g)	Pore volume (cm^3/g)	Average pore size/nm
CMT	18.384	0.195	30.366
NZVI	26.875	0.106	26.436
M-NZVI	36.431	0.162	24.963

and that of CMT with 18.384 m^2/g, and was also similar to the reported date of supported nano-iron materials. The specific surface area of M-NZVI increased significantly compared to CMT due to the large amount of iron particles loaded on the surface or interlayer of the organically modified montmorillonite. In addition, the pore volumes of CMT, NZVI and M-NZVI were 0.195, 0.106 and 0.162 cm^3/g, respectively, among which the pore volume of CMT and M-NZVI was slightly lower. This may be because some of the pores in the organically modified montmorillonite are blocked by iron nanoparticles.

(2) Nitrogen adsorption curve and pore size analysis of M-NZVI

The isothermal adsorption–desorption curves of the organic montmorillonite supported nano-iron material are shown in Figure 4.6. It can be seen from the figure that the isothermal adsorption–desorption curve of the material belonged to the type IV isothermal adsorption curve. The tendency of the isothermal adsorption–desorption curve showed that the pores in the sample were dominated by mesopores and a certain proportion of micropores existed. When the relative pressure P/P_0 was greater than 0.40, at the liquid nitrogen temperature of 77 K, the adsorption isotherms began

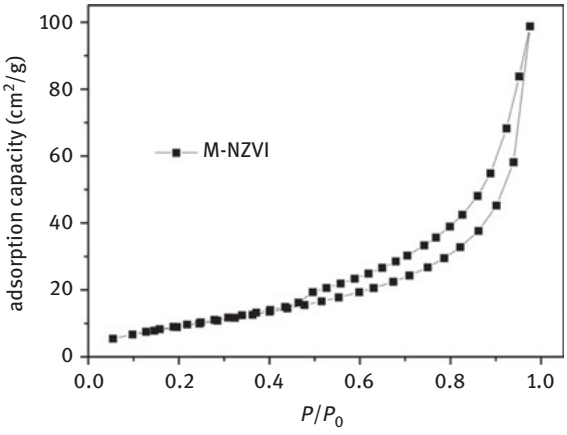

Figure 4.6: Nitrogen adsorption–desorption curves of organic montmorillonite supported nano-iron materials.

to show a relatively slow upward trend and the adsorption and desorption isotherms did not coincide at the same time. As can be seen from the figure, an obvious hysteresis regression phenomenon happened to the isothermal adsorption curve. According to a related research, these hysteresis loops are typical H3 hysteresis loops. Type H3 hysteresis loops are mainly given by granular materials such as clay minerals or flakes with slitty holes. They are characterized by unrestricted adsorption capacity under high relative pressures.

Figure 4.7 shows the pore size distribution curve of the organic montmorillonite loaded nano-iron material. It can be seen from the figure that in the curve at 3–4 nm, a small sharp peak appeared. The peak near 3.6 nm was mainly due to the mesopores formed by the organic matter entering the montmorillonite layers. There was also a smooth peak around 25 nm, indicating that the pore size of the material was not uniform.

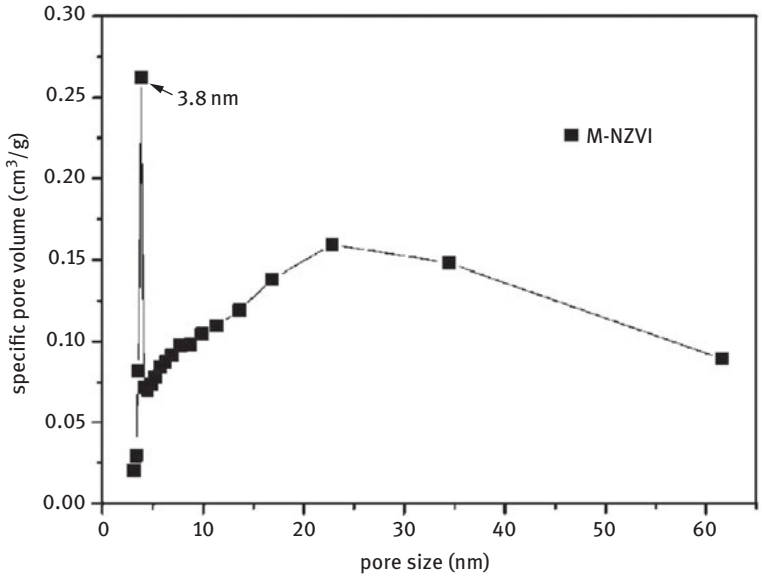

Figure 4.7: Pore size distribution of organic montmorillonite loaded nano-iron material.

4.3.3 Material morphology

The morphology and particle distribution of M-NZVI material was analyzed using SEM and TEM, and its classical images are shown in Figure 4.8 and Figure 4.9.

(1) SEM analysis

As can be seen from Figure 4.8(a) and Figure 4.8(b), the nano-iron particles in the M-NZVI material were evenly distributed over the entire surface and edge of the

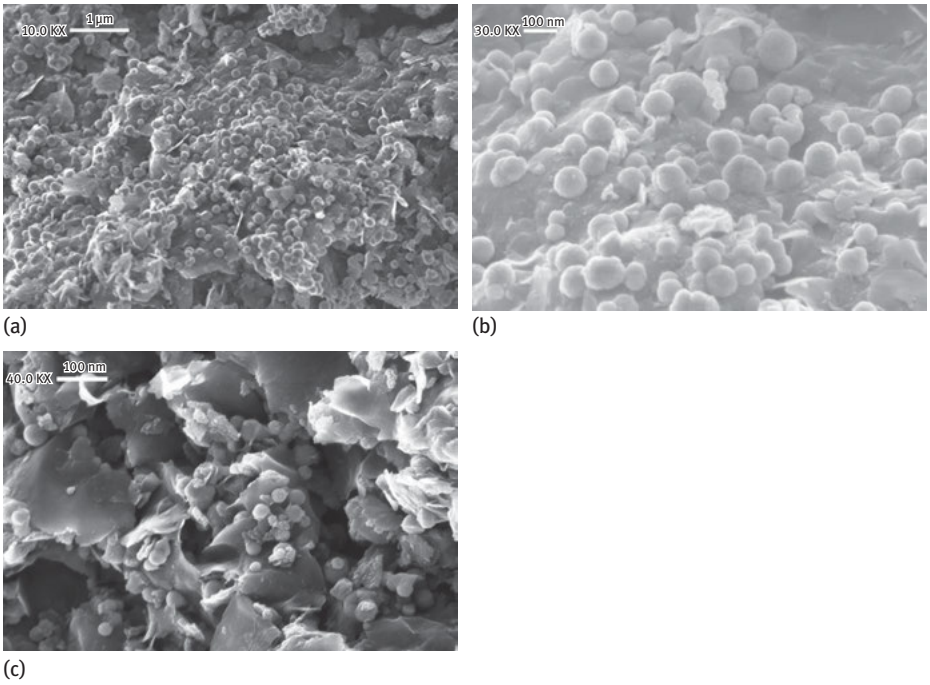

(a) (b)

(c)

Figure 4.8: SEM images of M-NZVI(10KX), M-NZVII(30KX) and M-NZVII(40KX).

organic montmorillonite. The nano-iron particles were spherical and it is hardly found that there were groups of nano-iron particles with chain-like structures due to agglomeration. Meanwhile, it can be seen that the size range of nano-iron particles in M-NZVI was between 30 and 90 nm, which was a typical nanomaterial and was consistent with the reported literature. The characterization results of M-NZVI indicate that the immobilization of iron nanoparticles on a porous material was an effective method to prevent the agglomeration of iron nanoparticles. Therefore, the introduction of organic montmorillonite improves the dispersibility of iron nanoparticles, inhibiting the contact between iron nanoparticles, and can effectively prevent the occurrence of agglomeration and enhance their reducing activity.

Figure 4.8(c) shows the distribution of nano-iron particles near the stacked gully and interlayer of M-NZVI. It can be seen from the figure that on that place the size of the nano-iron particles was smaller than that on the surface of montmorillonite, in the range of 5–40 nm. As for the size of the nano-iron particles in the interlayer, the SEM and TEM characterization was difficult to complete. Only the XRD results can be used for the analysis. From the abovementioned data, the substrate spacing d_{001} of M-NZVI was 2.450 nm, from which the thickness of the montmorillonite layer was removed (0.92 nm), then the interlayer spacing of the M-NZVI material was 1.530 nm, which means the size of the nano-iron particles in the interlayer was about 1.530 nm.

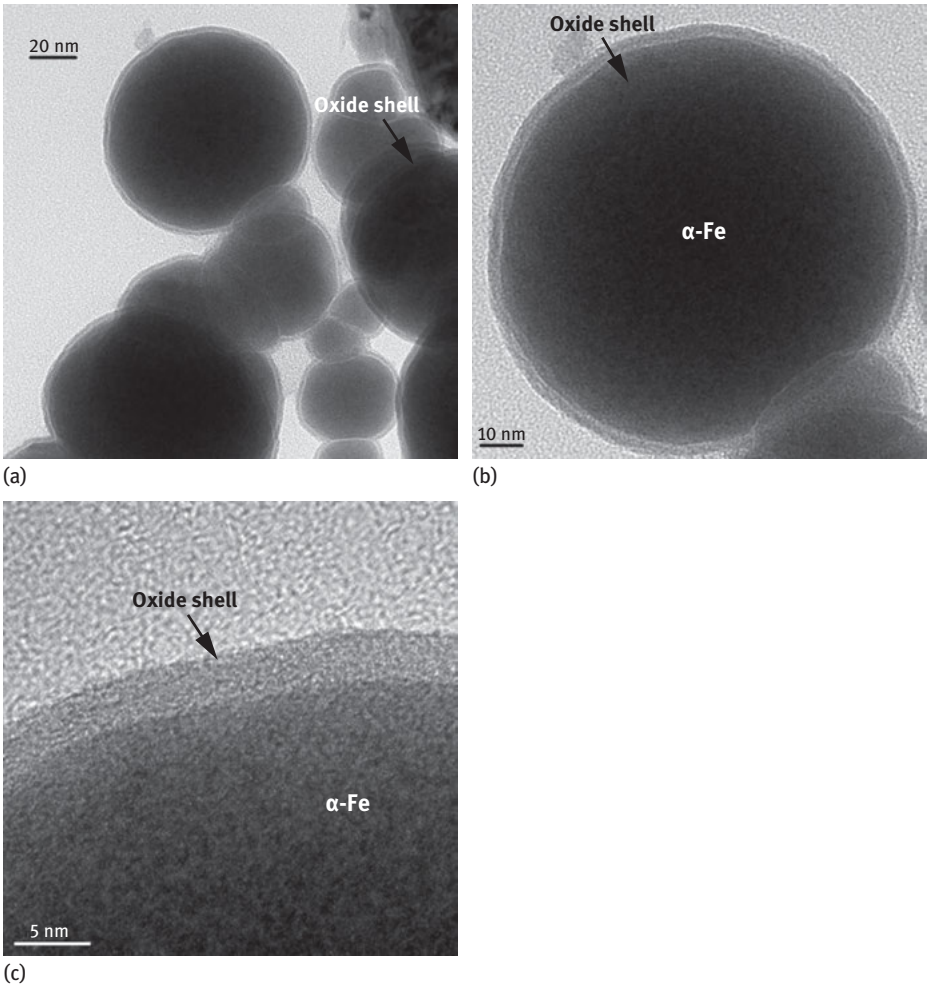

Figure 4.9: TEM images of the M-NZVI material.

(2) TEM analysis

As can be seen from Figure 4.9(a), the M-NZVI material showed good dispersion of the iron nanoparticles, which were spherically distributed on the surface and gully of the organo-montmorillonite. There was slight agglomeration. The particle size was between 30 and 90nm, which was consistent with the previous SEM characterization results and the reported results in the literature.

Figure 4.9(b) and Figure 4.9(c) clearly show the TEM images of the nano-iron particles with a shell–core structure. It can be seen that the iron particles were in a shell–core structure and the single nano-iron particle was made of a thick core surrounded by a thin shell. On the surface of the particles the iron oxide shell was

bright, whereas the α-Fe core was relatively dull. This phenomenon could be clearly seen on the outer surface of different iron particles and individual iron particle. Through measurement, the thickness of the shell was between 2.5 and 4.0 nm and many researchers had similar study results. It is also found that the outer shell of the nano-iron particles can effectively prevent the iron core from continuing oxidation. At the same time, some studies have shown that the iron particles with the shell–core structure continue to oxidize very slowly, which makes the application of the organic montmorillonite-loaded NZVI composite possible, which is prepared under natural environmental conditions.

The stability of the M-NZVI material can be well explained by the Caberra–Mott theory that says the oxide film is formed when the metal iron is oxidized and separates the iron from the oxygen. Then by the tunneling effect, the electrons are transferred from the iron atom to the oxygen atoms absorbed on the outer surface of the thin oxide film. The iron cations and oxygen anions are accumulated on different sides of the film, thereby forming a uniform electric field in the oxide film. The electric field thus formed drives the iron cations through the oxide film to maintain the growth of the oxide film. According to the theory of Caberra–Mott, the thickness of the iron oxide shell of this material increases by 1 nm in 600 years. Therefore, we can conclude that the M-NZVI material with a core–shell structure is stable under normal temperature and pressure, and has a strong antioxidant capacity.

4.3.4 Material composition analysis

The material composition was measured and analyzed by Energy Dispersive Spectrdmeter (EDS), X-ray photoelectron spectrometer (XPS), X-ray fluorescence spectrometer (XRF) and inductively coupled plasma emission spectrometer (ICP-AES).

(1) EDS analysis

The EDS images of CMT and M-NZVI are shown in Figure 4.10. As can be clearly seen in Figure 4.10(a), on the surface of the organically modified montmorillonite (CMT), there were mainly elements such as Si, O, Al and Mg, whereas elements such as Na, K and Ca were almost undetectable, indicating that the exchange of sodium montmorillonite with macromolecular organic modifiers has replaced most of the cations. Figure 4.10(b) shows the EDS spectrum of the loaded organic montmorillonite M-NZVI. As can be seen from the figure, the material composition was relatively complicated and its surface composition included Si, Fe, O, Al, Mg and other elements. Compared with NZVI, the content of Fe in M-NZVI was slightly lower than that in NZVI due to the montmorillonite/iron mass ratio of 4:1. Its higher oxygen content than NZVI was mainly because of the montmorillonite itself and the oxidation of nano iron. The specific component analysis by EDS detection of the three kinds of materials is described in the next section.

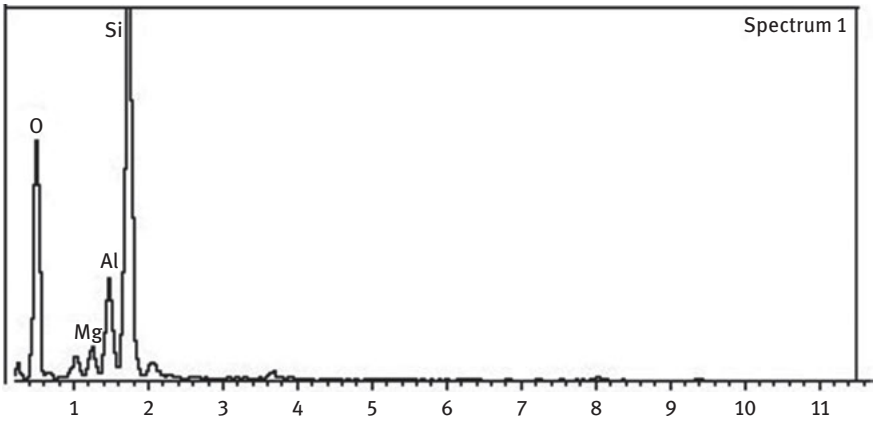

(a)

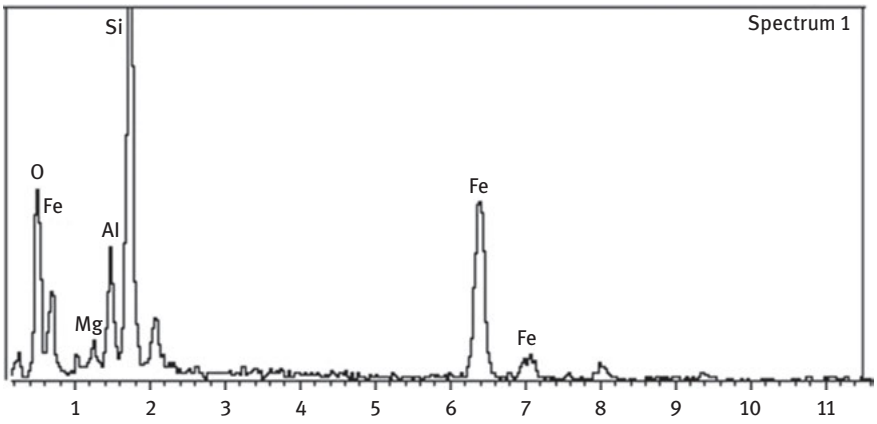

(b)

Figure 4.10: EDS spectrum: (a)CMT and (b)M-NZVI.

(2) XPS analysis

To further investigate the surface composition of the M-NZVI material, the M-NZVI material was analyzed using XPS, as shown in Figure 4.11. Figure 4.11 shows the Fe (2p) X-ray photoelectron spectra of M-NZVI before and after the reaction. The two curves clearly showed two characteristic peaks of the iron nanomaterial. The characteristic peak of the Fe ($2p_{3/2}$) photoelectron had a binding energy of 710.73 eV, which was similar to that of α-Fe_2O_3, indicating that the surface of the nano-iron particles was covered with a layer of iron oxide, which was also consistent with the previous XRD and TEM characterization results. Meanwhile, it can be seen from the XPS spectrum in Figure 4.11 (b) that after the reaction the characteristic peak of the Fe

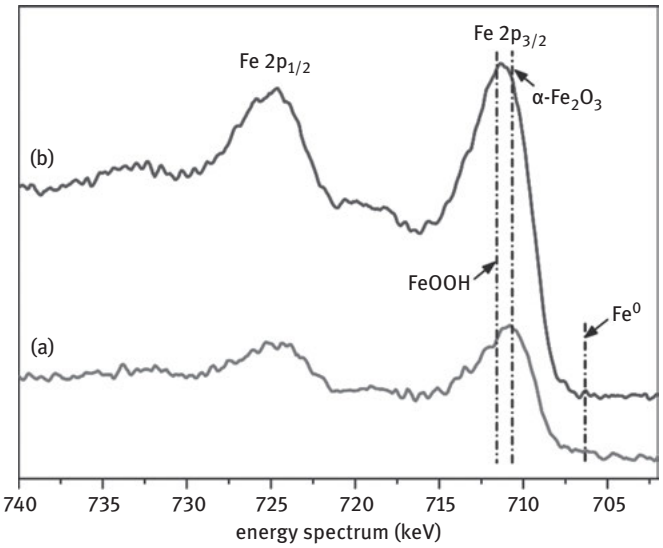

Figure 4.11: X-ray spectra of M-NZVI before and after reaction.

($2p_{3/2}$) photoelectron was significantly higher and sharper than that before the reaction (Figure 4.11 [a]). In addition, the binding energies of the Fe ($2p_{3/2}$) photoelectron peak decreased by 0.42 eV to 711.15 eV, compared with that before the reaction. This value was similar to the binding energy of FeOOH reported in the literature, indicating that the M-NZVI material interacted with pollutants in water. After the reaction, the surface of the material would form a hydroxide precipitate due to hydrolysis and adsorption. The oxide layer outside the iron particles after the reaction may be composed of various iron oxides (such as α-Fe_2O_3 and FeOOH). In addition, a smaller characteristic peak was found near the binding energy of 706.30 eV, implying the presence of zerovalent iron in the material. However, due to the outer iron oxide layer with 3–5 nm (see previous TEM characterization results), and the detection depth of XPS only with 3–5 nm, the chance of the X-ray penetrating into the iron core was reduced, resulting in less excited electrons. Thus, it was difficult to form obvious characteristic peaks.

(3) Composition analysis

In order to clarify the composition of the M-NZVI material, EDS, XRF and ICP-AES were used for the analysis. The results are shown in Table 4.4. The EDS spectrum of the M-NZVI material (see Figure 4.10) clearly shows that the composite contained elements such as Si, Fe, O, Al and Mg, indicating that the organically modified montmorillonite has been loaded with iron particles. The results of XRF and ICP-AES in Table 4.4 also demonstrate that the M-NZVI material contained iron. As can be seen from Table 4.4, the results obtained by the three measurement methods differed greatly, because EDS and XRF are mainly used to determine the surface composition

of materials, whereas ICP-AES uses the dissolution method to measure the ingredients. The results of the three method show that the main components of NZVI were iron. The content of iron in the material measured by ICP-AES was 85.3%, which was much higher than that of EDS and XRF. The results of EDS showed that the content of oxygen was relatively high, indicating that the surface of NZVI was oxidized.

The results of M-NZVI showed that M-NZVI mainly consisted of Si, Fe and O. The content of iron in M-NZVI measured by ICP-AES was 15.6%, which was consistent with the selected montmorillonite/iron mass ratio of 4:1 in the preparation, but lower than the iron content of EDS and XRF. This may be related to the exclusive determination of the surface composition of the latter two methods. As can also be seen from Table 4.4, the results of the three methods showed that the iron content of the M-NZVI material after the reaction was lower than that before the reaction and the oxygen content of the material was increased. It may be because some of the iron particles will dissolve in the aqueous solution, when the M-NZVI material reacts with the contaminants in the aqueous solution. Meanwhile, due to the continuous oxidation of the iron, the content of oxygen in the reacted M-NZVI material is increased.

Table 4.4: Material composition analysis.

Type	EDS results (%)	XRF results (%)	ICP-AES results (%)
M-NZVI (before reaction)	Fe=35.9, Si=26.4 O=29.2, other elements=8.5	Fe=29.1, Si=20.8 other elements=50.1	Fe=15.6, Si=39.1 other elements=45.3
M-NZVI (after reaction)	Fe=32.7, Si=25.8 O=31.4, other elements=10.1	Fe=27.6, Si=20.6 other elements=51.8	Fe=12.4, Si=38.5 other elements=49.1

4.4 Degradation of halogenated organic pollutants by montmorillonite-supported nano-iron materials

4.4.1 Overview

Organic pollutants in water (especially halogenated organic pollutants) are far more harmful than inorganic pollutants. Of the 129 basic pollutants released by the U.S. Environmental Protection Agency, 114 are organic matter. Among them, more than half are halogenated organic compounds such as chlorinated or brominated compounds, including dioxin, which are highly toxic and widely distributed. In order to understand the characteristics and effects of montmorillonite-supported nano-iron materials on the degradation of halogenated organic pollutants, three halogenated organic compounds: (1) 4-chlorophenol, (2) BDE and (3) tetrabromobisphenol A (TBBPA) were selected for the research of the degradation effect. The three halogenated organic compounds are summarized below.

(1) 4-chlorophenol

4-Chlorophenol is an isomer of chlorophenols (CPs) and is widely used in the industries related to preservatives, bactericides and pesticides. 4-Chlorophenol is almost insoluble in water and slightly soluble in benzene, ethanol and diethyl ether. The solubility in water (20 ° C) is 27.1 g/L and the pKa value (in water/25 °C) is 9.38. This substance is considered to be a persistent organic pollutant that is strongly toxic to organisms.

(2) Decabromodiphenyl ether

BDE-209 is one of the isomers with the highest bromine content in the polybrominated diphenyl ethers (PBDEs) family, and consists mainly of monomers of nonabromodiphenyl ether and BDE. It is also one of the most widely used efficient brominated flame retardant additives. BDE-209 has the characteristics of less addition, high flame retardancy and high thermal stability. It is widely used in industries related to rubber, textile, electronics and plastics. BDE-209 is a white to pale white crystalline powder with molecular formula $C_{12}Br_{10}O$, molecular weight of 959.2 and theoretical bromine content of 83.3%. It is very poorly soluble in water and common organic solvents. The value of lgK_{ow} is 10.0. The concentration of PBDEs in water is generally not higher than 1 μg/L. At high temperatures, it is soluble in toluene and xylene. The melting range is 295–305 °C. The density is 3.04 g/cm^3. The decomposition temperature is about 425 °C. It is hardly volatile. According to study findings, BDE has the characteristics of high hydrophobicity, persistence, bioaccumulation and toxicity, and has become a ubiquitous persistent pollutant in the environment.

(3) Tetrabromobisphenol A

TBBPA is a brominated flame retardant with the largest yield at present. It is a white powder with molecular formula of $C_{15}H_{12}Br_4O_2$, molecular weight of 543.87, density of 2.1 g/cm^3, melting point of 179–184 °C and boiling point of 316 °C. As reactive flame retardant, TBBPA can be used for epoxy resin, polyurethane resin and so on. As additive flame retardant, it can be used for polystyrene, styrene acrylonitrile (SAN) resin and acrylonitrile butadiene styrene (ABS) resin. TBBPA can be released into various environmental media such as air, wastewater, sludge, soil and organisms during production and use. As an endocrine disruptor, TBBPA also shows potential thyroid hormone interference activity, immunotoxicity, neurotoxicity and so on, causing great harm to the natural environment and human beings.

4.4.2 Degradation effect of montmorillonite-supported nano-iron material on three halogenated organic pollutants

The degradation of three kinds of halogenated organic compounds: (1) 4-chlorophenol, (2) BDE and (3) TBBPA by the montmorillonite-loaded nano-iron material is shown in Figure 4.12. It can be seen from Figure 4.12 that the montmorillonite-loaded

nano-iron material has a good degradation effect on all three halogenated organic compounds. 0.15 g of the M-NZVI material was added into the 4-chlorophenol reaction solution with an initial concentration of 50.0 mg/L and a volume of 50 mL. After 2 h reaction, the removal rate of 4-chlorophenol reached up to 86.5%. For the 2.0 mg/L BDE solution with a volume of 50 mL, 0.60 g M-NZVI was added. After 4 h reaction, a removal rate of 96.2% of BDE was achieved. For tetrabromobisphenol A, 0.02 g of M-NZVI was added to the reaction solution with the initial concentration of 10.0 mg/L and a volume of 50 mL. After 12 h reaction, the removal rate of TBBPA reached 97.5%.

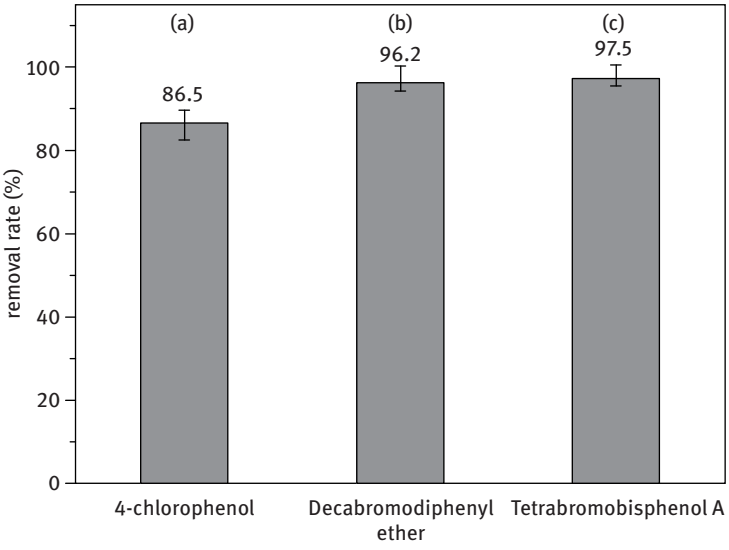

Figure 4.12: Degradation effect of montmorillonite-loaded nano-iron materials on three halogenated organic pollutants: (a) initial concentration of 4-chlorophenol =50.0 mg/L, material dosage =0.15 g, reaction time 2 h;(b)initial concentration of BDE =2.0 mg/L, material dosage = 0.60 g, reaction time 4 h; (c) initial concentration of TBBPA =10.0 mg/L, material dosage =0.02 g, reaction time 12 h

4.4.3 Factors affecting the degradation of halogenated organic pollutants by montmorillonite-loaded nano-iron material

The effect of montmorillonite-supported nano-iron materials on the degradation of halogenated organic compounds will be influenced by various factors. In order to understand their impact, BDE was used as an object. In addition, the various factors on the degradation of BDE by the montmorillonite-loaded nano-iron material were analyzed, including the initial concentration, material dosage, pH, reaction temperature, dissolved oxygen, solvent ratio and the times of material recycling.

(1) Effect of initial concentration

Under the conditions of the fixed M-NZVI dosage of 0.60 g, a reaction temperature of 25 °C±1 °C and a reaction solution of 50 mL, degradation effect of M-NZVI on BDE-209 was studied with three different initial concentrations (1.0 mg/L, 2.0 mg/L and 5.0 mg/L) as shown in Figure 4.13.

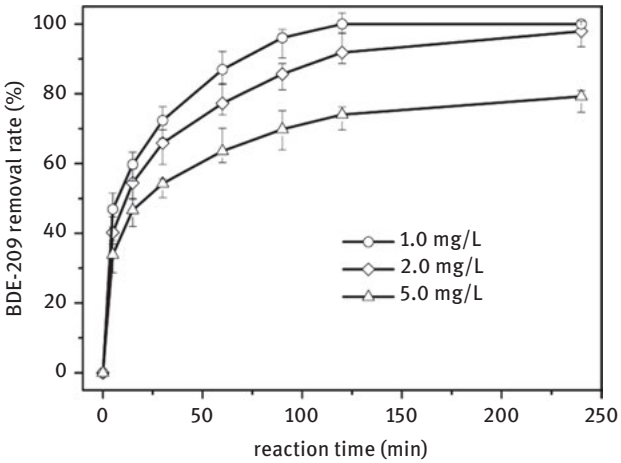

Figure 4.13: Effect of different initial solution concentrations on the removal of BDE-209 (experimental condition: material dosage=0.60 g, initial pH=5.5, reaction temperature=25 °C ±1 °C.

As can be seen from Figure 4.13, with the increase of the initial concentration of BDE-209 and a fixed dosage of M-NZVI, the removal rate of BDE-209 decreased. After 2 h of reaction, the removal efficiencies of BDE-209 with initial concentrations of 1.0 mg/L and 2.0 mg/L were above 80.0%, and BDE-209 in the reaction solution with the initial concentration of 1.0 mg/L was completely removed in 4 h. Compared with the initial concentration of 1.0 mg/L and 2.0 mg/L, the removal rate of BDE-209 in the reaction solution with the initial concentration of 5.0 mg/L was only 79.24% after 4 h. However, in the first 30 min, the removal rate of BDE-209 at an initial concentration of 5.0 mg/L was similar to that at the other two initial concentrations, and reached 54.27%. This was attributed to the strong specific surface area of M-NZVI. The degradation of BDE-209 by the M-NZVI material can be divided into two processes. The first 30 min was the rapid reaction process, and the reaction efficiency was very high. The removal rate of BDE-209 rapidly increased. After 30 min, the reaction entered the slow reaction stage. With the extended reaction time, the removal rate increased slowly. The abovementioned results indicate that the degradation of BDE-209 in the M-NZVI nanomaterial system is a heterogeneous reaction, which involves the adsorption reaction of BDE-209 on the surface of M-NZVI and the reduction of BDE-209. Although the increase of concentration of BDE-209 can make BDE-209 have

more contact opportunities with nano iron, but more contact opportunities are accompanied by the formation of iron oxides and hydroxides, resulting in the passivation of Fe^0 and the decrease of the reaction rate. In addition, with a fixed amount of M-NZVI, increasing the concentration of BDE-209 will lead to competitive adsorption between BDE-209 molecules, reducing the adsorption and reduction of BDE-209 on the surface of M-NZVI. On the other hand, the total active adsorption sites remain constant for a certain amount of M-NZVI material. As the concentration of BDE-209 increased, the active sites were gradually occupied, resulting that part of BDE-209 cannot be adsorbed and removed, thus reducing its removal rate.

(2) Effect of material dosage

The dosage is one of the most important factors for the degradation of BDE-209 by M-NZVI because the dosing amount determines the degradation capacity of M-NZVI under certain reaction conditions. The effects of dosage on the degradation of BDE-209 were studied by selecting four dosages of the M-NZVI material (0.20, 0.40, 0.60 and 0.80 g). The results are shown in Figure 4.14. As can be seen from Figure 4.14, the removal rate of BDE-209 increased with the increase of the M-NZVI dosage. When the M-NZVI dosage was 0.20, 0.40, 0.60 and 0.80 g, after 4 h reaction, the removal efficiencies of BDE-209 were 59.50%, 80.64%, 98.12% and 100%, respectively. When the M-NZVI dosage was 0.80 g, BDE-209 was completely removed within 2 h, and the removal efficiency was 1.04 times of that at dosage of 0.60 g, 1.24 times of that at dosage of 0.40 g and 1.68 times of that at dosage of 0.20 g. The abovementioned results indicate that the degradation of BDE-209 by M-NZVI is a surface reaction. Increasing the dosage of M-NZVI increases the effective surface area and the number of active sites. The larger the surface area of the material, the more reaction sites there are, and the better capacity of adsorption and degradation is obtained. Because of the huge specific surface area of the M-NZVI material, more active reaction sites are provided for the degradation of BDE-209, resulting in effective degradation and removal of BDE-209. When the dosage of the M-NZVI material becomes fewer, the surface area of nano iron is smaller, the corresponding reactive sites are fewer and the reaction rate is slower. When the dosage of M-NZVI is raised, the surface area and the reactive sites will be increased, as well as the contact chances of BDE-209 with fresh surface and the reaction rate.

It can also be seen from Figure 4.14 that in the first 30 min, the M-NZVI material degraded BDE-209 more rapidly and then the reaction rate became slower and slower because as the reaction proceeded, the zerovalent nano iron on the M-NZVI material will be gradually oxidized and a layer of oxide or hydroxide will be formed on its surface, which will continue to cover the reactive sites on the M-NZVI material, resulting in reduced removal efficiencies of the material to the BDE-209 in solution. The results show that the dosage of M-NZVI has a great effect on the debromination by nano-iron particles, because with the increase of the amount of nano-iron particles, their debromination efficiency is increased. However, taking into account the cost of the materials, the dosage of 0.60 g is considered to be better.

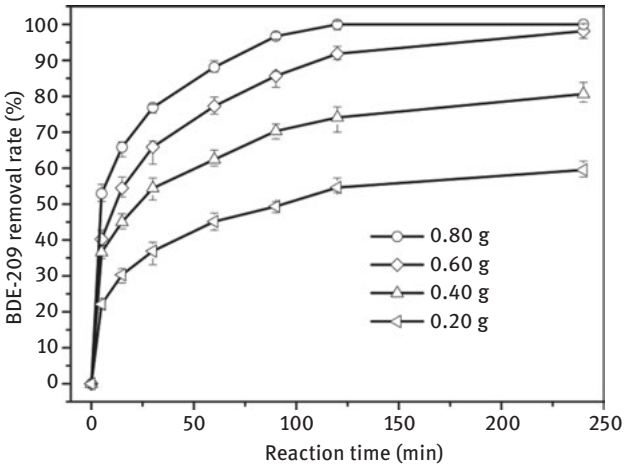

Figure 4.14: Effect of different dosages on the removal of BDE-209 (experimental condition: BDE-209 initial concentration=2.0 mg/L; initial pH=5.5; reaction temperature=25°C±1°C).

(3) Effect of pH

Some researchers have found that the pH of the reaction solution has a great impact on the degradation of halogenated organic pollutants by nano-iron materials. In order to study the influence of the initial pH of the reaction solution on the degradation of BDE-209 by M-NZVI, four initial pH values (pH = 3.0, pH = 5.5, pH = 7.0 and pH = 9.0) were chosen. The results are shown in Figure 4.15. It can be seen from Figure 4.15 that the BDE-209 removal efficiency of M-NZVI decreased with increasing pH in the reaction solution. In neutral (pH = 7.0) and alkaline (pH = 9.0) environments, after 4h reaction, BDE-209 removal rates were 76.04% and 65.90%, respectively. In comparison, under the reaction conditions of pH=5.5 and pH=3.0, the removal rate of BDE-209 after 4 h reaction were 98.25% and 100.0%, respectively, which were much higher than those under neutral and alkaline conditions. From the experimental results, it can also be seen that the removal rate of BDE-209 increases obviously with the decrease of pH in the first 30 min of the reaction, but the gap between the removal rates decreases with the reaction processing.

The abovementioned results show that low pH conditions are more beneficial for the removal of BDE-209 by M-NZVI. The reason can be summarized as follows: (1) The degradation of BDE-209 by zerovalent nano iron consumes H^+ ions, thus the reaction can be effectively promoted under acidic conditions; (2) previous TEM and XPS characterizations have confirmed that the nano-zerovalent iron particles supported on the organic montmorillonite are surrounded by a thin layer of oxide. While under acidic conditions, the surface oxide of the particles can be dissolved by acid, promoting the dehalogenation of BDE-209 by the zerovalent iron. At the same time, the presence of acid can effectively

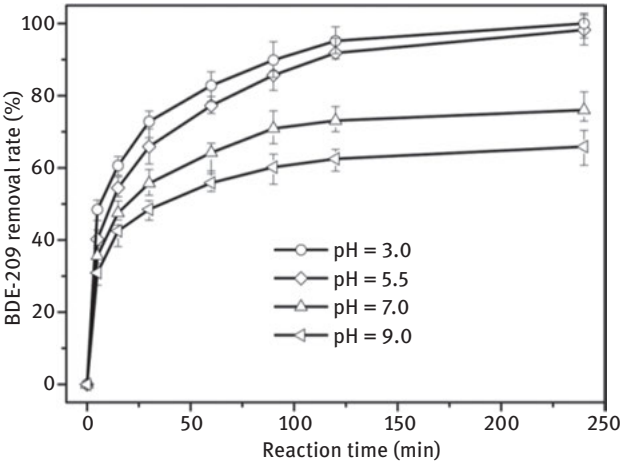

Figure 4.15: Effect of initial pH of reaction solution on the removal of BDE-209 (experimental condition: BDE-209 initial concentration=2.0 mg/L, material dosage=0.60 g, reaction temperature=25 °C±1 °C).

prevent the formation of iron oxide and hydroxide on the surface of M-NZVI, so as to maintain sufficient active sites on the surface of the material. The low pH, to a large extent, serves to pickle the iron particles, dissolving the hydroxide and the other protective layers of the iron particles in the M-NZVI material, so that more fresh active sites can be provided for the chemical reaction of nano iron and nitrate. However, under high pH conditions, the hydrogen ion concentration becomes very low. The iron ions generated by the corrosive reaction of zerovalent iron are converted into iron oxide and hydroxide precipitates, which adhere to the surface of zerovalent iron, preventing electron transfer between the zerovalent iron surface and the BDE-209, and inhibiting the reductive debromination reaction. This leads to the reduction of the BDE-209 removal efficiency of the M-NZVI material. At the same time, it can also be seen from Figure 4.15 that when the initial pH of the reaction solution was reduced from 5.5 to 3.0, the removal rate of BDE-209 was only increased by 1.75% after 4 h of reaction. In order to reduce the cost, the initial pH at 5.5 of the reaction solution is suitable.

(4) Effect of reaction temperature

The degradation of BDE-209 by M-NZVI with different reaction temperatures (10 °C, 25 °C and 40 °C) was studied under the conditions of a fixed M-NZVI dosage of 0.60 g and an initial BDE-209 concentration of 2.0 mg/L. The results are shown in Figure 4.16.

As can be seen from Figure 4.16, as the reaction temperature increased, the BDE-209 removal efficiency of M-NZVI was also rising. After 4 h reaction, the removal rates of BDE-209 reached 78.04%, 97.94% and 98.62% at 10 °C, 25 °C and 40 °C,

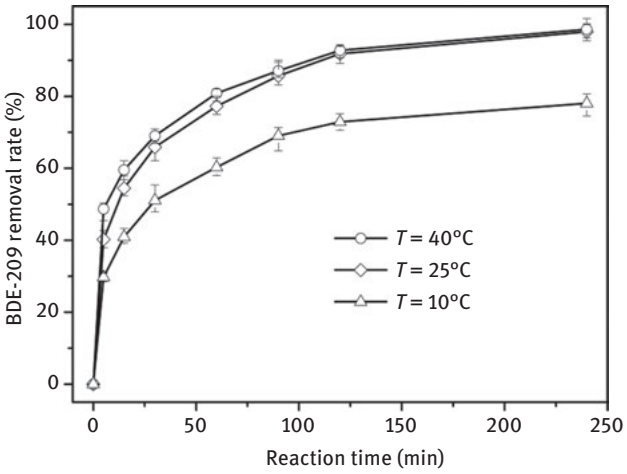

Figure 4.16: Effect of different reaction temperatures on the removal of BDE-209 (reaction condition: BDE-209 initial concentration=2.0 mg/L, material dosage=0.60 g, initial pH=5.5).

respectively. The BDE-209 removal efficiency of M-NZVI at room temperature or above room temperature (25 °C and 40 °C) was better than that at low temperature (10 °C), with 19.90% and 20.58% higher, respectively. However, the BDE-209 removal efficiency of M-NZVI at 25 °C and 40 °C did not differ significantly, with a slight difference of only 0.68%. The abovementioned results show that the reaction temperature has an effect on the BDE-209 removal efficiency of M-NZVI. The increase of temperature is favorable for debromination reaction of BDE-209. The increase of temperature improves the activity and transfer of electrons, increasing the chemical activity of NZVI on montmorillonite. However, the removal rate of BDE-209 changed a little when the temperature was further increased from 25 °C to 40 °C. Similar results were found by Zhang et al. (2011b). Therefore, it is proved that in this experiment setting the reaction temperature at 25 °C is suitable. On the one hand, the removal rate of BDE-209 at this temperature is already quite high. On the other hand, considering the energetic and practical aspects, the lower temperature makes the method more suitable for practical application and promotion.

(5) Effect of dissolved oxygen

It is well known that the NZVI iron is easily oxidized by oxygen in air or aqueous solution. For the study of the effect of DO (dissolved oxygen) on the removal rate of BDE-209, oxygenating the deionized water used for the reaction dilution was applied to adjust the initial DO content in the reaction solution. Different DO contents (DO = 0.0 mg/L, DO = 2.0 mg/L and DO = 4.0 mg/L) were selected for the batchwise experiment study. The results are shown in Figure 4.17. As shown in Figure 4.17, the removal rate of BDE-209 decreased with the increase of DO in the reaction solution.

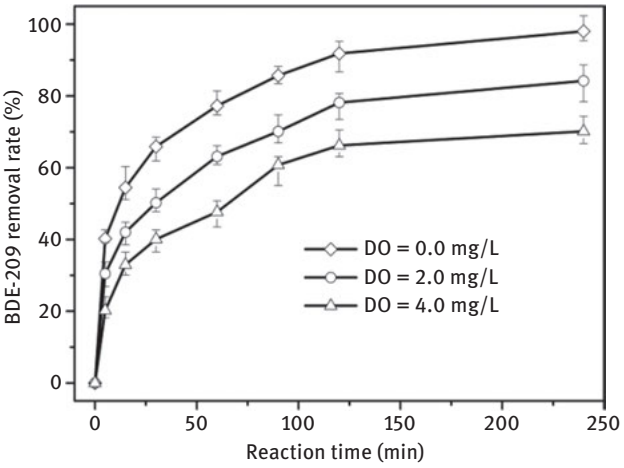

Figure 4.17: Effect of different initially dissolved oxygen (DO) concentrations on the removal of BDE-209 (experimental condition: BDE-209 initial concentration = 2.0 mg/L, material dosage=0.60 g, initial pH = 5.5, reaction temperature = 25 °C±1 °C).

When the DO concentration in the reaction solution is 0.0 mg/L, the BDE-209 removal efficiency of M-NZVI was up to 98.12% after 4 h reaction time, whereas the removal rate of BDE-209 decreased from 98.12% to 84.22% and 70.14%, respectively, when the DO increased from 0.0 mg/L to 2.0 mg/L and 4.0 mg/L, respectively, then reduced by 13.90% and 27.98%, respectively.

The abovementioned results show that the presence of DO in the reaction solution has a significant effect on the removal rate of BDE-209, which is mainly due to the oxidation effect. The nano-sized zerovalent iron particles supported on the organically modified montmorillonite are surrounded by a layer of iron oxide (as evidenced by the previous TEM characterization results). As the DO content of the reaction solution increases, the degree of oxidation of the nano-sized zerovalent iron particles is exacerbated and more iron oxides and hydrated oxides are formed on the surface of the M-NZVI material. The thickness of the iron oxide layer will also increase (XPS characterization results also proved that the oxygen content on the surface of the reacted M-NZVI material increased). This will reduce the activity of zerovalent nano-iron particles and hinder the contact between the BDE-209 molecules and the nano-iron particles, reducing the electron transfer from the zerovalent iron particles to BDE-209. As a result, the BDE-209 removal efficiency of the M-NZVI material is reduced.

(6) Effect of different cosolvent proportions

BDE-209 is a kind of highly hydrophobic halogenated organic pollutant, which is difficult to dissolve in water. When degradation studies are conducted, BDE-209 needs to be dissolved in water after dissolving in a certain proportion of tetra-

hydrofuran (THF) as a cosolvent, forming a "THF–water" system. In order to more realistically simulate the reaction conditions in the natural environment, the proportion of the cosolvent in the "THF-water" system should be as low as possible. Therefore, to study the effect of the ratio of cosolvent to water on the degradation of BDE-209, batch experiments were carried out using different THF/water ratios (THF: water = 3: 7, THF: water = 5: 5, THF: water = 7: 3 and THF: water = 10: 0). The results are shown in Figure 4.18.

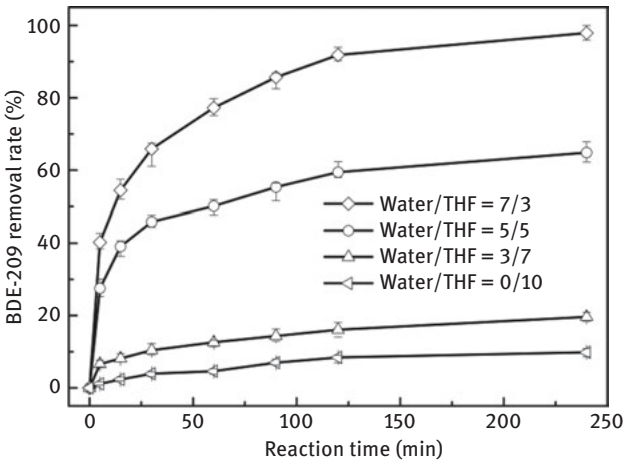

Figure 4.18: Effect of different proportions of cosolvent on the removal of BDE-209 (experimental condition: BDE-209 initial concentration = 2.0 mg/L, material dosage=0.60 g, initial pH = 5.5, reaction temperature = 25 °C±1 °C).

As can be seen from Figure 4.18, under the same reaction conditions, with the increase of the proportion of THF in the "THF–water" system, the BDE-209 removal efficiency of M-NZVI was continuously reduced. After 4 h of reaction, the removal rates of BDE-209 were 97.92%, 63.86%, 19.64% and 9.85%, respectively for THF/water ratios of 3: 7, 5: 5, 7: 3 and 10: 0. In the pure THF (THF: water=10: 0), the BDE-209 removal efficiency of M-NZVI was very low.

The abovementioned results show that the proportion of water in the BDE-209 reaction solution is very important. The larger the water proportion, the more favorable it is for the debromination reaction. The main reason is that the debromination of BDE-209 is a catalytic hydrogenation process. The debromination requires a certain amount of hydrogen ions, which can be obtained from the reaction solution. In the "THF–water" system, the higher the proportion of water, the more hydrogen ions can be provided. Meanwhile, the ionization constant of a variety of reaction solutions shows that the ionization constant of water is much greater than that of pure THF, so that in water more hydrogen ions can be generated, resulting in better debromination

of BDE-209. However, the proportion of water in the "THF–water" system cannot be infinitely enlarged in the experiment, because a certain amount of the cosolvent is required for completely dissolving BDE-209 in the "THF–water" system. The experimental results show that with the THF/Water ratio of 3:7, the solid BDE-209 can be completely dissolved in water providing maximal hydrogen ions. Thus, this ratio is more appropriate.

4.4.4 Effect of number of times of material recycling

The reuse efficiency of materials is an important evaluation parameter for the practical application of the material. In order to investigate the reuse efficiency of M-NZVI and NZVI materials for the removal of BDE-209 in the experiment, under the condition of room temperature (25 °C±1 °C), 50 mL of mixed solution with 2.0 mg/L BDE-209 were added into a 100 mL Erlenmeyer flask with a stopper, and then 0.60 g of M-NZVI and NZVI materials were added respectively. The reactor was sealed and placed in a thermostatic shaker, with a control speed of 150 r/min. After 4 h of reaction, the sample was centrifuged at 3,000 rpm for the solid–liquid separation. The concentration of BDE-209 in the filtrate after the separation was measured by high performance liquid chromatography (HPLC). The separated material was dried at 105 °C and then added to another flask containing 50 mL of BDE-209 mixed solution at a concentration of 2.0 mg/L. After 4 h reaction, the reaction mixture was subjected to solid–liquid separation. For the filtrate, the concentration of BDE-209 was measured. This operation was repeated five times. The results are shown in Figure 4.19.

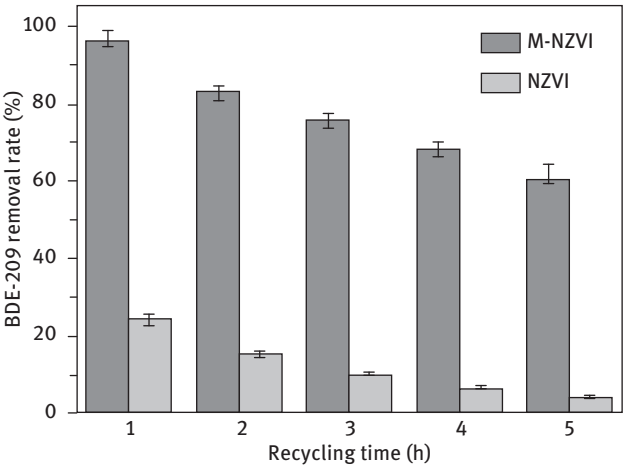

Figure 4.19: Effect of material recycling on the removal of BDE-209.

As can be seen from Figure 4.19, both M-NZVI and NZVI materials can repeatedly remove BDE-209, but the BDE-209 removal rate of the materials decreased with the increase in recycling times. The BDE-209 removal rate of the M-NZVI material decreased from 96.12% to 60.31%, which indicates that M-NZVI material still had certain ability to remove BDE-209 after five times recycling. With montmorillonite as the carrier of nano iron, the reusability and stability of the nano iron in the process of dealing with pollutants was improved. Compared with M-NZVI, the BDE-209 removal rate of NZVI decreased from 24.35% to 3.65%, which indicates that the BDE-209 removal ability of NZVI almost exhausted after the recycling of NZVI. The reason is that with the repeated contact with aqueous solution on the agglomerated material the surface oxide is increased, which makes the material inactive.

4.5 Kinetic study on degradation of decabromodiphenyl ether by organic-montmorillonite-loaded nano iron

4.5.1 Kinetic study

The reaction of iron particles or nano iron with halogenated organic pollutants in aqueous solution of the reaction belongs to heterogeneous reaction in solution including two phases: solid and liquid. The reaction occurs in a heterogeneous system and the most important factor affecting the kinetics of the reaction is the characteristic of the phase interface. The surface reaction between the solid and liquid phases generally has the following major steps: (1) molecules of halogenated organic pollutants diffuse to the surface of iron particles or nano iron; (2) the diffused iron particles or nano iron are adsorbed by the solid material; and (3) the molecules of the adsorbed halogenated organic pollutants react on the surfaces of the iron particles or nano iron, generating product molecules of the halogenated organic pollutants absorbed by the solid material. In the abovementioned three steps, the reaction step (3) is the main reaction step for the reduction and removal of halogenated organic pollutants, whereas steps (1) and (2) have a big influence on the progress of the entire reaction and the reaction rate, although they are not the main steps of the reaction.

In the aqueous solution of BDE-209, the surface of the nano-iron particles in contact with the BDE-209 aqueous solution can be referred to as the solid–liquid two-phase interface, where the debromination reaction of BDE-209 occurs. Therefore, the reaction steps of BDE-209 are basically the same as the degradation by nano iron of other halogenated organic pollutants. In recent years, many researchers have studied the reaction kinetics of BDE-209 degradation in aqueous solution by nano iron (or other metals). Most of them have found that the reaction of BDE-209 with nano iron (or other metals) obeys the pseudo-first-order reaction kinetic equation.

Therefore, in this study, the pseudo-first-order kinetic equation was used to study the kinetics of degradation of BDE-209 by the montmorillonite-supported nano-iron material. The pseudo-first-order kinetic equation can be written as follows:

$$\frac{dC_{BDE-209}}{dt} = -k_{obs}C_{BDE-209} \tag{4.7}$$

Formula (4.7) is integrated to obtain the following:

$$\ln\frac{C_{BDE-209}}{C_{0BDE-209}} = -k_{obs}t \tag{4.8}$$

where t is the reaction time, min; k_{obs} is the apparent rate constant in pseudo-first-order kinetic reaction, min^{-1}; $C_{BDE\text{-}209}$ is the concentration of BDE-209 in solution at reaction time t, mg/L; $C_{0BDE\text{-}209}$ is the initial concentration of BDE-209, mg/L.

The half-life time is calculated according to the following formula:

$$t_{1/2} = \frac{\ln 2}{k_{obs}} = \frac{0.6932}{k_{obs}} \tag{4.9}$$

For comparison purposes, two kinds of materials: M-NZVI and NZVI, were chosen to fit the degradation kinetics of BDE-209. The parameters are shown in Table 4.5 and the fitted curves are shown in Figure 4.20.

Table 4.5: Comparison of apparent rate constants and half-life time of degradation of BDE-209 by M-NZVI and NZVI.

Material type	k_{obs}/min^{-1}	$t_{1/2,obs}/min$	r^2
M-NZVI	1.525×10^{-2}	45.46	0.9622
NZVI	0.153×10^{-2}	453.08	0.9083

As can be seen from Figure 4.20, the linear fitting of ln (C_t/C_0) to the reaction time showed that the degradation reaction of BDE-209 by M-NZVI and NZVI both accorded with the pseudo-first-order reaction kinetics. As shown in Table 4.5, through the slope of the regression line, the apparent rate constants of degradation of BDE-209 by M-NZVI and NZVI were 1.525×10^{-2} and 0.153×10^{-2}, respectively. The apparent rate constant of M-NZVI was 9.96 times that of NZVI, indicating that the M-NZVI material has a higher reactivity.

As discussed earlier, the surface of the M-NZVI material in contact with the BDE-209 aqueous solution is where the debromination by the nano iron occurs. Therefore, the surface size, surface morphology and surface reactivity of the M-NZVI material have a great influence on the debromination reaction. The characterization results in

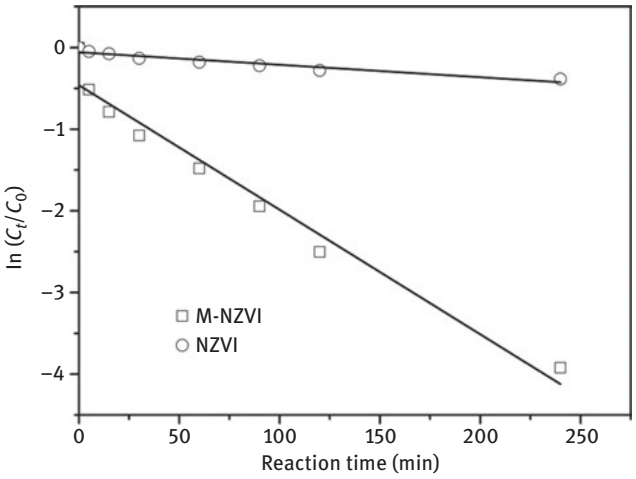

Figure 4.20: Kinetic data fitting of degradation of BDE-209 by M-NZVI and NZVI.

Section 4.3 show that compared with NZVI, M-NZVI has better dispersibility and larger specific surface area, which determine that with the same dosage, the M-NZVI material can provide more adsorption and reactive sites for the redox reaction, and thus the reaction rate is faster.

From Figure 4.20 and Table 4.5, we can see that the pseudo-first-order kinetic equation of the degradation of BDE-209 by M-NZVI after fitting is as follows:

$$y = -0.460\ 94 - 0.015\ 25x \tag{4.10}$$

In contrast to the Formula (4.8), the fitted degradation equation of BDE-209 is as follows:

$$C_{t\mathrm{BDE-209}} = C_0 \times \exp(-0.46094 - 0.01525t) \tag{4.11}$$

Substituting C_0 = 2.0 mg/L and reaction time (0, 5, 15, 30, 60, 90, 120 and 240 min) into Formula (4.11), the concentration of BDE-209 in the solution after the reaction time point is obtained and can be compared with the measured value, as shown in Table 4.6 and Figure 4.21.

Table 4.6: Comparison of measured and fitted concentrations of the remaining BDE-209 after reaction.

Reaction time (min)	5	15	30	60	90	120	240
Measured value(mg/L)	1.195	0.911	0.682	0.455	0.286	0.164	0.040
Fitted value(mg/L)	1.169	1.003	0.798	0.505	0.320	0.202	0.032
Error (%)	2.2	−10.1	−17.0	−12.4	−11.89	−23.17	20.0

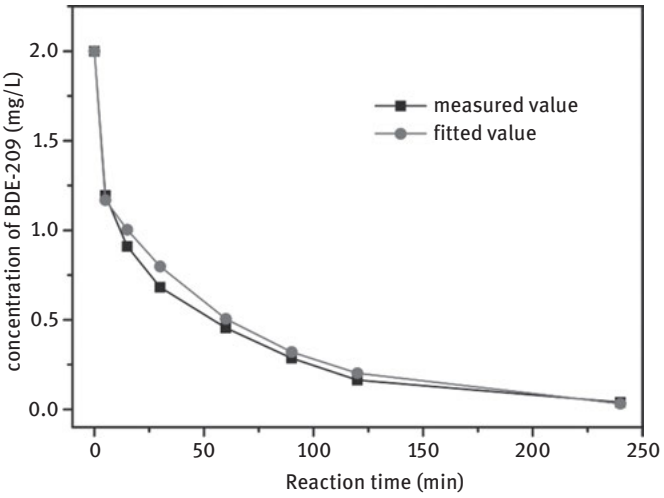

Figure 4.21: Comparison of measured and fitted concentrations of BDE-209 after reaction.

From Table 4.6 and Figure 4.21, it can be seen that there is a certain error between the measured and the fitted concentrations of the remaining BDE-209 after the reaction. Most of the measured values are smaller than the fitted values, but the absolute values are not much different. The fitted curve basically coincides with the curve of the measured values, indicating that the fitted pseudo-first-order kinetic equation is suitable for estimating the residual concentration after degradation of BDE-209 by M-NZVI after different reaction times.

4.5.2 Influence of different factors on the apparent rate constant k_{obs}

The results given in Section 4.4 show that the reaction of BDE-209 with M-NZVI is affected by various factors. In order to understand the influence of different factors on the apparent rate constant k_{obs}, the apparent rate constant k_{obs} was studied under consideration of the initial concentration of BDE-209, the material dosage, the initial reaction pH and the reaction temperature, altogether four factors.

(1) Effect of initial concentration of BDE-209 on the apparent rate constant k_{obs}

A large number of studies have shown that the apparent rate constant and the half-life time of the reduction reaction of halogenated organic compounds by zerovalent iron are affected by the initial concentration of halogenated organic compounds. This law is also applicable to the heterogeneous reaction, the degradation of BDE-209 by zerovalent iron. That is, both the apparent rate constant k_{obs} and the half-life time of the reaction are related to the initial concentration of BDE-209.

In the experiment, the initial concentration of BDE-209 was 1.0, 2.0 and 5.0 mg/L, respectively. The initial pH of the reaction solution was 5.5, the reaction time was 4.0 h, and the dosage of the material was 0.6 g. Based on the experimental conditions, the reaction kinetics of the degradation of BDE-209 by M-NZVI was linearly fitted. The relationship between the apparent rate constant and the initial concentration of BDE-209 is shown in Table 4.7 and Figure 4.22.

Table 4.7: Apparent rate constants at different initial concentrations of BDE-209.

BDE-209 initial concentrations (mg/L)	k_{obs} (min)	$t_{1/2,obs}$ (min)	r^2
1.0	2.821×10^{-2}	24.51	0.9185
2.0	1.55×10^{-2}	44.72	0.9853
5.0	0.633×10^{-2}	109.51	0.9403

It can be seen from Figure 4.22 that the reaction of BDE-209 degraded by M-NZVI at different initial BDE-209 concentrations was in accordance with the pseudo-first-order reaction kinetics. As can be seen from Table 4.7, the k_{obs} of BDE-209 at initial concentrations of 1.0, 2.0 and 5.0 mg/L were 2.821×10^{-2}, 1.550×10^{-2} and 0.633×10^{-2}, respectively. The results showed that with the increase of the initial concentration of BDE-209, its apparent reaction rate constant k_{obs} gradually decreased, that is, the degradation reaction rate of BDE-209 gradually decreased with the increase in BDE-209 concentration. This result is also consistent with results of many researchers. For

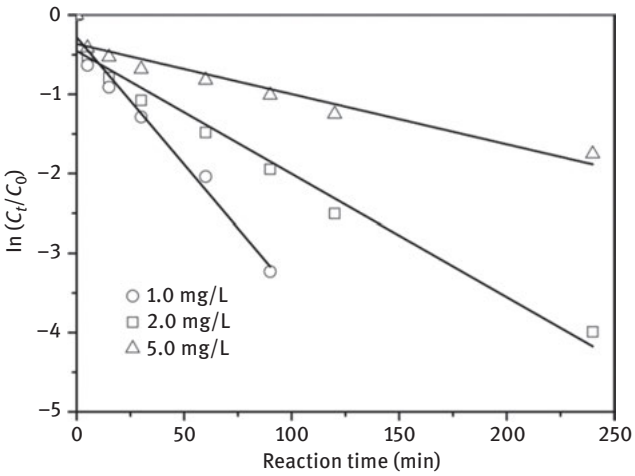

Figure 4.22: Kinetic data fitting of degradation of BDE-209 by M-NZVI at different initial concentrations.

a certain amount of the M-NZVI material, the total number of effective reactive sites in the material is certain. As the concentration of pollutants increases, the reactive sites are gradually occupied, and there is competition between the BDE-209 molecules due to increase of the number of molecules, resulting in reduced removal rates. So the rate constant of k_{obs} is gradually decreased.

(2) Effect of M-NZVI dosage on the apparent rate constant k_{obs}

In order to study the effect of the additional amount of M-NZVI on the apparent rate constant k_{obs}, the experimental conditions are as follows: the dosage of the material was respectively 0.20, 0.40, 0.60 and 0.80 g, respectively; the initial concentration of BDE-209 was 2.0 mg/L, the initial pH of the reaction solution was 5.5 and the reaction time was 24 h. The reaction kinetics of M-NZVI-degrading BDE-209 was linearly fitted according to the experimental conditions. The relationship between the apparent rate constant and the initial BDE-209 concentration is shown in Table 4.8 and Figure 4.23.

Table 4.8: Apparent rate constant at different material dosages.

M-NZVI material dosage (g)	k_{obs} (min^{-1})	$t_{1/2,obs}$ (min)	r^2
0.20	0.433×10^{-2}	160.09	0.9253
0.40	0.721×10^{-2}	96.14	0.9264
0.60	1.548×10^{-2}	44.78	0.9656
0.80	2.245×10^{-2}	21.36	0.9736

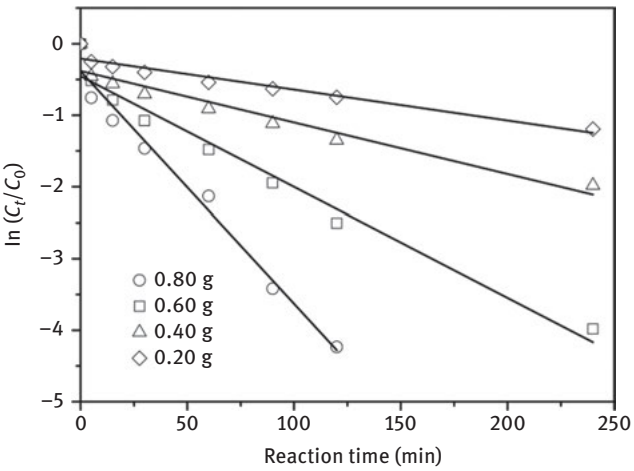

Figure 4.23: Kinetic data fitting of degradation of BDE-209 by M-NZVI at different material dosages.

From Figure 4.23, it can be seen that the reaction of BDE-209 degraded by M-NZVI with different amounts of M-NZVI also accords with pseudo-first-order reaction kinetics. As can be seen from Table 4.8, when the dosage of M-NZVI is 0.20, 0.40, 0.60 and 0.80 g, respectively; the apparent reaction rate constant k_{obs} increases gradually, with the value of 0.433×10^{-2}, 0.721×10^{-2}, 1.548×10^{-2} and 2.245×10^{-2}, respectively. The results show that the reaction rate of M-NZVI degrading BDE-209 gradually increases with the increase of the dosage of M-NZVI. The increase of the M-NZVI dosage means that the increase of the total specific surface area of the material also increases the total number of active sites in the material, which is favorable for the adsorption and reduction of BDE-209. As a result, the removal rate is improved and the rate constant k_{obs} gradually increases, which is also consistent with the previous trend that the increase of the dosage of M-NZVI is in favor of the degradation of BDE-209.

In order to understand the relationship between the added amount of M-NZVI and the apparent rate constant k_{obs}, the apparent reaction rate constant k_{obs} was used to plot and fit the material dosage of M-NZVI, as shown in Figure 4.24. It can be seen from the figure that in the system of removing BDE-209 by M-NZVI, the linear fitting curve between the apparent rate constant k_{obs} and the material dosage of M-NZVI did not pass through the origin of the coordinates. It was indicated that the degradation mechanism of BDE-209 included the reduction by nano-zerovalent iron and the adsorption by nano-zerovalent iron and montmorillonite.

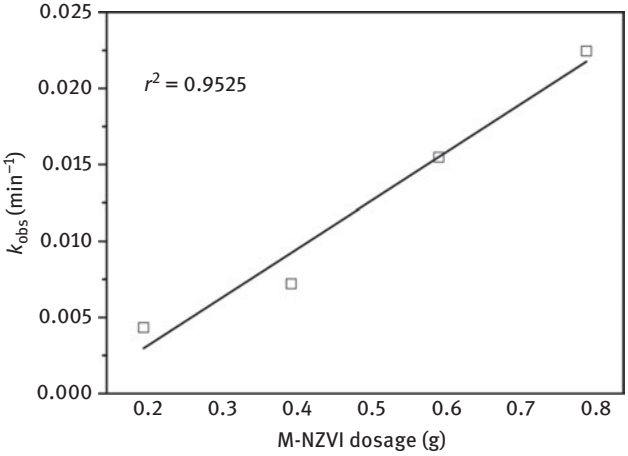

Figure 4.24: Relationship between dosage of M-NZVI and apparent reaction rate constant k_{obs}.

(3) Effect of the initial pH of the reaction solution on the apparent rate constant k_{obs}

The influence of the initial pH of the reaction solution on the apparent rate constant k_{obs} was studied mainly by adjusting the initial pH of the reaction solution. The pH was set to 3.0, 5.5, 7.0 and 9.0, in total 4 values, whereas other conditions remained unchanged.

According to the experimental conditions, the reaction kinetic of M-NZVI degrading BDE-209 was linearly fitted. The relationship between the apparent rate constant and the initial pH of the reaction solution is shown in Table 4.9 and Figure 4.25.

Table 4.9: Apparent rate constant at different initial pH.

Initial pH of the reaction solution	k_{obs} (min^{-1})	$t_{1/2,obs}$ (min)	r^2
3.0	2.184×10^{-2}	31.74	0.9448
5.5	1.502×10^{-2}	46.15	0.9594
7.0	0.722×10^{-2}	96.02	0.9517
9.0	0.576×10^{-2}	120.35	0.9290

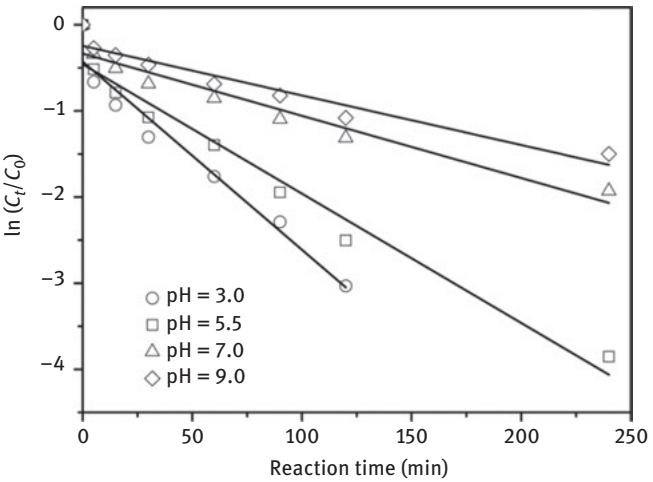

Figure 4.25: Kinetic data fitting of degradation of BDE-209 by M-NZVI at different initial pH.

As can be seen from Figure 4.25, the degradation of BDE-209 by M-NZVI at different initial pH values was in accordance with the pseudo-first-order reaction kinetic equation. The initial pH of the reaction solution had a great influence on the apparent reaction rate constant k_{obs}. The k_{obs} value decreased with the increase in the initial pH of the reaction solution. It can be seen from Table 4.9 that when the pH of the reaction solution was 3.0, 5.5, 7.0 and 9.0, the apparent reaction rate constants k_{obs} was 2.184×10^{-2}, 1.502×10^{-2}, and 0.722×10^{-2} and 0.576×10^{-2}, respectively. The apparent reaction rate constant k_{obs} at pH 3.0 was 3.79 times that at pH 9.0. The results showed that the acidic environment was favorable for the degradation of BDE-209 by M-NZVI. Under acidic conditions, the reaction rate of

BDE-209 was faster, and the results are similar to that of many researchers. The effect of pH on the degradation of BDE-209 has been discussed in this chapter. It was indicated that the acidic environment prevented the formation of iron oxide and hydroxide precipitates, and promoted the electron transfer between the surface of zerovalent iron and BDE-209, thereby increasing the degrading effect of BDE-209. So the apparent reaction rate constant k_{obs} decreased with increasing pH.

(4) Effect of different reaction temperatures on the apparent rate constant k_{obs}

The effect of reaction temperature on the degradation of BDE-209 has been discussed in this chapter. The results showed that the increase in temperature was beneficial to the degradation of BDE-209. However, the improved effect was not obvious when the temperature was above 25 °C. In order to study the effect of reaction temperature on the apparent rate constant k_{obs}, the experimental data were linearly fitted to the kinetics at reaction temperatures of 10 °C, 25 °C and 40 °C, respectively. The results are shown in Table 4.10 and Figure 4.26.

Table 4.10: Apparent rate constant at different reaction temperatures.

reaction temperature (°C)	k_{obs} (min^{-1})	$t_{1/2,obs}$ (min)	r^2
10.0	0.734×10^{-2}	94.444	0.9292
25.0	1.514×10^{-2}	45.79	0.9615
40.0	1.762×10^{-2}	39.34	0.9749

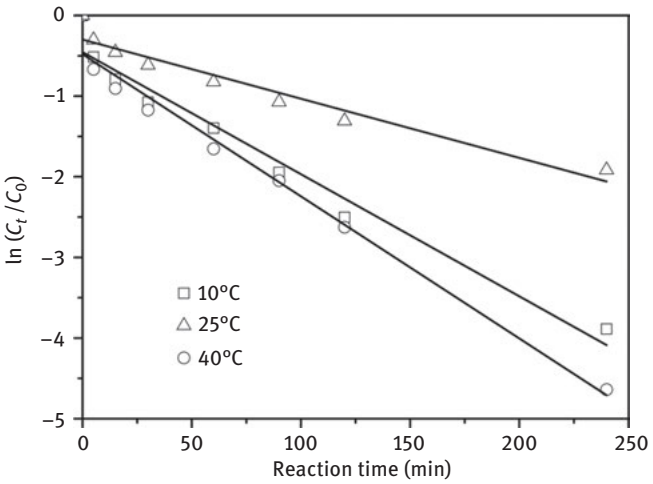

Figure 4.26: Kinetic data fitting of degradation of BDE-209 by M-NZVI at different reaction temperatures.

As can be seen from Figure 4.26 and Table 4.10, the apparent reaction rate constant k_{obs} increased with rising reaction temperature. When the reaction temperature was raised from 10 °C to 40 °C, the apparent reaction rate constant k_{obs} increased from 0.734×10^{-2} to 1.762×10^{-2}, increased more than two times. However, when the reaction temperature increased from 25 °C to 40 °C, the apparent reaction rate constant was increased only by 2.48×10^{-3}. The results showed that the increase of reaction temperature was beneficial for the increase of reaction rate constant k_{obs}, but not obviously over the room temperature. That is to say, the increase of BDE-209 was not obvious. This is consistent with the related results in this chapter.

4.6 Research of degradation mechanism and ways

4.6.1 Degradation process and mechanism analysis

The degradation of halogenated organic matter by nano iron occurs mainly through the following three ways: (1) direct electron transfer of Fe°; (2) reduction by electron transfer of Fe°-corrosion, producing Fe^{2+}; (3) Reduction by H^2 in the Fe°–H2O system. Way (1) plays a major role in the process of degradation and dehalogenation. The process can be expressed by the following equation:

$$Fe^0 \rightarrow Fe^{2+} + 2e^- \tag{4.12}$$

$$C_xH_yBr_z + zH^+ + ze^- \rightarrow C_xH_{y+z} + zBr \tag{4.13}$$

$$2Fe^{2+} + RBr + H^+ \rightarrow 2Fe^{3+} + RH^+Br^- \tag{4.14}$$

As discussed in the previous section, the degradation process of halogenated organic pollutants by nano iron is mainly an interfacial chemical process. The main process of degradation of BDE-209 by M-NZVI is as follows: M-NZVI is added to BDE-209 aqueous solution, the M-NZVI material and BDE-209 molecules will diffuse and migrate at the interface. When the molecule of BDE-209 in solution diffuses to the surface of M-NZVI, it is first adsorbed by the active site of M-NZVI and then the adsorbed BDE-209 molecule is reduced with Fe° on the surface or in the interstice of organic montmorillonite. The debrominated product after the reaction is desorbed from the surface of the M-NZVI material and transferred to the solution. This is the degradation process of BDE-209 degraded by the M-NZVI material.

In order to understand the degradation of BDE-209 at different times and the change of the debromination rate, the experimental results were plotted as shown in Figure 4.27. As can be seen from the figure, the M-NZVI material has a very high removal rate of nearly 50% in the first 30 min, because of the large

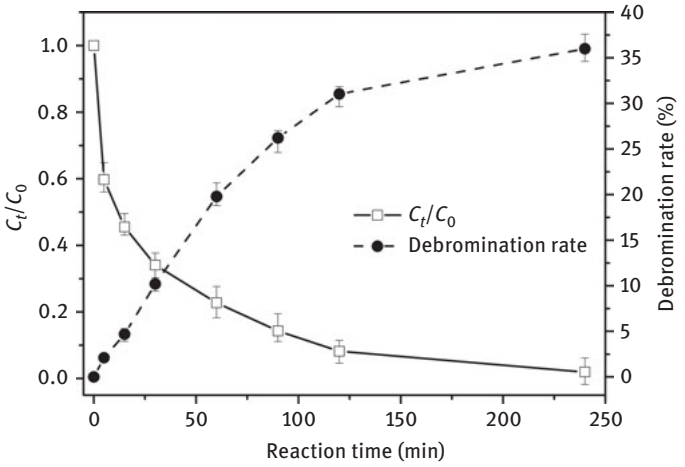

Figure 4.27: Degradation and debromination rate of BDE-209 at different time.

specific surface area of the M-NZVI material. In addition, as the adsorption capacity of montmorillonite to hydrophobic halogenated organic pollutants was greatly enhanced after the organic modification, the degradation process was mainly adsorption, accompanied by debromination and reduction (as evidenced by the subsequent HPLC and GC-MS measurements) in the first 30 min. The debromination rate curve also illustrates this. In the first 30 min, debromination rate grew more slowly and reached only 8.20%. After the reaction for 30 min, the debromination and reduction accounted mainly for the degradation process, assisted by adsorption. As can be seen from the figure, with the increase of reaction time, the removal rate of BDE-209 increased slowly, but the rate of debromination increased rapidly from 8.20% to 36.01%. The abovementioned results again showed that the degradation of BDE-209 by M-NZVI is a result of synergistic adsorption and reduction.

4.6.2 Analysis of degradation products

(1) Distribution of debromination products

In order to understand the distribution of each product after debromination of BDE-209, the reaction solution of BDE-209 degraded by M-NZVI was analyzed by LC-MS/MS and HPLC. The retention times of each product peak and the peak order were compared with the standard results of LC-MS/MS and HPLC. To ensure the accuracy, blank experiments were carried out, and no debromination products related to BDE-209 were detected. Figure 4.28 shows the columnar distribution of debromination products of BDE-209 over time, and Figure 4.29 shows the results of HPLC analysis of BDE-209 and of each debromination product at each reaction time point.

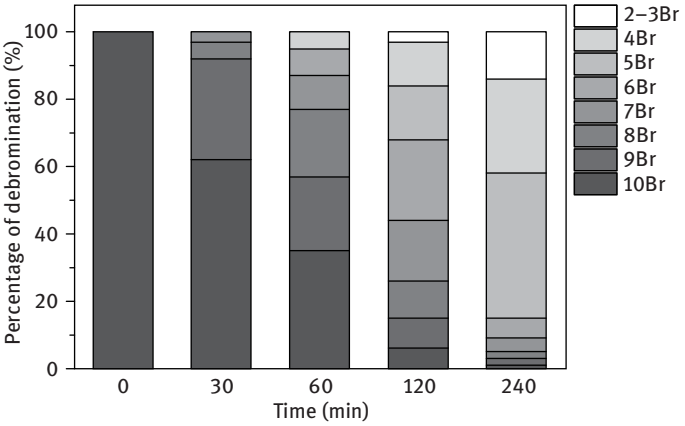

Figure 4.28: Columnar distribution of debromination products of BDE-209 over time.

As can be seen from Figure 4.29, the process of degradation of BDE-209 by M-NZVI follows the gradual debromination. Deca-brominated diphenyl ether (BDE)-209 was first debrominated from decabromo compounds to nona-BDEs and octa-BDEs with time, stepwise to hepta-BDEs and hexa-BDEs and finally to penta-BDEs, tetra-BDEs and tri-BDEs. The histogram of each debromination product of BDE-209 was obtained by plotting the ratio of the HPLC response of each debromination product of BDE-209 to the response of the BDE-209 precursor compound (see Figure 4.28). As can be seen from Figure 4.28, at different time points, the proportion of each debromination product constantly changed over time. The proportion of high-brominated compounds gradually decreased, whereas the proportion of all low-brominated compounds gradually increased. Hepta-BDEs and hexa-BDEs were the main debromination intermediates in the system. Penta-BDEs, tetra-BDEs and tri-BDEs were the final products of the debromination reaction, of which tetra-BDEs accounted for the largest proportion.

The debromination rate of BDE-209 is mainly obtained by calculating the ratio of the total amount of bromide ions released into the solution to the total amount of bromine atoms in BDE-209. Theoretically, when BDE-209 is totally debrominated, generating penta-BDEs, the debromination rate is 50%. As can be seen from Figure 4.28, after the reaction of M-NZVI with BDE-209 for 24 h, the penta-BDEs or less brominated homologues accounted for 82.15% of the debromination products, which was in agreement with the measured debromination rate (36.01 %).

(2) Identification of debrominated products

The intermediate and final products of degradation of BDE-209 by M-NZVI were identified by GC-MS and LC-MS/MS at 30, 120 and 240 min, respectively. The results can be seen in Figure 4.30 to Figure 4.32. In order to accurately identify the

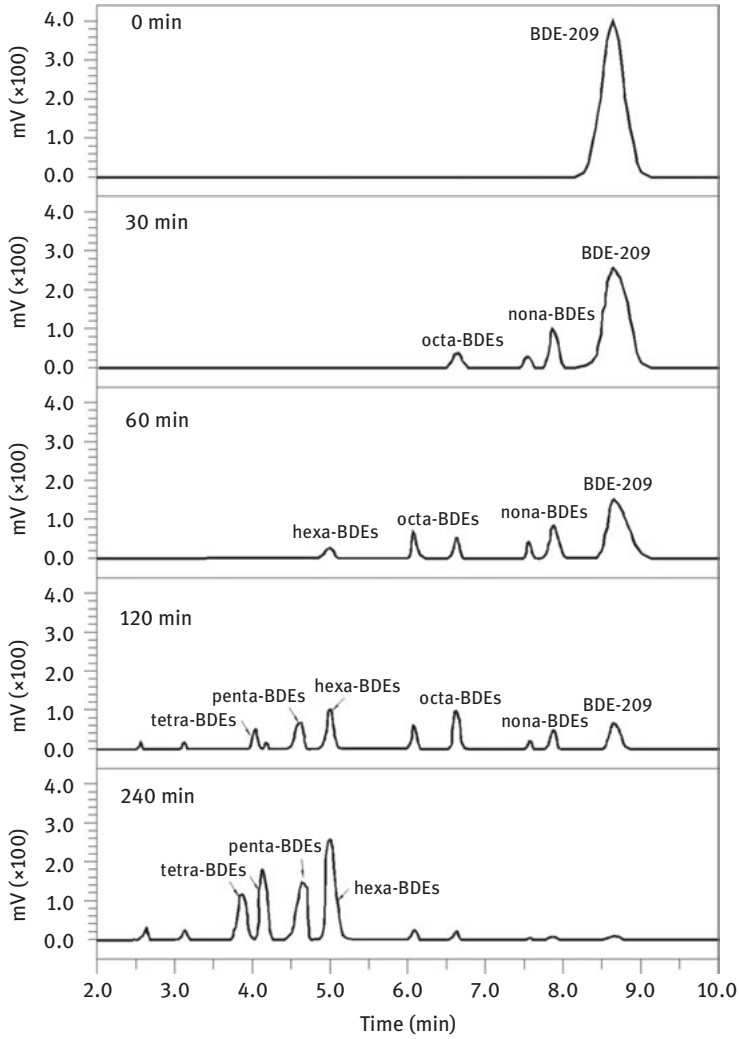

Figure 4.29: HPLC analysis of BDE-209 and degradation products at different times.

intermediates and final product types of the reductive debromination reaction of BDE-209, the exact peak time of PBDEs standard substances and the mass spectra were used for stacked processing and detailed comparison, according to the retention time and mass spectra of different brominated diphenyl ethers in the GC-MS spectra.

From Figure 4.30 to Figure 4.32, it can be seen that during the degradation of BDE-209 by M-NZVI, a total of 21 brominated biphenyl ether-like products were produced, from nona-BDEs to tri-BDEs, indicating again that the degradation of BDE-209 is a gradual debromination process. As can be seen from the GC-MS, the total ion

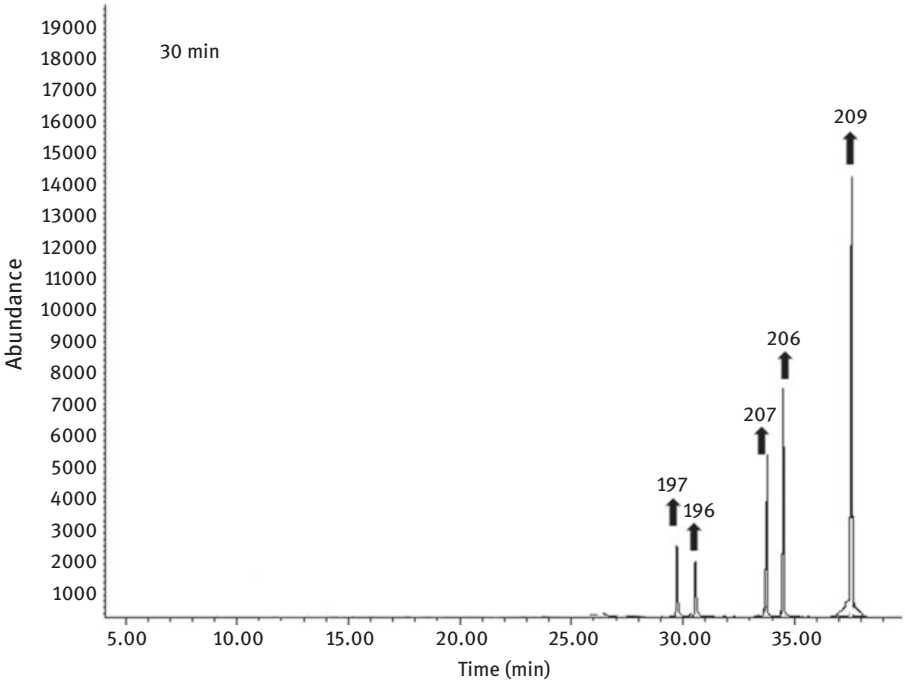

Figure 4.30: GC-MS analysis of BDE-209 and its degradation products (30 min).

chromatogram at 30 min is shown in Figure 4.30. In the debromination and reduction of BDE-209, first a bromine atom was taken to form nona-BDEs. The product mainly consists of two isomers: BDE-207 and BDE-206. Further, a bromine atom was removed, producing two octa-BDEs isomers, which were qualified as BDE-196 and BDE-197. However, BDE-203 was not found.

As can be seen from the GC-MS total ion chromatogram in Figure 4.31, two brominated isomers of hepta-BDEs were found after 120 min of reaction, one of which was BDE-191, and the other was BDE-183 that had a shorter peak time. It can also be seen from Figure 4.31 that four hexa-BDEs isomers were identified as BDE-153, BDE-154, BDE-138 and BDE-156, respectively, by comparison with standards. It was indicated that hexa-BDEs were the main debromination intermediates. The data in Figure 4.28 also show that hexa-BDEs accounted for a large proportion of the products at 120 min.

As can be observed from the GC-MS total ion chromatograms in Figure 4.31 and Figure 4.32, four penta-BDEs isomers were found in the reaction of BDE-209 degraded by M-NZVI: (1) BDE-126, (2) BDE-119, (3) BDE-99 and (4) BDE-100. Among them, BDE-119 had the highest abundance in the GC-MS total ion chromatogram at 240 min, whereas the data in Figure 4.28 also showed that penta-BDEs had the highest proportion of the final products. Four tetra-BDEs isomers were

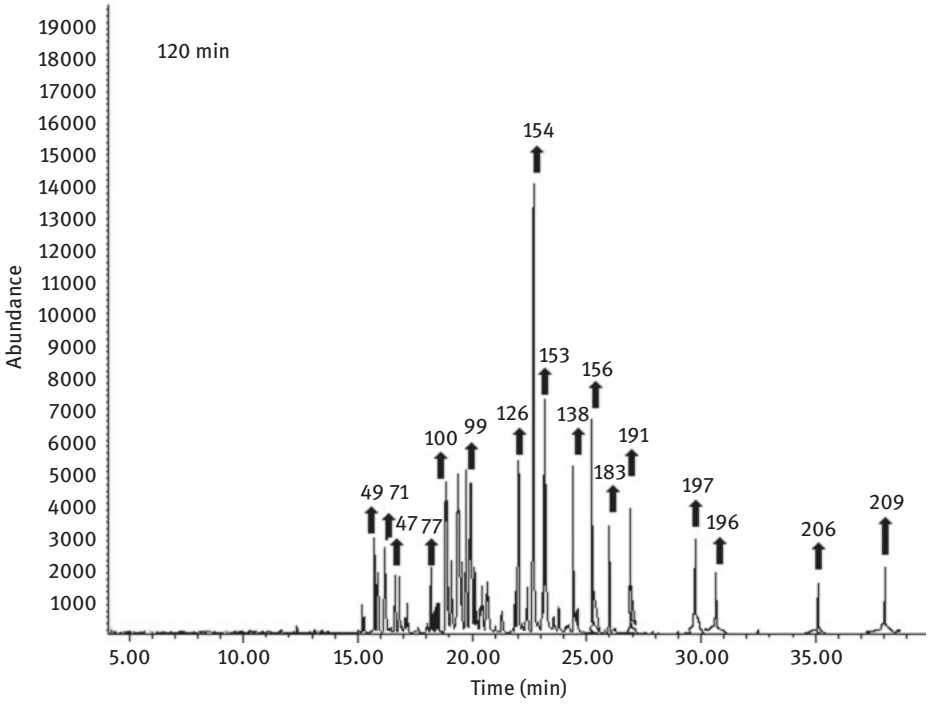

Figure 4.31: GC-MS analysis of BDE-209 and its degradation products (120 min).

found from Figure 4.32: (1) BDE-77, (2) BDE-71, (3) BDE-49 and (4) BDE-47. The proportion of such brominated compounds in the final products was second to that of penta-BDEs. Although BDE-47 is a relatively easy-to-detect class of PBDEs in real environment, its proportion of debrominated products in this study was not high. At the same time, one tri-BDEs and one di-BDEs isomer were also found in the debromination products after 240 min reaction. Compared to standards, they could be identified as BDE-17 and BDE-15. In addition, a small peak at the retention time of 15 min in the GC-MS total ion chromatogram failed to be identified.

4.6.3 Analysis of degradation pathway

Based on the previous degradation mechanism analysis of BDE-209 degraded by M-NZVI and the identification results of debromination intermediate and final product, it can be told that the degradation of BDE-209 by M-NZVI is a gradual debromination process. Mainly through the gradual replacement of bromine atoms with hydrogen atoms, the conversion of high-brominated diphenyl ether to low-brominated diphenyl ethers is completed. With the processing of the

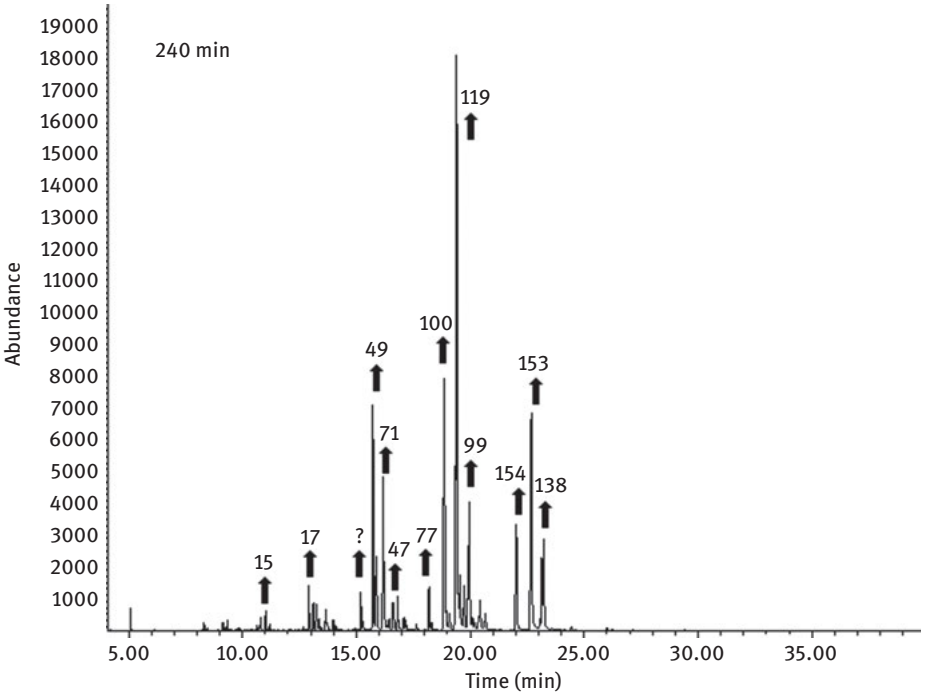

Figure 4.32: GC-MS analysis of BDE-209 and its degradation products (240 min).

debromination reaction, low-brominated diphenyl ether homologues increase in the proportion of the degradation products. The final degradation results show that the debromination effect of M-NZVI on BDE-209 is obviously good.

Table 4.11: GC-MS retention time of debromination products of BDE-209.

Serial number	Number of bromine atoms	Product	Retention time (min)	Serial number	Number of bromine atoms	Product	Retention time (min)
1	10	BDE-209	37.51	12	5	BDE-126	21.69
2	9	BDE-206	34.47	13		BDE-99	19.96
3		BDE-207	33.67	14		BDE-119	19.45
4	8	BDE-196	30.57	15		BDE-100	19.09
5		BDE-197	29.73	16		BDE-77	17.98
6	7	BDE-191	27.14	17	4	BDE-47	16.65
7		BDE-183	26.26	18		BDE-71	16.25
8	6	BDE-156	25.23	19		BDE-49	16.18
9		BDE-138	26.61	20	3	BDE-17	13.25
10		BDE-153	23.22	21	2	BDE-15	11.37
11		BDE-154	22.03	22		unknown	15.25

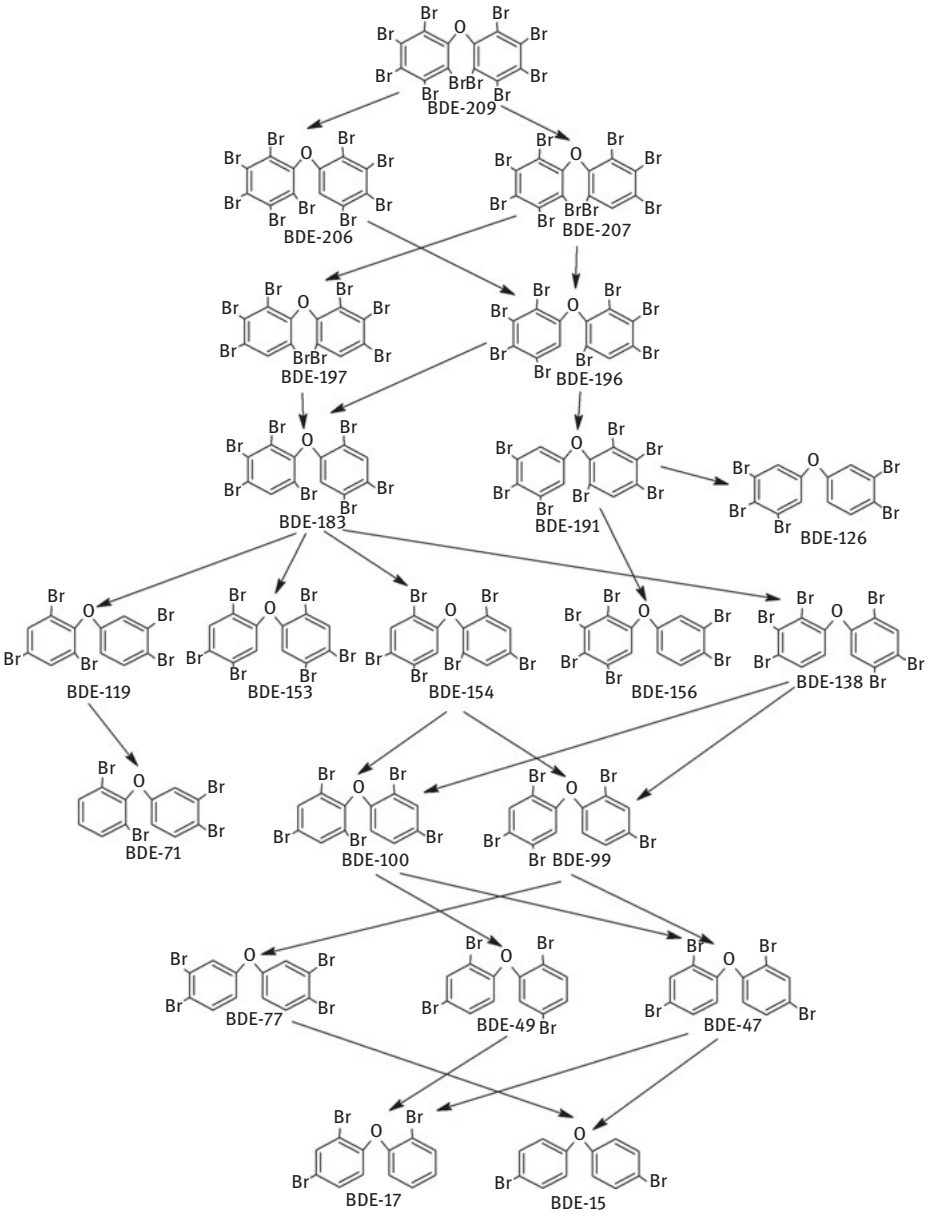

Figure 4.33: Major pathway of debromination of BDE-209 by M-NZVI.

According to the results of identification of the degradation products in this study, the main debromination reduction pathway of BDE-209 degraded by M-NZVI is summarized in Figure 4.33. The result is also consistent with that of Zhuang et al. (2011b) and Fang et al. (2011a).

4.7 Preliminary application of organic-montmorillonite-loaded nano-iron material

The organic-montmorillonite-loaded nano-iron material is preliminarily applied to the wastewater containing PBDEs.

4.7.1 Application background

BDE-209 is widely used in the manufacturing of printed circuit boards (PCBs), electronic products, textiles, plastics and rubber; thanks to its advantages of small additional amount, high flame retardancy and high thermal stability. However, BDE diphenyl ether may be released into the environment during the production and its related products are used and recycled. China is a big country that utilizes and produces DecaBDE (BDE-209) massively. In the Pearl River Delta and its surrounding areas, there is a largest production base of electronic products and PCBs in the world and there is also large-scale disposal and recycling activities of e-waste. As reported in literature, a high risk of exposure to PBDEs is shown in this region, and the levels of PBDEs in the surrounding river and sediments are high.

E-waste refers to electrical or electronic products that are abandoned or cannot be reused that include used electronic products and electrical products, such as used computers, televisions, mobile phones, refrigerators, circuit boards, electric motors, transformers and so on. With the global development of electronic technology and PCB technology, the replacement of electronic and electrical products is rapid. About 50 million tons of e-wastes are generated every year, and a large amount of electronic waste enters our country and is taken to electronic dismantling bases in various places for recycling e-waste. The dismantling base in Guangdong Qingyuan Longtang is one of Guangdong's two largest e-waste dismantling venues. The town has only 100,000 people, but has more than 1,000 dismantling plants. Dismantling teams of more than 50,000 people are daily and constantly working and nearly a million tons of e-wastes are dismantled each year. The extensive disassembly method has a serious impact on the local ecological environment. The polybrominated diphenyl ethers contained in the electronic rubbish are easy to enter the water body and soil after the e-waste is being eroded by rainwater during the laying process. Researchers also detected relatively high levels of PBDEs in various environmental media.

PCB is an important part of electrical and electronic products, almost all of the electrical and electronic products and computer accessories require the circuit board. A certain amount of brominated flame retardants (mainly PBDEs) need to be added to the PCB in production, to prevent self-ignition of the PCB. At the same time, BDE-209 will enter the waste water from the production of PCBs for various reasons. The amount of wastewater produced from the PCB in the Pearl River Delta and its surrounding areas is very large. The environmental protection department has long been focusing only on

the heavy metal standards of the PCB wastewater and has neglected trace amounts of toxic waste in the wastewater. Therefore, a large amount of wastewater containing brominated flame retardant pollutants (mainly PBDEs) is directly discharged into the water body causing long-term pollution in the surrounding environment.

Therefore, aiming at the situation that a large amount of PBDEs is contained in the effluent from the e-waste dismantling and PCB wastewater treatment, the prepared M-NZVI material is used to study the effect of degrading of two kinds of wastewater.

4.7.2 Degradation effect of effluent from e-waste disassembly

Figure 4.34 and Figure 4.35 show the degradation effect of the M-NZVI material degrading the effluent from e-waste disassembly. From Figure 4.34, it can be seen that the content of PBDEs in the effluent from the e-waste removal was very high, reaching 2326.90 ng/L, of which the total content of other brominated diphenyl ethers (Σ_9BDEs) except BDE-209 was 806.40 ng/L. So the content of BDE-209 was 1520.50 ng/L, which was 3 times higher than the PBDEs content in the influent of municipal wastewater treatment plant in South China (BDE-209 content of 550.20 ng/L), measured by Peng et al. The abovementioned results indicate that BDE-209 was the main component of the effluent from e-waste disassembly. The reason is that on the one hand, BDE was used as the main brominated flame retardant, and on the other hand, most of the BDE-209 was not decomposed into other low-brominated diphenyl ethers.

As can be seen from Figure 4.34, after the degradation by M-NZVI, the contents of Σ_9BDEs and BDE-209 in wastewater were 25.60 ng/L and 38.80 ng/L, respectively and

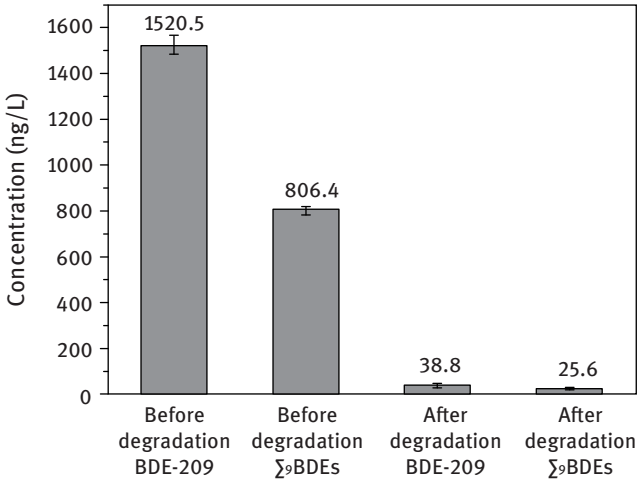

Figure 4.34: Comparison of the degradation by M-NZVI of PBDEs in wastewater from e-waste disassembly.

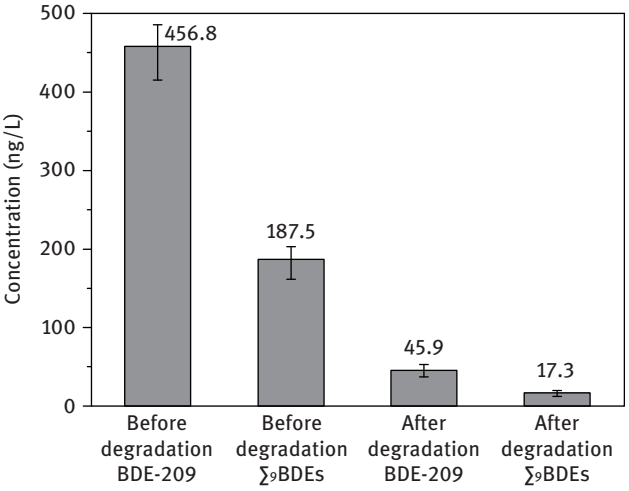

Figure 4.35: Comparison of the degradation by M-NZVI of PBDEs in printed circuit board wastewater.

the removal rates were 96.83% and 97.45%, respectively. The high removal rates indicate that the M-NZVI material has a very high degradation effect on the treatment of wastewater from e-waste.

4.7.3 Degradation effect of printed circuit board wastewater

Figure 4.35 shows the comparison of the results before and after the degradation of printing PCB wastewater by M-NZVI. As can be seen from Figure 4.35, the PBDEs content in PCB wastewater was about 60% lower than that in the e-waste disassembly, with 644.30 ng/L, among which the content of $\sum_9$BDEs was 187.50 ng/L and that of BDE-209 was 456.80 ng/L. The abovementioned results show that BDE-209 was still the main component of PCB wastewater, and BDE-209 accounted for about 80% of the total PBDEs, which was much higher than the proportion of BDE-209 in the wastewater of e-waste disassembly (about 50%). The reason may be that BDE-209, which is discharged into the wastewater during the preparation and cleaning of PCBs, is essentially not decomposed due to its short existence in the natural environment.

As can be seen from Figure 4.35, the contents of Σ_9BDEs and BDE-209 in the PCB wastewater after degradation by M-NZVI were 17.30 ng/L and 45.90 ng/L, respectively and the removal efficiencies were 90.77% and 89.95%, respectively. The removal rate was lower than that of the wastewater of e-waste disassembly. The results show that the M-NZVI material also had a good degradation effect on the PCB wastewater, but it may be affected by the heavy metals in the PCB wastewater.

4.7.4 Application analysis of the synthetic material

The application of the M-NZVI material in the degradation of PCB wastewater, wastewater of e-waste disassembly and other aspects can be analyzed from the following three aspects:

First, regarding removal efficiency of M-NZVI, the removal rate of PBDEs in the PCB wastewater and the effluent from e-waste disassembly both were more than 90%, which indicates that the M-NZVI material has a good removal effect on the two kinds of wastewater and can be applied to the treatment of wastewater containing PBDEs.

The second is the ease of use. The M-NZVI material is a synthetic powder material, which can be used instead of other coagulant materials or adsorbent materials for wastewater treatment; it can also be used together with other coagulants. In addition, the preparation process of M-NZVI is relatively simple and large-scale production is possible.

The third is the cost of the material preparation. The M-NZVI material is mainly composed of sodium montmorillonite, ferrous sulfate and a small amount of modifier. According to the preliminary calculation of the material prices on the market, the application of M-NZVI to the treatment of the two kinds of wastewater costs 30 to 40 yuan per ton of processed wastewater. The cost is relatively not that much high as compared to other treatments of highly concentrated wastewater. After the large-scale production of the material, the material preparation costs will be greatly reduced, making the possibility of large-scale application greatly increase.

References

BENTOUAMI A, OUALI M. Cadmium removal from aqueous solutions by hydroxy-8 quinoleine intercalated bentonite. Journal of Colloid and Interface Science, 2006, 293(2): 270–277.

CHEN B L, HUANG W H, MAO J F, et al. Enhanced sorption of naphthalene and nitroaromatic compounds to bentonite by potassium and cetyltrimethylammonium cations. Journal of Hazardous Materials, 2008, 158(1): 116–123.

CHEN D F, WANG Z. Study on the relation between the performance and the structure of organic bentonite. Journal of Xi'an Jiaotong University, 2000, 34(8): 92–95.

CHEN Z X, JIN X Y, CHEN Z L, et al. Removal of methyl orange from aqueous solution using bentonite-supported nanoscale zero-valent iron. Journal of Colloid and Interface Science, 2011, 363 (2): 601–607.

DING J X, LIAO Q L, YANG D, et al. Preparation of nano-α-Fe coated by Fe_2B in microemulsion and study on its properties. New chemical materials, 2007, 35(2): 25–26.

FANG Z, QIU X, CHEN J, et al. Debromination of polybrominated diphenyl ethers by Ni/Fe bimetallic nanoparticles:influencing factors, kinetics, and mechanism. Journal of Hazardous Materials, 2011b, 185(2): 958–969.

FANG Z, QIU X, CHEN J, et al. Degradation of the polybrominated diphenyl ethers by nanoscale zero-valent metallic particles prepared from steel pickling waste liquor. Desalination, 2011a, 267(1): 34–41.

FROST R L, XI Y, HE H. Synthesis, characterization of palygorskite supported zero-valent iron and its application for methylene blue adsorption. Journal of Colloid and Interface Science, 2010, 341(1): 153–161.

FU G Z, GONG W Q, C M. Preparation and characterization of montmorillonite organic intercalation complexes. Journal of Wuhan University of Technology, 2006, 28(8): 50–53.

GU C, JIA H, LI H, et al. Synthesis of highly reactive subnano-sized zero-valent iron using smectite clay templates. Environmental Science & Technology, 2010, 44(11): 4258–4263.

HU L J, LI Y M. Removal of nitrobenzene from wastewater by organic bentonite supported nano iron. Journal of Environmental Science, 2008, 28(6): 1107–1112.

JIA H, WANG C. Adsorption and dechlorination of 2,4-dichlorophenol(2,4-DCP)on a multi-functional organo-smectite templated zero-valent iron composite. Chemical Engineering Journal, 2012, 191: 202–209.

LEE J, HAN S, HYEON T. Synthesis of new nanoporous carbon materials using nanostructured silica materials as templates. Journal of Materials Chemistry, 2004, 14(4): 478–486.

LI L, FAN M, BROWN R C, et al. Synthesis, properties, and environmental applications of nanoscale iron-based materials:a review. Critical Reviews in Environmental Science and Technology, 2006, 36(5): 405–431.

LI Y, ZHANG Y, LI J, ZHENG X. Enhanced removal of pentachlorophenol by a novel composite: nanoscale zero valent iron immobilized on organobentonite. Environmental Pollution, 2011, 159 (12): 3744–3749.

LIU Y, LIU X L, WANG J D. Study on the clay modification conditions I. Bentonite modification. Environmental Chemistry, 2002, 21(2): 167–171.

MCBRIDE M, PINNAVAIA T, MORTLAND M. Adsorption of aromatic molecules by clays in aqueous suspension. Advances in Environmental Science and Technology(USA), 1977.

MEYER D, WOOD K, BACHAS L, et al. Degradation of chlorinated organics by membrane-immobilized nanosized metals. Environmental Progress, 2004, 23(3): 232–242.

MO W, MA S J, HAN Y X, et al. Study on surface modification of bentonite by aluminate ester. Metal mine, 2008(2): 78–82.

SHAKIR K, GHONEIMY H F, ELKAFRAWY A, et al. Removal of catechol from aqueous solutions by adsorption onto organophilic-bentonite. Journal of Hazardous Materials, 2008, 150(3): 765–773.

SHEN X Y, LU Y Y, ZHU L Z. Adsorption behavior of p-nitrophenol at water/organobentonite interface—Thermodynamic characteristics and mechanism. Chinese Environmental Science, 2003, 23(4): 367–370.

SHEN Y H. Preparations of organobentonite using nonionic surfactants. Chemosphere, 2001, 44(5): 989–995.

SUN H L. Study on the properties and mechanism of organic bentonites adsorbing heavy metals and organic pollutants in Water. Chemical Research and Application, 2007, 7.

TSENG H-H, SU J-G, LIANG C. Synthesis of granular activated carbon/zero valent iron composites for simultaneous adsorption/dechlorination of trichloroethylene. Journal of Hazardous Materials, 2011, 192(2): 500–506.

ÜZÜM C, SHAHWAN T, EROĞLU A, et al. Synthesis and characterization of kaolinite-supported zero-valent iron nanoparticles and their application for the removal of aqueous Cu^{2+} and Co^{2+} ions. Applied Clay Science, 2009, 43(2): 172–181.

WANG C B, ZHANG W X. Synthesizing nanoscale iron particles for rapid and complete dechlorination of TCE and PCBs. Environmental Science & Technology, 1997, 31(7): 2154–2156.

WANG Q, QIAN H J, YANG Y P, et al. Reduction of hexavalent chromium by carboxymethyl cellulose-stabilized zero-valent iron nanoparticles. Journal of Contaminant Hydrology, 2010, 114(1): 35–42.

WENG X L, LIN S, CHEN Z X, et al. Preparation of natural bentonite supported iron nanoparticles and their Degradation of amoxicillin. Science China:Chemistry, 2012, 42(1): 17–23.

WU L, RITCHIE S. Removal of trichloroethylene from water by cellulose acetate supported bimetallic Ni/Fe nanoparticles. Chemosphere, 2006, 63(2): 285–292.

YILDIZ N, GÖNÜLSEN R, KOYUNCU H, CALIMLI A. Adsorption of benzoic acid and hydroquinone by organically modified bentonites. Colloids and Surfaces A:Physicochemical and Engineering Aspects, 2005, 260(1): 87–94.

ZHANG B G, FENG C P, NI J R, et al. Simultaneous reduction of vanadium(V)and chromium(VI)with enhanced energy recovery based on microbial fuel cell technology. Journal of Power Sources, 2012, 204: 34–39.

ZHANG Y, LI Y M, LI J F, et al. Enhanced removal of nitrate by a novel composite:nanoscale zero valent iron supported on pillared clay. Chemical Engineering Journal, 2011a, 171(2): 526–531.

ZHANG Y, LI Y, ZHENG X. Removal of atrazine by nanoscale zero valent iron supported on organo-bentonite. Science of the Total Environment, 2011b, 409(3):625–630.

ZHAO Z S, LIU J F, TAI C, et al. Ion exchange resin loaded nanoscale zero-valent iron for rapid degradation of water-soluble azo dyes. Science China:B series, 2008, 38(1): 60–66.

ZHU H J, JIA Y F, WU X, et al. Removal of arsenic from water by supported nano zero-valent iron on activated carbon. Journal of Hazardous Materials, 2009, 172(2): 1591–1596.

ZHU L Z, Liu W H. Properties and applications of CTMAB-Bentonite adsorbing organic compounds in water. Environmental Chemistry, 1997, 16(3): 233–237.

ZHUANG Y, AHN S, LUTHY R G. Debromination of polybrominated diphenyl ethers by nanoscale zerovalent iron:pathways, kinetics, and reactivity. Environmental Science & Technology, 2010, 44 (21): 8236–8242.

5 Application of functional materials in permeability reactive barriers technology

5.1 Overview of permeable reactive barrier technology

With the improvement in human social production and living standards, a large number of industrial wastewater and domestic sewage is discharged; the penetration of chemical fertilizers and petrochemical products, as well as the invasion of coastal waters will cause groundwater contamination. Groundwater contamination has the characteristics of concealment and is difficult to be treated; once polluted it is difficult to be repaired. The traditional treatment method is as follows: pump-and-treat technology, which can effectively control the contaminated area at upstream of the pumping wells. However, this treatment method can only limit the further spread of contamination, but cannot repair the contaminated groundwater in situ. In addition, the pump-and-treat technology requires continuous energy input to ensure the operation of water pumping and water treatment systems. Furthermore, the requirement of long-term monitoring of the operation of the system leads to a very expensive installation cost (SHU & YUAN, 2002). This method cannot control the contamination source, therefore the pumping system will run for years or even decades if the source of contamination and plumes are present that causes a high cost, whereas removal of dense non-aqueous phase liquids (DNAPLs) is not well received (CUI et al., 2003). Second, the pumping of groundwater causes a decrease in the hydraulic gradient of groundwater, which activates the originally dormant DNAPLs and thereupon increases groundwater contamination (MARCUS 1999). To solve the abovementioned problems, it is better to repair the contaminated groundwater; for this, the in situ repair technology is developed, such as in situ bioremediation, permeable reactive barrier (PRB), in situ chemical reaction technology and so on (DI, 2005).

5.1.1 PRB basic concepts

The Handbook of "Permeable Reactive Barrier Technologies for Contaminant Remediation," published by the United States Environmental Protection Agency (USEPA) in 1998, defines PRB as follows:

> an emplacement of reactive materials in the subsurface designed to intercept a contaminant plume, provide a flow path through the reactive media, and transform the contaminant(s) into environmentally acceptable forms to attain remediation concentration goals downgradient of the barrier (POWELL et al., 1998; BAI & ZHANG, 2006).

By the abovementioned definition it can be concluded that PRB is an in situ treatment zone of interceptive reactive material. The reactive material is its core, which will be

https://doi.org/10.1515/9783110544381-005

emplaced perpendicular to the flow direction of contaminant plumes in groundwater. When these plumes flow through the reactive barrier by physical, chemical and biological reactions with the reactive material, the contaminant will be degraded, adsorbed, precipitated or removed, as shown in Figure 5.1. PRB can be widely used to treat organic and inorganic contaminants in groundwater. At present, the most studied contaminants are mainly chlorinated organic compounds, such as tetrachloroethylene (C_2Cl_4, abbreviated PCE), trichloroethylene (C_2HCl_3, abbreviated TCE), dichloroethylene ($C_2H_2Cl_2$, abbreviated DCE) and vinyl chloride (C_2H_3Cl, abbreviated VC). Inorganic contaminants are mainly heavy metals, including Cr, Cd, Zn, Pb, Hg, As, Ni, Cu and Ag (DI, 2005).

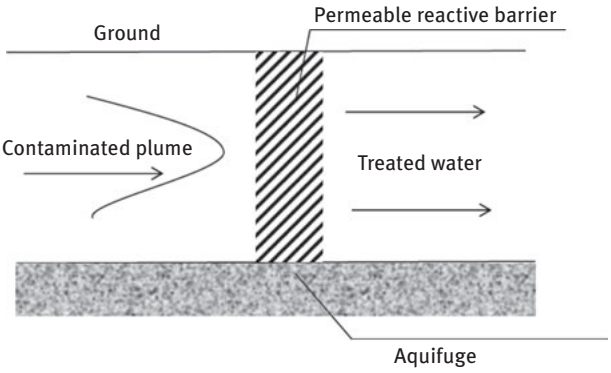

Figure 5.1: Schematic diagram of PRB.

5.1.2 PRB structure type

PRB has two basic structure types: (1) continuous wall PRB and (2) funnel-and-gate PRB. Continuous wall PRB is also often referred to as in situ reactive barrier; it is for establishing a continuous reactive barrier at the downstream of the contaminated plume. This reactive barrier can control the entire contaminated plume. However, one disadvantage of this type of reactive barrier is that in order to successfully treat a contaminated plume, the reactive barrier should be large enough to ensure that the entire contaminated plume can flow through the reactive barrier. Once the contaminated plume to be treated is especially wide or extended, the continuous reactive barrier must be very large and the corresponding installation costs are prohibitively expensive, which limits its application. In order to solve the above-mentioned problems, a low-permeability partition wall is used to guide the contaminated plume to flow through a smaller reactive barrier; the combination of the partition wall and the smaller reactive barrier is called funnel-and-gate PRB.

According to the number of in situ reactors, the funnel-and-gate PRB can be divided into single-channel system and multichannel system, and multichannel system can be further divided into parallel and series; parallel multichannel system is used mainly to deal with a wide plume in contaminated groundwater. Different types of in situ reactors are often required for groundwater treatment where different types of contaminants in groundwater are mixed. In this case, a series multichannel system is generally used. Moreover, the PRB is also divided into four forms by some researchers: (1) continuous wall PRB, (2) loading PRB, (3) combinative PRB of funnel-and-gate and caisson and (4) funnel-and-gate PRB (BAI & ZHANG, 2006).

According to nature of the reaction, PRB can be divided into chemical sedimentation reactive barrier, adsorption reactive barrier, oxidation–reduction reactive barrier and biodegradable reactive barrier, because of the different kinds of filled materials in the reactive barrier. If the filled material is activated carbon, zeolite, organic clay or other adsorption materials, it is an adsorption reactive barrier; if the reaction material is zerovalent iron (Fe^0) and other reductive metals, it is an oxidation–reduction reactive barrier.

5.2 Functional materials in the permeable reactive barrier

The reactive material is the core component of PRBs. Different reactive materials should be selected, according to different target pollutants, different geological conditions and other local conditions.

The selected reactive materials should have the following three characteristics: (1) when the contaminant plume passes through the reaction barrier, the reactive material can react with the pollutants physically, chemically or biologically, degrading or removing the pollutants; (2) reactive materials should be obtained easily, and the cost should be relatively low. At the same time, they should have certain stability and can be durable for a long time, because frequent replacement of the reactive materials will increase the operation and maintenance costs; (3) reactive materials cannot produce secondary pollution (BOWLES et al. 1995). In general, the choice of reactive materials should be effective, economical and safe. At present, most of the reactive materials used at home and abroad for practical projects are zerovalent iron and activated carbon (see Table 5.1). Other materials such as peat, straw, sawdust, leaves, rye seeds, urban composting are basically used in experimental studies. In addition, there are also some auxiliary active materials: (1) for physical adsorption such as activated carbon, zeolites, clay minerals, coal, aluminosilicates and the like; (2) for chemical adsorption such as phosphates, limestone, ferrites, bimetal, polymetal and microbial materials (BAI & ZHANG, 2006). Tire debris are also a reactive material and works well, especially for hydrophobic organic pollutants.

Table 5.1: Foreign application examples of permeable reactive barriers.

Location	Pollutant type and concentration	Reactive barrier type	Investment costs (USD)	Year	Treatment effect	Installation depth (m)	Reactive material	
							Type	Fe° Quantity (t)
Ontario	Ni, Fe	Continuous wall	—	—	—	4.3	Activated carbon	—
North Carolina	>4,320 μg/L(TCE) >3,430 μg/L(Cr^{6+})	Continuous wall	500,000	—	Pollutant concentration<MCLs	5.5	Fe°	450
North Carolina	—	Continuous wall	350,000	1996	—	12.2	Fe°	—
Dover	PCE, TCE, DCE	Funnel-and-gate	—	—	—	4.6	Fe°	—
California	50–200 μg/L (TCE)1,000–4,500 μg/L(DCE)	Funnel-and-gate	600,000	1995	DCE<5 μg/LTCE<6 μg/L	6.1	Fe°	220
Kansas	TCE, 1,1,1–TCA	Funnel-and-gate	350,000	1996	—	9.0	Fe°	—
Colorado	TCE	Funnel-and-gate	—	—	—	1.5	Fe°	—
New York	4,900 μg/L (1,2-DCE)260 μg/L (VC)	Continuous wall	797,000	1995	5 μg/L(1,2-DCE)23 μg/L(VC)	4.6	Fe°	742
New Jersey	1, 200 μg/L (1,1,1-TCE)19 μg/L (PCE)110 μg/L(TCE)	Continuous wall	875,000	—	VOCs concentration-from 4,500 μg/Lto 33 μg/L	—	Fe° and sand	720
Missouri	1, 377 μg/L (1,2-cDCE)291 μg/L (VC)	Continuous wall	1,500,000	—	Pollutant concentration<MCLs	—	Fe° and sand	220

Note: According to the requirements of the Safe Drinking Water Act Amendment of 1996, two concentration values are established as the current drinking water quality standards in the United States: (1) the Maximum Contaminant Level Goals (MCLGs) and the (2) Maximum Contaminant Levels (MCLs).
Source: CANTRELL et al. (1995); SNAPE et al. (2001); BELL etal. (2003); GUERIN et al. (2001); MU et al. (2004).

5.3 Application of functional materials in PRB for nitrogen and phosphorus removal

5.3.1 Overview

When the target pollutant treated by PRB technology is nitrogen, phosphorus or other nutrient pollutants, most of the selected reactive materials are materials with large specific surface area, rich organic matter or chemical reaction with nitrogen and phosphorus. Robertson et al. (1997) studied the removal of nitrate nitrogen by PRB. The chosen reaction materials were silty sand, sawdust, leaf compost, rye seeds and so on. Small-scale field experiments found that the nitrate nitrogen content decreased from 59 mg/L to 1 mg/L. Su et al. (2007) designed a one-, two-, and three-element system to remove nitrate in simulated wastewaters by using three kinds of reaction materials: (1) cotton compost, (2) Fe° and (3) low carbon deposits. It was found that when using cotton compost alone as the reaction material the nitrate removal effect was the best, and there was no accumulation of NH_4^+ during the reaction. Moon et al. (2004) found that the removal rate of nitrate by PRB with sulfur particles, autotrophic sulfur-oxidizing bacteria and limestone as reaction materials was 90%, and the removal rate increased with time. In the early stage of reaction nitrite accumulation occurred. However, with the passage of time, the content decreased gradually. After 12 days of reactor operation, the effluent nitrite concentration was less than 2 mg/L. It was also proved that when the initial nitrate concentration in the influent was less than 60 mg/L and the percolation rate was 1 m/d, the treatment requirements could be achieved with a wall thickness of only 30 cm. Baker et al. (1997) studied the removal of phosphorus using silica sand, limestone and metal oxide mixtures as reaction materials. It was found that the removal of total phosphorus by PRB could be stabilized at about 95% for a long time.

When dealing with inorganic pollutants such as nitrogen and phosphorus, special bacteria are often required. The effect of some of these on living conditions is very harsh. Therefore, it is particularly important to maintain the appropriate environment needed by bacterial community within the PRB system. When using Fe° as a reactive material to remove nitrate by chemical reduction, the product control is crucial and the required product is essentially N_2 that is harmless, but not other harmful substances such as ammonia or nitrite, of which the required content of the groundwater standards is lower than nitrate. In addition, the current domestic and foreign research mainly focuses on the application of reactive materials for removal of nutrient contaminants in groundwater. When PRB technology is applied to the removal of nutrient pollutants in surface water bodies, the research of the selection, application effects and characteristics of reactive materials are relatively few.

5.3.2 Basic principles of nitrogen and phosphorus removal

PRB's removal of nitrogen and phosphorus can be either be biological or nonbiological. The nonbiological principle includes adsorption, precipitation, oxidation–reduction, curing and physical transformation. At present, the most studied and the most commonly used principle in China and other countries for nitrogen removal by zerovalent iron is as follows:

$$10Fe + 6NO_2^- + 3H_2O \rightarrow Fe_2O_3 + 6OH^- + 3N_2 \uparrow \quad (5.1)$$

$$Fe + NO_2^- + 2H^+ \rightarrow Fe^{3+} + H_2O + NO_2^- \quad (5.2)$$

$$NO_2^- + 10H^+ + 4Fe \rightarrow NH_4^+ + 3H_2O + 4Fe^{2+} \quad (5.3)$$

Studies (SORG & LOGSDON, 1978; ZHOU et al., 2006; LI et al., 2006) have shown that the main product of removal of nitrate by metal iron is ammonia nitrogen, which accounts for more than 75% of nitrate removal. In this reaction, a small amount of nitrite nitrogen is generated; the rest may be converted into nitrogen or adsorbed by iron filings. The pH is the main factor of the reaction. The lower the pH, the faster the reaction is processed.

5.3.3 Selective study on nitrogen and phosphorus removal by functional materials

The most commonly used zerovalent iron in China and other countries was used as the main material for nitrogen and phosphorus removal, to study the impact of various factors on its nitrogen and phosphorus removal.

5.3.3.1 Removal of nitrogen by iron and influence factors

(1) Effect of initial influent pH on the removal of total nitrogen and nitrate nitrogen
At room temperature, with the initial nitrate concentration of 30 mg/L and the influent pH of 2.09, 3.93, 6.04, 8.08 and 9.91, 2 g of iron filings were added into 50 mL nitrate solutions and was reacted for 120 min. The results showed that at pH 2.09–9.91, the lower the initial influent pH was, the greater was the amount of removed total nitrogen and nitrate nitrogen, and the produced ammonia nitrogen per unit mass (per gram) of iron filings (Figure 5.2). This is because H^+ can accelerate the corrosion of iron filings and promotes redox reaction. When the pH was 2.09, the removal rates of total nitrogen, nitrate nitrogen and the production rate of ammonia nitrogen per unit mass of iron filings were 0.074, 0.18 and 0.099 mg, respectively. It can be seen that reducing the initial pH of the influent increased the amount of

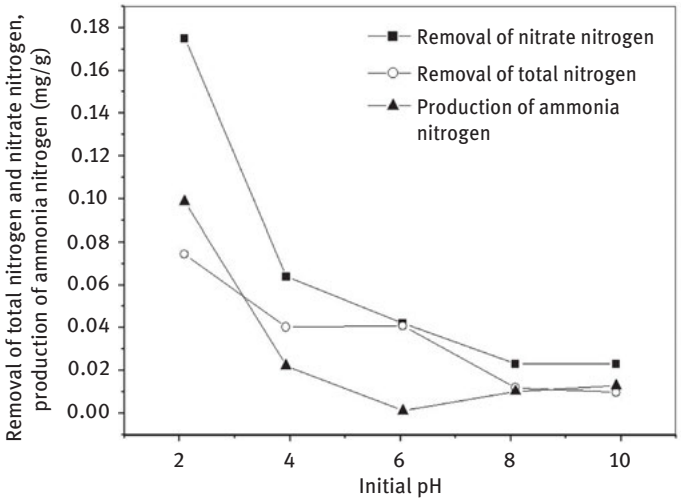

Figure 5.2: Effect of initial influent pH on removal of total nitrogen and nitrate nitrogen and on the production of ammonia nitrogen.

removed total nitrogen and nitrate nitrogen while also increasing the amount of produced ammonia nitrogen. However, the pH of supplied water is generally alkaline in practical applications. In combination with Figure 5.2 and considering the processing cost, initial influent pH adjustment to 6 to 8 is more appropriate in the practical application.

(2) Effect of reaction time on the removal of total nitrogen and nitrate nitrogen

Under the conditions of room temperature and pH 2, initial influent nitrate concentration of 30 mg/L, 50 mL nitrate solution and 2 g iron filings were added and the reaction time was changed. As can be seen from Figure 5.3, with the extension of reaction time, the amount of removed nitrate nitrogen and total nitrogen gradually increases, but the reaction rate gradually decreased. This may be due to the formation of Fe^{2+} during the reaction that forms insoluble substances such as Fe $(OH)_2$ or Fe $(OH)_3$ under aerobic conditions. Then more and more Fe^{2+} got deposited on the surface of the iron filings over time, thus hindering the reaction. The production of ammonia nitrogen was in the steady rise, then it gradually declined, reaching the maximum value of 0.19 mg/g at the reaction time of 300 min. This may be due to the increase in the concentration of ammonia nitrogen in the solution with the extension of the reaction time, which delayed or hindered the reaction of formula (5.3), but conducive to the occurrence of the reaction of formula (5.1).

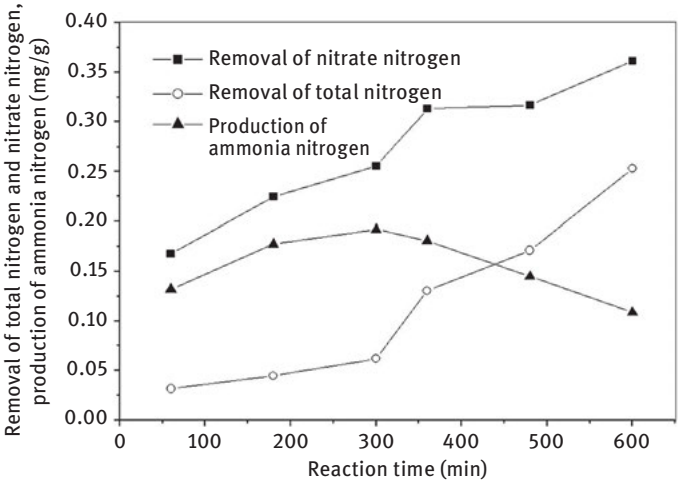

Figure 5.3: Effect of reaction time on removal of total nitrogen and nitrate nitrogen and on production of ammonia nitrogen.

(3) Effect of influent nitrate initial concentration on the removal of total nitrogen and nitrate nitrogen

Under the conditions of room temperature and pH 2 and different influent initial nitrate concentrations, 2 g iron filings were added to 50 mL nitrate solution and the reaction lasted 120 min. As can be seen from Figure 5.4, with the increase of the influent initial nitrate concentration ranging from 10.84 mg/L to 127.42 mg/L, the

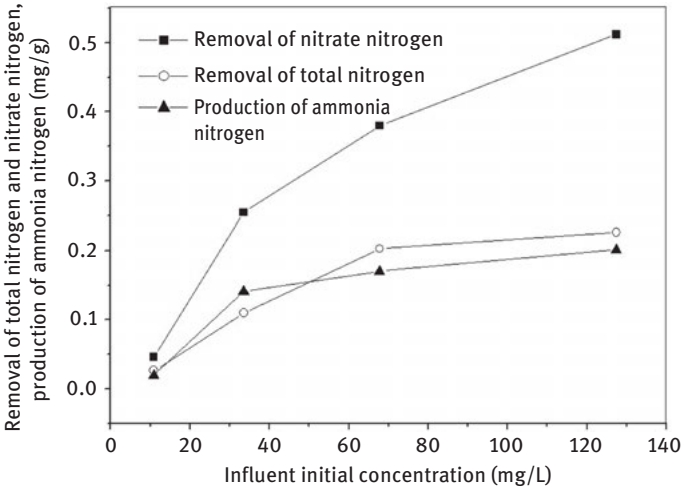

Figure 5.4: Effect of influent initial nitrate concentration on removal of total nitrogen and nitrate nitrogen and on production of ammonia nitrogen.

removal of total nitrogen and nitrate nitrogen per unit mass of iron filings gradually increased, and the amount of produced ammonia nitrogen also gradually increased. However, when the influent nitrate concentration was higher than 67.80mg/L, the increased rate of the removal of total nitrogen and nitrate nitrogen by iron filings decreased, and the production rate of ammonia nitrogen also tended to be flat. This was mainly because the surface area of the iron filings was a constant value. When the influent nitrate concentration was higher than 67.80 mg/L, the contacted nitrate amount with iron filings was close to the saturation reduction amount on the surface of iron filings. The formation of ammonia nitrogen showed an upward trend when the initial concentration was 10.84–33.54 mg/L. When the influent nitrate concentration was higher than 33.54 mg/L, the formation of ammonia nitrogen tended to be flat.

(4) Analysis of reaction products

Under the conditions of room temperature and pH 2, influent initial nitrate concentration of 30 mg/L, 2 g of iron filings were added to 50 mL nitrate solution for a reaction time of 180 min. It can be seen from Table 5.2 that under the experimental conditions, after 180 min of reaction, the removal rate of nitrate nitrogen was 29.73% and the production rate of ammonia nitrogen was 23.46%, which accounted for 78.91% of the removed nitrate nitrogen. Therefore, the main product of the reaction was ammonia nitrogen. A small amount of nitrite nitrogen was also produced during the experiment. According to the conservation of matter, the remaining nitrogen could be either produce N_2 or adsorbed by iron filings and their reaction by-products such as Fe $(OH)_3$. This is similar to the results of Zhou et al. (2006). The removal of nitrate nitrogen was lower than that studied by Zhou et al. The reason may be that the purity of the iron filings is relatively low.

Table 5.2: Products after 180 min reaction.

Residual nitrate and product	Initial nitrate concentration (30.27 mg/L)	
	Concentration (mg/L)	Nitrogen content (%)
Nitrate (residual)	21.27	70.27
Ammonia nitrogen	7.102	23.46
Nitrite	0.002	0.01
Other	1.896	6.26

(5) Effect of iron–carbon ratio on the removal of total nitrogen and nitrate nitrogen

Since the iron filings are iron–carbon alloy, carbon particles act as a cathode when in an electrolytic solution, whereas iron has a small potential and acts as an anode, thus constituting tens of thousands of tiny corrosion cells. Theoretically, with the addition

of activated carbon, coal and other cathode materials to the system, it will form macro-corrosion cells, thereby accelerating the rate of iron corrosion. Under the conditions of room temperature, pH 7.58 and influent initial nitrate concentration of 30 mg/L, a proper amount of iron filings and bamboo charcoal for a total material mass of 2g were added in proportion, making the iron–charcoal ratios 6:1, 1:1, 1:2, 1:3, 1:4, 1:5 and 1:6. As a control, 2 g iron filings were added to 50 mL nitrate solution in a conical flask for 120 min reaction. As can be seen from Figure 5.5, compared with the control, with the decrease of the iron–carbon ratio, the removal of total nitrogen and nitrate nitrogen showed a downward trend, so did the formation of ammonia nitrogen. It can be considered that the addition of macro-cathode similar to bamboo charcoal does not increase the amount of nitrate to be removed. The main reactor for the electrolytic reaction with iron-based micro-batteries in the system is the carbon contained in the iron filings, instead of the external cathode material such as bamboo charcoal.

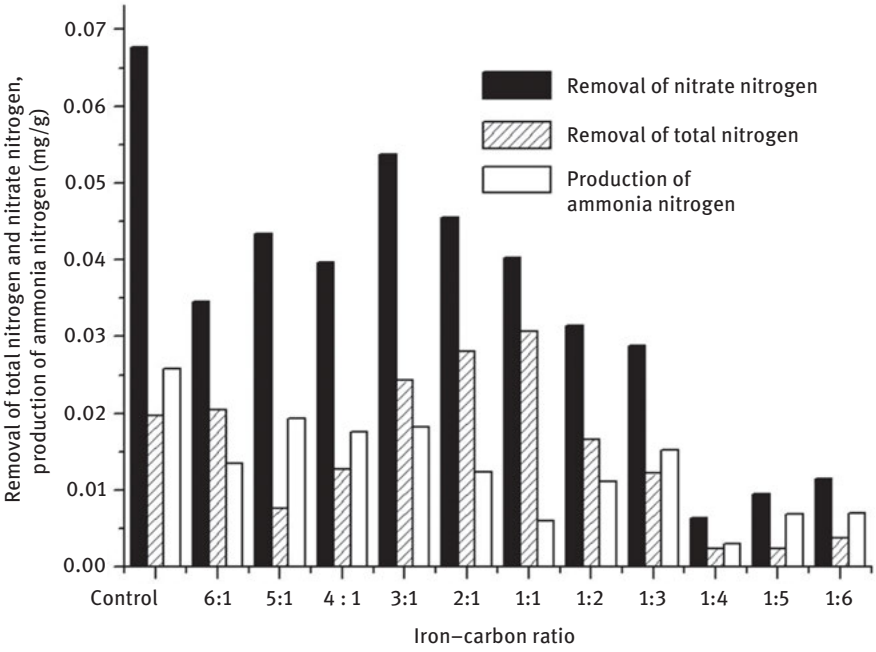

Figure 5.5: Effect of iron–carbon ratio on removal of total nitrogen and nitrate nitrogen and on production of ammonia nitrogen.

(6) Additive test

In this experiment, calcium chloride, alumina, copper oxide, manganese, potassium chloride and manganese dioxide were selected for additive test. At room temperature, with pH 7.4 and initial nitrate concentration of 30 mg/L in the feed water, 2 g iron filings and 1 g additive were weighed, so that the mass ratio of iron filings to

additives was 2:1. 2 g of iron filings were weighed and acted as a control. The materials were respectively added into 50 mL nitrate solution for 120 min reaction. As can be seen from Figure 5.6, the addition of copper oxide, aluminum oxide and manganese dioxide could significantly promote the removal of nitrate by iron filings, and the removal of nitrate nitrogen increased from 0.11 mg/g without additives to 0.23, 0.14 and 0.24 mg/g, respectively. It can also be seen from the figure that additives such as copper oxide and aluminum oxide also promoted the formation of ammonia nitrogen, which did not promote the removal of total nitrogen. However, manganese dioxide had a good effect and it was also good for the removal of total nitrogen by iron. The nitrogen removal increased from 0.05 mg/g to 0.17 mg/g without additives and the removal efficiency was 3 times as much as the original, whereas the formation of ammonia nitrogen of 0.037 mg/g was slightly lower than that of 0.054 mg/g without additives. Comprehensive analysis showed that adding manganese dioxide to iron could promote the chemical denitrification.

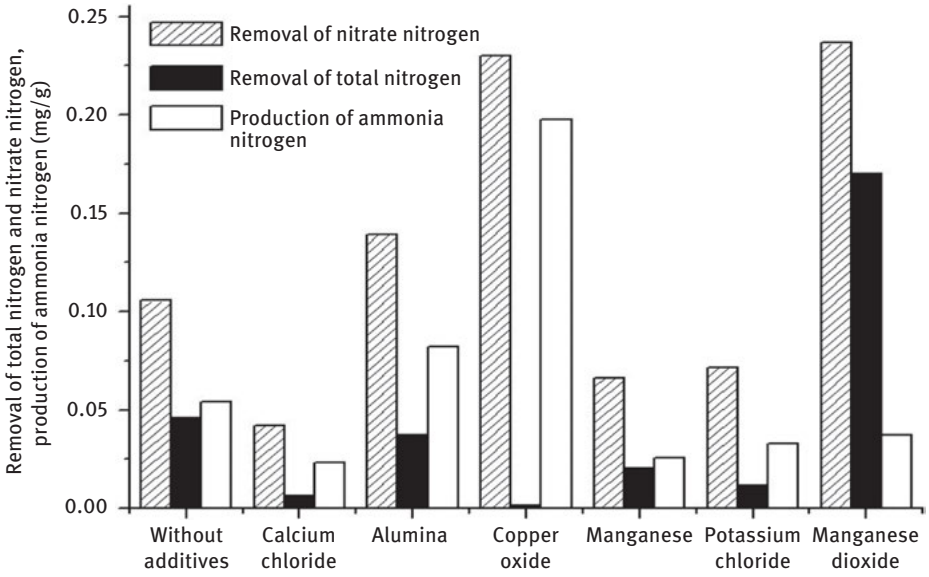

Figure 5.6: Effect of additives on removal of total nitrogen and nitrate nitrogen and on production of ammonia nitrogen.

In order to further investigate the effect of manganese dioxide, the following experiment was designed: at room temperature, with the influent initial nitrate concentration of 30 mg/L, 2 g iron filings were added, and an appropriate amount of manganese dioxide was added to make the mass ratio of iron filings to manganese dioxide 4:1, 2:1, 4:3, 1:1, 2:3 and 1:2. The results are shown in Figure 5.7.

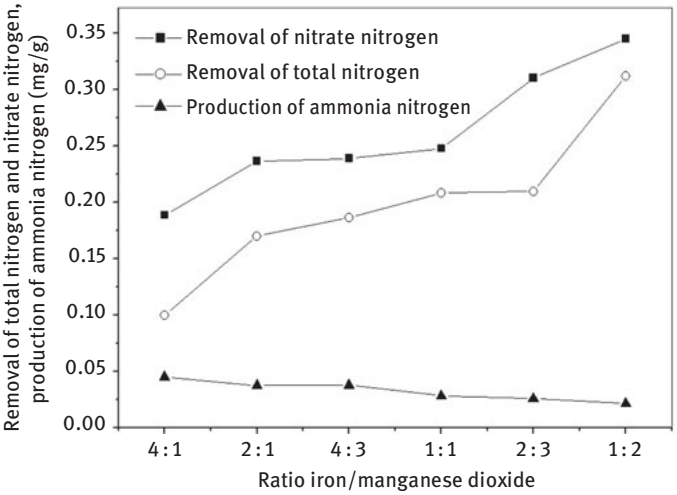

Figure 5.7: Effect of the amount of manganese dioxide on removal of total nitrogen and nitrate nitrogen and on production of ammonia nitrogen.

As can be seen from Figure 5.7, with the increase in the added amount of manganese dioxide, the removal of total nitrogen and nitrate nitrogen also increased, whereas the formation of ammonia nitrogen decreased. When the mass ratio of iron filings to manganese dioxide was 1: 2, the removal of total nitrogen and nitrate nitrogen per unit mass of iron was 0.31 and 0.35 mg/g, respectively, and the amount of ammonia nitrogen produced was 0.022 mg/g.

(7) Orthogonal test

In order to determine the main factors influencing the treatment effect and to avoid blind experiments, it can be seen from the previous static single-factor experimental results and references that the factors affecting the removal of total nitrogen and nitrate nitrogen are as follows: the amount of iron filings, reaction time, initial pH and initial concentration of nitrate in influent. In order to study the interaction of these factors on the removal of total nitrogen and nitrate nitrogen, this experiment would select iron filings, initial influent pH, reaction time and the initial influent nitrate concentration as four influence factors. For each of them, three levels were selected and a L_9 (3^4) orthogonal table was designed for the removal of total nitrogen and nitrate nitrogen, to determine the best reaction conditions.

From the orthogonal test and the range analysis (Table 5.3), it was suggested that the effect size of the influence factors on the removal of TN by iron under the test conditions was as follows: reaction time > initial concentration > amount of iron filings > pH. The optimum conditions were as follows: the amount of iron filings = 0.7 g, reaction time = 150 min, pH = 7, initial concentration = 30 mg/L.

Table 5.3: Orthogonal experiment design and results (total nitrogen).

Factor test (No.)	Iron filings (g)	Reaction time (min)	pH	TN initial concentration (mg/L)	Removal rate (%)
1	0.1	60	6	10	0.00
2	0.1	90	7	20	5.50
3	0.1	150	8	30	11.57
4	0.3	60	7	30	10.48
5	0.3	90	8	10	5.25
6	0.3	150	6	20	12.38
7	0.7	60	8	20	9.49
8	0.7	90	6	30	10.32
9	0.7	150	7	10	12.12
*K*1	17.07	19.97	22.70	17.37	—
*K*2	28.11	21.07	28.09	27.37	—
*K*3	31.93	36.07	26.32	32.37	—
*k*1	5.69	6.66	7.57	5.79	—
*k*2	9.37	7.02	9.36	9.12	—
*k*3	10.64	12.02	8.77	10.79	—
Range *R*	4.95	5.37	1.80	5.00	—

From the orthogonal test and the range analysis (Table 5.4), it was indicated that the effect size of the influence factors on the removal of nitrate nitrogen by iron under the test conditions was as follows: the amount of iron filings > the reaction time > the initial concentration > pH. The optimum conditions were as follows: the amount of iron filings = 0.7 g, reaction time = 150 min, pH = 7, initial concentration = 20 mg/L.

Table 5.4: Orthogonal experiment design and results (nitrate nitrogen).

Factor test (No.)	Iron filings (g)	Reaction time (min)	pH	NO_3-N initial concentration (mg/L)	Removal rate (%)
1	0.1	60	6	10	0.00
2	0.1	90	7	20	2.75
3	0.1	150	8	30	4.37

(continued)

Table 5.4: (continued)

Factor test (No.)	Iron filings (g)	Reaction time (min)	pH	NO_3-N initial concentration (mg/L)	Removal rate (%)
4	0.3	60	7	30	4.20
5	0.3	90	8	10	3.80
6	0.3	150	6	20	13.90
7	0.7	60	8	20	9.29
8	0.7	90	6	30	5.57
9	0.7	150	7	10	18.80
*K*1	7.12	13.50	19.47	22.60	—
*K*2	21.90	12.11	25.75	25.94	—
*K*3	33.66	37.07	17.47	14.15	—
*k*1	2.37	4.50	6.49	7.53	—
*k*2	7.30	4.04	8.58	8.65	—
*k*3	11.22	12.36	5.82	4.72	—
Range *R*	8.85	8.32	2.76	3.93	—

5.3.3.2 Removal of phosphorus and COD by iron filings and influence factors

(1) Effect of pH on removal of TP and COD by iron filings

At room temperature, with the initial concentration of influent TP of 2.14 mg/L and influent COD of 215.89 mg/L, and the initial influent pH of 6, 6.5, 7, 7.5 and 8 respectively, 0.7 g iron filings and 50 mL formulated solution were added in a 250 mL Erlenmeyer flask, which was reacted for 90 min on a rotary shaker with a speed of 180 r/min. It can be seen between Table 5.5 and Figure 5.8 that under the test conditions, the initial influent pH of had similar effects on the removal of TP and COD by iron filings. At pH of 6 to 8.57, the lower the initial influent pH, the greater was the removal rate. When pH was 6, the removal rates of TP and COD were 87.36% and 54.42%, respectively. At the same time, the amount of removed TP and COD per unit mass of iron filings increased. When pH was 6, the removal of TP and COD was 0.134 mg/g and 8.39 mg/g, respectively. The removal effect was significantly better than other pH values. It can be seen that reducing the initial influent pH of can increase the removal of TP and COD, because more electrons are released under acidic conditions, then more new Fe^{2+} are produced and H^+ participate in the redox reaction and accelerate the removal of COD. Fe^{2+} is oxidized by O_2 in water into Fe^{3+}. Fe^0 and Fe^{3+} combine

Table 5.5: Effect of initial influent pH on removal of TP and COD by iron filings.

Target pollutant	Initial pH	Effluent concentration (mg/L)	Removal rate (%)	Target pollutant	Initial pH	Effluent concentration (mg/L)	Removal rate (%)
TP	6.0	0.27	87.36	COD	6.0	98.41	54.42
	6.5	0.54	74.40		6.5	107.09	50.39
	7.0	0.64	70.31		7.0	122.35	43.32
	7.43	0.69	67.62		7.43	130.35	39.62
	7.93	0.79	63.78		7.93	136.70	36.68
	8.57	0.82	61.71		8.57	143.11	33.71

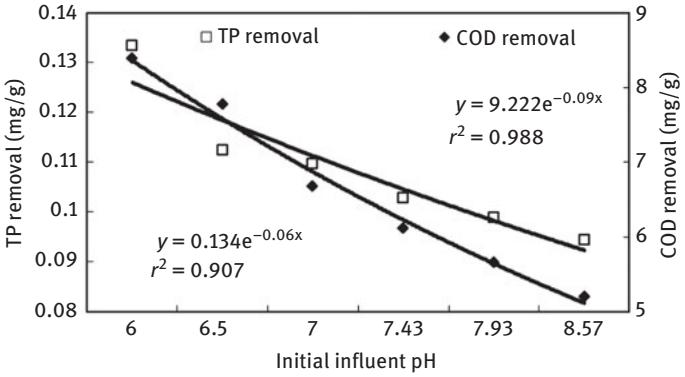

Figure 5.8: Effect of initial influent pH on removal of TP and COD by iron filings.

with phosphate, forming insoluble iron phosphate, so as to achieve the purpose of phosphorus removal.

As can also be seen from Figure 5.8, there is an exponential relationship between the initial pH of influent and the amount of TP and COD removed per unit of iron filings:

$$A = 0.134\ 1\ \exp[-0.062\ 1P] \tag{5.4}$$

where A is the TP removal; P is the initial pH; </UNL>

The correlation coefficient r^2 between A and P is 0.9078.

$$\mathrm{R---Cl + e + H_2O = R---H + Cl^- + OH^-} \tag{5.5}$$

where: A is the COD removal; P is the initial pH; the correlation coefficient r^2 between A and P is 0.9981.

(2) Effect of reaction time on removal of TP and COD by iron filings

At room temperature, with the initial influent concentration of TP of 4.27 mg/L and COD of 215.89 mg/L, 0.3 g (9 portions for TP removal test) and 2 g (10 portions for COD removal test) iron filings were respectively added in a 250 ml Erlenmeyer flask with 50 ml formulation solution on a rotary shaker at 180 r/min, while the reaction time is as shown in Table 5.6. From Table 5.6 and Figure 5.9, it can be seen that with the extension of the reaction time, the removal rate of TP and COD gradually increased. When the reaction time was more than 90 min, the removal rate of TP reached more than 80%, the removal amount was higher than 0.60 mg/g. When the reaction time was more than 150 min, the removal rate of COD was higher than and the removal amount was more than 3 mg/g. However, with the extension of the reaction time, the curves of the removal rate and removal amount of TP and COD tended to be flat, probably because Fe^{2+} produced during the reaction formed $Fe(OH)_2$ or $Fe(OH)_3$ and other insoluble substances under

Table 5.6: Effect of reaction time on removal of TP and COD by iron filings.

Target pollutant	Reaction time (min)	Effluent concentration (mg/L)	Removal rate (%)	Target pollutant	Reaction time (min)	Effluent concentration (mg/L)	Removal rate (%)
TP	5	3.63	14.82	COD	5	212.52	1.56
	10	3.19	25.14		10	195.65	9.38
	20	1.90	55.43		20	168.67	21.88
	40	1.34	68.48		40	153.82	28.75
	60	1.07	74.93		60	148.43	31.25
	90	0.74	82.67		90	131.56	39.06
	150	0.63	85.24		150	86.36	60.00
	360	0.53	87.66		240	87.71	59.38
	540	0.20	95.23		360	80.96	62.50
					580	67.47	68.75

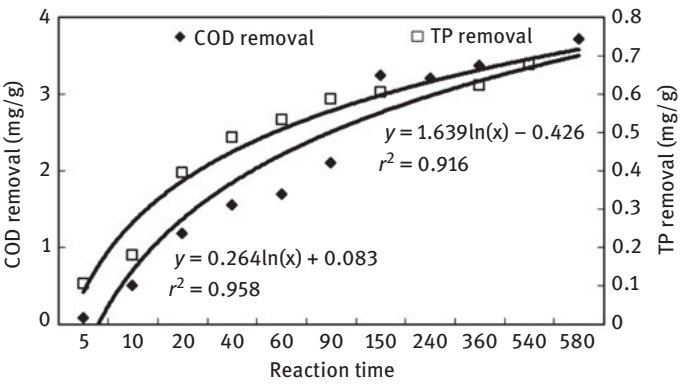

Figure 5.9: Effect of reaction time on removal of TP and COD by iron filings.

aerobic conditions. Over time more and more Fe^{2+} got deposited on the surface of the iron filings, thus hindering the reaction; and with the extension of the reaction time, the reaction consumed more H^+ ions. The concentration of H^+ would begin to decrease and the pH would increase, so that the reaction of micro-electrolysis would be weakened and the flocs would increase. At this time, the flocculation would be strengthened gradually. In addition, the residual concentration of pollutants would be lower and the reaction would become slower with the extension of the reaction time. Comparing the test results, it can be said that the reaction time had a significant effect on the removal efficiency of TP and COD in self-formulated wastewater. The optimal reaction time for TP was ≥90 min, and the optimal reaction time for COD was ≥150 min. In practical engineering application, considering the cost of engineering and so on, the optimal reaction time of 90 min for TP and the optimal reaction time of 150 min for COD are recommended.

As can also be seen from Figure 5.9, there is a logarithmic relationship between the reaction time and the amount of TP and COD removed per unit of iron filings:

$$A = 0.264\ 3\ln T + 0.083\ 2 \tag{5.6}$$

where A is TP removal; T is the reaction time; the correlation coefficient r^2 between A and T is 0.958 7.

$$A = 1.639\ln T - 0.426\ 8 \tag{5.7}$$

where: A is COD removal; T is the reaction time; the correlation coefficient r^2 between A and T is 0.916 6.

(3) Effect of initial influent concentration on removal of TP and COD by iron filings

At room temperature, with the initial influent concentrations of TP and COD as shown in Table 5.7, 1 g (6 portions for TP removal test) and 0.7 g (6 portions for COD removal test) of iron filings were added respectively in a 250 mL Erlenmeyer flask with 50 mL formulated solution at 180 r/min on a rotary shaker for 120 min reaction (TP removal test) and for 150 min reaction (COD removal test). The test results are shown in Table 5.7, Figure 5.10 and Figure 5.11. It can be seen that under the test conditions, when the target pollutant was TP, the removal rate showed a trend of first increasing and then decreasing within the initial influent concentration range in this test. When the initial influent concentration was 2.17 mg/L, the removal rate reached maximum of 88.97%, but the overall difference was not significant. When the TP influent concentration was 1 to 4 mg/L, the removal rates were above 85%, so the suitable range of initial influent concentration of TP was 1 to 4 mg/L. When the target pollutant was COD, the higher the initial influent concentration, the lower was the removal rate, because in the reaction process, the contact surface area with the wastewater was fixed. When the concentration is low, the chemical effects and flocculation function of primary battery can give full play, so that the wastewater

Table 5.7: Effect of initial influent concentration on removal of TP and COD by iron filings.

Target pollutant	Initial influent concentration (mg/L)	Effluent concentration (mg/L)	Removal rate (%)	Target pollutant	Initial influent concentration (mg/L)	Effluent concentration (mg/L)	Removal rate (%)
TP	0.56	0.13	76.73	COD	58.46	18.50	68.36
	0.83	0.15	82.29		102.14	46.37	54.61
	1.12	0.16	85.36		206.30	116.93	43.32
	2.17	0.24	88.97		350.78	229.82	34.48
	3.32	0.49	85.17		417.98	290.30	30.55
	4.22	0.60	85.90		1 034.88	821.18	20.65

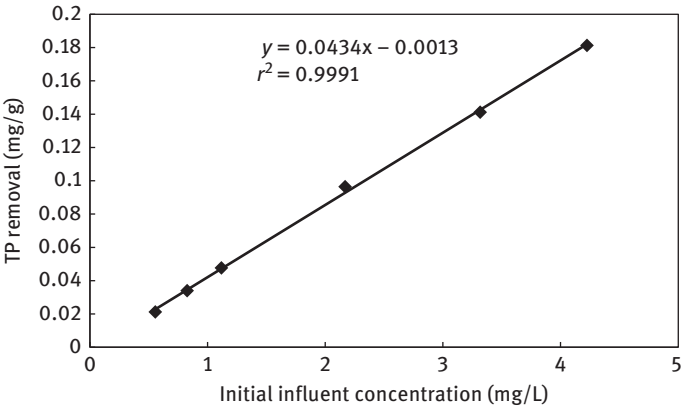

Figure 5.10: Effect of initial influent TP concentration on removal of TP by iron filings.

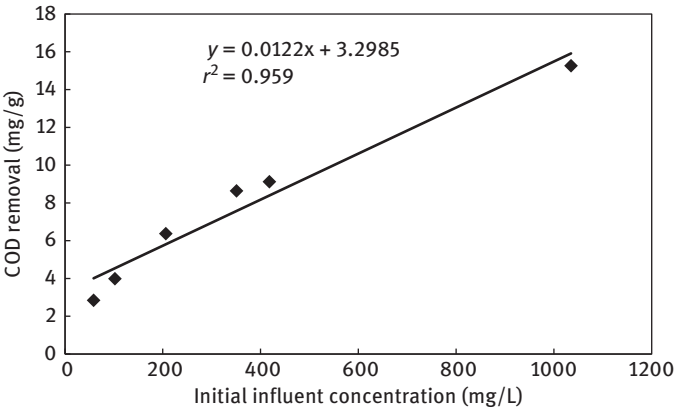

Figure 5.11: Effect of initial influent COD concentration on removal of COD by iron filings.

pollutants can be effectively removed. When the initial concentration of water reaches a certain value, the contaminants coming in contact with the iron filings will approach the saturation of the reduction capacity of the iron surface, and the removal rate will decrease. For the removal of TP and COD, the greater the initial influent concentration, the greater is the removal.

As can be seen from Figure 5.10 and Figure 5.11, there is a linear relationship between the initial influent concentration and the amount of TP and COD per unit of iron filings:

$$A = 0.043\ 4C - 0.001\ 3 \tag{5.8}$$

where A is TP removal; C is the initial influent concentration; the correlation coefficient R^2 between A and C is 0.999 1.

$$A = 0.012\ 2C + 3.298\ 5 \tag{5.9}$$

where A is COD removal; C is the initial influent concentration; the correlation coefficient R^2 between A and C is 0.959.

(4) Effect of the amount of iron filings on removal of TP and COD by iron

At room temperature, with the initial influent TP concentration of 4.16 mg/L and COD concentration of 214.19 mg/L, a certain amount of iron filings (shown in Table 5.8) was added to a 250 mL Erlenmeyer flask with 50 mL formulated solution. The reaction was performed on a rotary shaker at 180 r/min for 120 min. The test results are shown in Table 5.8 and Figure 5.12. With the increase in the amount of iron filings, the removal rates of TP and COD increased gradually. The removal amount of TP and COD decreased with the increase in the amount of iron filings, but the trend became

Table 5.8: Effect of the amount of iron filings on removal of TP and COD by iron.

Target pollutant	Amount of iron filings (g)	Effluent concentration(mg/L)	Removal rate (%)	Target pollutant	Amount of iron filings (g)	Effluent concentration(mg/L)	Removal rate (%)
TP	0.07	2.68	35.67	COD	0.1	184.07	14.06
	0.1	2.25	47.04		0.2	153.94	28.13
	0.2	1.08	74.52		0.3	143.91	32.81
	0.3	0.82	80.67		0.4	140.56	34.38
	0.4	0.81	80.99		0.5	133.87	37.50
	0.5	0.60	86.00		0.7	130.52	39.06
	0.7	0.53	87.46		1	107.09	50.00
	—	—	—		1.5	100.40	53.13
	—	—	—		2	92.37	56.88
	—	—	—		3	90.36	57.81

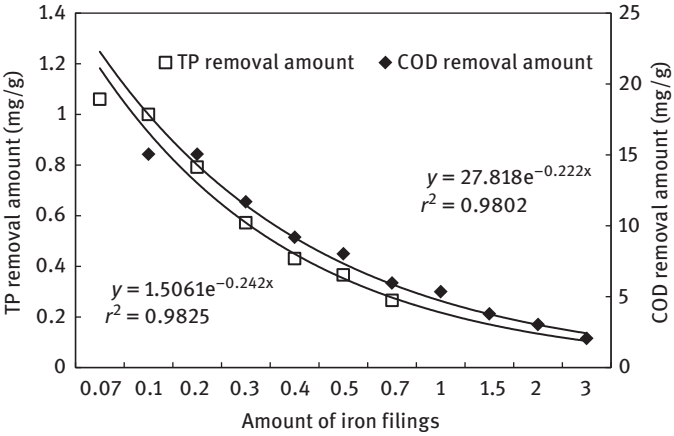

Figure 5.12: Eight effects of the amount of iron filings on removal amount of TP and COD by iron.

smooth with the increase in iron filings. The reason for the abovementioned phenomenon may be because the content of pollutants in water is certain. The more iron filings are added, the less the utilization rate of the reduction reaction sites per unit iron mass will be, resulting in the decrease of the removal amount.

It can also be seen from Figure 5.12 that under the test conditions, there is an exponential relationship between the amount of iron filings and the amount of TP and COD removed by unit iron filings:

$$A = 1.5061\exp(-0.242Y) \tag{5.10}$$

where A is TP removal; Y is the amount of iron filings; the correlation coefficient r^2 between A and Y is 0.982 5.

$$A = 27.818\exp(-0.222Y) \tag{5.11}$$

where A is COD removal; Y is the amount of iron filings; the correlation coefficient r^2 between A and Y is 0.980 2.

5.3.3.3 Summary

(1) Adding copper oxide, aluminum oxide and manganese dioxide could obviously promote the removal of nitrate nitrogen. Manganese dioxide had also a good effect on the removal of total nitrogen by iron filings, and the removal efficiency was increased from 0.05 mg/g without additives to 0.17 mg/g, more than three times that of the original one. Adding cathode materials such as bamboo charcoal did not significantly improve the removal of total nitrogen and nitrate nitrogen per unit mass of iron filings.

(2) Under experimental conditions for the removal of TN by iron filings, the effect size of the influence factors was as follows: reaction time > initial concentration > iron dosage > pH. For the removal of nitrate nitrogen by iron filings, the effect size of the influence factors was as follows: the amount of iron filings > reaction time > initial concentration > pH.
(3) According to the comprehensive analysis, under the conditions and scope of this experiment, the optimal reaction conditions were as follows: initial TN concentration of 20–30 mg/L, initial TP concentration of 1–4 mg/L, pH of 6 –7, optimal reaction time of 90–150 min and the dosage of iron filings of 14 g/L (0.7 g/50 mL).

5.3.4 Application effect and characteristics of functional materials in PRB in surface water treatment

On the basis of previous studies, through a more realistic field pilot test, polluted river water was taken as the research object to study the application effects and characteristics of the functional material for nitrogen and phosphorus removal in the PRB and provide the basic parameters for possible future engineering applications.

5.3.4.1 PRB reactor design

(1) Bed design

The PRB system consists of six separate units, each of which is made up of an intake tank, a reaction zone, and a water outlet tank. The dimensions of each part are as follows: water intake tank length 150 cm × width 72 cm × height 150 cm; reaction area length 276 cm × width 72 cm × height 120 cm; water outlet tank length 40 cm × width 72 cm × height 120 cm. The bed (wall) body is made of brick and cement brick. In order to increase the strength of the bed (wall) body, the ground girder and ring girder with steel-concrete structure are inlaid into the bed (wall) body. Along the flow direction, the sampling pipes are arranged in the reaction zone at a distance of 30, 54, 54, 54 and 54 cm. Each single reaction zone is 276 cm long. Therefore, five sampling ports are provided for each single reactor. The sampling tube is constructed in a PVC pipe embedded through the wall and the outer side is sleeved with valve control. From the inside the PVC pipe is perforated to collect water samples.

(2) Selection of reaction materials

(i) Reaction materials and ratio

The PRB system consists of six separate units, each of which is a separate PRB. According to water quality and geographical features, the reaction materials were selected from iron filings, limestone, coke and zeolite, as shown in Table 5.9.

Table 5.9: Material ratio for pilot test.

Reactive barrier (No.)	①	②	③	④	⑤	⑥
Reactive material	Iron filings — Limestone	Iron filings — Coke	Iron filings — Zeolite	Iron filings Coke Zeolite	Iron filings Coke Zeolite	Iron filings Coke Zeolite
Volume percentage	1 : 1	1 : 1	1 : 1	2 : 1 : 1	1 : 2 : 1	1 : 1 : 2

(ii) Filling way of reaction materials

A 300 mm thick limestone layer was filled in front of and behind each cell reaction zone. Mixed reaction materials with a thickness of 2,160 mm were filled between the two limestone layers. The three layers of media formed the entire reaction zone. The media was to mix well when filling in the middle 2,160 mm thick mixed reaction materials.

(3) Water distribution system

The PRB system designed in this study is aimed at treating surface polluted water (the object of this study is polluted water of a river). A purification system for polluted water is built on the embankment of the polluted water body or through appropriate reconstruction of the embankment. The artificial enhancement measures should play a role in purification of the river. In order to make the water distribution to meet the design goals and to make the water distribution as uniform as possible, the distribution with valve + flow meter + influent sink was applied. A submersible pump lifted the target contaminated water through 25 mm polypropylene random (PPR) pipe into the sink. Before entering the sink the flow was controlled by valves and flow meters. The influent sink and the reaction zone were connected as a whole and were separated only with iron grille. So the water distribution was uniform in the entire Permeable reactive barrier (PRB) cross section. With continuous operation of the system, the operating conditions of the parallel units were the same. The design parameters of the pilot plant are shown in Table 5.10.

The pilot plant and process flow chart are shown in Figure 5.13 and Figure 5.14.

Table 5.10: Design parameters of the pilot plant.

Unit	Composition	Length (m)	Width (m)	Granule diameter (cm)	Granule layer thickness (cm)	Bottom slope (cm)
①	Iron filings, limestone	4.66	0.72	2–5	100	0
②	Iron filings, coke	4.66	0.72	2–5	100	0
③	Iron filings, zeolite	4.66	0.72	2–5	100	0
④	Iron filings, coke and zeolite	4.66	0.72	2–5	100	0
⑤	Iron filings, coke and zeolite	4.66	0.72	2–5	100	0
⑥	Iron filings, coke and zeolite	4.66	0.72	2–5	100	0

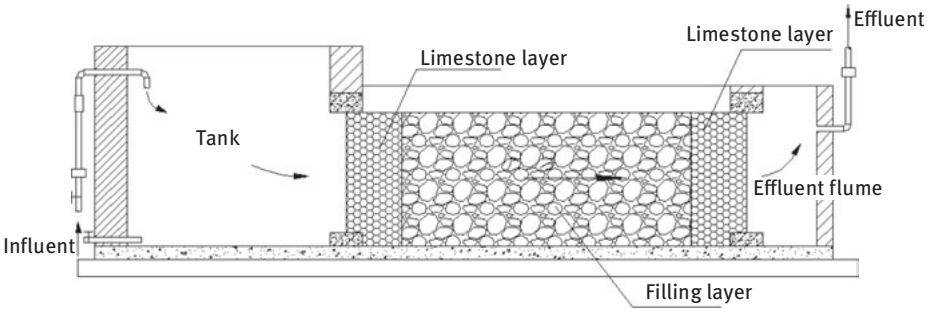

Figure 5.13: Pilot plant and process flow chart.

Figure 5.14: PRB pilot plant.

5.3.4.2 Test methods and processes

(1) Water quality

The pilot plant was built on the left bank of a river, about 70 m away from the embankment. After the water was lifted into the influent sink by a submerged pump, large particles were precipitated and removed, and the water flowed into the reaction zone. The water quality of the reaction zone (n = 47) is shown in Table 5.11.

(2) Test process

The PRB was tested in three stages. The first stage had a hydraulic load of 1 m/d. In the second stage the hydraulic load was increased to 2 m/d and in the third stage the hydraulic load was increased to 3 m/d. The operation status of PRB is shown in Table 5.12.

Table 5.11: Influent water quality of reaction zone.

Parameter	Highest value (mg/L)	Lowest value (mg/L)	Average value (mg/L)
COD_{Cr}	139.785	19.355	57.336
TP	1.594	0.091	0.606
TN	22.500	2.883	10.597
NH_4^+-N	18.621	0.702	6.867
NO_3^--N	4.643	0.666	2.567
NO_2^--N	0.889	0.018	0.406

Table 5.12: PRB operation status.

Test stage	Hydraulic load (m/d)	Flow (m^3/d)	Hydraulic retention time (HRT)(h)	Operation status
First stage	1	1.987 2	9.12	Continuous influent
Second stage	2	3.974 4	4.56	Continuous influent
Third stage	3	5.961 6	3.04	Continuous influent

(3) Hydraulic retention time

The following theoretical hydraulic retention time is calculated on the basis of the geometry of the PRB reaction zone, the porosity of the filling materials and the influent flow rate:

$$t_{th} = \frac{nV}{Q} \times 24 \tag{5.12}$$

where t_{th} is theoretical hydraulic retention time, h; n is the porosity of the filling material (using the beaker method and the porosity roughly measured of each PRB system was 0.38); V is the volume of PRB system, m^3; Q is influent flow rate of the system, m^3/d.

5.3.4.3 PRB treatment of polluted river water

During the period of experiment, there was aeration and reoxygenation equipment operated in the test river section, which had an impact on the river water quality. In addition, the water quality of the river had a slight tendency of gradual increase (the pilot plant had an interception pumping station on the upstream of the inlet of the test river section; at the end of the section there was seepage phenomenon), but it

was basically stable. The hydraulic load of each system was 1 m/d. The influent data and standard deviations of each system are shown in Table 5.13. An analysis of variance was performed on the removal rates of each pollutant by PRB. The results are shown in Table 5.14.

Table 5.13: Average value and standard deviation of influent data.

Parameter	Average value (mg/L)	Number of samples	Standard deviation (mg/L)
COD_{Cr}	75.907	15	27.983
TP	0.247	15	0.120
TN	5.019	15	1.896
NH_4^+-N	1.253	15	1.153
NO_3^--N	2.003	15	0.356
NO_2^--N	0.249	15	0.081

Table 5.14: Variance analysis of removal rate.

	F value	Degrees of freedom	*P* value
COD_{Cr}	0.835	15	0.528
TN	22.836	15	0.000***
NO_3^--N	2.075	15	0.076
NO_2^--N	2.952	15	0.017**
NH_4^+-N	14.395	15	0.000***
TP	2.087	15	0.075

Note: ** indicates significant difference at level of 0.05; ***indicates significant difference at level of 0.01.

(1) Removal of COD_{Cr} by PRB

The influent and effluent COD concentration and removal rate of the PRB system are shown in Figure 5.15. The results showed that the water quality in the experimental section fluctuated greatly: only 40 mg/L at low level and over 120 mg/L at high level. In the early stage of system operation, ①–⑥ PRB systems had low COD removal rates, which fluctuated significantly. This may be caused by the following two reasons: (1) on the one hand, the bed biofilm

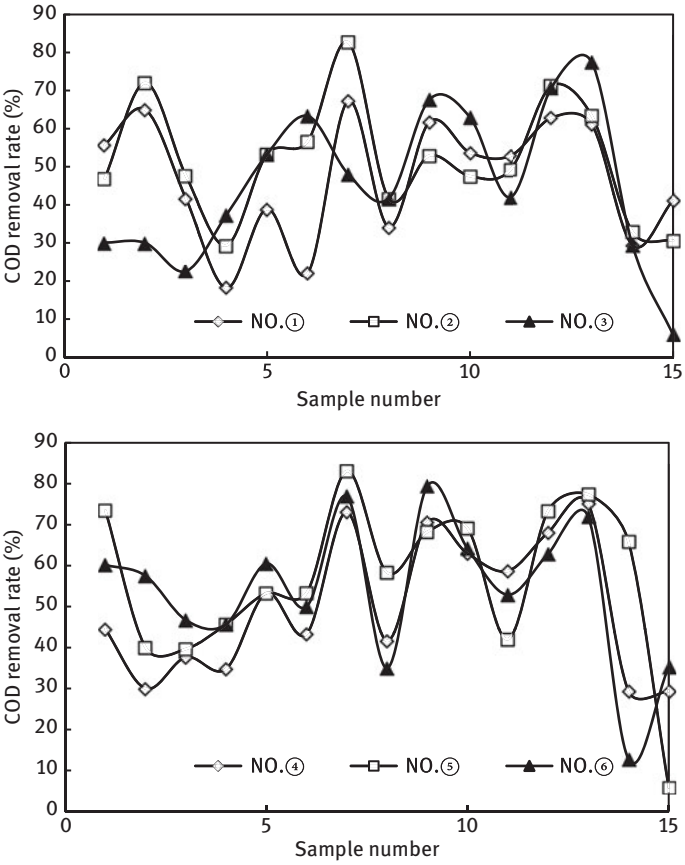

Figure 5.15: Effect of PRB system on removal of COD_{Cr}.

has not yet fully grown and the system has not yet completely activated; (2) on the other hand, the COD concentration of river water was very low at the beginning of operation, which belonged to the water quality of III–IV. For such low organic load, lower hydraulic load and longer hydraulic retention time are needed to achieve a higher removal rate.

The average removal rates of ①–⑥ PRB systems were 47.06%, 51.88%, 45.49%, 50.17%, 56.58%, 54.12%, respectively. From the numerical point of view, ⑤ and ⑥ PRB system's removal effect was slightly better than other systems. The results of variance analysis showed that with F = 0.835, P> 0.05, there was no significant difference between the removal rates of the PRB systems. It can also be seen from Figure 5.15 that the effluent concentration of COD_{Cr} after each PRB treatment increased with the increase in the influent concentration, but the variation range was not large, indicating that each PRB system had certain anti-shock loading capability.

Each reactor medium contains a certain amount of iron filings. The reduction of pollutants is based on the corrosion cell principle of iron filings. On the one hand, after the reaction of iron filings, the toxicity of the pollutants is reduced and the growth of microorganisms in the reactor is promoted. The organic pollutants can be biodegraded in other parts of the reactor, and the COD of the effluent can be further reduced. In addition to the provision of electrons, the corrosion cell can also form iron oxides, which have strong adsorption–flocculation activity (ZHAO & SHI, 2002), and can adsorb a large number of organic molecules and reduce the pollutant content of effluent. On the other hand, these reactions lead to an increase of pH that favors the precipitation of Fe $(OH)_3$, which is beneficial for reducing secondary pollution due to iron. However, due to adsorption and precipitation, it is possible to generate a reaction protective film on the surface of the zerovalent iron so as to prevent further reaction of iron filings, and the iron filings cannot be fully utilized. At the same time, the precipitation of Fe $(OH)_3$ on the surface will affect the permeability of PRB and become a limiting factor in practical application. Besides, the reaction material zeolite belongs to the family of shelf-structured hydrous aluminosilicate and has a large internal surface area, porous characteristic, strong adsorption capacity and ion exchange capacity. It can adsorb some organic matter, reducing the organic content of effluent. Among them, the role of iron filings is the main one. This is also the reason why there is a certain removal rate of COD_{Cr} in ①–⑥ PRB systems with no significant difference.

(2) Effect of PRB on TN removal

The TN influent and effluent concentration and the removal rate of the PRB system are shown in Figure 5.16. The results showed that there was a tendency that the water quality of the test river section gradually deteriorated. The removal rates of TN by PRB system from ① to ⑥ were all stable with the average removal rates of 54.29%, 73.18%, 70.91%, 70.75%, 85.83% and 79.24%, respectively. The removal effect of ⑤ and ⑥ PRB system was significantly better than the other systems. The variance analysis showed that there was a significant difference ($F = 22.836$, $P < 0.01$) between the PRB systems at the level of 0.01. It can also be seen from Figure 5.16 that the effluent TN concentration after each PRB treatment had little change with the increase of influent concentration, indicating that each PRB system had certain anti-shock loading capability.

The removal of TN by the PRB system is the result of a combination of physical, chemical and biological reaction. When the wastewater flows through the PRB system, the macromolecular organic nitrogen in it is physically retained by the reaction material, reducing the pollutant content in the effluent. Zeolite has a strong adsorption and ion exchange function for ammonia nitrogen and heavy metals (LI & XIAO, 2003), which can adsorb a large amount of ammonia ions. The nitrification–denitrification of microorganisms in the system is also an important reason for TN removal. The removal effect of ⑤, ⑥ PRB system was significantly better than

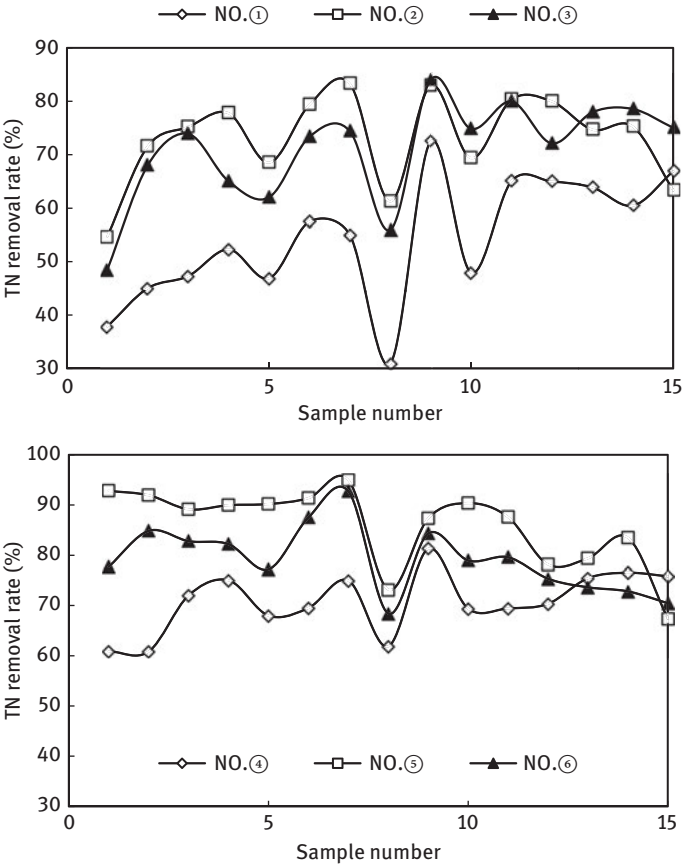

Figure 5.16: Effect of PRB system on removal of TN.

the other systems, because the reaction material ratio in ⑤ PRB system had an increased proportion of coke, which formed a macro-corrosion cell with iron filings, accelerating the corrosion of iron filings and improving the removal of NO_2^--N and NO_3^--N by the system. In ⑥ PRB system the proportion of zeolite in the reaction material was increased. As zeolite is a kind of shelf-structured hydrous aluminosilicate, which has a large internal surface area, porous characteristic, strong adsorption capacity and ion exchange capacity. Zeolite has a strong adsorption and ion exchange function for ammonia nitrogen and heavy metals (YAN et al., 2006) and NH_4^+-N was the main N-type pollutant in the experimental river section.

(3) Effect of PRB on removal of NO_2^--N

Figure 5.17 shows the influent and effluent concentration and the removal rate of NO_2^--N in the PRB system. The results showed that the removal rates of NO_2^--N by PRB systems

①–⑥ were all stable, with the average removal rates of 90.21%, 95.86%, 87.65%, 93.86%, 96.31% and 96.31%, respectively. In addition to ③ PRB system, the removal rate of other systems were more than 90%, of which the removal effect of ⑤ and ⑥ PRB systems were slightly better than the other systems. The variance analysis showed that there was no significant difference in removal rates between the PRB systems ($F = 2.075$, $P > 0.05$). It can also be seen from Figure 5.17 that the effluent concentration of NO_2^--N after each PRB treatment did not change much with the increase of influent concentration, indicating that each PRB system has certain anti-shock loading capability. The NO_2^--N removal capacity of each PRB system can be further improved.

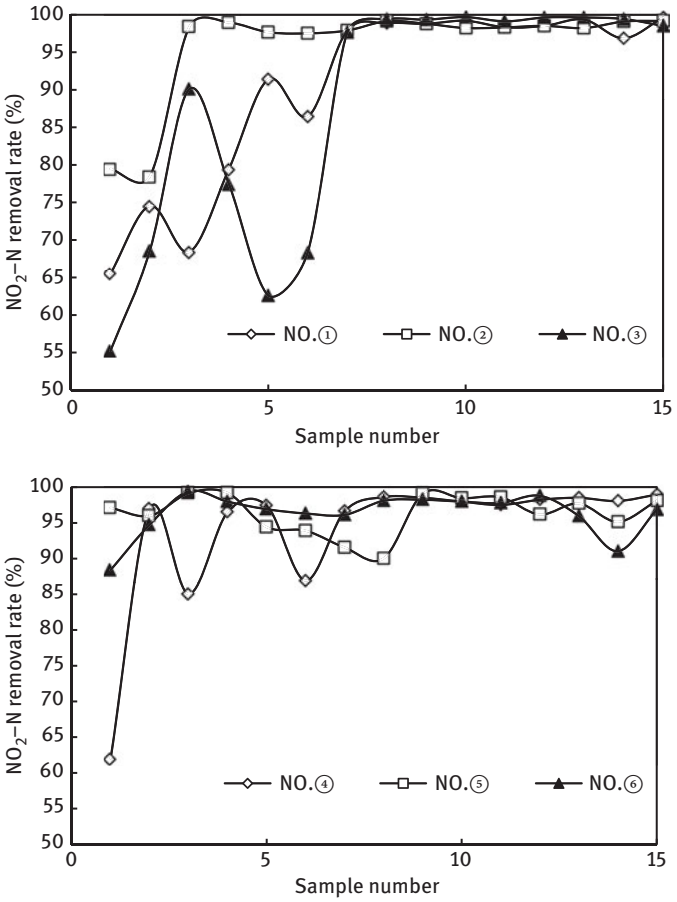

Figure 5.17: Effect of PRB system on removal of NO_2^--N.

NO_2^--N is an unstable intermediate valence state that can be easily oxidized or reduced. Therefore, in the presence of strong reducing iron filings, NO_2^--N can be easily reduced to other N species with a lower valence state, such as N_2, NH_4^+-N and so on.

(4) Effect of PRB on removal of NO_3^--N

Figure 5.18 shows the influent and effluent concentration and the removal rate of NO_3^--N in the PRB system. The results showed that the removal rates of NO_3^--N by PRB systems ①–⑥ were all stable, with the average removal rates of 66.36%, 70.07%, 66.07%, 71.12%, 76.62% and 75.69%, respectively. Among them, the removal rate of the ⑤ and ⑥ PRB system were better than the other systems. The variance analysis showed that the removal rate of each PRB system was significantly different at the level of 0.05 ($F = 2.952$, $P < 0.05$). It can also be seen from Figure 5.18 that the effluent concentration of NO_3^--N after each PRB treatment did not change much with the increase of influent concentration, indicating that each PRB system had certain anti-shock loading capability.

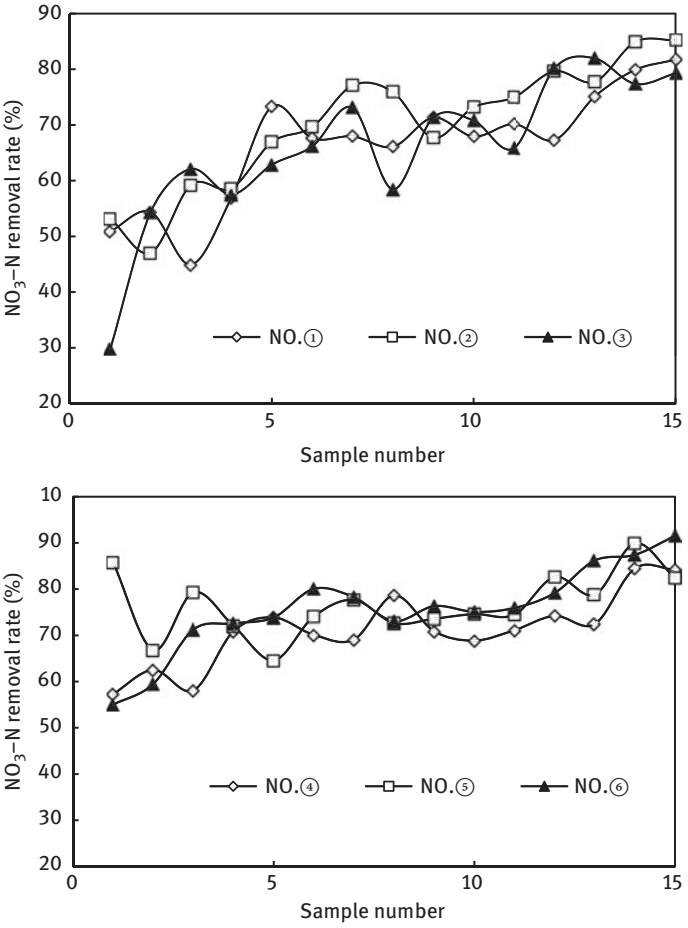

Figure 5.18: Effect of PRB system on removal of NO_3^--N.

Each reactor medium contained a certain amount of iron filings, which had a reduction reaction with NO_3^-. In addition, after the reaction of iron filings, the toxicity of pollutants was reduced, and the growth of microorganisms in the reactor was promoted. So NO_3^--N could be biodegraded in other parts of the reactor to further reduce the NO_3^--N content in the effluent.

(5) Effect of PRB on removal of NH_4^+-N

The influent and effluent concentration and the removal rate of NH_4^+-N in the PRB system are shown in Figure 5.19. The results showed that the removal rate of NH_4^+-N by PRB systems ①–⑥ were all stable, with average removal rates of −45.34%, −8.44%, 27.91%, 10.04%, 22.15%, 23.46%, respectively. Among them, the removal effect of ③, ⑤ and ⑥ PRB system was better than the other systems. The variance analysis showed that the removal rate of each PRB system

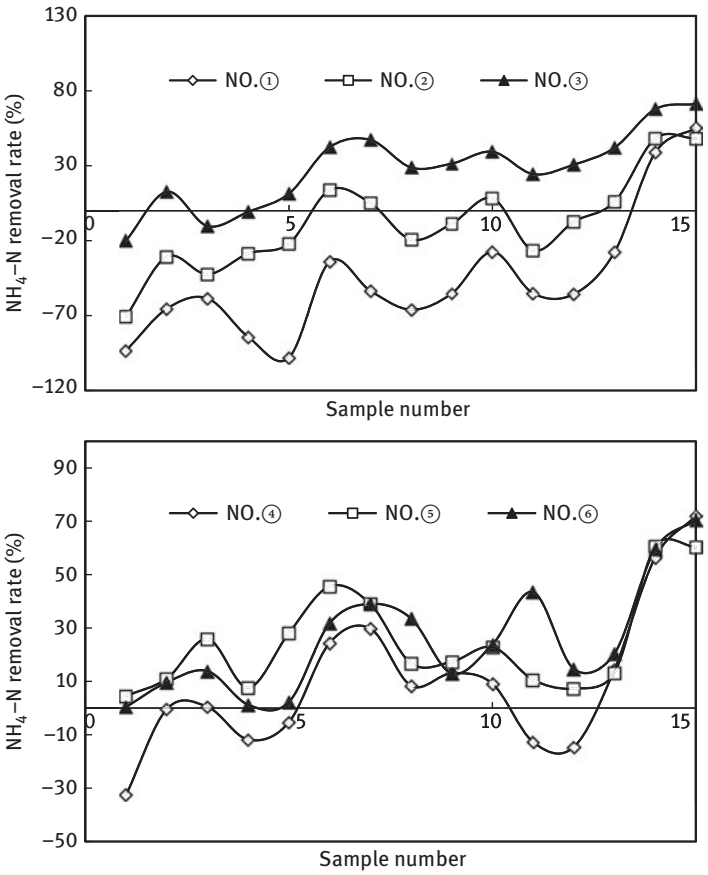

Figure 5.19: Effect of PRB system on removal of NH_4^+-N.

was significantly different at the level of 0.01 ($F = 14.395$, $P < 0.01$). It can also be seen from Figure 5.19 that the effluent concentration of NH_4^+-N after each PRB treatment increased with the increase of influent concentration, but the variation range was not large, indicating that each PRB system had certain capability to resist shock load.

The removal rate of PRB system was low or even negative at the beginning of the system operation. The reason was, on the one hand, instability of the system operation. On the other hand, as each reactor medium contained a certain amount of iron filings, the corrosion cell of iron filings reacted with NO_2^-. The reaction is as follows:

$$NO_2^- + 10H^+ + 4Fe \rightarrow NH_4^+ + 3H_2O + 4Fe^{2+} \tag{5.13}$$

A part of NH_4^+ was generated, which increased the NH_4^+-N content in wastewater. This had a great impact on the removal rate of each system, especially on the ①, ②, ④ PRB system, which had a big proportion of iron filings in the reaction material and the proportion was 50%. Thus, the removal rates were very low or even negative, −45.34%, −8.44%, 10.04%, respectively. However, with the same iron content of 50%, the ③ PRB system had an average removal rate of 27.91%, which was best of all the PRB systems, because its reaction material contained 50% zeolite and the situation was well alleviated. With the steady operation of the system, the adsorption of ammonia nitrogen by zeolite and other reaction materials and microbial nitrification, the removal rates of each PRB system were gradually increased.

(6) Effect of PRB on TP removal

The influent and effluent concentration and the removal rate of TP are shown in Figure 5.20. The results showed that ①–⑥ PRB systems had a good TP removal rate and the average removal rates were 75.39%, 82.05%, 74.71 %, 74.81%, 82.04% and 80.97%, respectively. The removal rates of ②, ⑤, ⑥ PRB system were better than other systems. The variance analysis showed no significant difference in removal rates between PRB systems ($F = 2.087$, $P > 0.05$). It can also be seen from Figure 5.20 that the effluent concentration of TP after each PRB treatment did not change much with the increase of influent concentration, indicating that each PRB system had certain anti-shock loading capability and its TP removal capacity can still be further improved.

The TP removal rate of PRB system in the initial operation stage was low, which may be caused by the unstable operation of the system. During the stabilization period, the TP removal rates of each PRB system were stable at over 60%. The treatment of TP may be mainly chemical adsorption and microbial function. Each reactor medium contained a certain amount of iron filings. Fe^0 in the water could be slowly formed into Fe (II) and Fe (III), which reacted with phosphate, generating precipitates of iron phosphate or iron hydroxyphosphate, so as to achieve the purpose of phosphorus

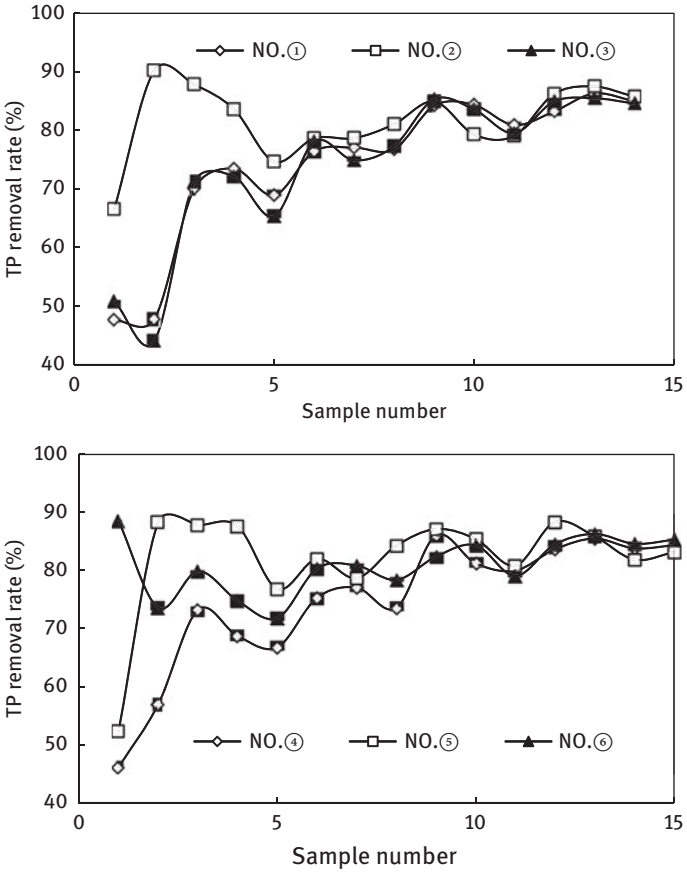

Figure 5.20: Effect of PRB system on removal of TP.

removal. This is consistent with the conclusions of the study of Yan et al. (2006). In addition to the provision of electrons, the corrosion cells of iron filings could also form iron oxide hydrate, which has strong adsorption–flocculation activity and can adsorb a large amount of free-form P in wastewater. In reaction material of ②, ⑤ PRB system, the proportion of coke was increased, which formed a macro-corrosion cell with iron filings, accelerating the corrosion of iron. In addition, the experimental river water may contain a certain concentration of Mg^{2+}, which can be combined with PO_4^{2-} and NH_4^+ to generate ammonium magnesium phosphate precipitate and to remove a certain amount of PO_4^{2-}, as well as NH_4^+ (which is also the mechanism of ammonia nitrogen removal). The reaction is as follows (ZHAO & LI, 1999):

$$Mg^{2+} + HPO_4^{2-} + NH_4^+ + 6H_2O \rightarrow MgNH_4PO_4 \cdot 6H_2O + H^+ \quad (5.14)$$

However, if more precipitate is produced in the reactor, the reactor will be clogged. Careful consideration should be given for its application in the field and measures should be taken to prevent precipitation, if necessary.

(7) Summary

The variance analysis showed that the removal efficiencies of TN, NO_3^--N and NH_4^+-N were significantly different at the level of 0.05 (and better) for each PRB system. Although the removal rates of NO_2^--N and TP were not significantly different, but as shown in Table 5.14, their P values were 0.076 and 0.075 respectively, which were also small. It was indicated that the reaction materials and the ratio of the PRB system play a key role in the removal of pollutants. Based on the abovementioned analysis, under experimental conditions, the tested PRB system with six different ratios of reaction materials had certain removal effect of COD_{Cr}, TN, NO_2^--N, NO_3^--N, NH_4^+-N and TP. The PRB system ⑤ und ⑥ showed good removal effect of each pollutant. The average removal rates for each pollutant in ⑤ system were 56.58% for COD_{Cr}, 85.83% for TN, 96.31% for NO_2^--N, 76.62% for NO_3^--N, 22.15% for NH_4^+-N and 82.04% for TP. The average removal rates of each pollutant in ⑥ system were 54.12% for COD_{Cr}, 79.24% for TN, 96.31% for NO_2^--N, 75.69% for NO_3^--N, 23.46% for NH_4^+-N and 80.97% for TP.

5.3.4.4 Change of PRB contaminant along the process

The removal of pollutants is closely related to the residence time. Under the condition of continuous influent, the residence time of wastewater is different at different positions along the wastewater process. Therefore, several sampling holes are arranged along the direction of the length in the PRB reaction zone. Sampling and analysis are conducted simultaneously in these sampling holes to obtain the dynamic change rule of the pollutants in the reaction zone.

The ⑤ and ⑥ PRB systems with better treatment effects were selected to study the changes of pollutants along the process. Five sampling ports (including the initial influent and the last effluent of the reaction zone) were set along the reaction zone. The monitoring of change of the water quality along the process was performed two times. The system's hydraulic load was 1 m/d and the hydraulic retention time (HRT) was 9.12 h according to Table 5.12. From the monitoring results, taking the concentration of COD_{Cr}, TN, NH_4^+-N and TP in wastewater as ordinate and the migration distance of water as horizontal axis, the changing trend of PRB pollutants along the ⑤ and ⑥ PRB can be obtained respectively (see Figure 5.25 to Figure 5.28 and Figure 5.33 to Figure 5.36).

Taking the quotient of the monitoring value of the pollutants at each monitoring point, C_L, and the initial value of the wastewater concentration, C_0, namely C_L/C_0 as the ordinate, the percentage L (%) of the distance between each monitoring point along the water flow direction to the water inlet end and the PRB length as the

abscissa, the dynamic model prediction curve of each pollutant in PRB can be obtained (see Figure 5.25 to Figure 5.28, Figure 5.33 to Figure 5.36).

(1) Change of pollutants along the process in ⑤ PRB system and its dynamic prediction model

From Figure 5.21 to Figure 5.24, it can be seen that the removal rate of the four major pollutants in the wastewater was very fast in the initial stage. At the first outlet of the effluent (the process where the outlet point was located accounted for one-fourth of the whole process), the average removal rates of the major pollutants COD_{Cr}, TN, NH_4^+-N and TP were 33.83%, 14.45%, 7.38% and 44.07%, respectively. At the second effluent sampling port, where the effluents flowed one-half of the whole process, the average removal rates of COD_{Cr}, TN, NH_4^+-N and TP were 48.82%, 31.46%, 21.99% and 56.64%, respectively. The total removal rates of COD_{Cr}, TN, NH_4^+-N and TP in the whole reaction zone were 57.78%, 42.23%, 40.31% and 65.59%, respectively. As can be seen, the removal of contaminants in ⑤ PRB system occurred mainly in the first half of the reaction zone.

After a rapid removal rate in the initial stage, the removal rate of each pollutant gradually decreased and tended to be flat, as the migration distance of wastewater in the reaction zone increased. This reflects that the PRB system had certain capability to resist shock load and had the advantage of good and stable effluent quality. The pollutants in the wastewater were not completely removed after being treated by the PRB system, but remained at a relatively stable concentration for a long distance at the end of the reaction zone, which may be due to the choice of reaction materials. Combined with the following analysis of ⑥ PRB system, it can be seen that the pollutant removal effect of PRB system mainly depends on the choice of reaction materials, and different reaction materials or different media will affect the removal effect. This reflects another characteristic of the PRB system. Therefore, for the actual operation of the PRB system in engineering, the selection of the appropriate reaction materials and the ratio is the key link.

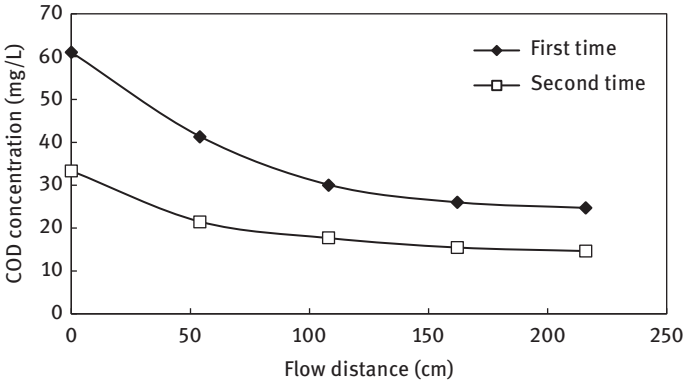

Figure 5.21: Change trend of COD_{Cr} along the process in ⑤ PRB system.

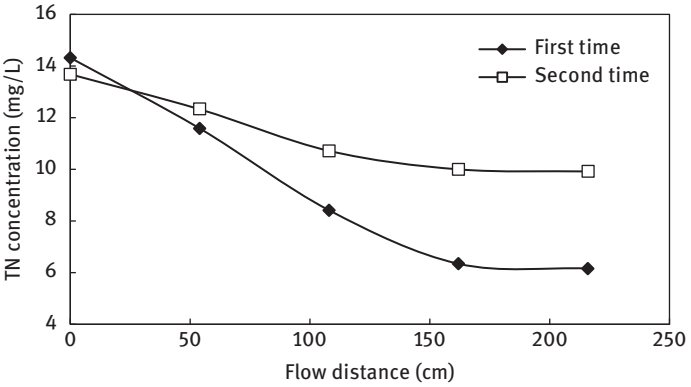

Figure 5.22: Change trend of TN along the process in ⑤ PRB system.

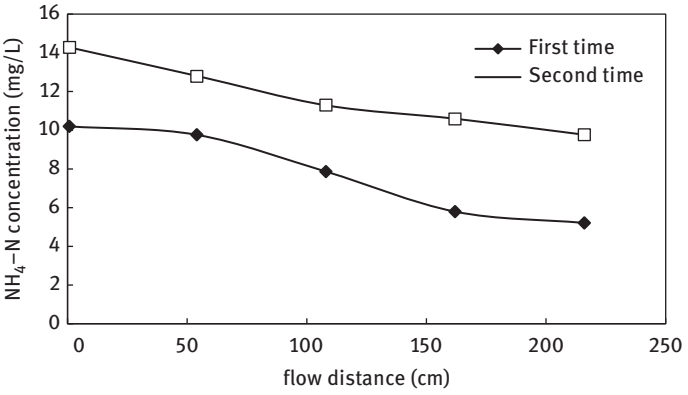

Figure 5.23: Change in the trend of NH_4^+-N along the process in ⑤ PRB system.

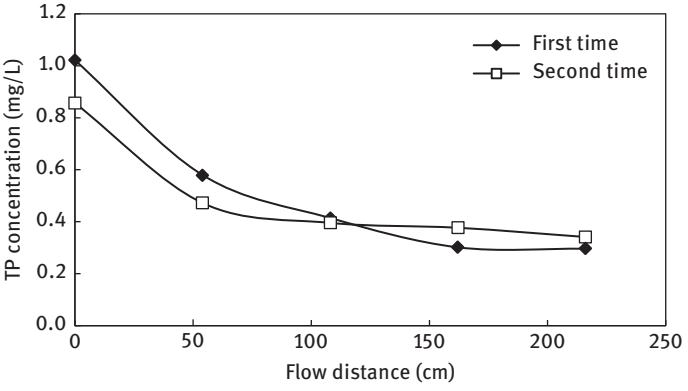

Figure 5.24: Change in the trend of TP along the process in ⑤ PRB system.

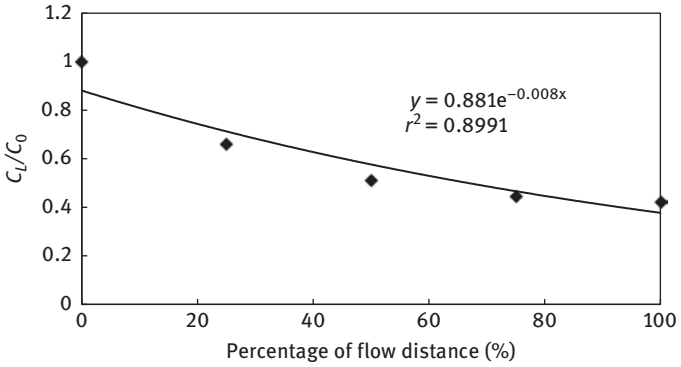

Figure 5.25: Dynamic prediction model of COD_{Cr} in ⑤ PRB system.

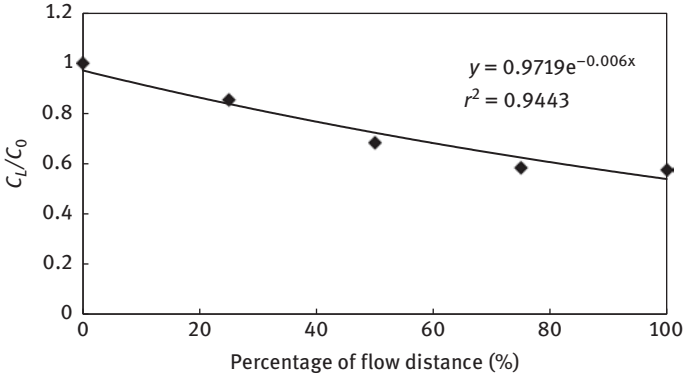

Figure 5.26: Dynamic prediction model of TN in ⑤ PRB system.

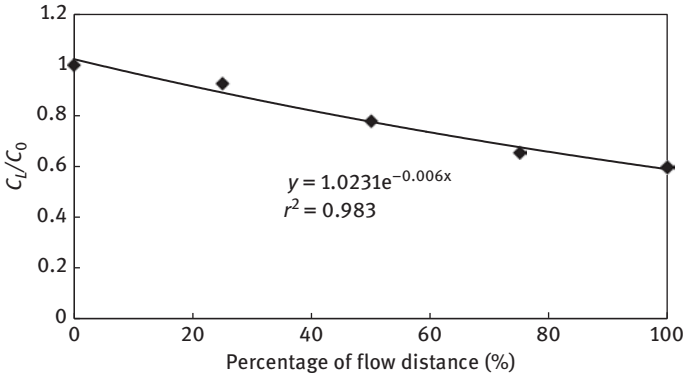

Figure 5.27: Dynamic prediction model of NH_4^+-N in ⑤ PRB system.

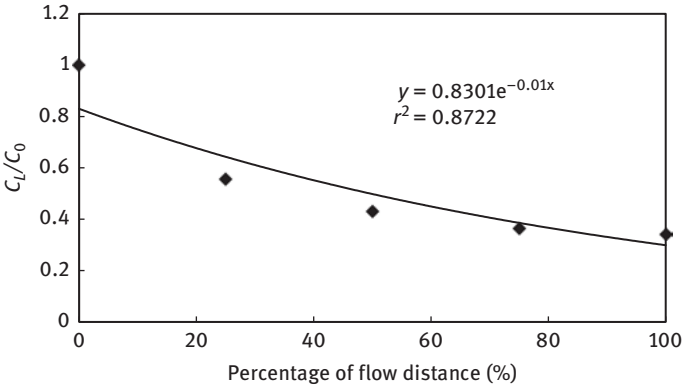

Figure 5.28: Dynamic prediction model of TN in ⑤ PRB system.

(2) Change of pollutants along the process in ⑥ PRB system and its dynamic prediction model

From Figure 5.29 to Figure 5.36, it can be seen that the removal rule of PRB system ⑥ was similar to that of PRB system ⑤. The removal rates of the four pollutants were also very fast at the initial stage. With the migration distance the removal rate of pollutants gradually slowed down. The average removal rates of COD_{Cr}, TN, NH_4^+-N and TP at the first effluent sampling port (accounted for one-fourth of the whole process) were 30.16 %, 16.57%, 20.50% and 40.40%, respectively. At the second effluent sampling port, where the process distance accounted for one-half of the whole process, the average removal rates of COD_{Cr}, TN, NH_4^+-N and TP were 41.13%, 44.49%, 45.17% and 59.89%, respectively. The total removal rates of COD_{Cr}, TN, NH_4^+-N and TP in the whole reaction zone were 57.44%, 70.21%, 69.66% and 72.56%, respectively. It can be seen that the

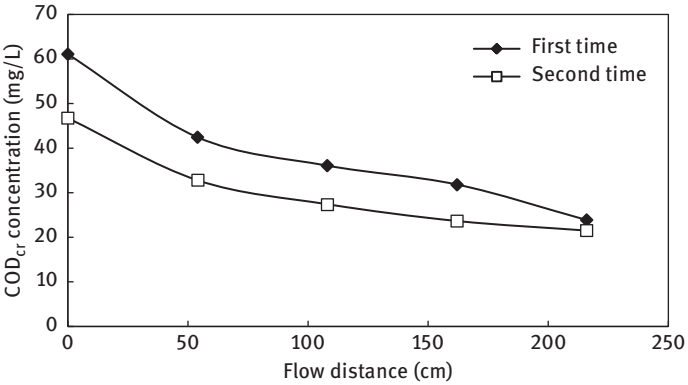

Figure 5.29: Change in the trend of COD_{Cr} along the process in ⑥ PRB system.

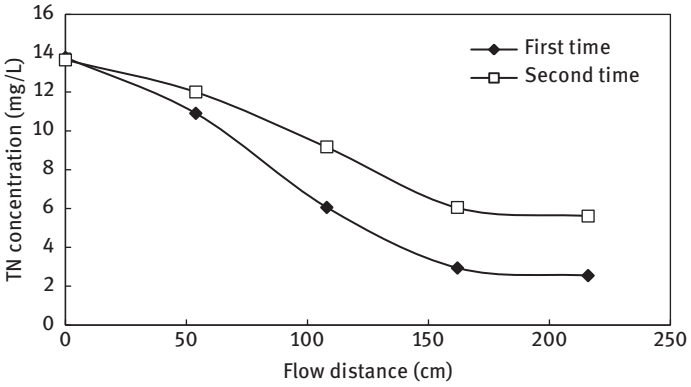

Figure 5.30: Change in the trend of TN along the process in ⑥ PRB system.

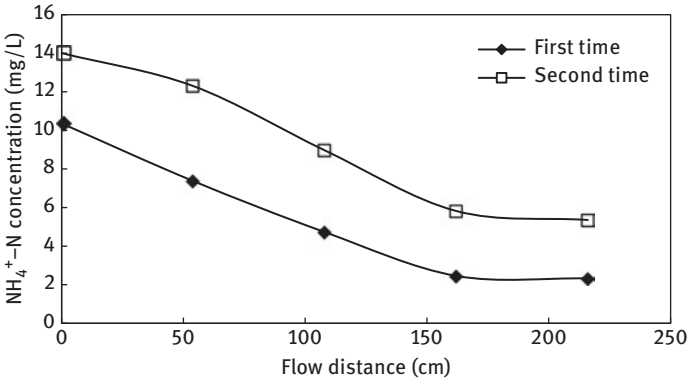

Figure 5.31: Change in the trend of NH_4^+-N along the process in ⑥ PRB system.

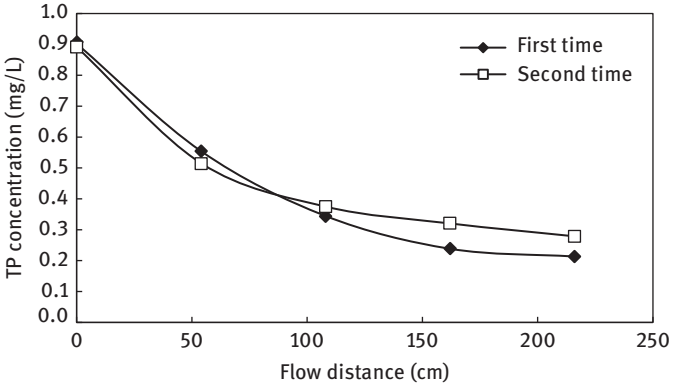

Figure 5.32: Change in the trend of TP along the process in ⑥ PRB system.

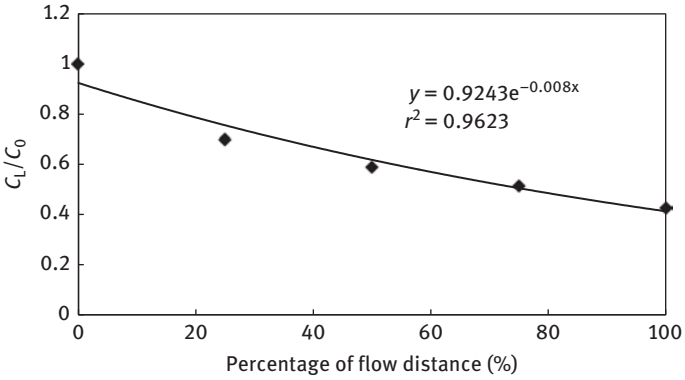

Figure 5.33: Dynamic prediction model of COD_{Cr} in ⑥ PRB system.

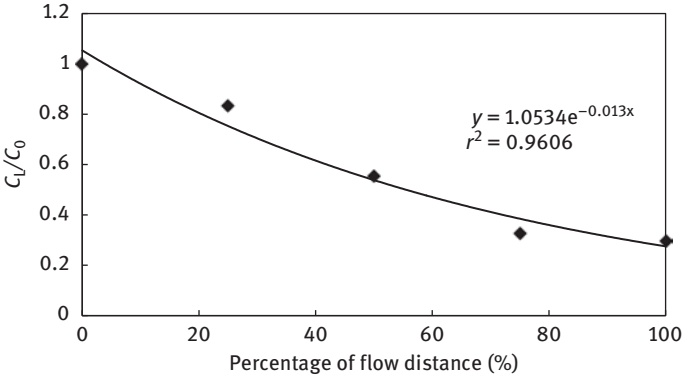

Figure 5.34: Dynamic prediction model of TN in ⑥ PRB system.

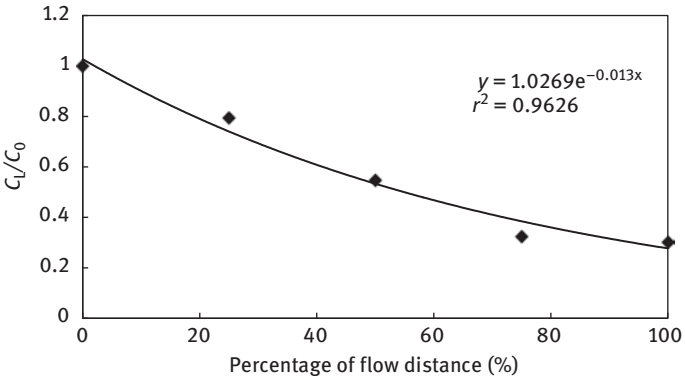

Figure 5.35: Dynamic prediction model of NH_4^+-N in ⑥ PRB system.

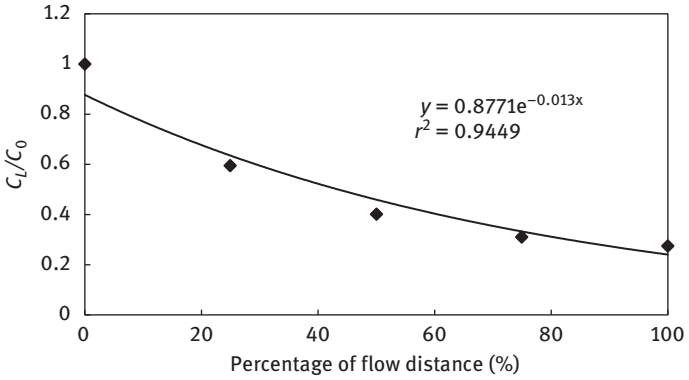

Figure 5.36: Dynamic prediction model of TP in ⑥ PRB system.

removal of pollutants in ⑥ PRB system mainly took place in the first half of the reaction zone, and the removal rates of the pollutants in the first half accounted for more than 60% of the total removal.

Combined with the abovementioned analysis of ⑤ PRB system, we can see that for the removal of TN and NH_4^+-N, ⑥ PRB system was better than ⑤ PRB system, whereas for the removal of other two pollutants, ⑤ PRB system was better than ⑥ PRB system. This was caused by the difference in the proportions of the reaction materials of the two PRB systems. In ⑥ PRB system the proportion of zeolite in the reaction material was increased. Zeolite is a kind of shelf-structured hydrous aluminosilicates with a large internal surface area, porous characteristic, strong adsorption capacity and ion exchange capacity. Zeolite has a strong adsorption and ion exchange capability for ammonia nitrogen and heavy metals (ZHAO & LI 1999). Moreover, NH_4^+-N was the main nitrogen pollutant in the polluted river water of the experimental section. This made ⑥ PRB system better than ⑤ PRB system for the removal of TN and NH_4^+-N. In ⑤ PRB system, the proportion of coke in the reaction material was increased, forming macro-corrosion cells with iron filings, which accelerated the corrosion of iron filings and improved the removal of COD_{Cr} and TP of the system.

From Figure 5.25 to Figure 5.28 and Figure 5.33 to Figure 5.36, it can be seen that the dynamic changes of the four main pollutants in the reaction zone can be described with exponential equations, whether in PRB system ⑥ or in PRB system ⑤.

5.3.4.5 Influence of pollution load on the system treatment effect

Although the hydraulic load of each stage was fixed in the process of system operation, the corresponding pollution load constantly fluctuated due to the changing pollutant concentration of the influent. The PRB systems ⑤ and ⑥ were studied. The pollution load of four major pollutants is shown in Table 5.15.

Table 5.15: Operating load of PRB system.

PRB	Hydraulic load[$m^3/(m^2 \cdot d)$]	COD_{Cr} load [$g/(m^2 \cdot d)$]	TN load [$g/(m^2 \cdot d)$]	NH_4^+-N load/ [$g/(m^2 \cdot d)$]	TP load [$g/(m^2 \cdot d)$]
⑤ PRB	1	29.71–139.78	2.88–22.5	0.70–18.62	0.09–1.59
⑥ PRB	1	29.71–139.78	2.88–22.5	0.70–18.62	0.09–1.59

During the operation of the system, the daily influent of the system is always kept at 1987.2 L. The maximum load and the minimum load of each pollutant in the system differed by about one order of magnitude. However, the removal rate of each pollutant in PRB system ⑤ or ⑥ was relatively high and stable. During the system operation, the relationship between the organic load, TN load, NH_4^+-N load, TP load of the two PRBs and the corresponding purification load is shown in Figure 5.37 to Figure 5.40, respectively.

From Figure 5.37 to Figure 5.40, it can be seen that the organic load, TN load, NH_4^+-N load and TP load of PRB system with two kinds of medium ratio had a significant linear relationship with the corresponding wastewater purification load. The correlation coefficient r^2 of ⑤ PRB system between organic load, TN load, NH_4^+-N load, TP load and the purification load was 0.9006,0.9075,0.9499 and 0.9932, respectively. The corresponding r^2 value of ⑥ PRB system was 0.9030, 0.9646, 0.9653, and 0.9859, respectively. It can be seen that the two systems showed relatively good reaction conditions. With higher pollution load the purification load also increased. From the rising trend of the line, a large residual purification capacity can still be used in the system. The result was related to the short running time of the system. For understanding the rules in the follow-up operation, further tests are needed.

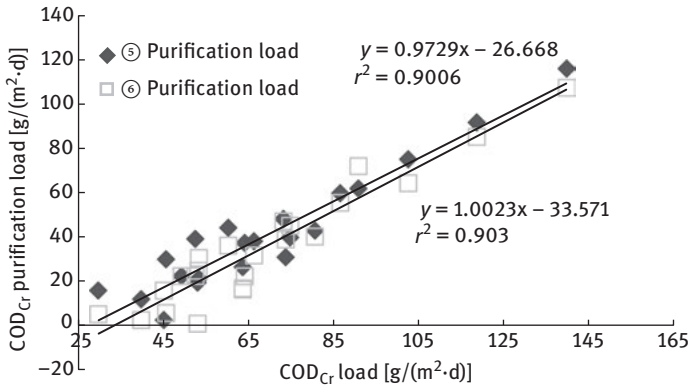

Figure 5.37: Effect of organic load on purification load in ⑤ and ⑥ PRB system.

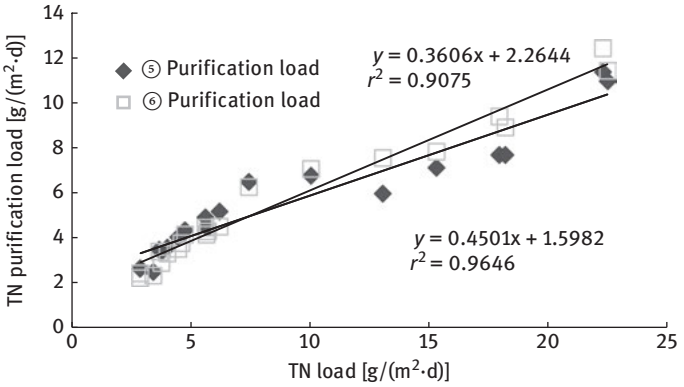

Figure 5.38: Effect of TN load on purification load in ⑤ and ⑥ PRB system.

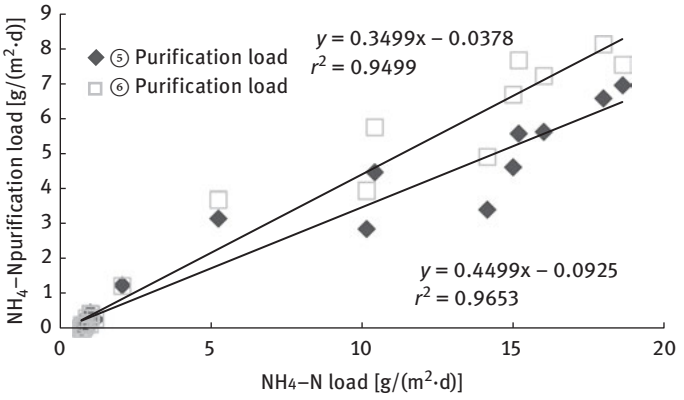

Figure 5.39: Effect of NH_4^+–N load on purification load in ⑤ and ⑥ PRB system.

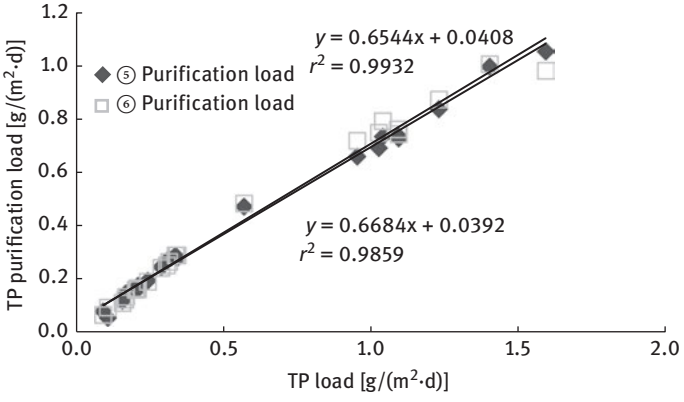

Figure 5.40: Effect of TP load on purification load in ⑤ and ⑥ PRB system.

In actual operation, the system load cannot be unlimitedly increased. In the beginning, the purification capacity of the system is very large, and some purification space cannot be reused after being used. In order that the system can run as long as possible, it is desirable to maintain a lower load. In addition, although the purification load and the total amount of removed pollutants also increases, when the pollution load of the system increases, it does not necessarily guarantee that the effluent quality will meet the standard.

5.3.4.6 Relation between iron concentration and system treatment effect

Since the reaction materials contain iron filings, the redox reaction of iron filings and oxidizing substances in water will increase the concentration of iron ion in the effluent. So the reaction status of the system can be known by monitoring of the iron ion content in the effluent. During the experiment, because of the limited field test conditions, the data of iron ion concentration in influent and effluent were relatively few. Four groups data of iron ion concentrations in the influent and effluent of were measured. The mean value of the iron ion concentration and the average concentration of the corresponding pollutants in water are shown in Table 5.16.

Table 5.16: Average value of effluent data and standard deviation

Pollutant (No.)	Iron ion concentration (mg/L)	COD_{Cr} concentration (mg/L)	TN concentration(mg/L)	NO_3^-–N concentration(mg/L)	NO_2^-–N concentration(mg/L)	NH_4^+–N concentration(mg/L)	TP concentration(mg/L)
Influent	0.39±0.01	43.36±17.8	6.77±0.33	0.37±0.05	4.51±0.16	1.19±0.14	0.29±0.01
①Effluent	0.43±0.06	29.69±6.24	2.23±0.49	0.07±0.02	1.00±0.07	1.15±0.22	0.10±0.02
②Effluent	0.93±0.27	27.10±7.98	2.26±0.48	0.05±0.02	0.75±0.21	1.32±0.16	0.10±0.01
③Effluent	0.35±0.07	29.93±8.76	2.87±0.47	0.04±0.03	0.85±0.14	1.89±0.16	0.09±0.02
④Effluent	0.82±0.12	31.71±14.3	3.11±1.10	0.03±0.02	0.90±0.50	2.06±0.21	0.09±0.03
⑤Effluent	0.79±0.13	28.62±11.5	2.72±0.69	0.06±0.04	0.83±0.45	1.85±0.11	0.08±0.02
⑥Effluent	20.57±0.09	28.18±8.09	2.99±0.85	0.04±0.04	0.83±0.54	2.06±0.12	0.09±0.03

In order to select the appropriate correlation coefficient for the correlation analysis of the iron ion concentration and the concentration of each pollutant in the influent and effluent, a normal distribution test was first made on the concentration of iron ion in the influent and the effluent (Figure 5.41). It was found that it accorded with the normal distribution. Therefore, a unilateral parametric correlation analysis was performed for the iron ion concentration and the concentration of pollutants in the influent and effluent. The results are shown in Table 5.17.

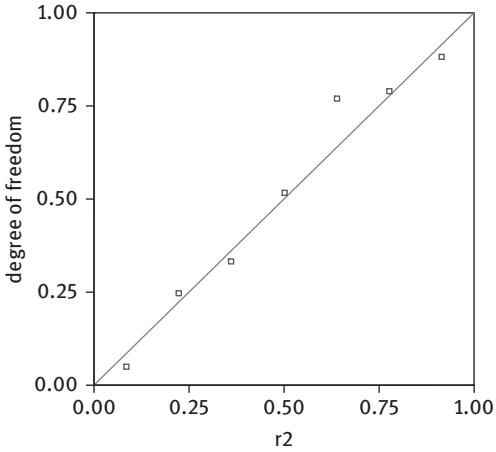

Figure 5.41: Normality test of iron ion concentration.

Table 5.17: Correlation analysis of iron ion concentration and concentration of each pollutant in effluent.

	r^2 value	Degree of freedom	*P* value
COD_{Cr}	−0.754	7	0.025*
TN	−0.721	7	0.034*
NO_3^--N	−0.736	7	0.030*
NO_2^--N	−0.750	7	0.026*
NH_4^+-N	0.379	7	0.201
TP	−0.755	7	0.025*

Note: * indicates significant correlation at level of 0.05.

The results showed that there was a significant negative correlation ($P < 0.05$) between the iron ion concentration and the concentration of each pollutant (except NH_4^+-N) in the effluent. This implies that the chemical reaction between iron filings and pollutants was significantly related to the removal of pollutants. The correlation between iron ion concentration and the concentration of COD_{Cr}, TP and NO_2^--N was better than other pollutants, indicating that the removal of COD_{Cr}, NO_2^--N and TP was more dependent on the reaction material iron filings than other pollutants within the scope of this study.

5.4 Application of functional materials in PRB for removal of trace organic pollutants

5.4.1 Overview

The application of PRB technology to treat trace organic pollutants in groundwater is the earliest research field of PRB technology. In 1992, the first PRB project in the

world utilized PRB technology to control TCE and PCE pollution. The project is located at Borden Air Force Base in Ontario, Canada. The reaction wall had a thickness of 1.5 m, with 21% iron filings and 79% grit. The content of TCE and PCE in the contaminant plumes was 200 mg/L and 60 mg/L, respectively. After the plumes passed through the reaction wall, 90% of the TCE and PCE in the wastewater were removed (MARCUS & BONDS, 1999). The trace organic pollutants that PRB technology targets are mainly chlorinated hydrocarbon organics. Zerovalent iron was the earliest and most widely used reactive material. As the technology developed, researchers have selected and developed many high quality reaction materials.

5.4.2 Basic principle of removal of trace organic pollutants

For the removal of trace organic pollutants the functions of the reaction material, including reduction, adsorption and degradation by special microorganisms is utilized. Particularly since cast iron is an iron–carbon alloy, carbon particles act as a cathode when it is in an electrolytic solution, whereas iron has a small potential and acts as an anode, thereby constituting tens of thousands of tiny corrosion cells (if activated carbon, coal and other cathode materials are additionally added in the reaction system, macro-corrosion cells will be formed, so as to speed up the reaction rate). The corrosion cells conduct reduction reaction with organic chlorine, converting the chlorinated organic matter into nontoxic inorganic salts or easily degradable organic matter. In addition, oxides formed after iron oxidation can adsorb chlorinated hydrocarbons. Therefore, as a reaction medium of PRB, zerovalent iron has drawn great attention from researchers in various countries. The reaction equation (chlorinated hydrocarbon is represented by R–Cl) is as follows:

$$\text{Anode process}: Fe^{2+} + 2e = Fe^{0}, E^{0} = -0.44V \tag{5.14}$$

$$\text{Cathode process}: \quad R---Cl + e + H_2O = R---H + Cl^{-} + OH^{-} \tag{5.15}$$

If the chlorocarbon molecule contains more than one chlorine atom, the dechlorination process of formula (5.15) continues. From equation (5.15), it can be seen that on the one hand, a large amount of OH^{-} generated in the dechlorination process will form Fe $(OH)_2$ and Fe $(OH)_3$ on the iron surface with the iron ions corroded by the anode. These are good colloidal flocculants and have stronger adsorption capacity, compared with the Fe^{3+} obtained by general pharmaceutical hydrolysis. They can absorb a large number of organic molecules, and can further reduce the water pollutant content. On the other hand, this is undoubtedly good for reducing the secondary pollution of iron in the water. However, the floc precipitate may also block the pores and reduce the water permeability. In addition, the deposits on the iron

surface will hinder further reaction. The results of Puls et al. (1999) also showed that elevated pH could lead to decreasing degradation rate of some pollutants, and at the same time easy formation of undissolved metal hydroxide precipitates surrounding the surface of iron, thereby reducing the permeability of PRB and even causing blockage. Although dissolved carbonate and bicarbonate play a buffering role in natural groundwater (MARCUS & BONDS, 1999), insoluble salts such as iron carbonate are also formed as the reaction progresses.

5.4.3 Application of zerovalent iron and its derivative materials

Fe° was first applied to PRB technology for trace organic contaminants. In 1996, a continuous wall of Fe°–PRB was installed in the southeastern Elizabeth region of the United States. The contaminated plume contained high concentrations of hexavalent chromium (> 10 mg/L), some TCE (> 19 mg/L), DCE and other organic pollutants. The concentration of chromium was less than 0.0l mg/L after the polluted plume passed through the reaction barrier. The concentration of TCE and DCE also reached the corresponding standard (PULS et al., 1999; WILKIN et al., 2003).

With the deepening of research, to overcome the shortcomings of the long-term running of zerovalent iron alone, the PRB technology of zerovalent iron combined with other reactive materials has been studied. For example, Baric et al. (2012) studied the effects of polyhydroxybutyrate (PHB) combined with zerovalent iron to remove chlorohexane. It was found that the presence of PHB and its fermentation environment (such as volatile acid and low pH) were beneficial to the redox reaction of zerovalent iron and extending the life of zerovalent iron. The PRB with added PHB could stably remove tetrachloroethane (TeCA) in the influent.

Yang et al. (2010) used modified activated carbon and zerovalent iron as the reaction material to remove 2,3-dichlorophenol in water. The activated carbon was modified with dichlorodimethylsilane. Its surface property became hydrophobic, though the modification made to the specific surface area of activated carbon decreased from 895 m^2/g to 835 m^2/g, but the adsorption capacity of 2,3-dichlorophenol was increased by 20%. Thereby, it was found that the modification of activated carbon was beneficial to the degradation of 2,3-dichlorophenol by PRB.

The passivation and plugging problems that affect the PRB effect and life of zerovalent iron have also been studied correspondingly. Ruhl et al. (2012a) studied the influence of zerovalent iron particle size on the PRB effect and life of zerovalent iron. The results showed that the combination of various diameters was more conducive to the long-term operation of the PRB than the single particle size. In the same year, Ruhl et al. (2012b) also studied the gas accumulation that caused the blockage of PRB with zerovalent iron. It was found that passivation of zerovalent iron due to the reaction of calcium with dissolved inorganic carbon prevented the production of gas in the PRB. The gas production per gram of zerovalent iron in the test was 13.5 mL.

In recent years, the bimetallic system developed on the basis of Fe° has been an active research field. The so-called bimetallic system consists of Fe° particles coated with a second metal, such as nickel and palladium, forming a Ni/Fe and Pd/Fe bimetallic system. The Pd/Fe system was first used by Muftikian et al. (1995) who suggested that Pd on the surface of Fe° accelerated the dechlorination of the target pollutants, and the reaction rate could be ten times greater than that of the Fe° system. Studies by Grittini et al. (1995) demonstrated that Pd/Fe bimetallic systems could degrade PCBs, which are very difficult to degrade.

Petersen et al. (2007) used Ti/metal oxide composite electrode to degrade TCE, and the removal rate was 80%–90%. Choi et al. (2007) used reaction materials of Pd/Fe binary metals and continuous PRB grafted with anaerobic bacteria for reductive dechlorination and biodegradation of 2,4,6-trichlorophenol (2,4,6-TCP). The PRB part of Pd/Fe binary metals had a reaction time of 21.2–30.2 h and could reduce 100 mg/L of 2,4,6-TCP to phenol in the reactor. The specific surface area reaction constant K_{SA} was 3.84 (±0.48)×10^{-5} L/(m^2·h). The biological part of PRB could completely remove 100 μmol/L phenols when the reaction time was 7–8 days. Predegradation of dechlorination prior to the biological treatment would increase the treatment effect of the entire PRB system.

5.4.4 Application of adsorption and biological carrier materials

Adsorption materials and biomaterials currently studied or applied include activated carbon, peat, zeolite, bentonite, limestone, sawdust and microorganisms (LI et al., 2006).

Öztürk et al. (2012) studied the degradation of TCE using organic natural substances such as eucalyptus bark and commercial composting, and found that the reaction material could degrade TCE under anaerobic conditions. Among them, the first biodegradation rates of TCE were 0.23 d^{-1} (eucalyptus bark) and 1.2 d^{-1} (commercial compost), with retarding factors of 35 (eucalyptus bark) and 301 (commercial compost), respectively.

Arora et al. (2011) studied the effect of temperature on the adsorption of toluene on activated carbon PRB. The results showed that low temperature decreased the adsorption of toluene on activated carbon. The diffusion coefficient in reaction kinetics also decreased from 5.112 × 10^{-13} m^2/s at 20 °C to 3.65×10^{-13} m^2/s at 4°C.

Ahmad et al. (2007) used natural organic materials as reactive materials to remedy groundwater contaminated with hexahydro-1,3,5-trinitro-1,3,5-triazine (RDX) and octahydro-1,3,5,7-tetranitro-1,3,5,7-tetrazocine (HMX). The results showed that the PRB could completely remove 90 ppb of RDX and 8 ppb of HMX in water. The best ratio (volume ratio) of natural organic matter and grit was 7:3. Vesela et al. (2006) studied the removal effects of benzene, toluene, ethylbenzene, xylene (BTEX), chlorobenzene, naphthalene, nitrophenol, phenol, TCE, total petroleum hydrocarbons (TPH) and other organic pollutants with bio-cinder (cinder is

both an adsorbent medium and microbial carrier). The results showed that biocinder had good removal efficiency, with a removal rate of 57.3% for naphthalene and 99.9% for nitrophenol and BTEX. The biological density of the reactor reached 105 cfu/mL.

5.5 Application of functional materials in PRB for removal of heavy metal pollutants

5.5.1 Overview

There are various types of reaction materials in the PRB technology for removal of heavy metals. The materials with strong adsorption capability, large specific surface area, ion exchange capability or chemical precipitation with heavy metal ions is mainly selected.

5.5.2 Basic principle of removal of heavy metal pollutants

The treatment of wastewater with heavy metals makes use of the adsorption capacity of the reaction material and the coprecipitation of certain components in the reaction material and metal ions to remove metal ions. Other reaction media (such as zerovalent iron) utilize their own reduction to precipitate heavy metals as pure substances or insoluble compounds (Morrison et al., 2002; Schäfer et al., 2006; Lien et al., 2005). Some of the chemical reactions are as follows:

$$Fe^0 + UO_2{}^{2+} = Fe^{2+} + UO_2(s) \tag{5.16}$$

$$4Fe^0 + 2HSeO_3{}^- + 10H^+ = 4Fe^{2+} + 2Se^0(s) + 6H_2O \tag{5.17}$$

$$Fe^0 + CrO_4{}^{2-} + 8H^+ = Fe^{3+} + Cr^{3+} + 4H_2O \tag{5.18}$$

$$(1-x)Fe^{3+} + (x)Cr^{3+} + 2H_2O = Fe_{(1-x)}Cr_{(x)}OOH(s) + 3H^+ \tag{5.19}$$

5.5.3 Application of chemical reaction materials

Heavy metal ions are often removed by coprecipitation of certain components of the reaction material with metal ions. In the vicinity of the Ninemile River in Idaho, USA, Conca et al. (2006) used 90t of Apatite II (chemical formula $[Ca_{10-x}Na_x(PO_4)_{6-x}(CO_3)_x(OH)_2]$, $x<1$) as the reaction material to build 16.3 m long, 5 m wide

and 4.5 m high PRBs, and studied the treatment effect of Zn, Pb, Cd, Cu, SO_3^- and NO_2^- in groundwater by using apatite II. The PRBs were completed and began to run in January 2001. The results showed that the content of Pb and Cd in effluent of PRB was less than 2×10^{-3} mg/L and the content of Zn was close to the local background value (about 0.1 mg/L). The concentration of SO_3^- was reduced to 100–200 mg/L and the concentration of NO_2^- was less than 0.05 mg/L. It was also found that 90% removal occurred in 20% of the front wall of PRB. From 5 years of field operation data from PRB operation till 2006 it was shown that 30% of Apatite II was consumed and the accumulated removal amount was 4,550 kg Zn, 91 kg Pb and 45 kg Cd.

Other researchers utilized redox reactions of reactive materials (such as zerovalent iron and cast iron) to remove heavy metal ions in water. Lee et al. (2004) used the iron scrap from the white iron casting industry as the reaction material of PRB and studied the removal of zinc ions from groundwater contaminated with zinc leachate. The results showed that when the initial zinc ion concentration was 100 mg/L, the removal rate reached up to 50%. Ahn et al. (2003) used by-products from steel industry such as evaporation cooler dust (ECD), oxygen gas sludge (OGS), basic oxygen furnace slag (BOFS) and electrostatic precipitator dust (EPD) to treat arsenic mine wastewater. ECD, OGS and BOFS could reduce the arsenic ion content from 25 mg/L to below 0.5 mg/L within 72 h. The use of PRB technology is a very effective remedy against heavy metal pollution.

Han et al. (2011) investigated the effect of removing arsenic (III) from groundwater under anaerobic conditions using quartz sand-supported iron sulfide as a PRB reaction material. The experiments showed that it had both the ability of removing arsenic (III) and overcoming the shortcomings that the nanoscale iron sulfide is too small to be applied in conventional PRBs. It was demonstrated that the arsenic (III) removal efficiency of the quartz sand-supported iron sulfide was 30% of the nanosized iron sulfides at pH 5 and 7, whereas at pH 9, arsenic (III) removal efficiency of the quartz sand-supported iron sulfide was 400% of the nanosized iron sulfide. This may be due to the natural oxidation of quartz sand surface or the presence of secondary minerals of quartet pyrite; while the quartz sand-loaded iron sulfide could achieve better removal effect of arsenic (III) in the harsher anaerobic conditions, compared with that of the quartz sand-supported iron oxide under aerobic conditions. As opposed to the generally accepted optimal arsenic (III) removal effect of zerovalent iron, the corrosion of which can lead to return of the removed arsenic to water, especially under prolonged anaerobic conditions, whereas the quartz sand-loaded iron sulfide did not have such a problem.

Moraci et al. (2010) studied the removal of heavy metals such as nickel and copper by using zerovalent iron and pumice as PRB reaction materials. Three control experiments were designed. They were zerovalent iron PRB, zerovalent

iron/pumice mixed PRB and zerovalent iron–pumice cascade PRB. The results showed that the zerovalent iron/pumice mixed PRB was superior to the other two PRBs in terms of the removal of nickel and copper or the permeability coefficient of PRBs, and the copper removal efficiency was better than that of the previous report. Some researchers also studied the effect of material ratio on the PRB treatment. Calabrò et al. (2012) designed three kinds of PRBs with zerovalent iron and pumice as reaction materials. The material ratio (weight ratio of zerovalent iron to pumice) was 10/90, 30/70 and 50/50, respectively. As control zerovalent iron was used alone, for each PRB two sets were made. The results showed that the PRB with the material ratio of 30/70 had a better nickel removal effect and a long-term stable operation.

There were also researchers using composting and other natural organic carbon mixtures to remove heavy metals. The removal principles contained physical adsorption, redox reaction and biodegradation. Gibert et al. (2011) observed the PRB constructed with limestone and plant compost as reactive material in Aznalcóllar, southwestern Spain (the PRB was used to control groundwater pollution from the discharge of acidic mine wastewater). It was found that the PRB in Aznalcóllar effectively neutralized the pH of groundwater and removed the heavy metal pollutants from groundwater. The removal rates of Al, Zn and Cu exceeded 96%, 95% and 98%, respectively. Amos et al. (2003) studied the leachate treatment effect of PRB containing cow dung, organic compost, limestone flake and gravel. The results showed that the mixed medium containing 50% limestone had a stronger ability to increase the alkalinity of the solution and to remove metal ions than the mixed medium containing 50% grit. The mix medium with limestone flakes and organic compost (1:1) achieved the maximum metal ion removal within 24 h, whereas mixed media with 25% organic compost and 25% cow dung realized the maximum removal rate of metal ion within 4h.

5.5.4 Application of physical adsorption materials

Physical adsorption commonly uses reactive materials, including zeolite, activated carbon and so on. The degree of adsorption depends on the nature and pH of the reaction material. Woinarski et al. (2003) designed a reaction material using the clinoptilolite and simulated the removal effect of Cu^{2+} at low temperature in the Antarctic. It was found that the adsorption capacity of zeolite at 2 °C was much smaller than that at 22 °C, and the adsorption capacity decreased by 32%–50%. Thus, low temperature reduced the removal rate of Cu^{2+}.

Park et al. (2002) used clinoptilolite as the reaction material to construct PRB. The experiment showed that clinoptilolite had a good removing effect on heavy metal pollution in groundwater.

References

AHMAD F, SCHNITKER S P, NEWELL C J. Remediation of RDX-and HMX-contaminated groundwater using organic mulch permeable reactive barriers. Journal of Contaminant Hydrology, 2007, 90 (1):1–20.

AHN J S, CHON C-M, MOON H-S, et al. Arsenic removal using steel manufacturing byproducts as permeable reactive materials in mine tailing containment systems. Water Research, 2003, 37(10):2478–2488.

AMOS P W, YOUNGER P L. Substrate characterisation for a subsurface reactive barrier to treat colliery spoil leachate. Water Research, 2003, 37(1):108–120.

ARORA M, SNAPE I, STEVENS G W. The effect of temperature on toluene sorption by granular activated carbon and its use in permeable reactive barriers in cold regions. Cold Regions Science and Technology, 2011, 66(1):12–16.

BAI Y H, ZHANG S J. Remediation technologies for groundwater pollution: permeable reactive barrier. Yunnan Environmental Science, 2006, 24(4):51–54.

BAKER M J, BLOWES D W, PLACEK C. Phosphorous adsorption and precipitation in a permeable reactive wall:applications for wastewater disposal systems. Land Contamination & Reclamation, 1997, 5(3):189–193.

BARIC M, MAJONE M, BECCARI M, PAPINI M P. Coupling of polyhydroxybutyrate(PHB)and zero valent iron(ZVI)for enhanced treatment of chlorinated ethanes in permeable reactive barriers(PRBs). Chemical Engineering Journal, 2012, 195:22–30.

BELL L, DEVLIN J, GILLHAM R, et al. A sequential zero valent iron and aerobic biodegradation treatment system for nitrobenzene. Journal of Contaminant Hydrology, 2003, 66(3):201–217.

CALABRÒ P, MORACI N, SURACI P. Estimate of the optimum weight ratio in zero-valent iron/pumice granular mixtures used in permeable reactive barriers for the remediation of nickel contaminated groundwater. Journal of Hazardous Materials, 2012, 207:111–116.

CANTRELL K J, KAPLAN D I, WIETSMA T W. Zero-valent iron for the in situ remediation of selected metals in groundwater. Journal of Hazardous Materials, 1995, 42(2):201–212.

CHOI J H, KIM Y H, CHOI S J. Reductive dechlorination and biodegradation of 2,4,6-trichlorophenol using sequential permeable reactive barriers:Laboratory studies. Chemosphere, 2007, 67 (8):1551–1557.

CONCA J L, WRIGHT J. An Apatite II permeable reactive barrier to remediate groundwater containing Zn, Pb and Cd. Applied Geochemistry, 2006, 21(8):1288–1300.

CUI J F, ZHENG X L, LIN G Q. Permeable reactive wall technology for organic pollution treatment of groundwater. Advances in Water Science, 2003, 14(3):363–367.

DONG J, ZHAO Y S, ZHAO X B, et al. Analysis of factors influencing the groundwater pollution treatment by PRB Technology. Journal of Jilin University: Earth Science Edition, 2005, 35(2): 226–230.

GIBERT O, RÖTTING T, CORTINA J L, et al. In-situ remediation of acid mine drainage using a permeable reactive barrier in Aznalcollar(Sw Spain). Journal of Hazardous Materials, 2011, 191(1):287–295.

GRITTINI C, MALCOMSON M, FERNANDO Q, et al. Rapid dechlorination of polychlorinated biphenyls on the surface of a Pd/Fe bimetallic system. Environmental Science & Technology, 1995, 29 (11):2898–2900.

GUERIN T, MCGOVERN T, HORNER S. A funnel and gate system for remediation of dissolved phase petroleum hydrocarbons in groundwater. Land Contamination & Reclamation, 2001, 9(2): 209–224.

GUSMÃO A D, DE CAMPOS T M P, NOBRE M D M M, et al. Laboratory tests for reactive barrier design. Journal of Hazardous Materials, 2004, 110(1):105–112.

HAN Y S, GALLEGOS T J, DEMOND A H, et al. FeS-coated sand for removal of arsenic(III)under anaerobic conditions in permeable reactive barriers. Water Research, 2011, 45(2):593–604.
LEE T, PARK J W, LEE J H. Waste green sands as reactive media for the removal of zinc from water. Chemosphere, 2004, 56(6):571–581.
LI T L, KANG H Y, LIU H S, et al. Preparation of nanoscale iron and products and mechanism of its reducing nitrate. Environmental Chemistry, 2006, 25(3):294–296.
LI Y, XIAO W J. Modification of zeolite and its effect on ammonia nitrogen wastewater treatment. Non-Metallic Mines, 2003, 26(2):53–55.
MARCUS D L, BONDS C. Results of the reactant sand-fracking pilot test and implications for the in situ remediation of chlorinated VOCs and metals in deep and fractured bedrock aquifers. Journal of Hazardous Materials, 1999, 68(1):125–153.
MOON H S, AHN K-H, LEE S, et al. Use of autotrophic sulfur-oxidizers to remove nitrate from bank filtrate in a permeable reactive barrier system. Environmental Pollution, 2004, 129(3):499–507.
MORACI N, CALABRÒ P S. Heavy metals removal and hydraulic performance in zero-valent iron/pumice permeable reactive barriers. Journal of Environmental Management, 2010, 91(11):2336–2341.
MORRISON S J, METZLER D R, DWYER B P. Removal of As, Mn, Mo, Se, U, V and Zn from groundwater by zero-valent iron in a passive treatment cell:reaction progress modeling. Journal of Contaminant Hydrology, 2002, 56(1):99–116.
MU Y, YU H Q, ZHENG J C, et al. Reductive degradation of nitrobenzene in aqueous solution by zero-valent iron. Chemosphere, 2004, 54(7):789–794.
MUFTIKIAN R, FERNANDO Q, KORTE N. A method for the rapid dechlorination of low molecular weight chlorinated hydrocarbons in water. Water Research, 1995, 29(10):2434–2439.
ÖZTÜRK Z, TANSEL B, KATSENOVICH Y, et al. Highly organic natural media as permeable reactive barriers:TCE partitioning and anaerobic degradation profile in eucalyptus mulch and compost. Chemosphere, 2012, 89(6):665–671.
PARK J B, LEE S H, LEE J W, et al. Lab scale experiments for permeable reactive barriers against contaminated groundwater with ammonium and heavy metals using clinoptilolite(01-29B). Journal of Hazardous Materials, 2002, 95(1):65–79.
PETERSEN M A, SALE T C, REARDON K F. Electrolytic trichloroethene degradation using mixed metal oxide coated titanium mesh electrodes. Chemosphere, 2007, 67(8):1573–1581.
PULS R W, BLOWES D W, GILLHAM R W. Long-term performance monitoring for a permeable reactive barrier at the US Coast Guard Support Center, Elizabeth City, North Carolina. Journal of Hazardous Materials, 1999, 68(1):109–124.
ROBERTSON W, CHERRY J. Long term performance of the Waterloo denitrification barrier. 1997.
RUHL A S, JEKEL M. Impacts of Fe(0)grain sizes and grain size distributions in permeable reactive barriers. Chemical Engineering Journal, 2012a, 213:245–250.
RUHL A S, WEBER A, JEKEL M. Influence of dissolved inorganic carbon and calcium on gas formation and accumulation in iron permeable reactive barriers. Journal of Contaminant Hydrology, 2012b, 142:22–32.
SCHÄFER D, KÖBER R, DAHMKE A. Competing TCE and *cis*-DCE degradation kinetics by zero-valent iron – experimental results and numerical simulation. Journal of Contaminant Hydrology, 2003, 65(3):183–202.
SHU S Z, YUAN Y. In situ treatment methods of pollution of groundwater: permeable reaction wall:. Techniques and Equipment for Environmental Pollution Control, 2002, 3(1):47–51.
SNAPE I, MORRIS C, COLE C. The use of permeable reactive barriers to control contaminant dispersal during site remediation in Antarctica. Cold Regions Science and Technology, 2001, 32(2):157–174.

SORG T J, LOGSDON G S. Treatment technology to meet the interim primary drinking water regulations for inorganics:Part 2. Journal(American Water Works Association), 1978, 70(7):379–393.

SU C, PULS R W. Removal of added nitrate in the single, binary, and ternary systems of cotton burr compost, zerovalent iron, and sediment:Implications for groundwater nitrate remediation using permeable reactive barriers. Chemosphere, 2007, 67(8):1653–1662.

VESELA L, NEMECEK J, SIGLOVA M, et al. The biofiltration permeable reactive barrier:practical experience from Synthesia. International Biodeterioration & Biodegradation, 2006, 58(3):224–230.

WILKIN R T, PULS R W, SEWELL G W. Long-term performance of permeable reactive barriers using zero-valent iron: geochemical and microbiological effects. Ground Water, 2003, 41(4):493–503.

WOINARSKI A, SNAPE I, STEVENS G, et al. The effects of cold temperature on copper ion exchange by natural zeolite for use in a permeable reactive barrier in Antarctica. Cold Regions Science and Technology, 2003, 37(2):159–168.

YAN Z C, LONG T R, HE Q, et al. Phosphorus Removal by Chemical Precipitation with Aeration Filtration from Municipal Sewage. China Water and Wastewater, 2006, 22(3):86–88.

YANG J, CAO L M, GUO R, JIA J P. Permeable reactive barrier of surface hydrophobic granular activated carbon coupled with elemental iron for the removal of 2,4-dichlorophenol in water. Journal of Hazardous Materials, 2010, 184(1):782–787.

ZHAI B. Application of PRB in groundwater pollution remediation. Environmental Protection Industry, 2005, (2):33–35.

ZHAO D M, SHI H X. Study on pretreatment of 4-fluoronitrobenzene wastewater by microelectrolysis. Environmental Protection of Chemical Industry, 2002, 22(1):15–18.

ZHAO Q L, LI X Z. Chemical precipitation to remove ammonia nitrogen in landfill leachate. Environmental Science, 1999, 20(5):90–92.

ZHOU L, LI T L, QUAN H M, et al. Study on removal of nitrate nitrogen from groundwater by iron powder reduction. Journal of Agro – Environment Science, 2006, 25(2):368–372.

6 Application of functional materials in constructed wetland

6.1 The development and research status of constructed wetland

The "Technical specification of constructed wetlands for wastewater treatment engineering" (HJ 2005–2010) issued by Ministry of Environmental Protection in 2012 refers to a constructed wetland as an artificial pool or trench. The leak-resistant impermeable layer is laid on the bottom, a certain depth of the substrate layer is filled and aquatic plants are planted. The wastewater is treated with the triple physical, chemical and biological synergies of substrate, plant and microbial. According to different water distribution methods or different water ways, it can be roughly divided into free surface flow constructed wetlands and subsurface flow constructed wetlands. The subsurface flow constructed wetlands mainly include horizontal and vertical subsurface flow constructed wetlands.

Constructed wetlands are widely used in Europe and the United States. In Europe, there are about 10,000 constructed wetlands, while there are nearly 20,000 in North America. Subsurface flow constructed wetlands are commonly applied in Europe and use gravel as filler. Planting of reedbeds are also popular in Europe, such as reeds, calamus and cattail. About two-thirds of the wetlands in North America are surface wetlands, of which half are surface-flowed wetlands. System water depths range from 30 to 40 cm. In recent years, vertical flow constructed wetlands have received more attention and evaluation, but they have not been widely promoted because of the more detailed construction and substrate selection. Vertical flow constructed wetlands will be an important direction for the development of constructed wetlands in the future.

According to the Technical specification of constructed wetlands for wastewater treatment engineering (HJ 2005–2010), the influent water quality of constructed wetland system shall meet the requirements listed in Table 6.1.

The removal rate of pollutants in a constructed wetland system can refer to the data in Table 6.2.

6.2 The selection of constructed wetland substrate

Constructed wetlands are widely used in the removal of SS, BOD, NH_3-N, phosphate, metal ions and other pollutants, which are due to the combined action of plants, microorganisms and substrate.

Constructed wetland substrates have a great influence on the treatment effect of constructed wetlands. Substrates should be selected for different water quality. Traditional constructed wetland substrates mainly include soil, sand and gravel.

https://doi.org/10.1515/9783110544381-006

Table 6.1: Influent water quality of constructed wetland system.

Types of constructed wetlands	BOD (mg/L)	COD (mg/L)	SS (mg/L)	NH_3-N (mg/L)	TP (mg/L)
Surface flow	≤50	≤125	≤200	≤10	≤3
Horizontal subsurface flow	≤80	≤200	≤60	≤25	≤5
Vertical subsurface flow	≤80	≤200	≤80	≤25	≤5

Table 6.2: Pollutant removal efficiency of constructed wetland system.

Types of constructed wetlands	BOD (%)	COD (%)	SS (%)	NH_3-N (%)	TP (%)
Surface flow	40–70	50–60	50–60	20–50	35–70
Horizontal subsurface flow	45–85	55–75	50–80	40–70	70–80
Vertical subsurface flow	50–90	60–80	50–80	50–75	60–80

In recent years, zeolite, limestone, shale, plastic and ceramsite have been included. According to the literature, substrate types can be divided into three categories: natural materials, industrial by-products and artificial products. Natural materials are mainly dolomite, limestone, wollastonite, zeolite, shale, bauxite, sand, gravel, ash, soil, protein soil and shell sand. Industrial by-products are blast furnace slag, steel slag of electric arc furnace (EAF), slag, mineral waste residue and fly ash; artificial products mainly refers to the light expansive clay aggregate (LECA), also known as light polymer (LWA). Considering economic and practical operation and management, sand and stone mixing are still considered the most common matrices in China.

The choice of substrate should follow the principles of readily available materials, high efficiency, low cost, safety and non-toxicity. Primarily, local materials with strong ability of removing pollutants should be selected; these not only improve the purification capacity and cost of constructed wetlands but also prolong the service life of ecological projects. In addition, owing to large differences in the permeability coefficients of different substrates, which should be selected according to different design of constructed wetlands. For surface flow constructed wetlands, soil may be chosen as the substrate. The subsurface flow and vertical flow constructed wetlands need substrates with relatively high permeability coefficients. Sand, slag or their mixture with soil should be selected as the substrate of constructed wetlands.

The distribution of substrate particle size plays a decisive role in pore volume and water flow patterns in wetlands. Stratified laying of the substrate should be uniform on each layer. If the particle size is not uniform, filler porosity will be reduced, affecting water flow distribution, changing the hydraulic state, affecting

the permeability of the substrate, thus affecting the removal effect. Large particle size can effectively prevent clogging, but too large a size will reduce the hydraulic retention time and affect the purification effect, so it is necessary to find an optimal balance point. Therefore, different sizes of the filler ratio should also be considered in a multi-layered vertical flow of artificial wetland. The size of the substrate should be able to meet design requirements. For subsurface flow wetlands, the structure of the substrate should meet requirements of large-scale aquatic plant growth to provide root attachment and to ensure good filtration and treatment. The low hydraulic conductivity of fine sand substrate can maintain the stagnant water state, so that water is evenly distributed. According to "Technical specification of constructed wetlands for wastewater treatment engineering" (HJ 2005-2010), the selection of wetland substrate should be determined based on the mechanical strength, specific surface area, stability, porosity, surface roughness and other factors. Especially when there are higher requirements of nitrogen and phosphorus concentrations in effluent, the functional substrate to improve nitrogen and phosphorus removal rate should be used. The initial porosity of the substrate should be controlled at 35%–40%. Since the surface soil of constructed wetlands will sink after soaking, the elevation of the surface of the filler layer should be 10%–15% higher than the designed value.

6.3 Study on nitrogen and phosphorus removal by using functional materials in constructed wetland

The selection of functional materials for enhanced removal of nitrogen and phosphorus in constructed wetlands is carried out in the South China Institute of Environmental Science, Ministry of Environmental Protection. Emission of laboratory wastewater after rigorous treatment is an important part of laboratory standardization (PANG Zhihua et al., 2012). In general, the commonly used chemical reagents in the laboratory, including acid, alkali, heavy metal salts, phenols and other organic matter, according to the main components, wastewater can be divided into inorganic wastewater, organic wastewater and integrated wastewater (ZHANG Yi et al., 2006). Inorganic wastewater mainly contains mercury, plumbum, chromium, cyanide, arsenide, fluoride and other heavy metals. Organic wastewater mainly contains phenol, benzene, nitro compounds, polycyclic aromatic hydrocarbons and other carcinogens (SHEN Xiaojun et al., 2008). The integrated wastewater contains both organic pollutants and inorganic pollutants, and is the main part of the experimental wastewater. Its high concentration of pollutants, complex composition and pH changes increase the difficulty of its treatment.

Constructed wetland is a part of the laboratory wastewater treatment project of South China Institute of Environmental Science. The flow chart is shown in Figure 6.1. The original design of the total treatment scale: Q=10.0 m^3/d, intermittent operation, treatment scale is Q=0.90 m^3/h. The effluent water of this project should be in accordance with the first-grade standard of the second period of

"Water Pollution Emission Limit" (GB 44/26-2001) of Guangdong Province. The future will be used in the watering, washing the ground. First of all, heavy metal ions or toxic substances in laboratory wastewater were pretreated with coagulation and precipitation, then physically and chemically treated in the contact oxidation pond. After the sedimentation, the suspended organic matter in the water is further removed in the sand filter tank and finally discharged.

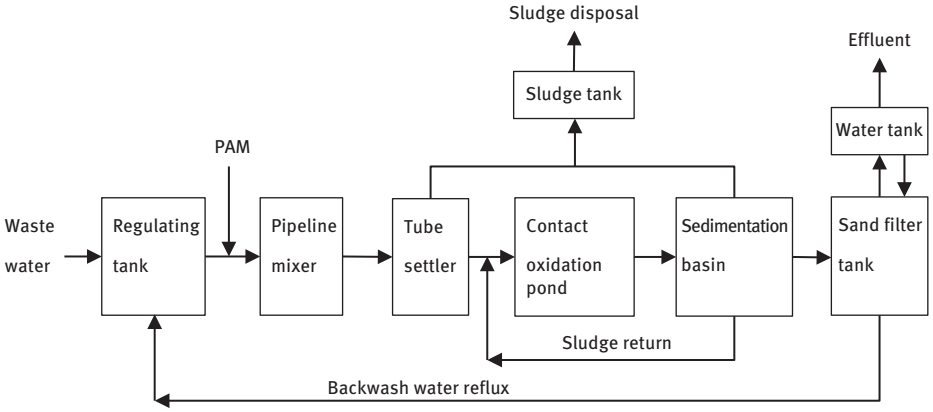

Figure 6.1: Treatment technology.

Two levels of constructed wetlands were built on the reserve zone of the original wastewater treatment plant, of which constructed wetlands of the first level were used as pilot experiments. The constructed wetland is a vertical flow type wetland; fillers such as artificial zeolite, ceramsite and the mixture are filled separately. Laboratory wastewater is treated with two level wetlands. The experimental results were compared with the pure gravel bed constructed wetlands.

Constructed wetlands run intermittently throughout the day. The treatment facilities are designed and constructed according to Q=1.20 m^3/h and run for 9h per day with the total design capacity of 10.8 t. The purpose of this pilot experiment is to serve advanced treatment of effluent. The effluent quality should reach the Level 1-A standard, that is, the total phosphorus concentration should not be more than 0.5 mg/L and the ammonia concentration is not more than 5 mg/L.

The artificial wetland pool is divided into four grids: (1) artificial zeolite + gravel layer; (2) ceramsite + gravel layer; (3) ceramsite + artificial zeolite + gravel layer; (4) pure gravel layer. Water distribution is carried out by a main pipe. Four grids are separated with impermeable steel to avoid mutual influence. The effluent area is also divided into four grids, respectively; water samples were analyzed and determined. After having covered with zeolite and ceramsite, wetlands plants such as canna, calamus, papyrus and thalia dealbata are planted on their surface.

The overall size of constructed wetland is 2 700×2 000×700 (mm), which is separated by a waterproof partition (PVC board, thickness can be ignored); the cell size is 2 700×500×700 (mm). The height of water distribution is 500 mm and there is 200 mm free.

(1) The results of first test

The first test lasted 60 days. In general, the removal of NH_3-N, TN, TP and COD from the pure gravel bed wetlands was the lowest of the four wetlands. And the removal effect of zeolite + ceramsite wetlands is the best. The zeolite + gravel bed wetlands have a good effect on the removal of ammonia, but the removal of TP is normal. While ceramsite + gravel bed wetlands have a good removal of TP, the ammonia reduction effect is not obvious. The average effect of the first experiment is shown in Table 6.3.

Table 6.3: The average effect of the first experiment.

Types	COD (mg/L)	NH_3-N (mg/L)	TN (mg/L)	TP (mg/L)
Influent concentration	26.79	8.56	12.32	1.96
Gravel wetlands	23.89	6.32	11.23	1.55
Gravel + ceramsite wetland	21.56	6.15	11.34	0.46
Gravel + zeolite wetland	20.56	1.68	4.36	1.38
Gravel + zeolite + ceramsite wetland	19.68	1.76	4.29	0.42

The average removal rates of COD, NH_3-N, TN and TP of gravel wetlands were 10.8%, 26.2%, 8.8% and 20.9%, respectively, indicating that it had certain pollutant removal capacity but not enough. The TP removal of wetland filled with ceramsite significantly improved, TP removal rate reached 76.5%. However, the removal efficiencies of COD, NH_3-N and TN were generally 19.5%, 28.2% and 8.0%, respectively. There is hardly any difference compared with the gravel wetlands. Zeolites remove ammonia primarily by adsorption. Therefore, zeolite-filled constructed wetlands have obvious removal effects on NH_3-N and TN. The removal rates of NH_3-N and TN of gravel + zeolite wetland reached 80.4% and 64.6%, respectively. However, the removal efficiency of TP was poor, only 29.6%, while the removal efficiency of COD was 19.5%. Gravel + zeolite + ceramsite wetlands were the best in four types of constructed wetlands for pollutant removal. In the pilot test, it obtained a good effect of strengthening the removal of nitrogen and phosphorus. The average removal rates of NH_3-N, TN and TP reached 79.4%, 65.2 and 78.6%, respectively, and the removal efficiency of COD was also 26.5%.

The results of the first experiment showed that the removal of nitrogen and phosphorus by zeolite and ceramsite wetlands is feasible. However, in the later period of the first experiment, hardening of zeolite-filled artificial wetland occurred, which greatly reduced the capacity of passing water, even stagnant, as shown in

Figure 6.2: The late situation of the first experiment.

Figure 6.2. Based on the above situation, the constructed wetland was simply modified, and zeolite was granulated and then used for the second test.

(2) The results of second test

The second test time was 120 days. Before the plants were planted, the average treatment effect on the pollutants is shown in Table 6.4.

Table 6.4: The average effect of the second experiment.

Types	COD (mg/L)	NH_3-N (mg/L)	TN (mg/L)	TP (mg/L)
Influent concentration	25.34	8.69	12.59	1.93
Gravel wetlands	23.69	6.48	11.65	1.57
Gravel + ceramsite wetland	21.96	6.09	11.26	0.47
Gravel + zeolite wetland	20.74	1.65	4.42	1.42
Gravel + zeolite + ceramsite wetland	19.58	1.72	4.31	0.44

Among them, the average removal rates of COD, NH_3-N, TN and TP of the gravel wetlands were 6.5%, 25.4%, 7.5% and 18.7%, respectively; The removal rate of TP by artificial wetland after filling ceramsite reached 75.6%, while the removal rates of COD, NH_3-N and TN were 13.3%, 29.9% and 10.6%, respectively. The removal rate of NH_3-N and TN reached 81.0% and 64.9% of gravel + zeolite wetland, respectively. The removal efficiency of TP was 26.4% and that of COD was 18.1%. The pollutants removal of gravel + zeolite + ceramsite wetland is still the best in the four constructed wetlands, the average removal rates of NH_3-N, TN and TP reached 80.2%, 65.8 and 77.2%, respectively; the COD removal efficiency was also 22.7%.

Figure 6.3: The second experiment of constructed wetlands after the stable operation.

After the stable operation of wetlands, Dracaena sanderiana, elaine, anthurium and other wetland plants were planted. Plant growth was good, as shown in Figure 6.3. The removal effect on contaminants after plantation is shown in Table 6.5. The addition of plants further improves the treatment effect of constructed wetlands.

Table 6.5: The average effect of the second experiment.

Types	COD (mg/L)	NH_3-N (mg/L)	TN (mg/L)	TP (mg/L)
Influent co)centration	25.68	8.49	12.32	1.87
Gravel wetlands	23.52	6.42	11.52	1.52
Gravel + ceramsite wetland	21.67	6.01	10.98	0.45
Gravel + zeolite wetland	20.64	1.63	4.28	1.38
Zeolite + ceramsite wetland	19.46	1.68	4.15	0.42

6.4 Study on continuous oxygen enrichment technology combined with constructed river wetland in Shixi River

6.4.1 Overview of demonstration project

(1) Application Technology

(i) River continuous reoxygenation technology

The dissolved oxygen of Pingshan River is low with poor self-purification ability, so the application of continuous reoxygenation technology is much needed. The important

engineering parameters were formulated through the construction of river reactors simulation, the pilot experiment of aeration and oxygenation, studying the aeration technology of polluted river water and the relationship between pollutant degradation and aeration.

(ii) Artificial flow construction technology

Aiming at the short residence time of rainwater source river, the continuous reoxygenation technique of the river is combined and flow blocking facilities and ditch construction techniques are identified by increasing the flow blocking facilities or artificial structure retention ditch, studying the pollutants removal rules of obstruction facilities and retention ditch and analyzing the purifying effect under oxygenating conditions after residence time increase.

(2) Design scale and water quality of influent

The design treatment scale is: Q=15000 t/d. The influent quality is as shown in Table 6.6.

Table 6.6: The indicators of influent quality.

Water quality indicators	COD (mg/L)	NH_3-N (mg/L)	TN (mg/L)	TP (mg/L)
Water quality of Influent	60.0	20.0	25.0	2.0
Water quality of Effluent	<20.0	<5.0	<8.0	<0.50

(3) Technological process

The process flow of the constructed wetland demonstration project is shown in Figure 6.4, and its main processing unit is shown in Figures 6.5 and 6.6.

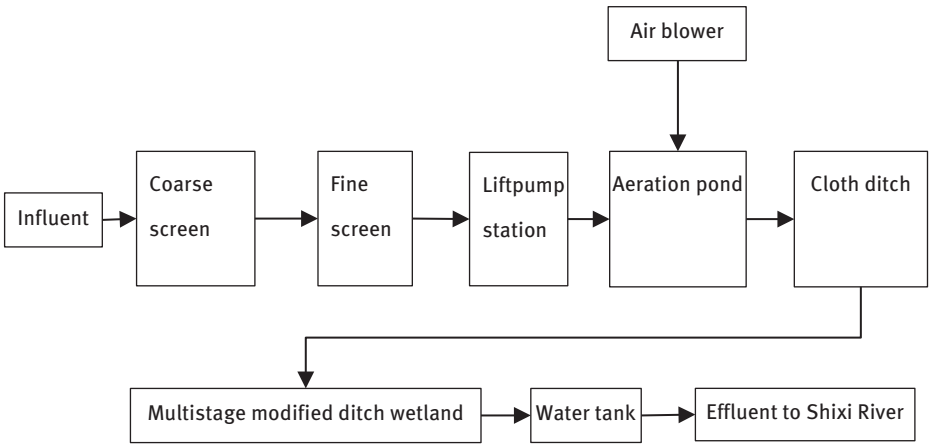

Figure 6.4: Technological process of the demonstration project.

Figure 6.5: Liftpump station.

Figure 6.6: Aeration pond.

6.4.2 Project operational effectiveness analysis

The water system and cultivation plants of the project have been completed in early June 2010. The scene before and after the construction is shown in Figure 6.7 and Figure 6.8. The official operation started in mid-June. Operating analysis data for the past 6 months show that the treatment facilities of the demonstration project have a

Figure 6.7: Before the construction.

Figure 6.8: After the construction.

relatively good purification effect on polluted river water. The status of wetland ecological restoration is shown in Figure 6.9. The COD removal rate was 50%–70%, the NH_3-N and TN removal rate was 50%–60%, the TP removal rate was 40%–50%, the removal of trace toxicants (bisphenol A, nonylphenol, triclosan etc.) was 30%–40%.

Figure 6.9: Wetland status quo of ecological restoration.

6.4.3 Engineering technical point, innovation and application analysis

Aiming at the existing problems of water pollution control and ecological restoration of rain-sourced river in China, based on the summarization of existing river-control technologies, according to the situation of pilot study on ecological simulation of rivers, the integrative water purification technology of improved wetlands has been researched and developed.

Based on a variety of research and development technologies such as energy-saving and low-intensity aeration, enhanced plant water purification technology and wetland technology, water purification and ecological restoration and reconstruction of polluted river system were carried out. The pollution load in the river channel is reduced along the route, the environment of drinking water source river is improved and the ecosystem structure is gradually improved. It could construct a multi-functional river improved wetland system with water purification, wetland restoration and increased river biodiversity.

On the basis of wetland technology, the project has been innovated and partially rebuilt by increasing the ditches along the vertical inflow of wetlands. The size of ditch section is $B \times H$=0.50 m×0.30 m, the length depends on the situation. The distance between the two ditches is about 1.0 m. The main function of ditches is to increase the reaction volume of polluted river to prolong the contact time between the aerated polluted river and the microorganisms in the wetland and to obtain purification. According to the existing plant species in the wetland, the plants that can reduce the pollution load and increase the river biodiversity are selected for planting.

Four to five species of plants are planted in improved wetlands, including lemongrass, cyperus altrnlifolius, mosaic reed, scirpus tabernaemontani and fish-scale bamboo. Plants are planted in areas or mixed. Through the rational allocation

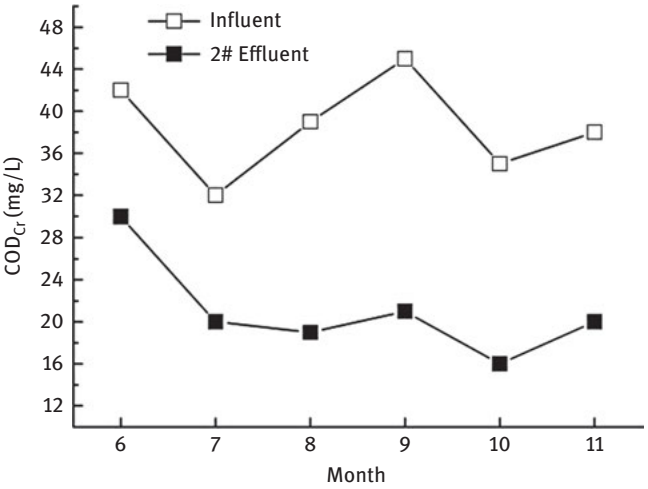

Figure 6.10: COD removal effect curve over time.

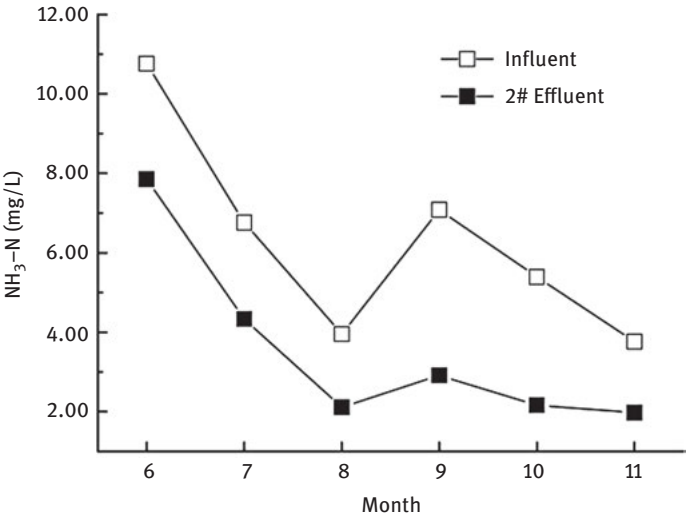

Figure 6.11: NH_3-N removal effect curve over time.

of plants in the wetland, the improved wetland can adapt to the suburban area with heavy rainfall intensity. After the storm flood, the modified wetland can quickly restore its ecological purification function because of more reasonable planting and configuration. The project investment is not higher than 120 Yuan/t water, operating costs less than 0.06 Yuan/t water.

In this project, COD removal rate is 60%–80%; the removal rate of NH_3-N and TN are 60%–70%, TP removal rate is 50%–70%, the removal rate of trace toxicants (bisphenol A, nonylphenol, triclosan etc.) is 40%–50%. The curves of the pollutant removal rates are shown in Figure 6.10 to Figure 6.14.

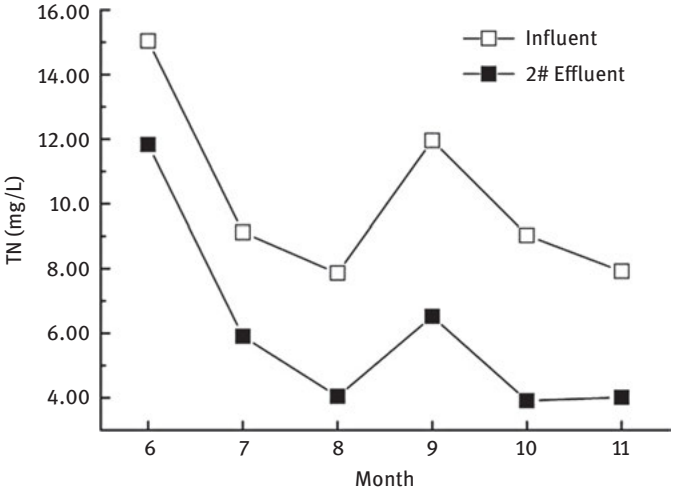

Figure 6.12: TN removal effect curve over time.

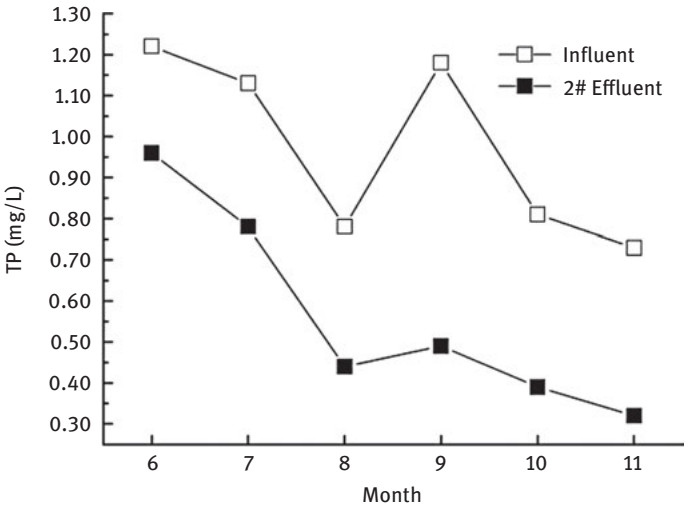

Figure 6.13: TP removal effect curve over time.

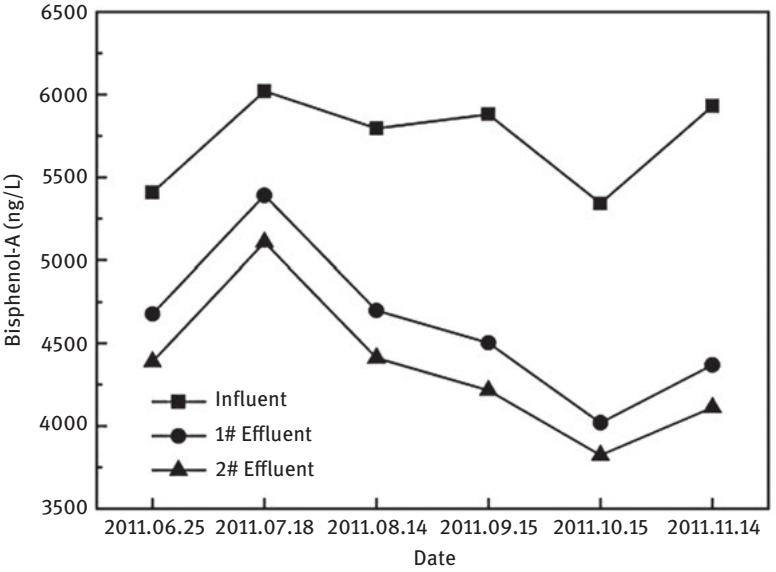

Figure 6.14: Bisphenol A removal effect curve over time.

6.5 The combined technical demonstration project of multifunctional bypass water purification

(1) The main engineering process

Conventional treatment + depth treatment combination process is implemented. On the basis of the original design discharge standards, the water is deeply treated to raise effluent standards and the combination demonstration project of multifunction bypass water purification was constructed. Demonstration projects mainly use the following two technologies:

(i) Preparation technology of functional materials for nutritional contaminants (N, P) degradation. For the practical application of functional material for nutrient-based pollutant degradation, research group developed synthesis preparation technology of artificial modified zeolite and porous ceramic using fly ash as the main raw material and received the patented product. These two newly developed products are used as filler media for the wetlands and percolation reactors.

(ii) Combinatorial technology of multifunctional bypass water purification. Using of functional materials and the process parameters of pilot test, percolation reaction wall of multifunctional wetland was built. Combined with enhanced aeration and ecological floating bed technology, the process operating parameters and removal efficiency of organic and nutrient contaminants (N, P) under different process conditions were determined. The combinatorial technology of multifunctional bypass water purification was integrated.

The project selected "natural active filler technology + ecological purification technology + percolation reaction wall based on functional material" as the main technology, which have a smaller impact on the landscape.

(2) Design scale and water quality of influent

The design treatment scale is: Q=6 500 t/d.

Table 6.7: The indicators of influent and effluent quality.

Water quality indicators	COD (mg/L)	NH_3-N (mg/L)	TN (mg/L)	TP (mg/L)
Water quality of Influent	140	25	30	2.20
Water quality of Effluent according to Level 1-A of "Discharge standard of pollutants for municipal wastewater treatment plant" (GB 18918—2002)	<30	<5	<10	<0.50

Note: COD according to Class IV water standards of "Environmental quality standards for surface water" (GB 18918-2002).

(3) Technological process of Demonstration Project

The technological process of demonstration project is shown in Figure 6.15.

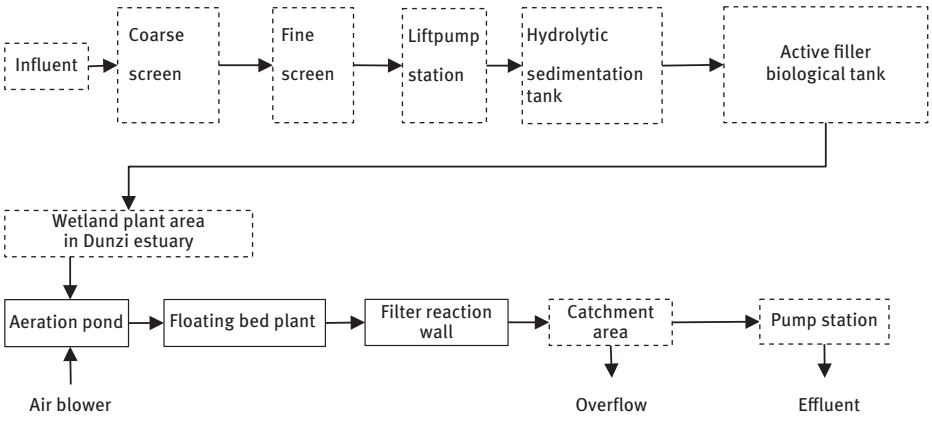

Figure 6.15: Technological process of demonstration project.

(4) Main content of Demonstration project construction

(i) Conventional treatment facilities include diversion canal, coarse and fine screen, a liftpump station, a hydrolytic sedimentation tank, an active filler biological tank. Parameter optimization and technological upgrade are necessary.

(ii) Depth treatment facilities include an aeration pond, a floating bed plant area, a filter reaction wall (1 000 m^2) and other ancillary facilities.

(5) Process improvement of conventional treatment area

The original conventional treatment area is not ideal, which can not reach the Level 1-B of "Discharge standard of pollutants for municipal wastewater treatment plant" (GB 18918–2002). After the discussion with the original design institute and agreed with the owners, the conventional treatment area was remodeled. The improvements include adjusting the filter composition, adjusting the aeration of the biochemical tank and strengthening the backwash. Among them, the largest improvement project

Figure 6.16: The status of conventional treatment.

Figure 6.17: The status of depth treatment 1.

Figure 6.18: The status of depth treatment 2.

is to adjust the filter composition of biochemical pool. In order to strengthen the treatment effect, the lower 1/3 filter was replaced by self-prepared fly ash ceramsite. The current status of the processing unit is shown in Figure 6.16-6.18.

In this demonstration project, COD removal rate is 50%–70%; the removal rate of NH_3-N and TN are 50%–60%, TP removal rate is 40%–50%, the removal rate of trace toxicants (bisphenol A, nonylphenol, triclosan etc.) is 30% to 40%.

The curves of the pollutant removal rates are shown in Figure 6.19 to Figure 6.25.

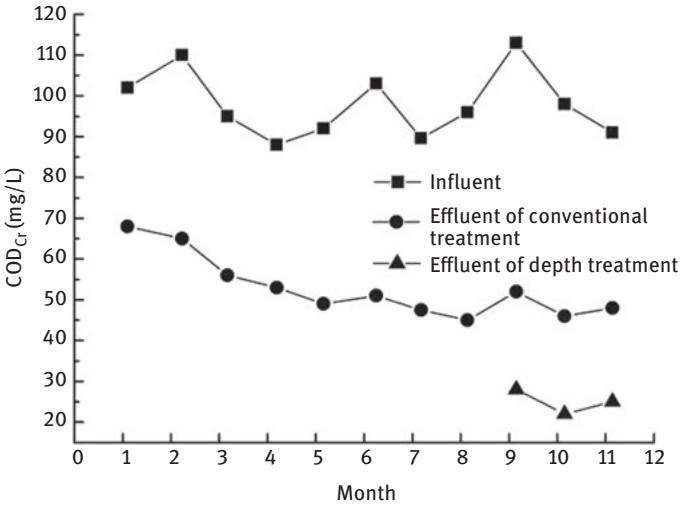

Figure 6.19: COD removal effect curve over time.

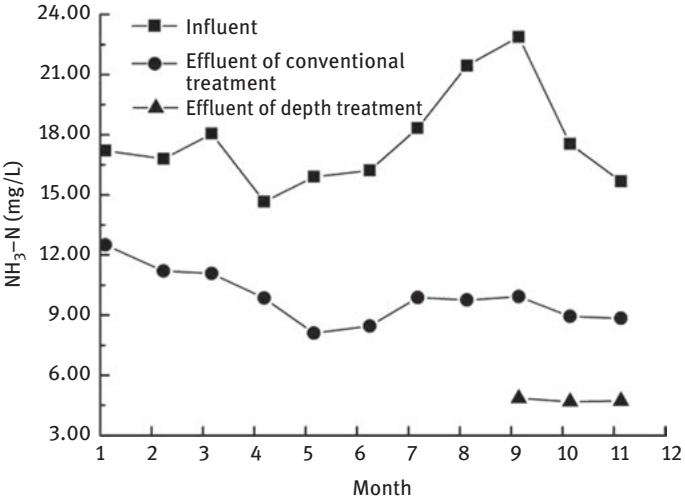

Figure 6.20: NH_3-N removal effect curve over time.

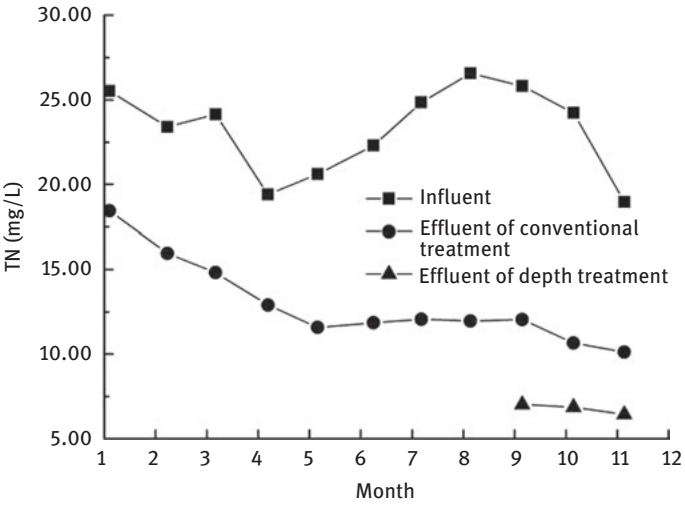

Figure 6.21: TN removal effect curve over time.

6.6 Routine maintenance and filler replacement of constructed wetland

Fillers are a core component of constructed wetlands. After years of operation, constructed wetlands tend to have clogging problems. The clogging process is often divided into three stages: (1) Penetration rate is closed to the normal level,

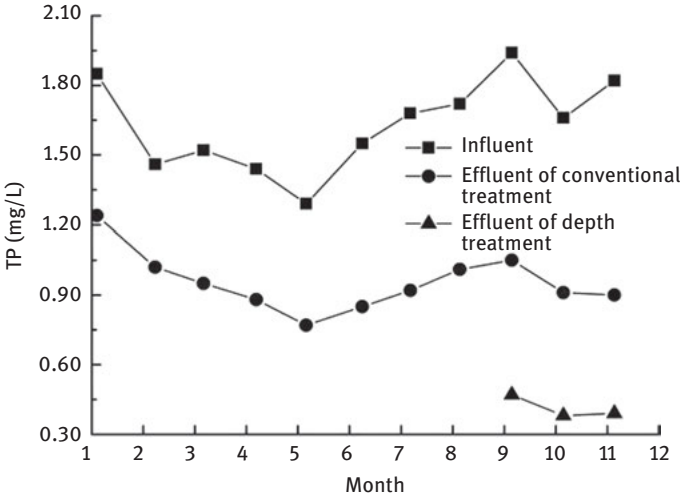

Figure 6.22: TP removal effect curve over time.

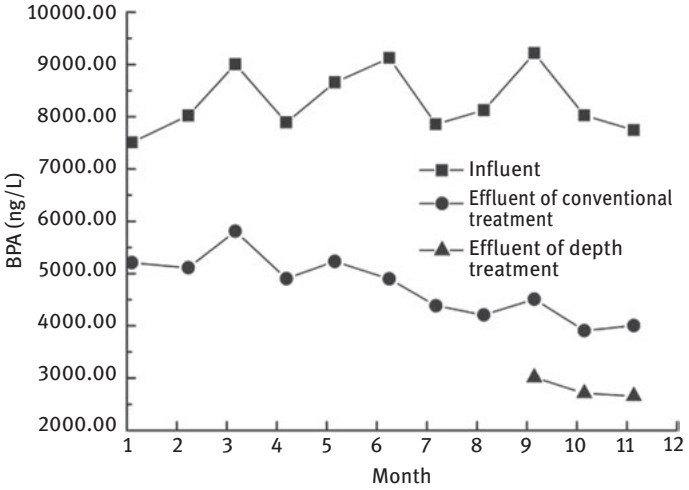

Figure 6.23: Bisphenol A removal effect curve over time.

but showed a downward trend; (2) Penetration rate decreased slowly and steadily; (3) There are accumulation of water of the filler surface from intermittent to continuous. The clogging is related with filler, temperature, biological mechanism, mode of operation and so on. The clogging is mainly due to suspended solids precipitation and organic growth during operation. Decrease in permeability leads to system clogging. The clogging layer is formed by the sedimentation and filtration of solid particles accumulated by microorganisms.

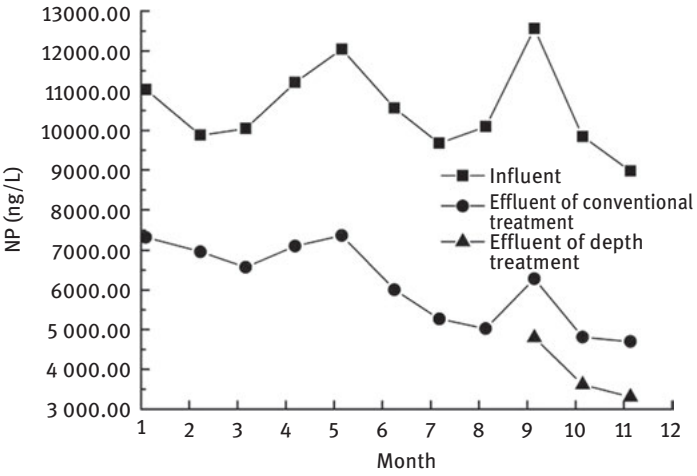

Figure 6.24: Nonylphenol removal effect curve over time.

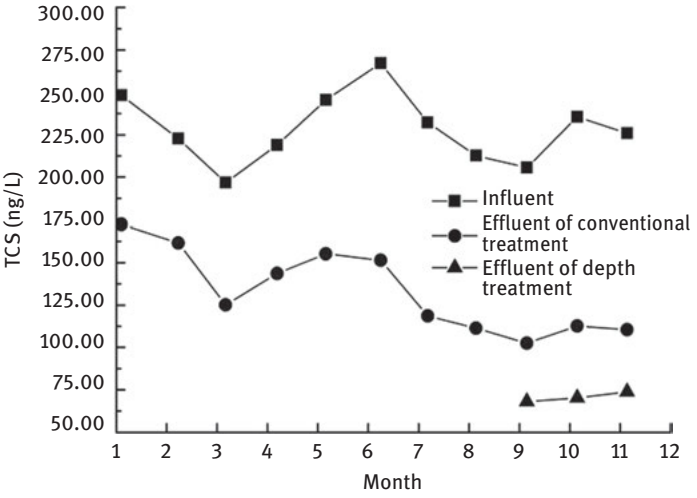

Figure 6.25: Triclosan removal effect curve over time.

In the design phase of constructed wetlands, the following measures can be taken to solve the clogging problem:

(1) Select the appropriate particle size and grading;
(2) Select plants with strong rhizospheric reoxygenation ability and less secretion of nonbiodegradable substances, and regularly harvested the plant;
(3) Effective pretreatment of wastewater into the wetland to remove suspended solids and floating debris;

(4) Reasonable water distribution strategy, intermittent water distribution, a reasonable choice of the total amount of water, load and distribution intervals.

During system operation, the system can be repaired by using the following methods to restore the system's permeability and solve the system clogging problem:

(1) Timely clean up of the wetland surface to improve the permeability of the system. Regular dredging, cleaning, trimming the surface of constructed wetland plants in order to ensure good seepage.
(2) During system operation, replace surface fillers with permissible conditions. The accumulated organic matter in the constructed wetland mainly stays on the surface layer, and the clogging generally at 0–15 cm of the wetland surface. When using wetting fillers with adsorption properties such as zeolites and functional ceramsite, the fillers needs to be replaced to achieve the relevant properties. However, in this case, the constructed wetlands with mature plants are more severely damaged, and the construction volume is too large for large-scale wetlands.

References

PANG Zhihua, SU Zhaozheng, LUO Xiu et al: Design and Analysis of Laboratory Wastewater Treatment Engineering in Research Institutes, Water Supply and Sewerage, 2012, 38(1): 70–72.

SHEN Xiaojun, HUA Dezun, LI Chunyan: Research on Laboratory Wastewater Treatment and Pollution Prevention and Control Measures in Colleges and Universities, Environmental Science and Management, 2008, 32(10): 107–109.

ZHANG Yi, HE Ying, CHENG Wentao: Preliminary Study on Laboratory Wastewater Treatment and Pollution Prevention and Control Measures in Colleges and Universities, Environmental Science and Technology, 2006, 29(8): 54–56.

7 Application of functional materials in biological aerated filter

7.1 Technology development and research status of biological aerated filter

Biological aerated filter (BAF) is a common biofilm wastewater treatment technology. Compared with the common activated sludge method, BAF has the advantages of high organic loading, small area, less investment, no sludge expansion, high oxygen transmission efficiency and good water quality. However, there are more stringent requirements on the influent SS (generally SSe stringent requirementso water pretreatment is necessary. At the same time, its backwash water volume and head loss are large. At present, the larger environmental companies in the world, such as the French company Degremont, the German Möllerwerke company and the French OTV company have put it as a fist product for promotion in the world. BAF in China is also constantly developing.

The structure of the BAF is basically the same as that of ordinary fast filter, except that the aeration system is added to the bottom of the BAF. According to the direction of the water flow BAF can be divided into upflow and downflow filter. Earlier, most BAF was downflow filter, such as BIOCARBON. Because of the efficiency of downstream, BAF was not high enough, easy to plug and has short operating cycle. Therefore, at present, the upstream flow mode is mostly used to make the cloth for water and gas more uniform. At the same time, in the process of rising water, the SS at the bottom of the filter can be trapped in the upper surface, which increases the holding capacity of the filter and prolongs the work cycle. At present, there are BIOFOR®, BIOSTY®, COLOX®, DeepBed®, BIOPUR® and many other forms on the upstream aerated biological filter, of which BIOFOR is the most widely used. At present, CECS 265: 2009 "Technical Specification of Biological Aerated Filter" promulgated by China Engineering Construction Association has standardized the design, construction, installation, commissioning and operation of BAF.

A single BAF can complete the carbonation, nitrification, denitrification, phosphorus removal and other functions, combined with other processes, which can be used for secondary or tertiary treatment of urban sewage or industrial wastewater. Table 7.1 is a typical process for treating effluent with an aerated biological filter.

As the realization of each function on the size of filter media, filter thickness, load, aeration and other parameters are not the same, it is not appropriate to put all kinds of functions in the same BAF to complete.

The physical adsorption and filtration retention of the BAF filler and the biological oxidation of biofilms determine the SS and organic removal efficiency. Desbos et al. (1990) in the study of the relationship between filtration rate and SS and COD removal

https://doi.org/10.1515/9783110544381-007

Table 7.1: Typical treating process with BAF.

Function	Typical treating process
Carbonation	S/C+BF/C
Carbonation + nitrification	S/C+BF/C/N
Carbonation + nitrification + denitrification	S/C+BF/C/N+BF/DN
Carbonation + nitrification + denitrification	AS+BF/N+ BF/DN

Annotations: S/C is chemical precipitation, BF is aerated filter, C is carbonation, N is nitrification, DN is denitrification, AS is activated sludge.

rate found that, when the load increase is not due to more SS in the influent, but due to higher flow rates and lower residence times, the total SS removal efficiency is between 80% and 90% with COD removal between 70%–80%. Dalian Meilan River Sewage Treatment Plant adopts BIOFOR type BAF. When the treatment capacity is 120,000 m^3/d and the maximum COD load is 6 kg/(m^3·d), the effluent COD is less than 75 mg/L. BAF has mature capacity on organic matter and suspended solids, the handling capacity is large and the removal effect is significant (QI Bingqiang, 2000).

Short hydraulic retention time and long sludge age are consolidated in the BAF, which is conducive to the growth of nitrifying bacteria with a long generation, which has a high removal efficiency of ammonia. Cromphout (1992) utilized upflow BAF to treat ammonia-rich eutrophic water with a gas/water ratio of 1:1 and a filtration rate of 5.18 m/h, the nitration efficiency can reach 100% at 10 °C. Dillon et al. (1990) showed that the NH_3-N removal rate was 90% when the ammonia load was 0.63 kg/(m^3·d). Two years of research on the upflow BAF at the Achresh treatment plant has shown that when the NH_3-N volume load is 1.5 kg/(m^3·d), the removal rate of ammonia in BAF keeps 80%–100%, according to Pujol (2010). Denitrification is carried out due to the presence of anaerobic and facultative microorganisms in the aerated biological filter. According to Pujol's research, it is best to use a carbon source in denitrification. When the optimum filtration rate is 10–15 m/h, the denitrification capacity can reach 100%.

7.2 The filler of biological aerated filter and its characteristics

Filler is a key part of BAF, which has a direct impact on the effectiveness of BAF, but also affect the structure and cost of BAF. At present, BAF filler is mostly a patented product or in a confidential state; commonly used filler are quartz sand, ceramic and plastic products (synthetic fibers, polystyrene beads, corrugated board, etc.). In addition to the specific optimization of the BAF process, the study of BAF filler is a top priority in BAF research. Material and particle size grading of BAF filler may have a significant impact on the effectiveness of biological wastewater treatment.

According to their use of raw materials, filler of BAF can be divided into inorganic filler and organic polymer filler; according to the different density, it can be divided into floating and submerged filler. Inorganic filler is generally submerged filler; organic polymer filler is generally floating filler. Common inorganic fillers are ceramsite, coke, quartz sand, activated carbon and expanded aluminosilicate; organic polymer fillers are polystyrene, polyvinyl chloride and polypropylene.

At present, foreign researchers have done a lot of research on the filler of BAF. Moore et al. (2001) studied the effects of filter media with size range of 1.5–3.5 mm and 2.5–4.5 mm on BAF performance. It was found that BAF with small particle size (1.5–3.5 mm) had better denitrification effect but could not meet the high hydraulic load. The large particles (2.5–4.5 mm) filter although improve the operating conditions of the filter, it reduce the number of backwash, but it is not conducive to the removal of nitrogen and SS. This provides a theoretical basis for the reasonable determination of particle size of BAF filter material. Mann Allan et al. (1999) found through researches that compared with submerged filter, the floating filter had higher removal rate of organic matter and SS, and less affected by hydraulic load and organic load. Chang et al. (2002) studied the treatment effect of textile wastewater by using sand and natural zeolite as BAF filter material. The results show that natural zeolite has better treatment effect on textile wastewater than sand, which may be due to the larger specific surface area of natural zeolite and stronger cation exchange capacity than sand. Kent et al. (1996) systematically analyzed the foam columnar clay, prismatic calcined clay, expanded refractory clay, powdered fuel ash, old prismatic shale, new prismatic shale and swelling clay, which may be used as BAF filter media. The most suitable for BAF filter is the swelling clay, followed by shale. This shows that with the development of BAF wastewater treatment technology, the replacement of high-density lightweight filler is the inevitable trend in the development of biological wastewater treatment technology.

Most of China's research on BAF filter is ceramic. This is because ceramic filter has the advantages of large specific surface area and it is cheap, which is especially suitable for China's conditions. Most of the early ceramsites were fired, broken and sieved directly from shale, most were irregular (flaky majority). Later, there are spherical ceramsite, which uses clay as the main raw material, adding appropriate chemicals as expansion agent. It was fired from high temperature. It has the advantages of rough surface, strong biological adhesion, good film-forming performance, good water flow pattern, easy backwash, strong interception ability and good development prospects. In recent years, on the basis of early ceramsite, enzymatic ceramsite, nano-modified ceramsite and spherical light ceramsite have been developed. Enzymatic ceramsite enhance its treatment effect through the catalytic effect of enzymes. Nanotechnology has been used to modify the filter material, so that the filter surface of nano-modified ceramsite contains nanoparticles, which have more processing power. The surface of spherical lightweight ceramsite is rough and rub-resistant, whose strength is high, and density is moderate. ZHU Lehui et al. (2000)

developed a spherical lightweight ceramic, after the sewage treatment test found that the ceramic has a strong biological adhesion, good water flow pattern, good film properties, easy to backwash, interception ability and so on, compared with the regular shape of the organic filter. JIANG ping et al. (2002) conducted experiments on BAF wastewater treatment using clay ceramsite. It was observed by scanning electron microscopy that a large amount of microorganisms could be attached to the internal pores of clay ceramsite, which is considered as an ideal BAF filter. YU Ying et al. (2005) developed a nano-modified ceramic; the physical and chemical properties were tested and electron microscopy microstructure was observed. Through BAF testing it was found that, compared with other domestic media, it has advantages such as quick-hanging film, anti-impact load capacity and good biological affinity, so it is suitable for BAF filter.

At the same time, some experts in China also studied other media for filter. TIAN Wenhua et al. (2003) developed a zeolite filter in which the filter media was used in BAF sewage treatment so that the effluent quality can meet the cooling water quality standards (III) of relevant provisions. ZHANG Wanyou et al. (2003) developed a new type of soft media in the study of aerobic biofilm filtration device. The filter has high porosity, large specific surface area, good biofilm adhesion performance and is durable. Tsinghua University Laboratory screened different filters such as clay ceramsite, shale ceramsite, sand, zeolite, medical stone, slag, coke and so on. Compared with bioactivated carbon, they thought ceramsite, sand, maifanite and Datong zeolite are superior to other filter media. At present, there are many research and application of volcanic rocks and spherical bentonite and other media.

There are stringent criteria on the BAF in Europe and the United States, but not yet in China. When the filler size, traits, density and other factors on the removal of pollutants are fully understood, it is of far-reaching significance to formulate a suitable filter standard for aerated biological filters in China.

7.3 Research progress of combined media biological aerated filter

Because of the drawbacks of single media BAF in practice, in recent years, the combination of BAF filter media technology has gradually been concerned.

QIU Chi et al. (2008) selected combined media of the activated carbon, coke and stone for the treatment of slightly polluted water. Dynamic tests showed that it has a good removal effect on organic matter and turbidity in water. The removal rate of COD_{Mn} was 25.55%–80.92% and the turbidity removal rate was 25.55%–98.80%. The combination of BAF fillers not only reduces costs, but also improves the treatment effect.

WANG Ying et al. (2007) studied the treatment of COD_{Cr} and NH_3-N in urban wastewater by using the combination of slag–zeolite filter media of BAF. The results showed that the biofilters had good complementarity. The removal rates of COD_{Cr} and NH_3-N in the filter were stable, and were less affected by the impact load.

QI Xiang et al. (2006) carried out a comprehensive filter test and comparison of quartz sand and ceramic double-layer filter. Experiments showed that the water purification performances of quartz sand and ceramic filter composed of double-layer filter was significantly better than single-layer quartz sand filter media. Especially in the effluent turbidity, micro-flocculation, backwash cycle, removal of algae, in the use of flocculant and other indicators they have obvious advantages.

LIU Jinxiang et al. (2008) discussed the influencing factors of zeolite–ceramsite BAF to treat the slightly polluted source water. The results showed that the zeolite–ceramsite BAF has a good effect on slightly polluted water, and the required filter height is small and the gas–water ratio is low.

DU Yongxiang et al. (2012) used contaminated filter BAF of ceramsite– zeolite–activated carbon to treat surface water body. The results showed that under the conditions of temperature of 16–24 °C, hydraulic retention time of 6 h and gas–water ratio of 1: 1, contaminated filter has good effect on the polluted surface water body. The effluent permanganate index and ammonia concentration dropped to 2 mg/L and 0.1 mg/L, respectively. The removal rates of permanganate index and ammonia in the ceramsite layer stabilized at 50% and 85%, respectively.

ZHANG Liang et al. (2007) established a biofilter process of quartz sand–granular activated carbon–zeolite, and used this process to pretreat the water used by Yaojiang. The research shows that the filter technology has good removal effect on turbidity, ammonia and organic matter.

Osorio et al. (2002) at the University of Granada in Spain tried to perform a wastewater treatment test using the BAF with a two-layer filter made of ceramic and plastic filter media. When influent BOD and SS concentrations were 250 mg/L and 110 mg/L respectively, effluent BOD and SS concentrations were controlled at 20 mg/L and 25 mg/L, respectively. As a good treatment effect in the larger load range, the impact load capacity of the filter tank is obviously improved compared with the conventional BAF, so the process will be more widely used in sewage treatment.

7.4 Study on pollutant removal characteristics of integrated multilayer filter of BAF

7.4.1 Filter and equipment

7.4.1.1 Test filter

The filters used in this experiment were volcanic rock, fly ash ceramsite and styrofoam filter beads. Among them, volcanic rocks were purchased from a Beijing Environmental Protection Technology Co., Ltd. Fly ash ceramic is self-developed from the Ministry of Environmental Protection, South China Institute of Environmental Science. Styrofoam

filter beads were purchased from Henan Water Treatment Materials Co., Ltd. The filter used in this test is shown in Figure 7.1, and its performance parameters are shown in Table 7.2.

Table 7.2: The performance parameters of three filters.

Filter types	Particle size (mm)	Bulk density （kg/m^3）	Specific surface area （m^2/kg）	Porosity(%)
Volcanic rock	4–6/3–5	900	100	60
Fly ash ceramsite	3–5	877	8 500	41.9
Styrofoam filter beads	2–4	60	11	50

Figure 7.1: Volcanic rock, fly ash ceramsite and styrofoam filter beads.

7.4.1.2 Equipment and process

The experimental setup and procedure are shown in Figure 7.2. There are three parallel plexiglass pillars of DN 150 mm and height 2.4 m. From left to right are BAF with volcanic, multilayered media and ceramsite. Each BAF system has an oxygen and oxygen layer in one structure. The bottom of the BAF system has a distribution area with height of 0.3 m. The perforated filter plate and gravel support layer are on the top of the distribution area; the supporting layer is 0.15 m high; and the filter layer is 1.5 m high. There is a sampling port at every 0.2 m height along the media layer. Above the filter layer were clear water area and high area, respectively, 0.3 m and 0.15 m high. In the volcanic BAF system, the anaerobic layer volcanic media has a diameter of 4–6 mm, and the aerobic layer has a diameter of 3–5 mm. The multilayer filter is divided into three layers, of which the anoxic layer is 0.4 m high, the filter material is volcanic, and the particle size is 4 to 6 mm. Aerobic layer I is 0.8 m high; the filter material is fly ash ceramsite; the uppermost layer is aerobic layer II with height of 0.3 m. The filter is polystyrene foam beads. Ceramsite BAF used fly ash ceramic filter media with a diameter of 3–5 mm.

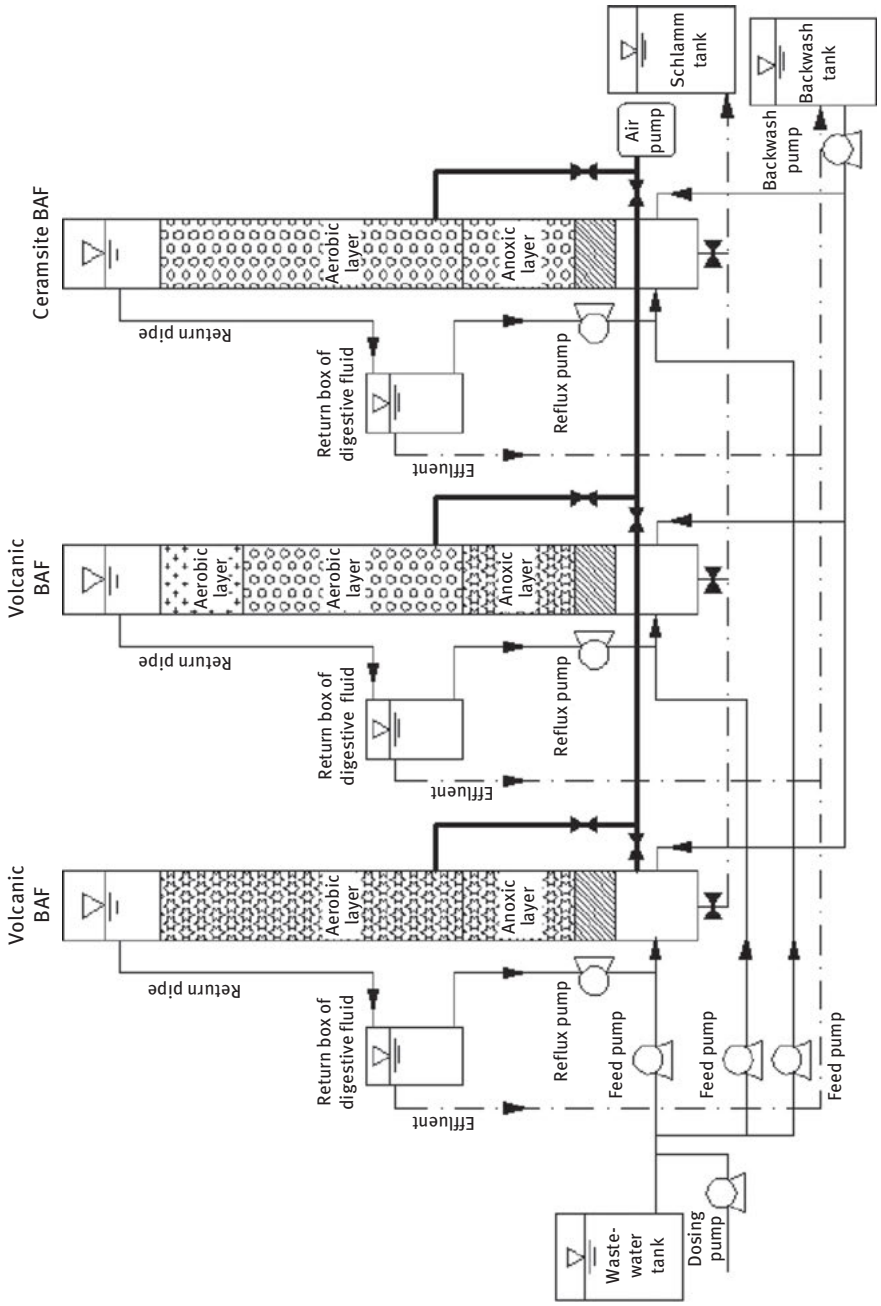

Figure 7.2: Technological process of BAF.

The effective volume per unit is 39.7 L, the designed hydraulic load is 1.7 $m^3/(m^2 \cdot h)$, the hydraulic retention time is 26 min and the daily capacity is 0.75 m^3. Each system has an anoxic layer and an aerobic layer in one structure. The total height of the filter layer is 1.5 m, of which the lower layer is anoxic layer with 0.4 m high; the upper layer is aerobic layer with 1.1 m high. The three sets of BAF systems are all upstream. The urban sewage through the feed pump first flows into the anoxic layer at the bottom of the filter media, and then flows upward through the aerobic layer. The effluent of the aerobic layer is partially returned to the anoxic layer and the remaining effluent is discharged into the backwash tank.

The photo of the test device is shown in Figure 7.3.

Figure 7.3: The photo of the test device.

7.4.1.3 Backwash

In order to avoid the blockage of stuffing and sedimentation at the bottom of the BAF during operation, and to ensure continuous and stable operation of the system, the backwashing with water and gas are used during this test. At first, the gas backwash of 5 min, then backwash with gas and water of 6 min and finally backwash with water of 8 min. The gas backwash intensity is 15.7 $L/(m^2 \cdot s)$ and the water backwash intensity is 7.9 $L/(m^2 \cdot s)$. Backwash cycle is 2–3 d.

7.4.2 Decontamination characteristics of integrated multilayer filter BAF

7.4.2.1 COD and SS change with the filter height

The changes of COD and SS with the filter height are shown in Figure 7.4. The "0" site in figure corresponds to the concentration of water and reflux digestive fluid after

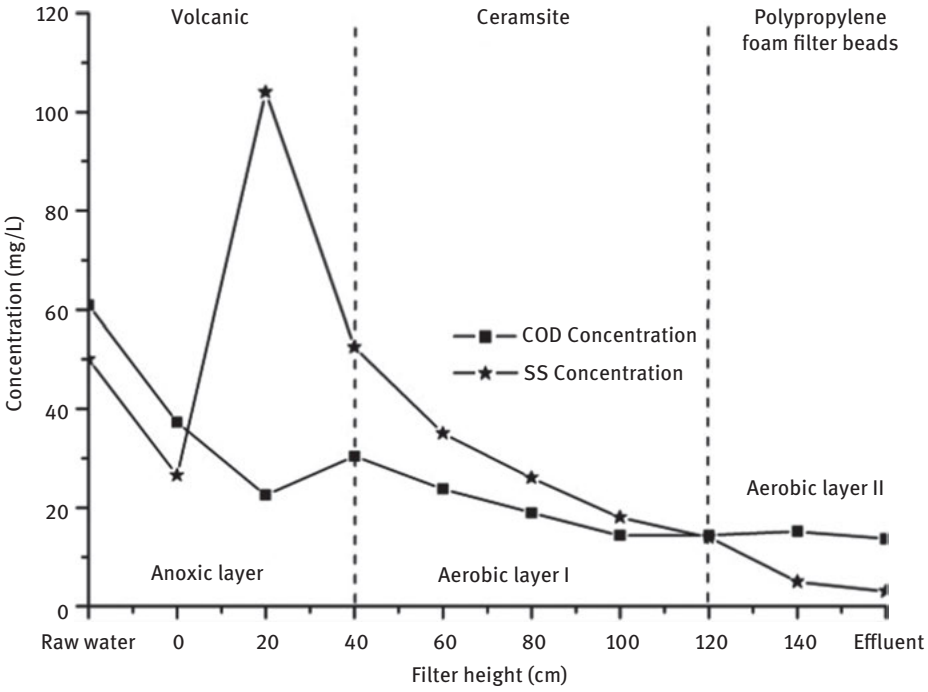

Figure 7.4: COD and SS change with the filter height.

mixing. After diluting with reflux, COD and SS concentrations of raw water decreased sharply from 60.84 mg/L and 50 mg/L to 38.79 mg/L and 26.5 mg/L, respectively. The COD concentration decreased from 38.79 mg/L to 20.58 mg/L in the 0–20 cm section of the anoxic layer, whereas the SS concentration increased sharply to 104 mg/L. In the 20–40 cm section, COD concentration increased to 30.42 mg/L. Although the SS concentration decreased significantly compared with the previous stage, the SS concentration was still higher than that of the influent SS. In aerobic layer I, the COD concentration decreased rapidly from 30.42 mg/L to 14.42 mg/L, and the SS also showed a decreasing trend. The SS concentration at a height of 120 cm was reduced to 14 mg/L. After the polypropylene foam bead layer, COD concentration remained unchanged, whereas the effluent SS concentration was reduced to 3 mg/L.

COD removal rate in the lower anoxic layer of volcanic rocks decreased significantly, mainly due to the following conditions: first, the denitrification of the anoxic layer consumes part of the carbon source; second, the section of filter media retained more suspended organic pollutants. With the increase of the filter layer, the easily degradable organic matter gradually decreases and the COD removing effect decreases. In general, the removal of organic matter decreases exponentially along the depth of the filter. In general, the removal of organic matter decreases exponentially along the depth of the filter.

In the 20–40 cm section, the concentration of organic matter is high, the heterotrophic bacteria are well-nourished and reproduce fast, and some of them are in the form of suspended sludge. In addition, suspended matter in the BAF system accumulates in the anoxic layer, resulting in an increase in SS concentration in this section. In the aerobic layer I and II, SS concentration gradually decreased. Thus, SS removal occurs mainly in the ceramsite layer and polypropylene foam bead layer.

7.4.2.2 Change of different forms of nitrogen with the filter layer height

The changes in different forms of nitrogen with the filter height are shown in Figure 7.5. As can be seen from the figure, the concentrations of NH_3-N and TN significantly decreased after mixing of raw water and reflux liquid. However, NO_3-N and NO_2-N concentrations increased. NH_3-N and NO_2-N concentrations in the anoxic layer did not change. The concentration of NO_3-N decreased from 5 mg/L to below 2 mg/L in the 0–20 cm section of the anoxic layer, but remained unchanged in the range of 20–40 cm. Because of the denitrification of anoxic bacteria and the dilution effect of reflux liquid, the anoxic phase TN decreased from 17.21 mg/L to 10.18 mg/L. The concentration of NH_3-N decreased sharply from 7.3 mg/L to 2.17 mg/L in 40–120 cm ceramsite layer, the concentrations of NO_3-N and NO_2-N increased and the TN concentration

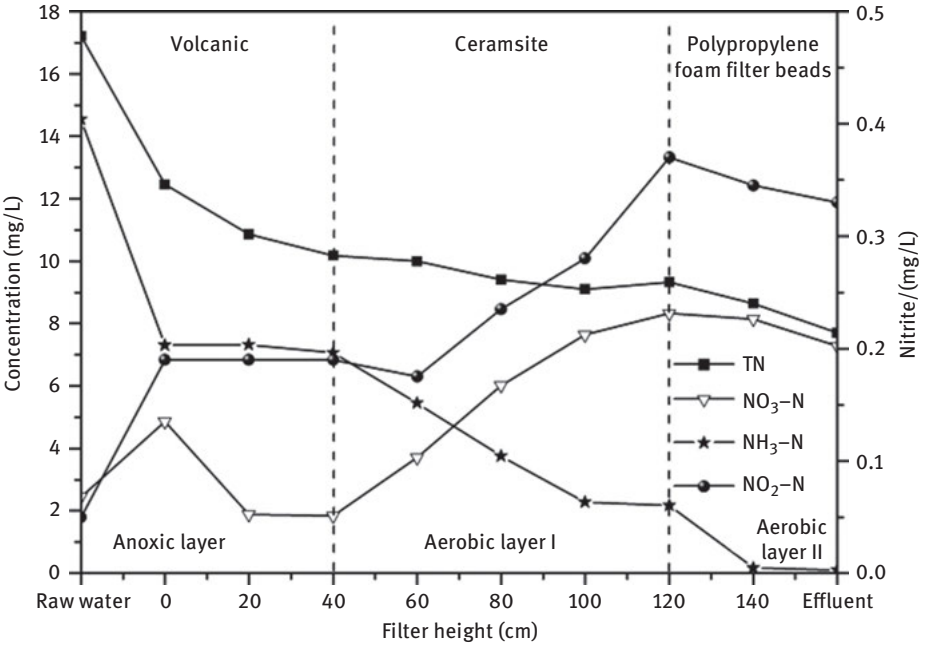

Figure 7.5: Change of different forms of nitrogen with the filter height.

decreased from 10.18 mg/L to 9.33 mg/L. The concentration of NH_3-N decreased to 0.1 mg/L and the NO_3-N and NO_2-N also decreased after passing through polypropylene foam bead layer. TN decreased from 9.33 mg/L to 7.7 mg/L.

Thus, multilayer filter BAF showed a functional partition at different filter media levels. In the lower volcanic–anoxic layer, denitrification is the main function, the removal rate of TN is 40.85%. In the ceramsite-aerobic layer I, nitrification was the main function, and the degradation of NH_3-N was strong. In the top layer of polypropylene foam beads–aerobic layer II, there was simultaneous nitrification and denitrification, TN and NH_3-N have better degradation.

7.4.2.3 Biofilm distribution with the filter height

The relationship between biofilm and filter height is shown in Figure 7.6. Along the inflow direction, in the anoxic zone, the biofilm gradually increased. In aerobic zone I, the amount of biofilm first rapidly increased and reached the maximum at a sampling point of 80 cm, with a measured value of 94.49 nmolP/g of filter media, corresponding to 94.49×10^8 *E.coli* cells. After this, the biofilm volume gradually decreased at 80–120 cm. In the aerobic zone II, the biofilm decreased rapidly and the amount of biofilm at the effluent decreased to 25.14 nmolP/g of filter media. Overall, the amount of biofilm in aerobic zone I is higher than that in anoxic zone and aerobic zone II.

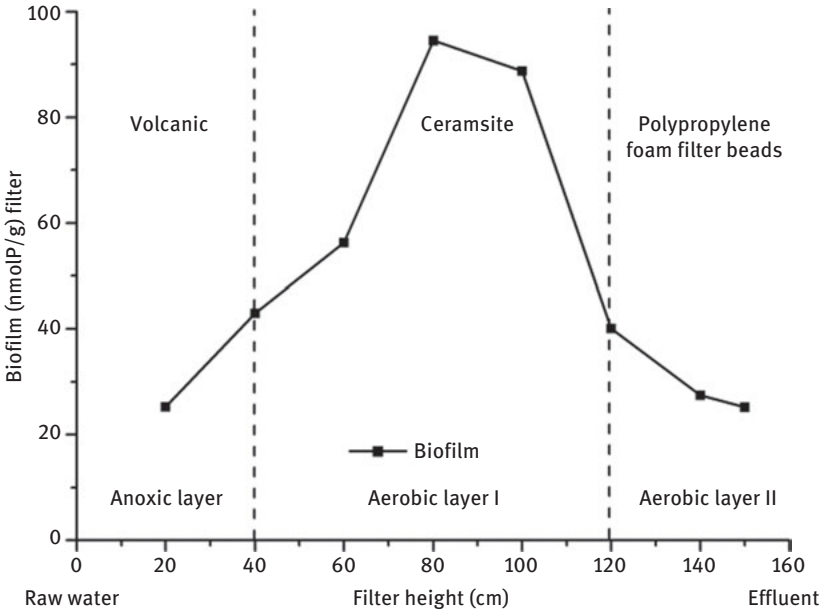

Figure 7.6: Biofilm distribution with the height of the filter.

The biofilm in the anoxic zone is generally less than that in the aerobic zone I. The reason may be as follows: there is mainly denitrifying bacteria in the anoxic zone. Compared with the heterotrophic bacteria, denitrifying bacteria grow slowly, and they are sensitive to changes in external conditions, so the biomass in the anoxic zone is small. In the aerobic zone I of 40–80 cm filter layer, the organic substrate concentration is high, and the aeration is sufficient. Therefore, heterotrophic bacteria multiply in large quantities and the biomass showed a clear upward trend. The biofilm growth rate of 60–80 cm section was higher than that of the 40–60 cm section. This may be due to 40–60 cm section of the filter layer close to the aeration tube, and the uneven distribution of tube caused the uneven aeration. Part of the surface of the filter was black, so the growth and reproduction of heterotrophic bacteria are inhibited. In the 60–80 cm section, filter is loose, and there is good aeration, therefore heterotrophic bacteria grew faster. In the aerobic zone I 80–120 cm section and the aerobic zone II, the organic pollutants in the sewage has dropped to a low level. Microorganisms lack nutrients and grow more slowly, resulting in a rapid decrease in biofilm per unit of filter media.

7.4.2.4 The distribution of TTC-dehydrogenase activity along the filter height

The distribution of triphenyltetrazolium chloride (TTC)-dehydrogenase activity along the filter height is shown in Figure 7.7. Along the water inflow direction, the TTC-dehydrogenase activity in the anoxic zone gradually increased; in aerobic zone I, TTC-dehydrogenase activity first increased and reached the highest at 60 cm, which

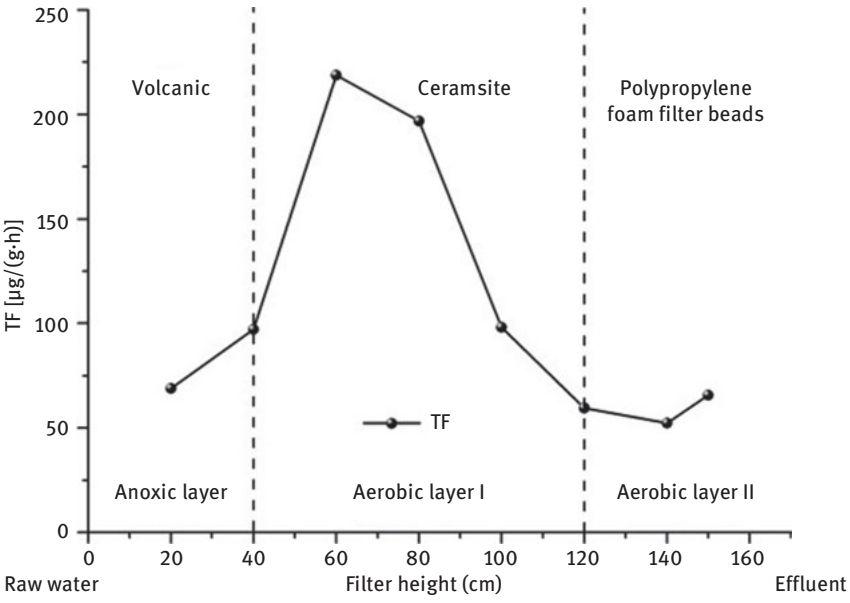

Figure 7.7: Distribution of TTC-dehydrogenase activity along the height of the filter.

was 218.68 μg/(g·h), and then began to decline. In aerobic zone II, TTC-dehydrogenase activity decreased first and then increased slightly. Overall, biofilm in the aerobic zone I has the highest TTC-dehydrogenase activity, the measured value is 59.56–218.68 μg/(g·h). While the TTC-dehydrogenase activity of biofilm in anoxic and aerobic zone II was 68.81–97.10 μg/(g·h) and 59.56–65.68 μg/(g·h), respectively.

At the inlet of 20 cm, TTC-dehydrogenase activity is low. This may be due to the large number of suspended solids retained by the filter at the inlet side, which contained more inert material, limiting the diffusion of the nutrient matrix and the rate of microbial proliferation and resulting in lower bioactivity. With the increase of filter layer, the microbial membrane was less affected by suspended matter and inert substances, the mass transfer effect was better and the TTC-dehydrogenase activity increased gradually. In the aerobic zone I 40–60 cm section, the organic substrate concentration is higher, aeration is more adequate, heterotrophic bacteria and nitrifying bacteria and other microorganisms grow faster, TTC-dehydrogenase activity increased rapidly. The TTC-dehydrogenase activity began to decline at the 60 cm sampling port, which may be due to the gradual decrease in the substrate concentration of the organic substance. Nutrients become a limiting factor in the growth and reproduction of microorganisms, leading to a decrease in the biofilm activity.

The TTC-dehydrogenase activity data was divided by the biofilm amount to obtain the bioactivity values per unit biomass for further analysis of the biofilm matrix-specific abilities, as shown in Figure 7.8.

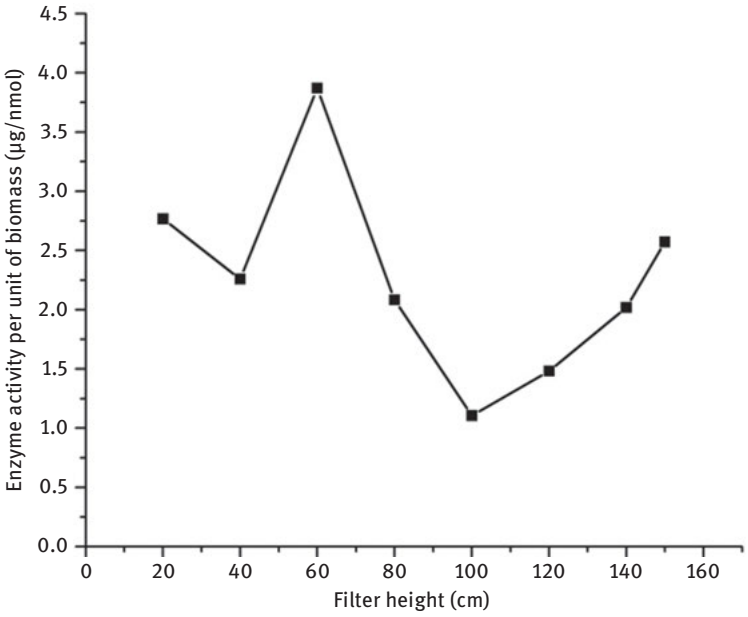

Figure 7.8: TTC-dechlorination activity per unit of biomass.

The trends of TTC-dehydrogenase activity per unit biofilm and TTC-dehydrogenase activity of unit filter were similar. The difference is that in the anoxic zone of 20–40 cm, the biological activity of the biofilm gradually decreased, whereas the biological activity of the filter was gradually increased. In addition, at 100 cm, the bioactivity of biofilm began to increase, whereas the bioactivity per unit filter still showed a downward trend. This shows that in BAF, the biological activity per unit biofilm at different filter heights and the trend of per unit filter are not exactly the same.

7.4.3 Efficiency comparison of multilayer filter BAF and single-layer filter BAF

After completing the pretest, all the filter of the multilayer BAF was drained, and the BAF device was cleaned. Volcanic rocks, multilayer media and ceramsite are then refilled in BAF. Under the same conditions (water temperature of 20 °C–35 °C, pH of 6.6–6.9, gas–water ratio of 3:1, reflux ratio of 1:1, hydraulic load of 1.7 $m^3/(m^2 \cdot h)$], hanging film is activated. After the start-up of the hanging film, the stable operation for 32 days was carried out to further investigate the efficiency differences of three kinds of filter media BAF on the municipal wastewater treatment.

7.4.3.1 Comparison and analysis of average removal rate of pollutants

In the stable operation stage, the average removal rates of the three BAFs for each pollutant are shown in Table 7.3 and Figure 7.9. The removal efficiency of NH_3-N by volcanic rock and multilayer BAF is close, with the removal rates of 95.60% and 94.69%, respectively. Compared with the former two, the removal efficiency of NH_3-N by ceramsite filter is poor, and the removal rate is only 86.04%. The removal rate of TN of volcanic rocks and multilayer filter BAF is also very close, both about 50%. The TN removal of ceramsite BAF is relatively poor; the removal rate was only 43.62%. The COD removal rate of three kinds of BAF was close; the average removal rate was about 70%. The removal efficiency of multilayer filter BAF was slightly better than the other two, with the average removal rate of 71.71%. In the SS removal, the multilayer filter BAF is still the best. The removal rates of SS from three kinds of BAFs were as follows: BAF (86.06%) > BAF (83.51%) > BAF (80.42%).

Table 7.3: The average removal rate of pollutants.

BAF	NH_3-N (%)	COD (%)	SS (%)	TN (%)
Volcanic BAF	95.60±4.73	68.74±7.63	80.42±7.12	49.54±4.31
Multilayer filter BAF	94.69±5.07	71.71±5.04	86.06±4.58	50.01±5.08
Ceramsite BAF	86.04±6.30	69.21±6.97	83.51±4.4	43.62±7.54

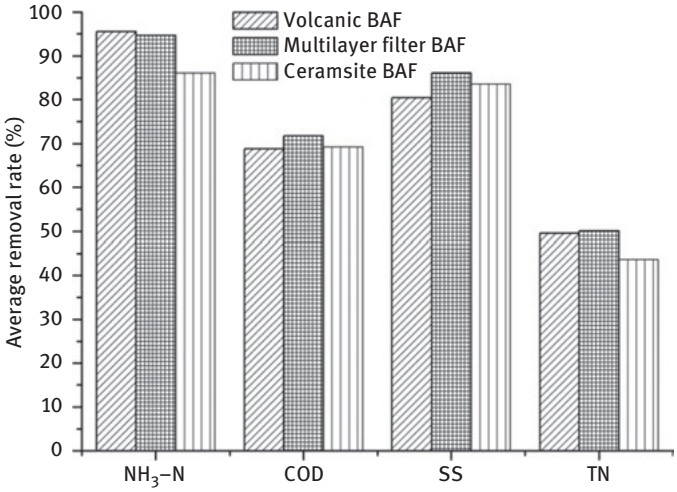

Figure 7.9: BAF Average removal of contaminants.

7.4.3.2 Comparison and analysis of COD removal rules

The COD removal rate of three sets of BAF is shown in Figure 7.10. During the first five days of hanging-film stage, the removal efficiency of volcanic BAF was better than 70%, whereas for multilayer filter and ceramsite BAF it was only 50% and 60%, respectively. With the progress of the experiment, the removal efficiency of COD by multilayer filter and ceramsite BAF is gradually improved. On the 8th day, the COD removal rate of both BAF increased to about 75%. On the 12th day, with the increase of influent flow from 20 L/h to 30 L/h and the return flow on the 14th day, the hydraulic impact load increased, and the COD removal rates of the three BAFs tended to decrease and then get stabilized. This shows that all three BAFs have strong resistance to hydraulic load shocks.

In the stable operation stage, although the influent COD concentration fluctuated between 37.5 and 70.6 mg/L, the effluent from the three BAFs was relatively 10–25 mg/L, the average removal rate is about 70%. It can be seen that the three BAF filters have strong impact resistance on COD volume load.

7.4.3.3 Comparison and analysis of SS removal rules

Under the same experimental conditions, the SS removal efficiencies of three BAFs are shown in Figure 7.11. During the start-up phase of the hanging film, the SS removal rates of three kinds of filter BAF showed a gradual upward trend, but the SS removal rate of multilayer filter BAF was slightly higher than that of the other two and was more stable. From the 12th day to the end of the hanging film, the effluent SS concentration of multilayer filter BAF was stable from 3.5 to 18.5 mg/L, whereas for volcanic rocks and ceramsite it was between 13.5 and 42.5 mg/L and between 9.5 and 19.0 mg/L.

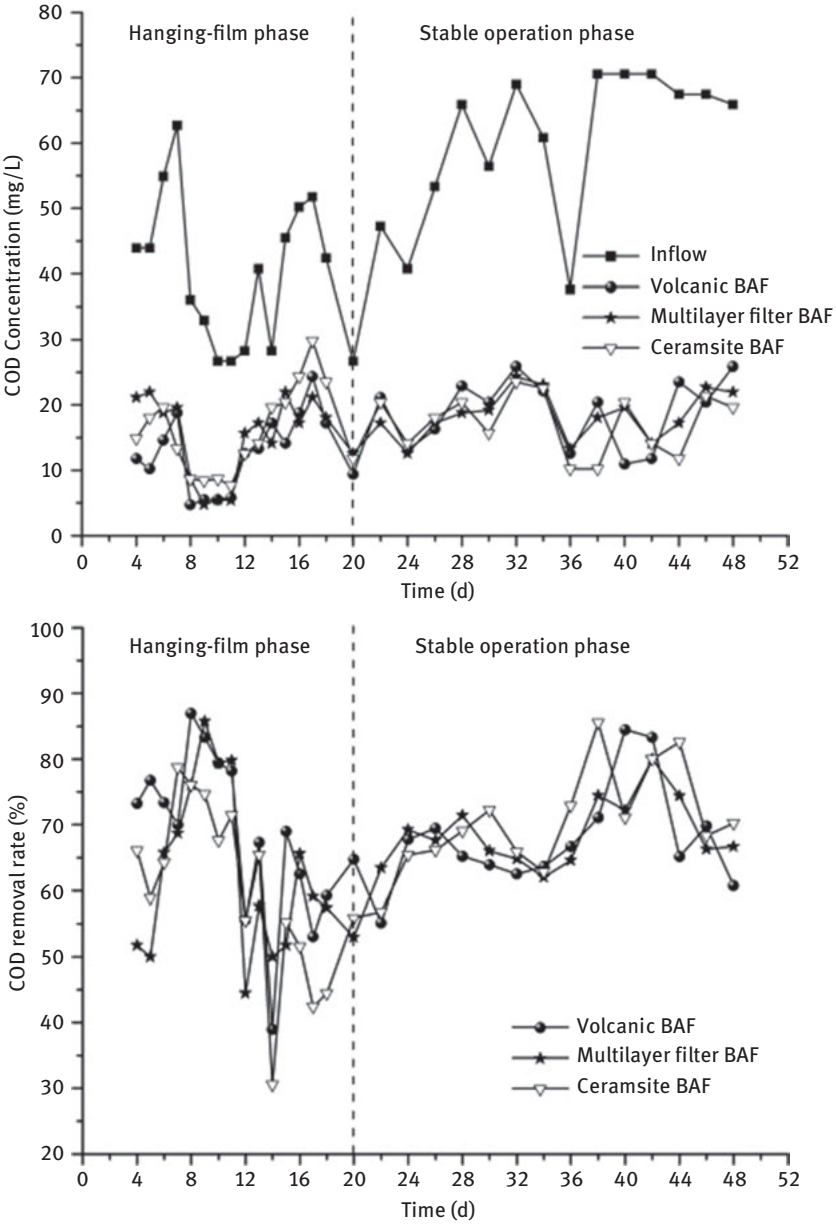

Figure 7.10: COD removal effect of three BAFs.

In the stable operation stage, the SS removal efficiencies of three kinds of BAFs are relatively stable, the SS concentration of influent water is between 32 and 92 mg/L. The average effluent SS concentration of multilayer filter BAF was (7.1±2.9) mg/L and the removal rate was (86.06±4.78)%. The mean effluent SS concentration of volcanic BAF

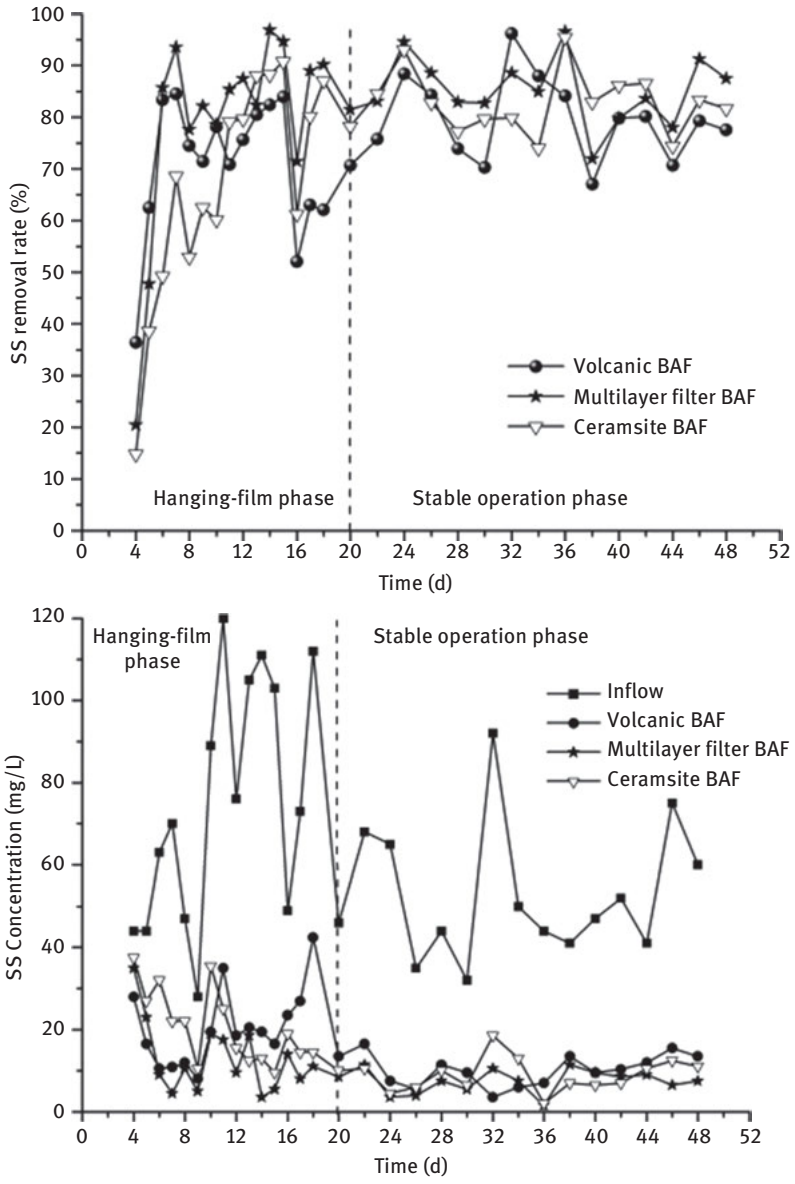

Figure 7.11: SS removal effect of three BAFs.

was (9.6±3.57) mg/L, and the removal rate was (80.42±8.29)%. The mean effluent SS concentration of ceramsite BAF was (8.8±4.3) mg/L, and the removal rate was (83.51 ±6.39)%. As can be seen from Figure 7.11, the multilayer filter BAF has a higher SS removal rate and a more stable removal effect. This is probably because the multilayer filter BAF achieves a combination of different filter media gradation, and that the

lightweight filter has a high retention capacity so that the system shows good filtration and interception ability.

7.4.3.4 Comparison and analysis of NH_3-N removal rules

The NH_3-N removal of three BAFs during the test is shown in Figure 7.12. As can be seen in Figure 7.12, the removal rate of NH_3-N by volcanic BAF rose to 98.78% on the 6th day of hanging-film stage, and the average removal rate reached 95% after 6–20 days. It shows that the aerobic biofilm in volcanic BAF grows fast and its biological activity is stable. The NH_3-N removal efficiency of multilayer filter and ceramsite BAF was lower than that of volcanic BAF at the first two days of hanging-film stage. On the 6th day, the NH_3-N removal rate of multilayer filter BAF also increased to more than 98%, and the average removal rate reached 96.21% in 6–13 days. However, the average removal rate of ceramsite BAF at 6–13 days was only 72.99%. From the 14th day, with the increase in the influent flow rate and the opening of reflux, the hydraulic load greatly increased, resulting in a decrease of NH_3-N removal rate of multilayer filter and ceramsite BAF. The removal rate of NH_3-N of both BAFs reached about 70% when the hanging-film phase was completed.

In a stable operation stage, the average NH_3-N removal rate of volcanic BAF was (95.57±4.73)%, and the effluent NH_3-N concentration was stable at 0.1–2.1 mg/L. The NH_3-N removal rate of multilayer filter and ceramsite BAF fluctuated greatly from 20 to 30 days, and stabilized after 32 days. The average effluent NH_3-N concentration of multilayer filter BAF stabilized at 0.12–4.1 mg/L, the average removal rate was (94.69±5.07)%. The average effluent NH_3-N concentration of ceramsite BAF stabilized at 0.2–5.1 mg/L with an average removal rate of (86.04±6.3)%. Thus, the NH_3-N removal of multilayer filter BAF is better than that of volcanic BAF. However, the NH_3-N removal rate of ceramsite BAF fluctuated greatly and the removal rate was lower than the former two BAFs.

The reasons may be due to the large porosity of volcanic BAF, which provides more room for microbial growth and reproduction, and the biomass per unit volume is also larger, thus showing a better NH_3-N removal effect. In addition, the resistance of light filter to water flow is large, which can ensure the uniform distribution of water flow and good mass transfer conditions; it is conducive to the growth of nitrifying bacteria, the NH_3-N removal is better than that of ceramsite BAF. Because the polypropylene foam beads are used in the aerobic layer II of multilayer filter BAF, resulting in better NH_3-N removal.

7.4.3.5 Comparison and analysis of TN removal rules

The TN removal of three BAFs during the test is shown in Figure 7.13. In the hanging stage, the TN removal rates of three BAFs are generally on the rise. On the 16th day, the TN removal rate of three kinds of filter media BAF increased to about 40%, and

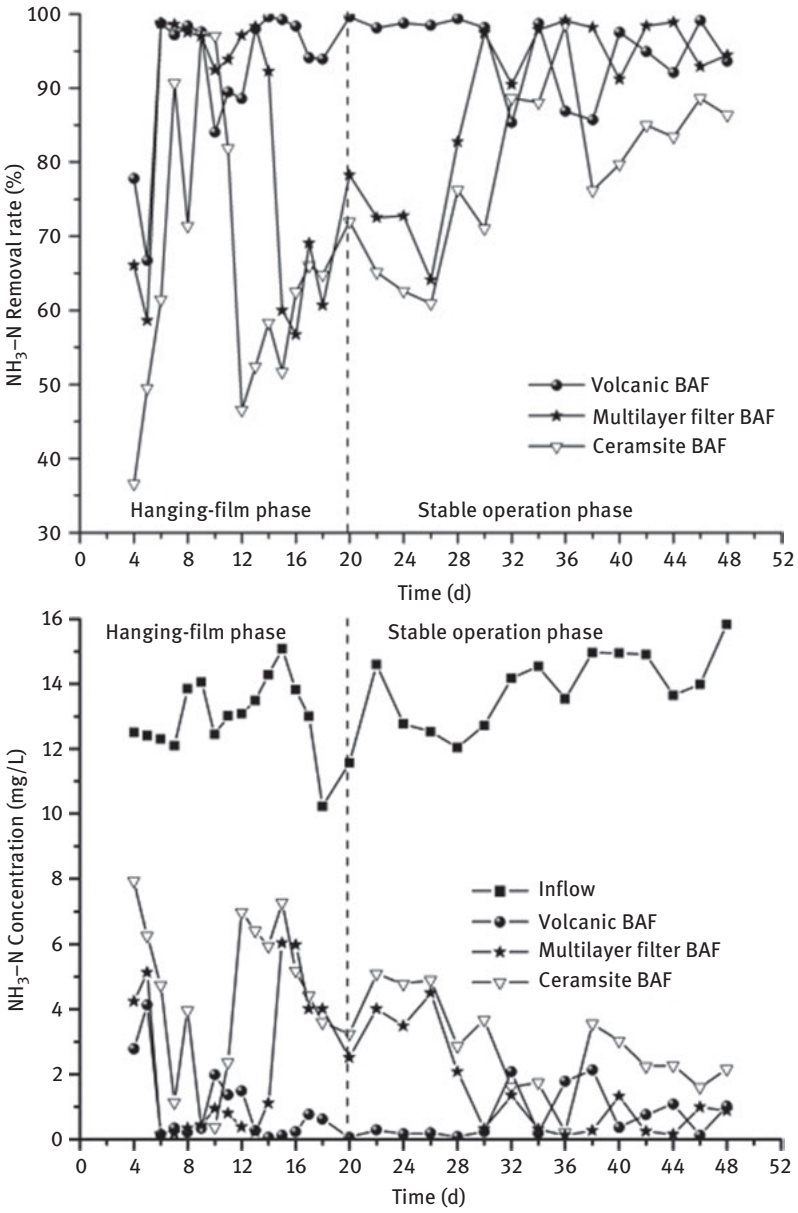

Figure 7.12: NH_3-N removal effect of three BAFs.

basically remained stable after that. Compared with ceramsite BAF, volcanic and multilayer BAF have a relatively stable TN removal in stable operation. And the average removal rate was higher, reaching 49.5% and 50.0%, respectively, whereas the TN removal rate of ceramsite BAF was only 43.6%. TN is mainly removed by

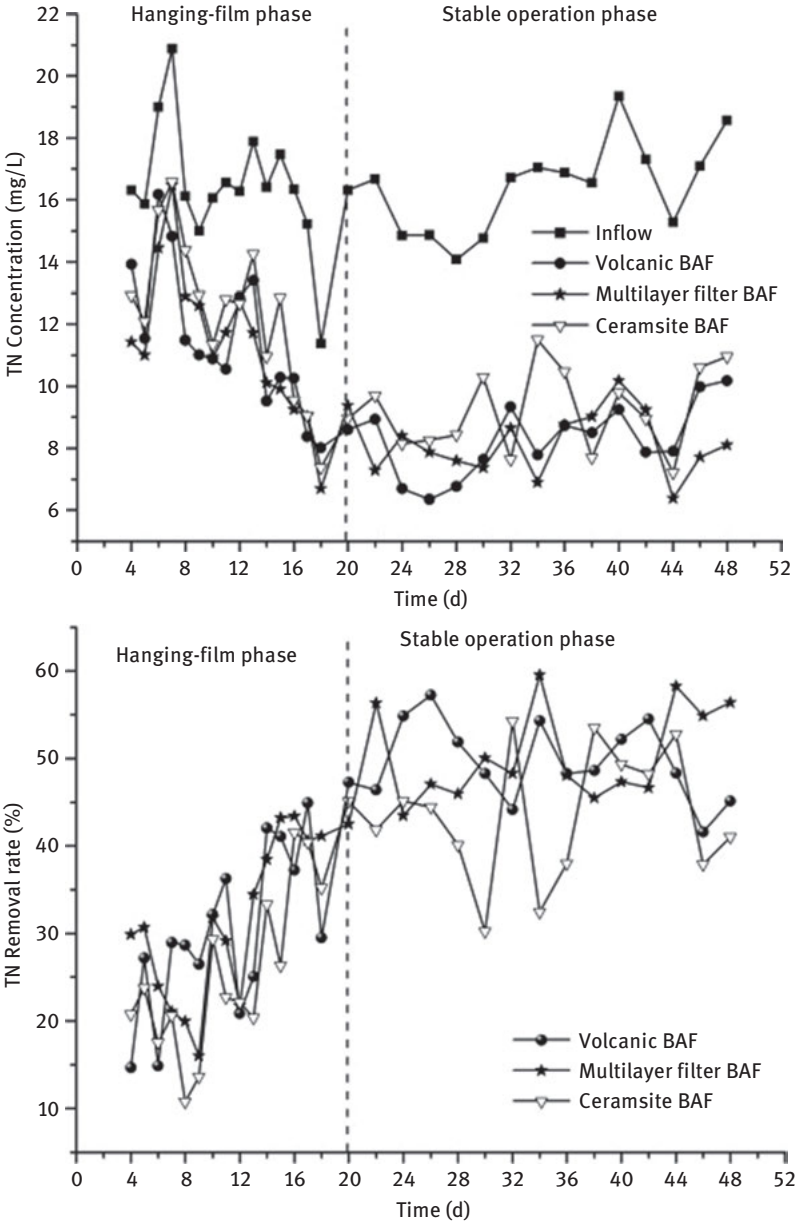

Figure 7.13: TN removal effect of three BAFs.

denitrification in the anoxic layer. 4–6 mm volcanic BAFs are filled in the anoxic layer of volcanic rocks and multilayer BAF. Compared to ceramsite BAFs, volcanic BAF is more developed in the inner pore, and it is easier to form an oxygen-deficient environment inside the filter material so as to have a better denitrification effect.

7.5 Study on phosphate removal in functional material in BAF

Under normal circumstances, BAF reactor can use nitrification process to remove ammonia in wastewater, but it has very limited effect on phosphorus removal; chemical phosphorus removal is usually utilized in actual engineering applications. It is generally believed that there is no alternation in anaerobic and aerobic environment in the BAF. The removal of total nitrogen and total phosphorus by microorganisms is often only used during microbial growth. Therefore, the effect of biological nitrogen and phosphorus removal by BAF is weak. In order to reach the discharge standard, chemical sludge will often be produced by chemical phosphorus removal, which will increase the difficulty of sludge treatment and disposal. Therefore, how to improve the efficiency of biological nitrogen and phosphorus removal by BAF has become one of the key problems in the current BAF research. In the previous study, our research group aimed at the characteristics of BAF reactor filler; they developed a new type of fly ash ceramsite, which is good in phosphorus removal. For this purpose, a BAF reactor device with this fly ash ceramsite as the main filler was designed to investigate the removal of pollutants during the start-up and hanging-film process and provide the necessary data for the future engineering application of the new filler.

The main experimental device is a set of BAFs with a square cross section of 400 mm × 400 mm in length and width and 2,500 mm in height. The whole device is made of plexiglass. Water distribution of the reactor is upward flow with perforated pipe. The tray aerators are used for aeration to ensure uniform aeration, based on the prevention of clogging considerations. One centrifugal pump and one roots blower were used to supply water and air respectively to two aerated biological filters. The reactor design is shown in Figure 7.14.

BAF reactor is filled with 30 cm gravel layer as a supporting layer. Among them, the thickness of the larger gravel layer with diameter of 12–15 mm is 10 cm (height, similarly hereinafter), the thickness of the medium-sized gravel layer with diameter of 10–12 mm is 10 cm, and the small gravel layer with diameter of 8–10 mm is 10 cm. After paving, self-developed fly ash ceramsite is filled in as the main filler; layer height was 100 cm and 120 cm, respectively. The upper part of the filler layer is 20 cm blank and the wastewater drains into the sewer from the upper discharge port. The installed BAF photo is shown in Figure 7.15.

The core filler of the reactor is self-developed fly ash ceramsite. Specific parameters are as follows: particle size: ϕ 4–6 mm; bulk density: 0.85–0.90 g/cm^3; apparent density: 1.4–1.6 g/cm^3; bulk porosity: ≥40%; breakage rate: ≤0.03%; wear rate: ≤2.0%; specific surface area: ≥1×10^4 cm^2/g; loss on ignition: $<$0.03%; uneven coefficient: K_{60}:≤1.40; hydrochloric acid soluble rate: ≤3%; barrel strength: ≥6.5 MPa.

In the initial stage of the experiment, self-made water was used as the reactor inlet. The main components of self-made water are glucose (to provide COD), NH_3Cl (to provide ammonia) and KH_2PO_4 (to provide phosphate) and tap water. The main pollutants in the water were COD 300 mg/L, NH_3-N 20 mg/L and phosphate 2.5 mg/L.

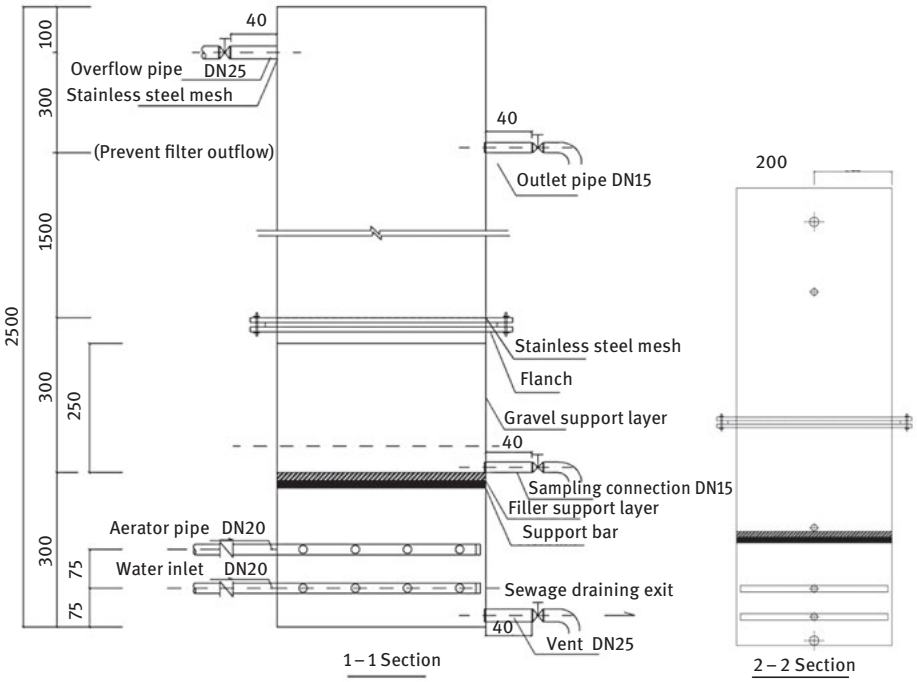

Figure 7.14: Diagram of experimental device.

Figure 7.15: Photo of BAF reactor.

The BAF reactor was operated with continuous water inflow and the operation time was 9 h per day. The water inflow is 80 L/h and the air intake is 480 L/h. Rotameters are used for water and gas flow regulation. Since start-up phase of the reactor takes a

certain amount of time, the effluent was sampled only once a day during this time. After the reactor is started and stable operated, the sampling frequency is increased. During the start-up period, the change of COD, NH_3-N and TP concentrations in influent and outflow water were the main targets investigated.

During the hanging-film phase, the influent flow rate was 80 L/h, the inflow rate was 480 L/h and the gas–water ratio was 6:1. Hanging process lasted about 20 d. The water temperature was about 25 °C. The pH of the water was between 6 and 8.

7.5.1 COD removal effect

The removal efficiency of pollutants of reactor are often first reflected in the COD removal rate. Since this BAF directly treats the self-made wastewater with high COD concentration, it is not expected that the removal efficiency of COD will be high. Figure 7.16 shows the change of COD in influent and effluent during hanging-film phase and the removal rate is shown in Figure 7.17.

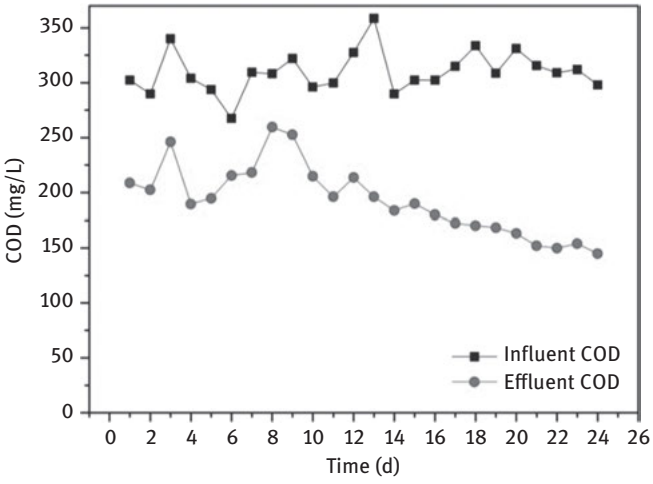

Figure 7.16: COD in influent and effluent during hanging-film phase of BAF.

When BAF is used directly to treat wastewater with high concentration; its removal efficiency will not be too high due to its short hydraulic retention time and other characteristics. It is generally believed that when the filter on the COD removal rate reached 30% or more, the hanging film is successful. In this experiment, the main component of COD from the self-made water is glucose, which has good biodegradability. Therefore, the removal rate of COD is also relatively high. The influent COD concentration of this reactor was set at 300 mg/L. After 25 days, the effluent COD concentration remained at 150–250 mg/L. It can be seen from Figure 7.17 that in the initial operation period of BAF reactor, because of the unstable operation of the reactor

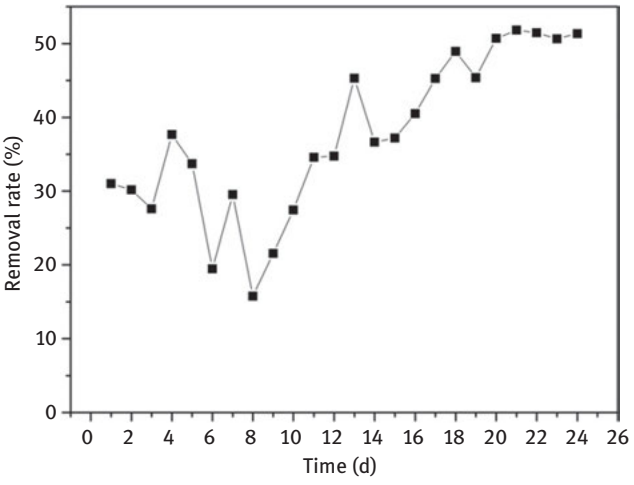

Figure 7.17: COD removal rate during hanging film phase of BAF.

and basically no growth of the biofilm and other factors, the COD removal rate was only from 10% to 30%. After 6 days, the COD removal efficiency of the reactor started to increase steadily and began to rise to 40% and on the 13th day it remained above 40% until the 20th day, and then it rose to about 50% and remained stable. From COD removal efficiency to infer, at this time, the biofilm hanging reached a mature stage.

In view of this process of hanging film, although the effluent concentration of COD fluctuates in the early stage of hanging film, but on the whole, the efficiency of removal COD from the reactor is constantly rising. This may be in the early stages of the reactor, which is affected by the temperature of the incoming water and the heterotrophic microorganisms on the filler. Although the heterotrophic microorganisms reproduce rapidly at the initial stage, their COD removal efficiency will be fluctuated due to the limited ability to adhere on the filler material under the impact of water flow and air flow. After a period of cultivation and acclimation, the number and types of heterotrophic microorganisms on the filler tend to be stable, and the removal of organic substances in the wastewater is relatively stable, so the removal rate of COD tends to be stable in the later stage of the start-up process.

7.5.2 NH_3-N removal effect

The NH_3-N removal rate is an important indicator of the hanging film success of the filler material. It is generally believed that when the NH_3-N removal rate reached 60% and more, the filler is successful at hanging film. Figure 7.18 shows the change of NH_3-N in the influent and outflow during the hanging film, and Figure 7.19 shows the change of NH_3-N removal efficiency in the BAF reactor during the hanging film. The concentration of NH_3-N in reactor influent is maintained at about 20 mg/L, and the effluent concentration was about 12 mg/L in the first 9 days, and the removal of NH_3-

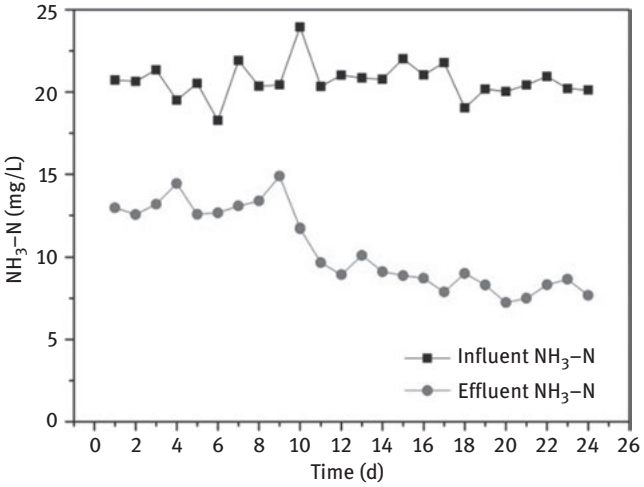

Figure 7.18: NH_3-N in influent and effluent during hanging-film phase of BAF.

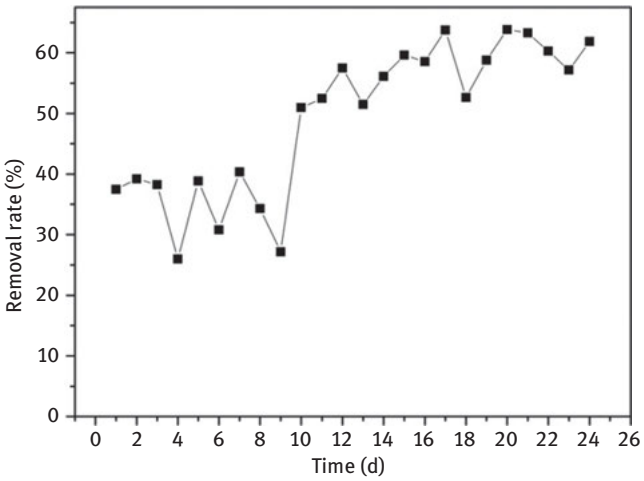

Figure 7.19: NH_3-N removal rate during hanging-film phase of BAF.

N began to increase on the 10th day. The effluent NH_3-N concentration from the 11th day was below 10 mg/L. Examining the change of NH_3-N removal rate, it can be found that the removal rate of NH_3-N in the first 9 days is relatively low, about 40% or less, and the removal rate of NH_3-N gradually increases after the 11th day, and after 20 days the removal rate can be stabilized at about 60%.

As can be seen from Figure 7.18, the difference of NH_3-N concentrations in inlet and outlet are small mainly because these days are the stage of attachment and

adaptation of nitrifying bacteria to the filter in the pool. Moreover, the organic matter concentration of influent is high, which is the dominant environment of carbonated heterotrophic bacteria, which inhibit the growth and reproduction of autotrophic nitrifying bacteria; biofilter has not yet fully nitrification function. However, there is still a certain degree of removal of NH_3-N by the BAF reactor due to the following reasons: first, the NH_3-N removal rate is mainly from the ammonia consumption by heterotrophic assimilation; second, the BAF has a certain degree of NH_3-N removal. The NH_3-N removal started to be improved obviously after the 10th day, because the filter had a higher removal rate of organic matter at this stage. This leads to decreased concentration of organic matter, the inhibition of heterotrophic bacteria on the autotrophic nitrifying bacteria is gradually eased; nitrifying bacteria began to grow and reproduce, so NH_3-N removal rate also will rise.

The nitrification in the BAF is often considered as the main reason for the removal of ammonia from wastewater. More and more researchers pay attention to the research on the nitrification performance of BAF. Most of the previous studies have tried to improve the nitrification efficiency of BAF by optimizing the operating parameters. The results showed that the efficiency of nitrification could reach 100% when the BAF was used to treat the eutrophic water containing ammonia under the conditions of 1:1 gas–water ratio, 5.18 m/h filtration rate and temperature 10 °C. Dillon et al. (1990) studied the nitrification ability of BAF and found that the NH_3-N removal rate can reach 90% when the nitrogen volumetric load is 0.63 kg/(m^3·d). Although the effectiveness of ammonia removal by BAF has been tested in practice, further studies are needed on the influent load, the concentration of organic compounds and the distribution characteristics of nitrifying bacteria.

7.5.3 TP removal effect

Because of the characteristics of BAF reactor, TP removal efficiency has always been low; they are required for adding chemicals to increase TP removal in the operation of conventional BAF. However, the fly ash ceramsite developed by our group has a good phosphorus removal effect. In the earlier experiment, 1.0 g of ceramsite could completely remove the phosphorus concentration of 5 mg/L in 50 mL. Therefore, BAF filler can enhance the reactor's ability to remove phosphorus. Figure 7.20 shows the change of TP inlet and outlet of water during the hanging film, and Figure 7.21 shows the change of TP removal efficiency of the BAF reactor during the hanging film.

The main difference with the conventional BAF is that TP in this BAF has a very good removal effect at the start of the reactor. Although the initial concentration of TP in the influent was lower, the BAF reactor still showed a high TP removal efficiency. Once it reached about 70%, although the TP removal efficiency during the process of fluctuations was maintained at about 60%. The effluent TP concentration was below 1.0 mg/L for most of the time, even close to 0.5 mg/L. In the late stage of the hanging

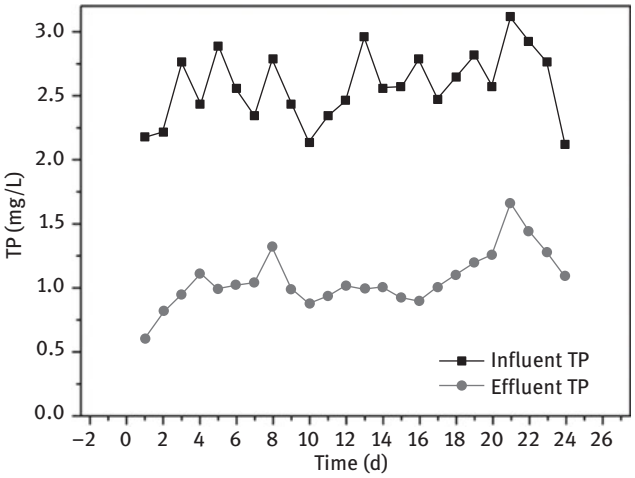

Figure 7.20: TP in influent and effluent during hanging-film phase of BAF.

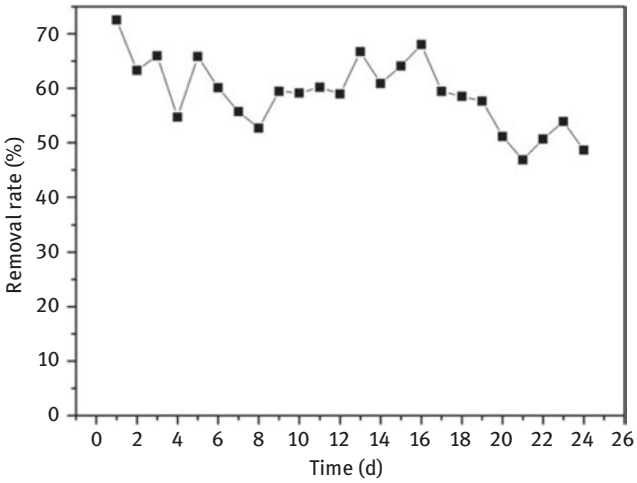

Figure 7.21: TP removal rate during hanging-film phase of BAF.

film, TP removal efficiency decreased. Especially after the 20th day, it will fall back to about 50%, but the TP concentration in the effluent can still be maintained at about 1.0 mg/L.

The biological effect of BAF is not easy to achieve the actual treatment effect of phosphorus removal; it is usually needed to take chemical methods to remove phosphorus. Many studies were the biological methods for phosphorus removal, such as Goncalves et al. (1992) found the way the influent has little effect on phosphorus removal during a study of simultaneous removal of nitrogen and

phosphorus in BAF. AEsoy et al. (1998) found that when denitrification in aerated biofilters, such as using hydrolyzed sludge or hydrolyzed solid waste as external carbon source, the three times higher phosphorus than the growth requirement of microorganisms can be simultaneously removed. Castillo et al. (1999) in the study of biological phosphorus removal of sequencing batch BAF found that while maintaining the raw water of COD:N:P 20: 5:1, influent COD <15 g/(m^2·d), the phosphorus removal rate can reach 72%. However, in general, it is still difficult to achieve simultaneous nitrogen and phosphorus removal only by adjusting operating parameters during the BAF operation. In particular, it is difficult to obtain the phosphorus removal effect and a stable phosphorus removal rate.

Therefore, it is a relatively ideal way to obtain the simultaneous denitrification and dephosphorization effect of BAF reactor treatment in this research. Through biological treatment the denitrification effect is achieved, and through physical and chemical phosphorus treatment the simultaneous removal of nitrogen and phosphorus is achieved. The results show that the self-developed fly ash ceramsite can be used as an auxiliary phosphorus removal material in sewage treatment. The experiment results showed that the phosphorus removal efficiencies in the BAF reactor decreased in the late stage of the hanging film. After backwashing, the removal efficiency was remarkably improved, and the removal rate of TP returned to about 60% again. The phosphorus removal effect in the BAF reactor is mainly caused by the coprecipitation of phosphate by the ceramsite and the phosphorus in the influent. After the experiment goes on for a certain period of time, part of the formed precipitate is attached to the ceramsite surface, so that the contact area between the ceramsite and the inflowing water becomes smaller, resulting in a decrease of the phosphorus removal efficiency. Therefore, after the completion of the hanging-film process, when the BAF reactor is operated normally and the backwashing is carried out regularly, the sediment of the ceramsite surface can be removed during backwashing, so that stable TP removal efficiency can be maintained.

The main raw material of the fly ash ceramic is fly ash from coal-fired power plant and bentonite, $CaCO_3$ and so on. Raw materials are readily available and their preparation is relatively simple. Ceramsite has a large capacity for phosphorus adsorption and other characteristics; it is a BAF filler with promising application.

References

ÆsØy A, Ødegaard H, BACH K, et al. Denitrification in a packed bed biofilm reactor(BIOFOR) – Experiments with different carbon sources. Water Research, 1998, 32(5):1463–1470.

CASTILLOP A, GONZÁLez-MARTÍNezS, TEJEROI.Biological phosphorus removal using a biofilm membrane reactor:Operation at high organic loading rates. Water Science and Technology, 1999, 40(4):321–329.

CHANG W S, HONG S W, PARK J.: Effect of zeolite media for the treatment of textile wastewater in a biological aerated filter. Process Biochemistry, 2002, 37(7):693–698.
CROMPHOUT J.: Design of an upflow biofilm reactor for the elimination of high ammonia concentrations in eutrophic surface water. Water Supply, 1992, 10(3):145–150.
DESBOS G, ROGALLA F, SIBONY J, et al.: Biofiltration as a compact technique for small waste water treatment plants. Water Science & Technology, 1990, 22(3–4):145–152.
DILLON G, THOMAS V.: A pilot-scale evaluation of the“biocarbone process”for the treatment of settled sewage and for tertiary nitrification of secondary effluent. Water Science & Technology, 1990, 22(1–2):305–316.
DU Yongxiang, SHEN Yaoliang, XU Songyu et al.: Study on the Combined Biological Aerated Filter for the Treatment of Polluted Surface Water, Water treatment technology, 2012, 37(12):120–123.
GONCALVES R, ROGALLA F. Continuous biological phosphorus removal in a biofilm reactor. Water Science & Technology, 1992, 26(9–11):2027–2030.
JIANG Ping, HU Jiucheng: Domestic light spherical ceramic used in biological aerated filter, Journal of Environmental Science, 2002, 22(4):459–464.
KENT T, FITZPATRICK C, WILLIAMS S.: Testing of biological aerated filter(BAF)media. Water Science and Technology, 1996, 34(3):363–370.
LIU Jinxiang, LUO Jinsheng, CHEN Chunjing: Influence Factors of Zeolite – Ceramsite BAF Treating polluted Water, Journal of Safety and Environment, 2008, 7(3):48–50.
MANN A T, ESPINET M. STEMPHENSON TOM.: Performance of floating and sunken media biological aerated filter under unsteady state contitions. Water Research, 1999, 33(4):1108–1113.
MOORE R, QUARMBY J, STEPHENSON T.: The effects of media size on the performance of biological aerated filters. Water Research, 2001, 35(10):2514–2522.
OSORIO F, HONTORIA E.: Wastewater treatment with a double-layer submerged biological aerated filter, using waste materials as biofilm support. Journal of Environmental Management, 2002, 65(1):79–84.
PUJOL R.: Process improvements for upflow submerged biofilters. IWA Publishing, 2010.
QI Bingqiang: Application of Biological Aerated Filter in Sewage Treatment, Water Supply and Sewerage, 2000, 26(10):4–8.
QI Xiang, WANG Feiji, WANG Liwei et al.: Comprehensive filtration test and comparison of quartz sand and ceramsite double layer, Energy and Environmental Protection, 2006, 19(5):31–33.
QIU Chi, BAI Yu, ZHOU Xiaojing: Effect of Combined Filter Media on Treating polluted Water, Liaoning Chemical Industry, 2008, 37(9):615–617.
TIAN Wenhua, WEN Xianghua, YANG Aihua et al.: Performance and Influencing Factors of Zeolite Biofilter for Treatment of Low Concentration Domestic Sewage, Environmental Science, 2003, 24(5):97–101.
WANG Ying, LI Shaoming, FAN Kai et al.: Experimental Study on Removal of COD (Cr) and NH_3-N from Municipal Sewage by Biofilter, Journal of Lanzhou University of Technology, 2007, 33(2):73–76.
YU Ying, HUANG Jiangnan, LIN Bo et al.: Development of New Type Water Treatment Filler – Nano Modified Ceramsite, Water Supply and Sewerage, 2005, 30(12):95–99.
ZHANG Liang, ZHANG Yuxian, BAO Weibin et al:. Biological filter media to treat micro-polluted source water in Yao River, Water treatment technology, 2007, 33(1):58–62.
ZHANG Wanyou, CHI Lijuan, CHEN Xuemei et al.: Works and characteristics of several kinds of fiber filter, Water Supply and Drainage in China, 2003, 19(6):23–25.
ZHU Lehui, ZHU Zhongbang: Preparation of Water Treatment Media – Spherical Lightweight Ceramsite, Environmental protection, 2000(1):35–36.

8 The safety assessment and resource utilization of new functional materials

Whether it is “molecular sieve” type or “biofilm carrier” type functional ceramic material, after long-term application in sewage treatment, purification material eventually inevitably needs to be replaced. Waste products are at risk of possible leaching and eventual enrichment of toxic pollutants; therefore, they have to be scientifically disposed. Therefore, it is necessary to study the environmental safety of material residues and pollutants enrichment and their disposal technologies.

8.1 Material environmental safety assessment

For material environmental safety assessment, we need to consider material properties, the application process and the final product. When some low-cost or waste materials using as filler for wastewater treatment, the leaching toxicity and final waste product categories received the most attention. It is necessary to understand the m3ain components and characteristic of pollutants by analyzing and monitoring various enrichment poisonous pollutants of purification materials and further evaluate their environmental safety to provide the basis for their resource utilization.

8.1.1 Leaching toxicity standards

Fly ash and other solid waste are the major components of functional materials such as bio-ceramist, artificial zeolite (or modified artificial zeolite) and BAF ceramsite. Heavy metal contamination may occur during use. The main risk factors for the use of functional materials are product leaching toxicity and the enrichment or leaching of heavy metals on the impact of emission standards.

In general, leaching toxicity can be identified according to the relevant provisions of “Identification standards for hazardous wastes-Identification for extraction toxicity” (GB 5085.3-2007). In addition, the “Solid waste extraction procedure for leaching toxicity-Acetic acid buffer solution method” (HJ/T 300-2007) is also one of the commonly used methods for identifying the leaching toxicity of solid waste. Six kinds of common heavy metal ions (chromium, cadmium, lead, copper, nickel and zinc) in fly ash raw materials were selected as monitoring objects. According to “Identification standards for hazardous wastes-Identification for extraction toxicity” (GB 5085.3-2007), for common heavy metal pollution, if any one of the hazardous components in the solid waste leachate exceeds the concentration limits listed in Table 8.1, then it is hazardous waste with leaching toxicity characteristics. The impact of drainage water

https://doi.org/10.1515/9783110544381-008

Table 8.1: Leaching toxicity results and standard limits.

Heavy metal	Standard limits (mg/L)
Total Cd	1
Total Cu	100
Total Pb	5
Total Zn	100
Total Ni	5
Total Cr	15

quality can be compared with "Discharge standard of pollutants for municipal wastewater treatment plant" (GB 18918-2002) to analyze the characteristics of pollutants.

8.1.2 Monitoring results and analysis

Artificial zeolite (or modified artificial zeolite): The results of product leaching toxicity test are shown in Table 8.2. None of the tested six heavy metal concentrations exceeded the reference standard, indicating that zeolites and modified zeolites meet environmental safety standards. The actual test results of application for the sewage treatment process are shown in Table 8.3. The measured concentrations of heavy

Table 8.2: Leaching toxicity test results.

No.	Heavy metal	Synthetic zeolite (mg/L)	Modified zeolite (mg/L)
1	Cr	not detected	0.239 2
2	Cd	0.019 6	not detected
3	Pb	0.313 9	0.128 6
4	Cu	not detected	not detected
5	Ni	not detected	not detected
6	Zn	0.012 9	0.047 4

Table 8.3: Test results of heavy metals in effluent.

No.	Heavy metal	Synthetic zeolite (mg/L)	Modified zeolite (mg/L)
1	Cr	0.028 9	0.039 2
2	Cd	not detected	not detected
3	Pb	not detected	not detected
4	Cu	0.041 8	0.106 1
5	Ni	not detected	not detected
6	Zn	0.033 6	0.024 4

Table 8.4: Leaching toxicity results and standard limits.

Heavy metal	Leachate concentration (mg/L)	Standard limits (mg/L)
Total Cd	0.001 3	1
Total Cu	not detected	100
Total Pb	0.031 4	5
Total Zn	not detected	100
Total Ni	not detected	5
Total Cr	not detected	15

metal ions were within the allowable limits as compared to discharge standard of pollutants for municipal wastewater treatment plant (Table 8.4). This shows that the environmental safety of synthetic zeolite and modified zeolite is reliable, and it can be used in sewage treatment.

Bio-ceramsite or BAF media: The results of product leaching toxicity test are shown in Table 8.4. The comparison of leachate concentration and standard limits showed that six kinds of heavy metal concentrations in fly ash ceramsite leachate are low. Some indicators of heavy metals are even below the lower limit of detection, and the concentration did not exceed the leaching toxicity identification standard value, indicating that under natural conditions fly ash ceramsite meet environmental safety standards and will not cause secondary pollution to the environment. In addition, to investigate the heavy metals leaching of fly ash ceramsite in practical application, the actual application test results, which are shown in Table 8.5, are compared with "Discharge standard of pollutants for municipal wastewater treatment plant"(GB 18918-2002). The results showed that the concentration of heavy metal ions were within the allowable range. The ceramsite prepared by sintering fixed heavy metals in the raw materials, and the heavy metals leached out under natural conditions met the environmental safety standards.

Table 8.5: The effluent heavy metals and standard results.

Heavy metal	Water concentration (mg/L)	Standard limits (mg/L)
Total Cd	0.000 2	0.01
Total Cu	not detected	0.5
Total Pb	0.004 6	0.1
Total Zn	not detected	1.0
Total Ni	not detected	0.05
Total Cr	not detected	0.1

8.2 Study on resource utilization of N-, P-rich waste materials of functional materials

For the application of environmental functional materials, the disposal of waste and other outlets is still one of the key issues. When functional materials are used for removal of nutrient-based pollutants by deep treatment, the waste of the functional materials is enriched with a large amount of nitrogen and phosphorus nutrient substances and can be comprehensively utilized after being properly treated. Waste as a raw material for preparation of soil improver, planting substrate of soilless cultivation is one of the important development directions. Owing to the inherent properties of artificial zeolite and ceramsite, their use in horticultural cultivation and as soil amendment have been reported for some time. Slow release of artificial zeolite and the fluffing action of ceramsite on the soil have been confirmed. Artificial zeolite can absorb a large amount of nitrogen and phosphorus, and ceramsite can also adsorb a large amount of phosphorus. The environmental safety should be ensured with especially the heavy metals leaching concentration. The nitrogen-rich artificial zeolite and ceramsite can be used as a substrate for plant cultivation or as a soil conditioner to change soil properties and fertility. In this book, corn was chosen as a test plant to examine the effect of artificial zeolite and ceramsite as a soil conditioner.

8.2.1 Effect of nitrogen and phosphorus-rich artificial zeolite waste as soil conditioner on corn growth and development

The main test materials for pot experiment include corn seeds and artificial zeolite. The test plant is corn. Zhen Tian No. 1 and Hua Nong 2008 two kinds of corn are chosen for the test. After selecting the plants, the planting time per pot of corn was 2 months. After 30 days of planting, the chlorophyll content, plant height and stem diameter were measured. The corn was harvested after 60 days, and soil samples and artificial zeolite were taken for analysis.

(1) Foliar growth

Corn leaf area calculation formula: maximum length × maximum width × 0.75; Calculation method of corn leaf area: the total area of the leaves of the plant. The effect of different treatment on the foliage growth is shown in Figures 8.1 through 8.3. These figures show that the zeolite-corn has obvious advantages over the control group. The number of leaves and the total area of leaves with zeolite were larger than that of the control group. The average leaf area was 89.19 cm^2 and 67.94 cm^2, which increased by 31.28%. The average length of leaves and the maximum width of leaves with zeolite were bigger than those in control group, which were 40.03 cm and 34.90 cm, 2.80 cm and 2.47 cm, respectively – increased by 14.70% and 13.36%.

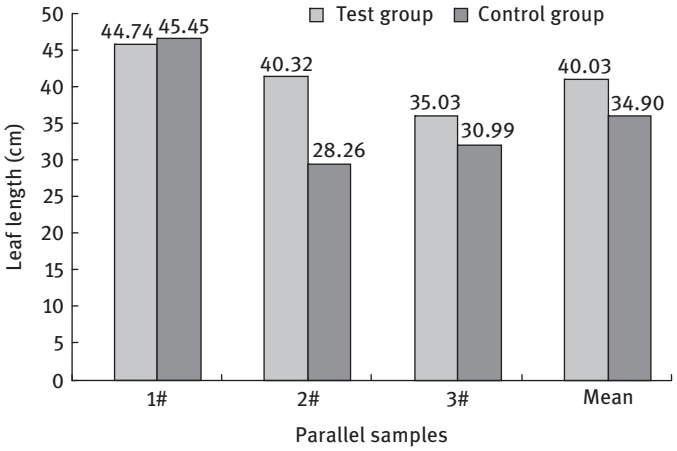

Figure 8.1: The mean value of leaves length of each treatment group.

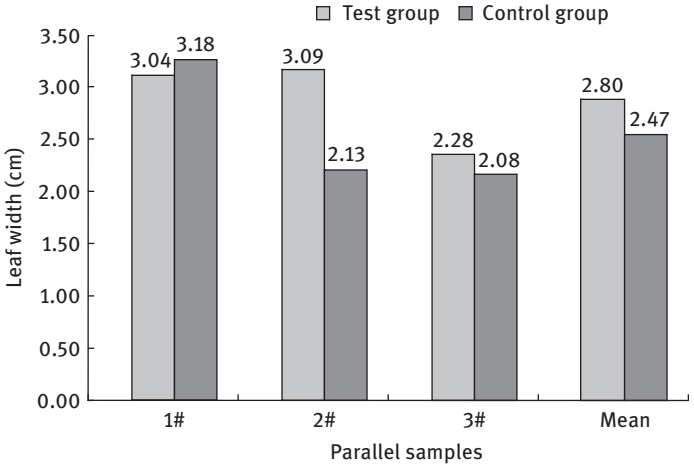

Figure 8.2: The mean value of leaves wide of each treatment group.

(2) Biomass and dry matter accumulation

The wet weight and dry weight of roots and leaves means the fresh part of the weight of the plant and dry matter accumulation, respectively. The results are shown in Table 8.6 and Figure 8.4 based on plant wet weight and dry matter accumulation. It can be seen from the test results that the wet weight and dry weight of roots and leaves with zeolite were higher than those of the control group, and the quantity is the absolute advantage. The leaf wet weight and dry weight increased by 85.29% and 84.03%, respectively. The wet and dry stem weights increased by 83.66% and 100%, respectively, and the wet and dry root weights increased by 155.17% and 125%, respectively.

Table 8.6: The wet and dry weight of corn roots, stems and leaves.

Soil samples	Roots wet weight (g)	Roots dry weight (g)	Stems wet weight (g)	Stems dry weight	Leaves wet weight (g)	Leaves dry weight (g)
Test group 1	3.211 1	0.368	23.416 8	2.271 8	13.549 1	1.267 2
Test group 2	2.368 4	0.519 4	22.499 9	3.226 7	13.579 5	2.545
Test group 3	1.720 5	0.732 2	15.123 6	2.776 7	6.505 4	2.757 2
Control group 1	1.801 3	0.451 4	19.840 7	2.502 2	11.682 2	2.297 8
Control group 2	0.704 3	0.196 6	6.045 1	0.732 8	1.914 6	0.906 6
Control group 3	0.409 5	0.069 1	7.363 6	0.916	4.54	0.364 6

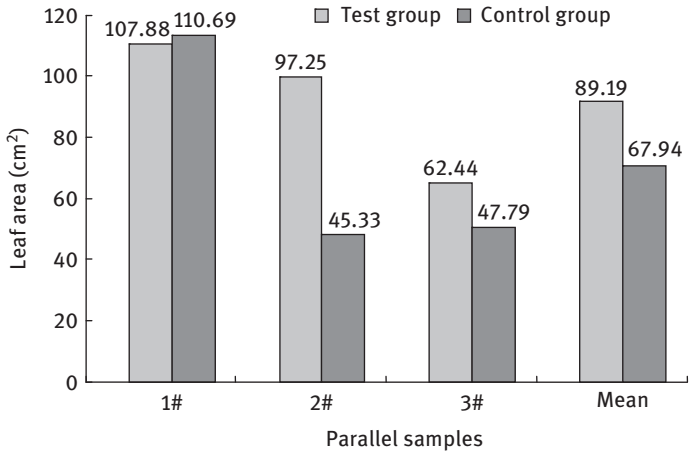

Figure 8.3: The leaves area of each treatment group.

(3) Root growth

The root number is the root number of the underground part of the plant; the root length is the longest root length of the underground part of the plant. For the underground part, the inspection indicators are the degree of root development, the number of roots and the maximum root length. The root growth of different treatment groups is shown in Table 8.7 and Figure 8.5. From the test results, it can be seen that the root system of that with zeolite was significantly developed than the control group, an average of roots are 11.7 with zeolite and 10.7 of control group. The average root length was 30.30 cm, while the control group was 25.06 cm.

As a fertilizers protector and soil conditioner, zeolite has good effect on corn fertilization and significant increase in corn yield. Zeolite has the role of hardening of seedlings and strong seedlings. Although the plant height, leaf length and the number of leaves are slightly smaller and less in the seedling stage of corn, the

Table 8.7: The number of roots and root length of each soil sample.

Soil samples	Root number	Root length/cm
Test group 1	12	39.64
Test group 2	11	28.80
Test group 3	12	22.45
Control group 1	12	42.53
Control group 2	10	24.34
Control group 3	10	8.32

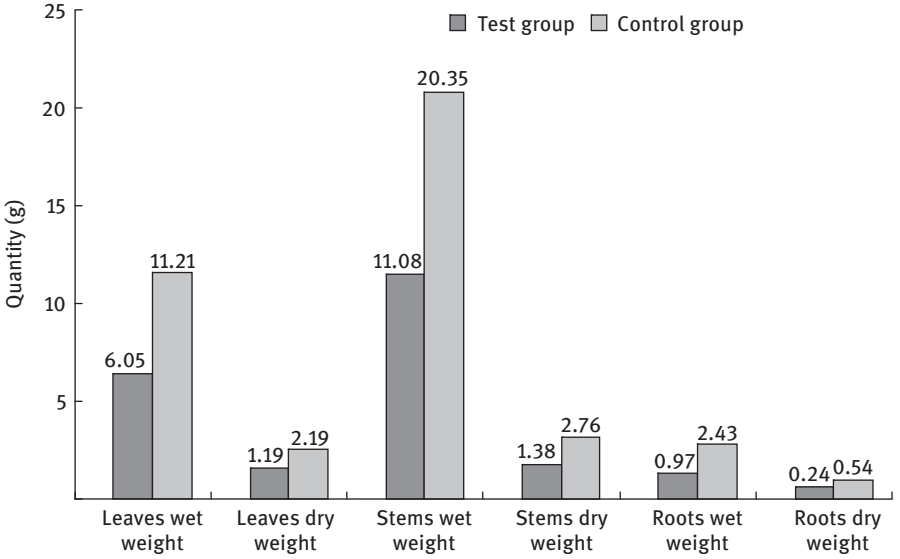

Figure 8.4: The mean value of wet and dry weight of corn roots, stems and leaves.

stem diameter and leaf width increased, roots developed, lateral roots grew in abundance and longer. Zeolite can slowly release fertilizer to ensure the supply of nutrients during the growth of corn and to prevent the premature decline of plants, which prolong the functional period of the leaves and create conditions for increased production. ZHANG Xiang et al. (2000) discussed the application effect of zeolite and its compound fertilizer and found that from the analysis of reproductive traits, the treatment with zeolite compound fertilizer is best. It is pointed out that zeolite is a mineral fertilizer that has a special function as a fertilizer additive. Because of its strong adsorption, it can reduce the loss of fertilizer available component. It contains a variety of nutrients and is conducive to nutrient balance of fertilizers. It promotes nutrient uptake and improves fertilizer utilization and economic benefits of the fertilizer application.

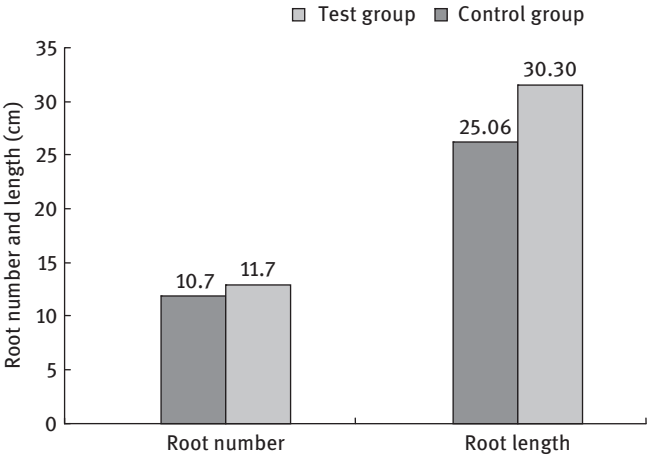

Figure 8.5: The number of roots and the average root length of each treatment group.

The results showed that the synthetic zeolites and modified zeolites had the same functions of keeping fertilizer and slow release as natural zeolite, which was beneficial to the plant growth. It showed that zeolite was feasible as a soil additive and modifier.

8.2.2 Environmental risk and resource disposal of agricultural utilization of water treatment ceramsite waste

The effects of phosphorus-rich ceramsite waste on soil improvement and the growth and development of corn were investigated by pot planting methods. These mainly include the effect of phosphorus-rich ceramsite waste on soil available phosphorus and total phosphorus and effects to improve soil and primal soil on growth and development of corn. In view of the ceramsite waste disposal after domestic wastewater treatment, ceramsite as a soil improver was mixed with a certain percentage of soil to do the study on potted corn. By comparing with the control group, the dissolution of heavy metals under natural conditions and the impact on corn growth were investigated, which provides a reference for safe agriculture utilization of ceramsite waste.

Two corn cultivars, Huanong 2008 (waxy corn) and Zhentian 1 (sweet corn), were selected for a pot experiment. Ceramsite waste materials were taken from the waste of domestic wastewater treatment in the laboratory. The bulk density of ceramsite was 877 kg/m^3, its shape was uniform spherical particles with a diameter of about 5 mm. The dry weight of the test soil was 1.0 kg/L, pH was 5.49, with available phosphorus of 6.1 mg/kg, total phosphorus of 0.7 g/kg.

The direct sowing technology is used to grow corn, and three seeds are planted in each pot. After 5 days, the best growing plant was retained in each pot.

Irrigation management is carried out according to conventional methods to ensure the same water amount per pot. The corn was collected after 60 days for testing. The plant height and stem diameter were determined at the same time of each week during the 6 weeks before harvest. At harvest, corn organs were separately washed with tap water and deionized water. Surface water is blotted up with absorbent paper. Leaf length, leaf width, leaf area (aspect ratio method, the coefficient of leaf area is 0.75), root length, root number and other indicators were determined. The stem dry weight: after 30 min deactivation of enzymes under 90 °C the stem was dried to constant weight of 70 °C.The leave and the root dry weight: after 15 min deactivation of enzymes under 80 °C the leaf and root was dried to constant weight of 60 °C. The root-shoot ratio is calculated accordingly (QI Jian et al., 2006; BAO Shidan, 2000). The various indicators of the experimental data were analyzed according to MANOVA (multivariate analysis of variance) by SPSS12.0. The same factor within the different levels was tested by LSD (Least-Significant Difference).

(1) Effect of different treatments on growth and dry matter accumulation of corn

Ceramsite waste and soil are mixed for potting corn; two varieties of corn grow in good condition. The plant height, stem diameter and other indicators are measured regularly during the growth of corn, and other physiological indexes are also measured to comprehensively analyze the indicators of corn growth under different treatment with a view to understand the feasibility of agricultural utilization of ceramsite wastes by comparing.

(i) Effect of different treatments on the growth of corn stems

By measuring the stem diameter and plant height of corn regularly (Figure 8.6, Figure 8.7), it was found that the plant height and stem diameter of each treatment group increased rapidly in the early period and then stabilized, and some declined slightly later. Overall, the plant height of corn in late growth stage was test group 1> test group 2> control group 1> control group 2, and the size of stem diameter was test group 2> test group 1> control group 2> control group 1. This shows that the plant height and stem diameter of the test group 1 and 2 with the ceramsite were greater than the control group 1 and 2 without ceramisite. Although the plant height of test group 2 was similar to that of control group 2 in the early growth stage, the difference gradually appeared in the later stage.

In order to further understand the effects of different treatments on the growth of corn stems, the plant height and stem diameter were measured on the harvest day and statistically analyzed (Table 8.8). The results showed that there were significant differences in the plant height and stem diameter of two varieties of corn by with or without ceramsite. The plant height of test group 1 and 2 increased by 14.5% and 23.6%, respectively, compared with that of the control group 1 and 2. Similarly, stem diameters increased by 16.2% and 24.5%, respectively.

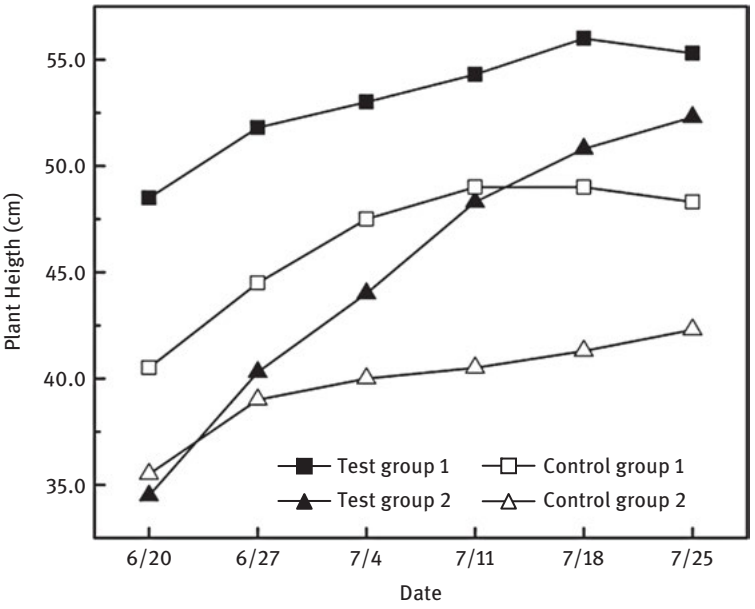

Figure 8.6: Effect of different treatments on plant height of corn.

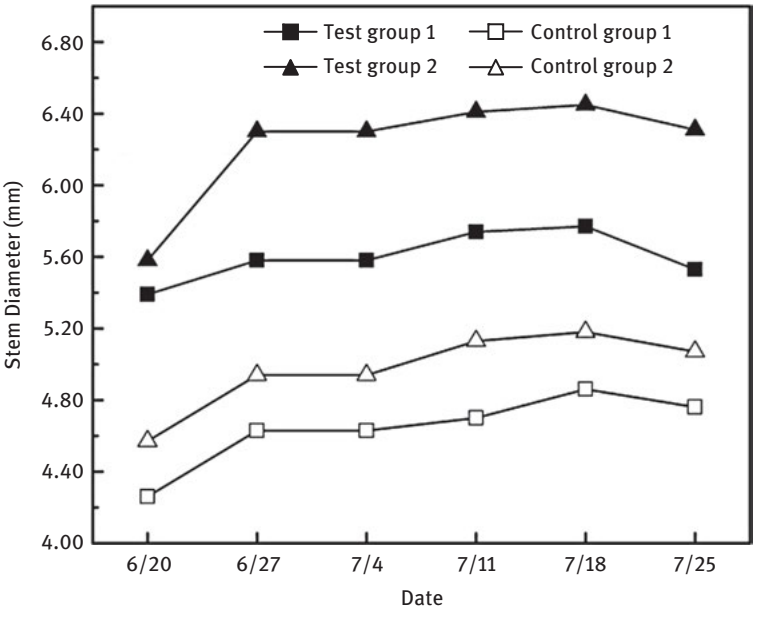

Figure 8.7: Effect of different treatments on stem diameter of corn.

Table 8.8: The plant height and stem diameter of corn.

Treatment	Plant height/cm	Stem diameter/mm
Test group 1	55.3 a	5.53 a
Test group 2	52.3 a	6.31 a
Control group 1	48.3 b	4.76 b
Control group 2	42.4 b	5.07 b

Note: According to LSD test ($P = 0.05$), there is no significant difference between the same column with the same letter, $n = 4$, the same below.

(ii) Effect of different treatments on the growth of corn leaves

As can be seen from Table 8.9, the corn leaves treated by ceramsite grew better than that of the control group. The leaf length of test group 1 and 2 increased by 23.0% and 20.6%, respectively, compared with that of the control group 1 and 2. Similarly, leaves width increased by 42.9% and 36.2%, respectively. The leaf area expanded by 75.9% and 64.6%, respectively. All three indicators achieved significant differences between the two treatments. It is consistent with the stems differences, indicating that the agricultural use of ceramsite waste has a promoting effect on the growth of aboveground parts of corn.

Table 8.9: Effect of different treatments on leaf growth.

Treatment	Leaves length/cm	Leaves wide/cm	Leaves area/cm^2
Test group 1	51.69 a	3.10 a	480.68 a
Test group 2	47.12 a	2.90 a	409.92 a
Control group 1	42.03 b	2.17 b	273.22 b
Control group 2	39.07 b	2.13 b	249.09 b

(iii) Effect of different treatments on the growth of corn roots

There was no significant difference in the roots growth between the two treatments of with or without ceramsite. However, the root growth of test group 1 and 2 was better than that of control group 1 and 2 (Table 8.10). Although there is hardly any difference in root number of Huanong 2008 corn between the two groups, the difference of root length is larger, which of the test group 1 increased nearly by 17.2% than the control group 1. In addition, the root number and root length of Zhentian 1 differ greatly in the two groups. The root number and root length of test group 2 were increased by 33.1% and 24.1%, respectively, compared with that of control group 2.

Table 8.10: Effect of different treatments on root growth.

Treatment	Root number	Root length/cm
Test group 1	12.8 a	22.15 a
Test group 2	23.3 b	26.40 a
Control group 1	12.3 a	18.90 a
Control group 2	17.5 b	21.27 a

(iv) Effect of different treatments on dry matter accumulation of corn

It can be seen from Table 8.11 that the accumulation of corn dry matter is larger than that of the control group. The total mass above ground of test group 1 and 2 was increased by 185% and 150%, respectively, compared with control group 1 and 2. The root mass increased by 309% and 378%, respectively, and the root-shoot ratio increased by 1.23% and 4.72%, respectively. Except root-shoot ratio, the four indicators of stem quality, leaf quality, total quality above ground and root quality were significantly different in the above two treatments. This shows that the application of a certain amount of ceramsite waste may change the soil physical and chemical properties to make it more suitable for the corn growth and increase the biomass so as to produce more dry matter.

Table 8.11: Effect of different treatments on dry matter accumulation in corn.

Treatment	Stem quality/g	Leaf quality/g	Total quality/g	Root quality/g	Root-shoot ratio/%
Test group 1	2.70 a	4.22 a	6.92 a	0.27 a	3.94 a
Test group 2	3.83 a	5.11 a	8.94 a	0.86 a	9.67 b
Control group 1	0.88 b	1.55 b	2.43 b	0.066 b	2.71 a
Control group 2	1.16 b	2.41 b	3.57 b	0.18 b	4.95 b

(v) Influence of applying ceramsite on related physiological indexes of corn

In order to understand the impact of applying ceramsite waste on the physiological indexes of corn, to further understand the value of agricultural waste, the relevant data were analyzed by ANOVA and the results of significance analysis are shown in Table 8.12.

As can be seen from Table 8.12, application of ceramsite has a highly significant effect on indicators of leaf width, leaf area, stem quality and leaf quality of corn. However, there was no significant effect on root number, root length, root-shoot ratio and other indexes, which shows that the aboveground part of corn is affected more than the underground part.

Through analysis and comparison, it was found that agricultural use of ceramsite waste can promote the growth and development of corn. This is due to the ceramsite waste after domestic wastewater treatment with a certain amount of organic matter,

Table 8.12: Effect of ceramsite utilization on corn growth related indicators.

Indicators	Plant height	Stem diameter	Leaves length	Leaves wide	Leaves area	Root number
Significance	*	*	*	**	**	
Indicators	Root length	Stem quality	Leaf quality	Total quality aboveground	Root quality	Root-shoot ratio
Significance		**	**	**	*	

Note: Two "*" indicate highly significant effects (α = 0.01), one "*" indicates significant effect (α = 0.05), and "*" indicates no significant effect.

nitrogen, phosphorus and other nutrients, which can improve soil fertility. In addition, the granular shape can improve the soil pore structure, enhance soil permeability and increase the air amount in the soil, which is more conducive to the growth and development of corn (SAAS, 2004). Therefore, the agricultural utilization of ceramsite waste is a feasible and promising resource-recycling way.

8.3 Conclusion

1. The soil is improved by phosphorus-rich ceramsite waste. The physiological indicators of potted corn with the improved soil were significantly increased than that of the control group, which can promote the growth and development of corn. The corn growth of test group 1 and 2 with ceramsite was significantly better than that of the control group 1 and 2 without ceramsite waste. The application of ceramsite had a highly significant effect on leaf width, leaf area, leaf quality, stem quality, plant height, stem diameter, leaf length and root quality.
2. Ceramsite waste from wastewater treatment has some application prospects in agricultural utilization. Phosphorous-rich ceramsite waste can be used as a red soil conditioner.

References

BAO Shidan: Analysis of soil agriculture, Beijing, China Agricultural Press, 2000.

QI Jian, SONG Fengbin, LIU Shengqun: Physiological responses of maize roots and leaves to drought stress at seedling stage, ecosystem, 2006, 15(6):1264–1268.

Shandong Academy of Agricultural Sciences (SAAS): China Corn Cultivation. Shanghai, Shanghai Science and Technology Press, 2004.

ZHANG Xiang, ZHU Hongxun, SUN Chunhe et al: Effect of Zeolite Compound Fertilizer on Corn, Agricultural Science and Technology, 2000, 2:25–29.

Index

https://doi.org/10.1515/9783110544381-009